SELF-HEALING CORROSION PROTECTION COATINGS BASED ON CORROSION INHIBITOR ENCAPSULATED NANOCONTAINERS FOR MILD STEEL

THESIS

SUBMITTED IN PARTIAL FULFILMENT OF THE REQUIREMENTS FOR THE AWARD OF THE DEGREE OF

Doctor of Philosophy

IN

CHEMISTRY

BY

AARTI GAUTAM

(Roll. No: 719116)

RESEARCH SUPERVISORS

Dr. K. V. GOBI

Professor, NITW

Dr. R. SUBASRI

Scientist 'G', ARCI, Hyderabad

DEPARTMENT OF CHEMISTRY

NATIONAL INSTITUTE OF TECHNOLOGY WARANGAL

WARANGAL – 506 004, TELANGANA, INDIA

APRIL-2024

DECLARATION

This is to certify that the work presented in the thesis entitled *“Self-Healing Corrosion Protection Coatings based on Corrosion Inhibitor Encapsulated Nanocontainers for Mild Steel”,* is a bonafide work done by me under the supervision of **Dr. R. Subasri**, Scientist 'G', Centre for Sol-gel Coatings, ARCI Hyderabad and **Prof. K. V. Gobi**, Professor, Department of Chemistry, NIT Warangal and was not submitted elsewhere for the award of any degree.

I declare that this written submission represents my ideas in my own words and where others' ideas or words have been included, I have adequately cited and referenced the original sources. I also declare that I have adhered to all principles of academic honesty and integrity and have not misrepresented or fabricated or falsified any idea / data / fact / source in my submission. I understand that any violation of the above will be a cause for disciplinary action by the Institute and can also evoke penal action from the sources which have thus not been properly cited or from whom proper permission has not been taken when needed.

Date: (Signature of the student)

Place: **HYDERABAD**   (**AARTI GAUTAM**)

(Roll No.**719116**)

CERTIFICATE

This is to certify that the work presented in the thesis entitled *"Self-Healing Corrosion Protection Coatings based on Corrosion Inhibitor Encapsulated Nanocontainers for Mild Steel"* is a bonafide work carried out by **Ms. Aarti Gautam** under our supervision and was not submitted elsewhere for the award of any degree.

Prof. K. V. GOBI   **Dr. R. SUBASRI**

(Research Supervisor - Internal)   **(Research Supervisor - External)**

Professor   Scientist - G

Department of Chemistry   Centre for Sol-gel Coatings

NIT Warangal   ARCI Hyderabad

This Thesis Dedicated to My Beloved Parents, Brother

and

Fiancé-Deepak Joshi

<u>ACKNOWLEDGEMENTS</u>

LIST OF SYMBOLS AND ABBREVIATIONS

MS	Mild steel
BTA	Benzotriazole
HNT/H	Halloysite nanotube
LbL	Layer-by-Layer
NC	Nanocontainer
FESEM	Field Emission Scanning Electron Microscopy
TEM	Transmission Electron Microscopy
EDX	Energy Dispersive X-ray spectroscopy
BET	Brunauer-Emmett-Teller
XRD	X-ray Diffraction
FTIR	Fourier Transform Infrared Spectroscopy
UV-Vis-NIR	Ultraviolet Visible Near Infrared Spectroscopy
WCA	Water Contact Angle
EIS	Electrochemical Impedance Spectroscopy
PPS	Potentiodynamic Polarization Studies
OCP	Open circuit potential
SVET	Scanning Vibrating Electrode Technique
SST	Salt Spray Test
Z"	Real Impedance
-Z"	Imaginary Impedance
kHz	Kilohertz
V	Volt
mV	Millivolt
R_{ct}	Charge transfer resistance
R_s	Solution resistance
R_{coat}	Coating resistance
CPE	Constant Phase Element
C_{dl}	Double layer capacitance
C_{coat}	Coating capacitance
E_{corr}	Corrosion potential
i_{corr}	Corrosion current density
μA	Microampere

βc	Cathodic Beta coefficient
βa	Anodic Beta coefficient
dec	Decade
cps	Counts per second
Ω	Ohm
deg/$^\circ$	Degree
eV	Electron Volt
$^\circ$C	Degree centigrade
nm	Nanometer
cm^{-1}	Centimeter^{-1}
mm	millimeter
μm	micrometer
θ	Theta
M	Molarity
s	Second
Q_t	amount of corrosion inhibitor released
Q_0	initial amount of corrosion inhibitor
K_0	Zero-order rate constant
K	First-order rate constant
K_H	Higuchi dissociation constant
W_0	remaining weight of corrosion inhibitor at time zero
W_t	remaining weight of corrosion inhibitor at time t
min	minute
mg	milligram
g	gram
RE	Rare-earth
REH	Rare-earth corrosion inhibitors encapsulated into halloysite nanotube

TABLE OF CONTENTS

Contents

CHAPTER-1

Introduction

CHAPTER-1

Introduction

1.1. Mild steel properties and applications

Mild steel (MS) is one of the most important and versatile materials in Civil Engineering field. Properties such as ductility, malleability, and high elasticity make it a more prominent material that can be tailored as per the requirement [1]. MS is quite flexible and possesses high tensile strength, which gives it high wear and tear resistance. It is a cost effective material, which can be recycled over a period of time. Because of all these salient properties, mild steel is used as a significant component, be it infrastructure, construction, chemical industries, oil pipelines, etc. [2].

According to the World steel association, steel utilization in 2022 was 1762 MT with building, and infrastructure accounting for 52 %, mechanical equipment - 16 %, automotive industries 12 %, and remaining for electrical equipment, domestic appliances, other transport, etc., as shown in Fig. 1.1 [3]. Chemical composition of mild steel as per ASTM standard is Carbon (C) 0.25 to 0.29 %, Copper (Cu) 0.20 %, Manganese (Mn) 1.03 %, Phosphorus (P) 0.04 %, Silicon (Si) 0.28 %, Sulphur (S) 0.05 % and rest is Iron. Density of mild steel is 7.85 g/cm^3. Despite possessing several attractive properties, a key issue that obviates the usage of mild steel for long-term applications is its corrosion.
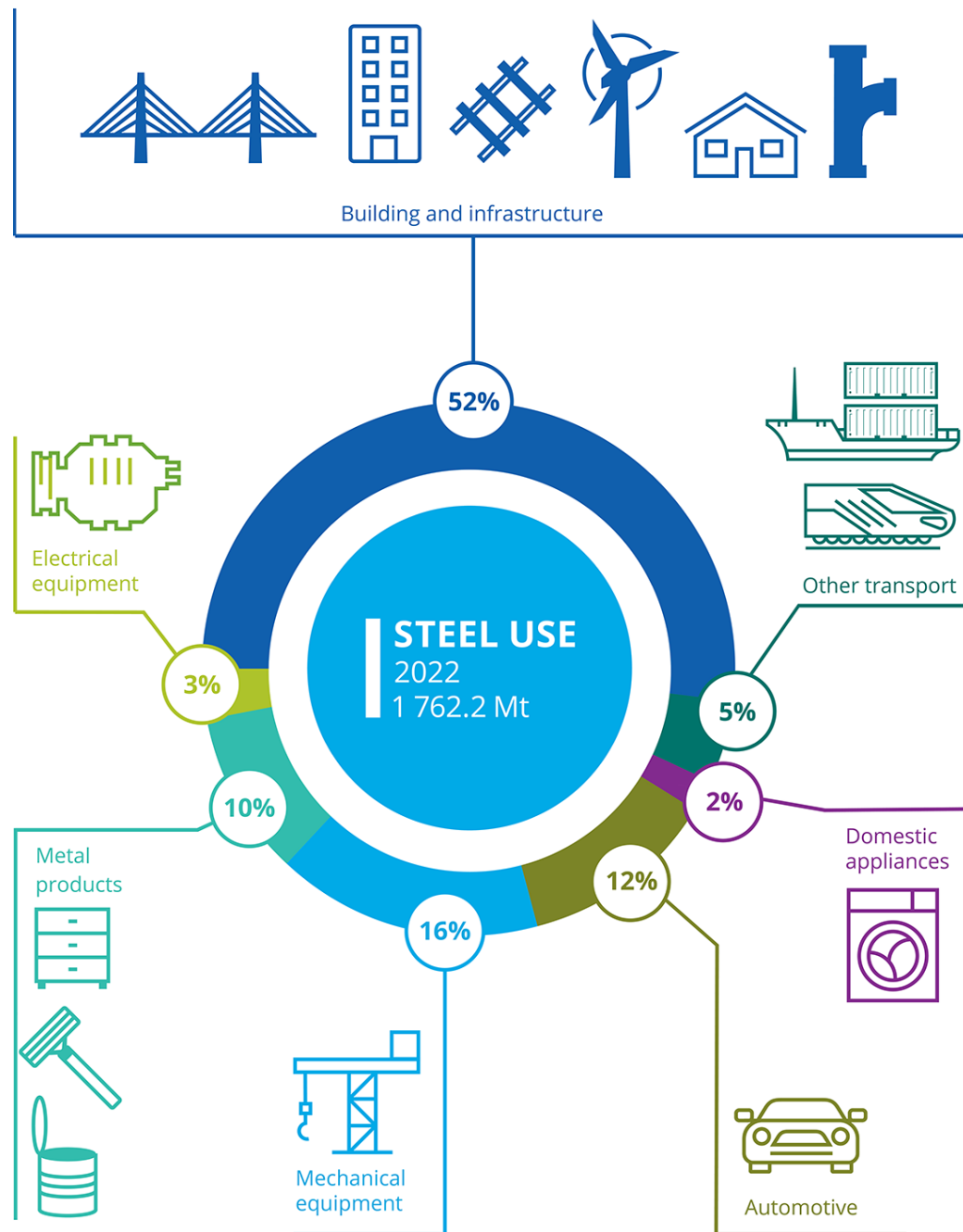
Fig. 1.1 Applications of steel in different sectors (www.worldsteel.org)

Corrosion: Prime reason of engineering failures

Corrosion is a naturally occurring electrochemical process, where the metal or substance starts getting degraded over a period of time due to interaction with aggressive environmental conditions. The metal involved during corrosion in combination with oxygen and water, tends to move towards a more stable state i.e., lowest energy state by forming

stable oxide as corrosion products [4]. Different types of corrosion are shown in Fig. 1.2 and discussed as follows:
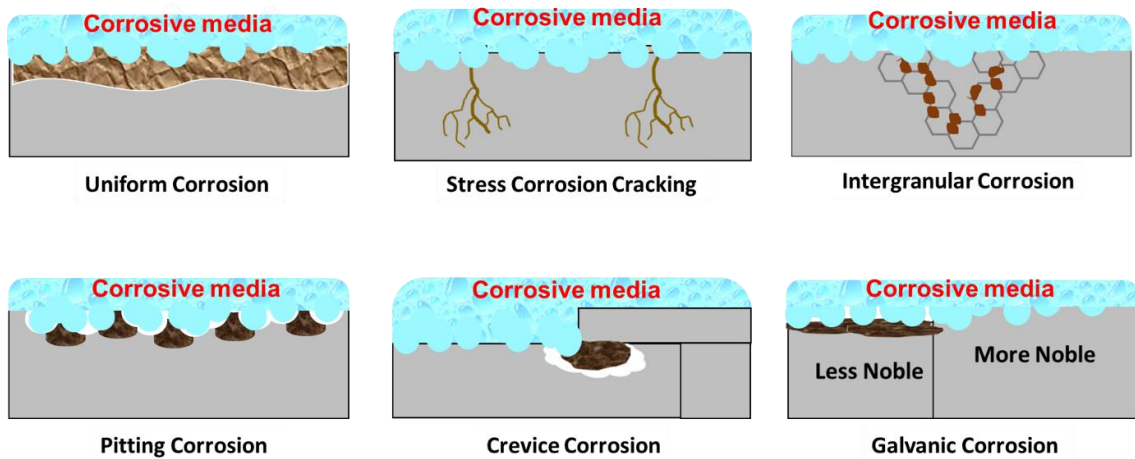
Fig. 1.2. Different types of corrosion (Redrawn from Ref. [4])

1.1.1. Uniform corrosion

It is the type of corrosion where the metal surface degrades or destroys uniformly at the same rate over the barren area. Oxygen is the prime reason for this type of corrosion. It usually occurs on cast iron and steel surfaces. Makhlouf et al. [5] discuss that metal, when kept over water, showed signs of superficial corrosion on the surface.

1.1.2. Stress corrosion cracking

This type of corrosion occurs when the metal is subjected to any stress, which results in crack initiation. Eliaz et al. [6] report that corrosion accelerates at higher temperatures, higher residual internal stress or external stress, respectively.

1.1.3. Localized corrosion

On exposure to corrosive media, smaller localized areas are affected more when compared to bulk [7]. Here, the area with minimum oxygen supply acts as the anode, and the area where full oxygen supply is present acts as the cathode. This can be further categorized into (a) Pitting Corrosion: It occurs when the oxide film on the metal surface breaks down, causing the metal underneath exposed to corrosive media [8]. The electrochemical reaction during the process leads to the formation of cavities or pits and hence its name "Pitting Corrosion" and (b) Crevice Corrosion: It occurs when the two metal surfaces are in close contact with each other causing the

accumulation of electrolyte or corrosive media in the crevice or gaps e.g., metal surfaces exposed to marine water conditions [9,10].

1.1.4. Inter granular corrosion

Intergranular corrosion usually occurs at grain boundaries or areas adjacent to the grains of the metal or alloys. This type of corrosion occurs due to the precipitation of a secondary phase or depletion of one of the alloying elements near the grain boundary causing poor strength of the metal or alloy [4].

1.1.5. Galvanic corrosion

It is also called as "bimetallic corrosion". It occurs when two unlike metals are connected electrically with a suitable electrolyte. The metal connected at cathode is the less reactive one which is protected, while the one connected at anode gets corroded. The corrosion accelerates when there is an increase in the potential difference of the two connected metals [4].

1.2. Economic Impact of Corrosion

NACE International started the International Measures of Prevention, Application, and Economics of Corrosion Technologies (IMPACT) study to analyse the current situation and role of corrosion management by government and industries, so as to establish best protocols [11].

Corrosion is estimated to cost the world $2.5 trillion, or 3.4 % of global GDP (2013). It is estimated that by using available corrosion control practises, savings of between 15 % and 35 % of the cost of corrosion could be realized, i.e. between US$375 and $875 billion annually on a global scale. Individual safety or environmental consequences are typically excluded from these costs. Several industries have realized that a lack of corrosion management can be very costly through near misses, incidents, forced shutdowns (outages), accidents, and so on, and that proper corrosion management can result in significant cost savings over the lifetime of an asset [12].

1.3. Corrosion Mechanism of Mild Steel

Mild steel substrates, when exposed to coastal atmosphere, show noticeable corrosion products on their surface. Reasons for mild steel corrosion can be (i) the presence

of chloride ions in the vicinity of metal surface that increase the conductivity of the electrolyte film, thereby causing the passive film to breakdown; (b) chloride ions present in sea-salt are hygroscopic in nature (sodium chloride, NaCl) which initiates the corrosion on steel surface at relative humidity values of below 100 % [13,14].

Mild steel corrosion reaction at anode:

$$Fe \longrightarrow Fe^{2+} + 2e^- \quad\text{------------------------} \quad (1)$$

Reaction at cathode involves the reduction of oxygen:

$$\frac{1}{2}\, O_2 + H_2O + 2e^- \longrightarrow 2OH^- \quad\text{------------------} \quad (2)$$

The OH$^-$ ions thus formed migrate toward the anodic site to form iron (II) hydroxide (first stage of rust product):

$$Fe^{2+} + 2OH^- \longrightarrow Fe(OH)_2 \quad\text{--------------------} \quad (3)$$
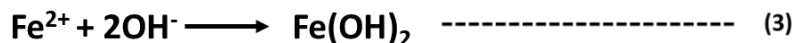
The ferrous ions generated at anodic sites are balanced by chloride ion migration, thus forming:

$$Fe^{2+} + 2Cl^- \longrightarrow FeCl_2 \quad\text{------------------------} \quad (4)$$

On prolonged exposure to oxygen and moisture, the formed iron chlorides are converted into rust product:

$$FeCl_2 + \frac{3}{2} H_2O + \frac{1}{4} O_2 \longrightarrow FeOOH + 2HCl \uparrow \text{------------------} \quad (5)$$

As per Evans et al [15], the oxyhydroxide formed in equations 3 and 5, reduces to magnetite i.e., Fe_3O_4 which further reduces to hematite i.e., Fe_2O_3 (during drying state):

$$8FeOOH + Fe^{2+} + 2e^- \longrightarrow 3Fe_3O_4 + 4H_2O \quad\text{----------------} \quad (6)$$

$$3Fe_3O_4 + \frac{3}{4} O_2 \longrightarrow \frac{9}{2} Fe_2O_3 \quad\text{------------------------} \quad (7)$$
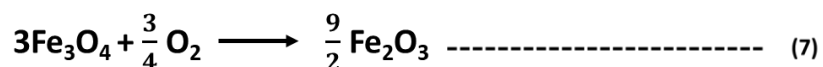
1.4. Combating Corrosion

Protection of the metal component is necessary to prevent the surface from being corroded. Various ways that are practised to do so are as follows:

1.4.1. Galvanization

This corrosion prevention method involves dipping steel into molten zinc. The iron in the steel reacts with the zinc to create a tightly bonded alloy coating which serves as protection. For more than 250 years, this procedure has been employed to prevent corrosion on items like playground equipment and creative sculptures. The object that is to be coated is submerged in molten zinc; a metal which is more electronegative than the object itself, during the pre-treatment process which is referred to as galvanization and shown in Fig. 1.3.
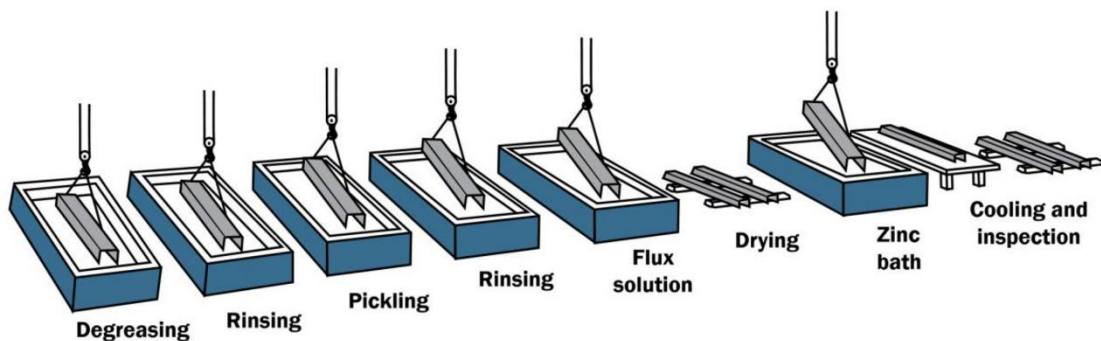
Fig. 1.3. Schematic representation of hot-dip galvanization process (Reproduced from ref. [17] with permission)

When taken out of the zinc bath, the zinc oxidizes, creating a passivated surface with a distinctive pattern [16].

Unfortunately, galvanization can't be done on-site, as some equipment may simply be too massive for the process to be carried out. In addition, zinc can chip or peel off if exposed to an aggressive environment and can speed up the process of zinc wear, leading to increased maintenance. Lastly, the zinc fumes that are released from the galvanization process are highly toxic.

1.4.2. Cathodic protection

In this process, in order to mitigate the tendency for corrosion, the mild steel surface potential is shifted in a cathodic direction using the electrochemical technique, where electrons are supplied from a different source, often using galvanic anodes connected on or near the surface, the active sites on the metal surface are transformed into passive sites as shown in Fig. 1.4. Metals used for anodes include aluminum, magnesium, or zinc [18].
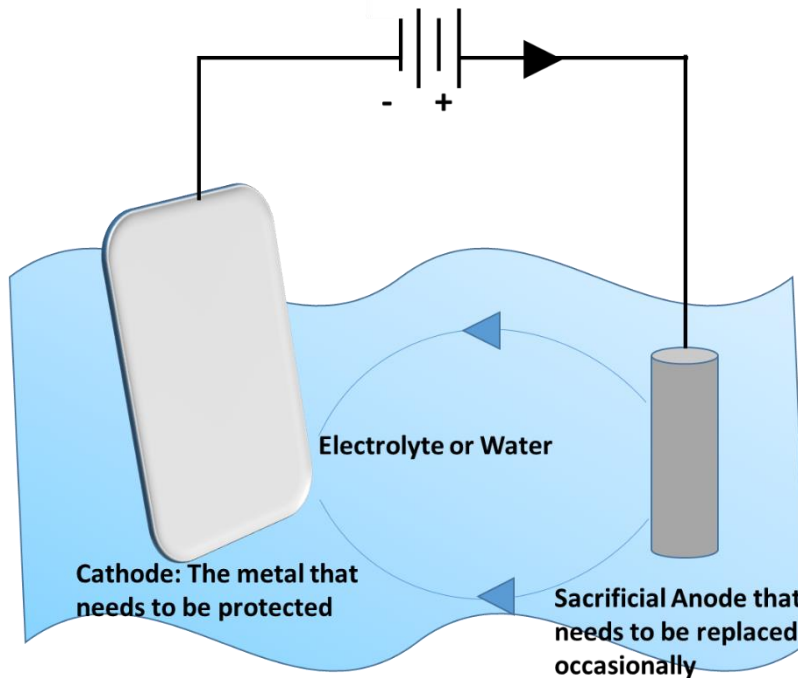
Fig. 1.4. Schematic showing cathodic protection

Cathodic protection is quite effective, however anodes wear out and need to be examined and/or replaced frequently, which might raise maintenance expenses. Additionally, they add to the weight of the attached structure and occasionally fail in high-resistance settings.

1.4.3. Anodic protection

Anodic protection is the preservation of a metal in its passive condition. This method depends on the concept of passivity. The structure is shielded from the corrosive environment by applying a set voltage to the metal, which needs to be protected in order to create a passive film on it as shown in Fig. 1.5 [18].
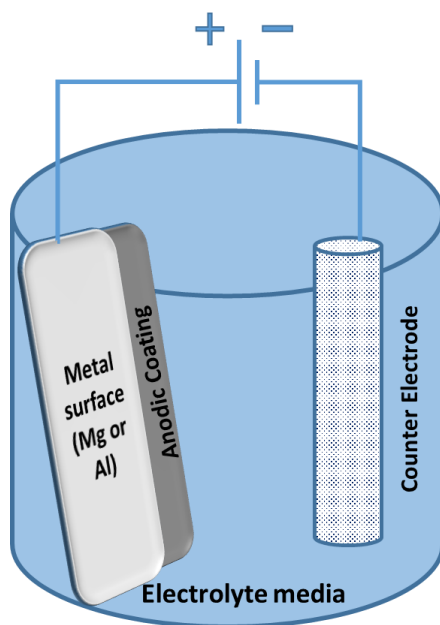
Fig. 1.5. Set-up for anodic protection

1.4.4. Barrier coatings

By isolating the metal from the corrosive environment, corrosion can be avoided using protective coatings. Their main characteristics include (i) good resistance to corrosion, (ii) perfect adherence to the underlying metal and (iii) continuity so as to cover the metal surface completely.

Traditional surface treatment for steel surfaces was derived from conversion coating, capable of resisting any chemical attack by forming a corrosion-protective film.

1.4.4.1. *Phosphate conversion coating*

Phosphate conversion coatings (phosphating) are usually porous and have good adherence, acting as perfect base for any top coat such as primers, paints or oils [19]. Phosphate coating results in small unevenly distributed anodic areas, which remain uncoated on metal surface, forming pinholes. These pinhole structures serve as a path for penetration of corrosive species e.g., chloride ions from salt water, resulting in damage of the coating [20]. Phosphating is a tedious and time-consuming approach, hence better alternatives such as smart coating becomes necessary.

1.4.4.2. *Chromate conversion coating*

The chromate conversion coating (chromating) is similar to phosphating and can be used for materials other than steel. Chromating process is fast, easy and cost-

effective, where the formed film is in the form of thin-gel like structure giving excellent adherence properties [21].

Figure. 1.6 (a) shows the schematic of barrier coatings which restricts the entry of foreign corrosive species, whereas, Fig. 1.6 (b) shows the use of phosphate and chromate conversion coating below the primer layer and top-coat.
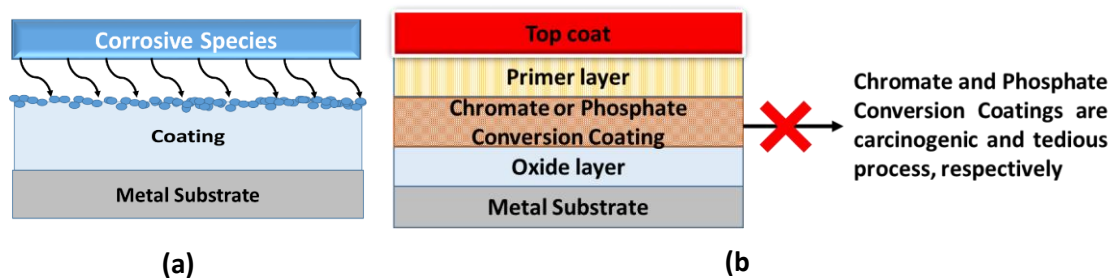
Fig. 1.6. (a) Schematic representation of a barrier coating, and (b) illustration of chromate and phosphate conversion coatings underneath the primer and top-coat

As the development of new technologies takes place, it brings different aspects such as health, and environment into consideration. Hexavalent chromium compounds used in chromating process cause serious threat to environment as they are carcinogenic. As per recent legislation concerning human health, the use of chromate-free coatings for corrosion prevention is strictly monitored [22].

Concerning the above facts, paint industries are looking for an alternative where the chances of toxicity and emission of low volatile compounds are bare minimum with excellent corrosion protection capability. Sol-gel methodology is a potential alternative to develop cheap, easy to fabricate, cost-effective and environment friendly coatings [20].

1.5. Evolution of Sol-gel Coatings Technology

1.5.1. Insights from past

J. J. Ebelmen was the first one to synthesize a transparent material via sol-gel synthesis in the year 1845. On close observation, he analyzed that the ester of silicic acid hydrolyses very slowly to give hydrated silica [23]. Approximately a century later, in the year 1930, Geffcen and Berger from Schott Company used sol-gel process for developing oxide layers on glass using different metal-based precursors. Sol-gel chemistry got its

popularization among scientists from the work carried out by Dislich in the early 1970s [24]. Dislich developed borosilicate glass by heating baths of oxide powders obtained via low-temperature sol-gel process [25]. The first ever international conference "Glasses and Glass Ceramics obtained from Gels" to mark the significance of sol-gel technology was held in Padova, Italy in the year 1981. S. Sakka (Editor-in-chief) established a special Journal of Sol-gel Science and Technology in 1993 to facilitate the exchange of new ideas and knowledge related to sol-gel science among the scientific community [24].

1.5.2. Sol-gel chemistry

The potential to create a solid-state material from a chemically homogenous precursor is one of the primary advantages of sol-gel chemistry among the above techniques. One should be able to manufacture complex inorganic compounds with lower processing temperatures and shorter synthesis durations [26]. Sol-gel process is a bottom-up approach of producing solid materials from small molecules. Sol-gel consists of two parts, "sol" and "gel". Sol is a stable suspension of colloidal solid particles in a liquid. Gel is a semi-rigid mass formed when the solvent tends to evaporate, which causes the left out particles to bind and form a 3-D network. Sol-gel process typically involves four steps: Hydrolysis, Polycondensation, Growth of Particles and Agglomeration of polymeric structures to form a continuous network in liquid making a thick gel [27]. Both the hydrolysis and polycondensation reactions occur simultaneously, where precursors like Silicon Alkoxides / Metal Alkoxides / Metal Salts forming Siloxane, i.e. –silicon-oxo-silicon-(-Si-O-Si-) / Metalloxane i.e. –metal-oxo-metal- (-M-O-M-) bonds as shown in Fig. 1.7 [20].

Hydrolysis Reaction

$$RO-\underset{\underset{OR}{|}}{\overset{\overset{OR}{|}}{Si}}-OR \quad + \quad H_2O \quad \xrightarrow{H^+} \quad RO-\underset{\underset{OR}{|}}{\overset{\overset{OR}{|}}{Si}}-OH \quad + \quad ROH$$
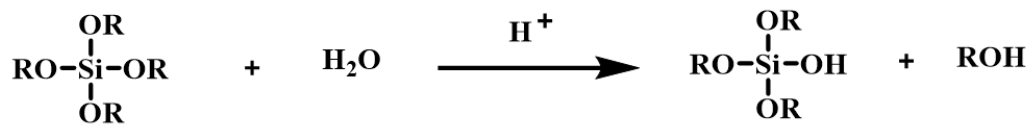
Condensation Reaction with water formation

$$RO-\underset{\underset{OR}{|}}{\overset{\overset{OR}{|}}{Si}}-OH \quad + \quad OH-\underset{\underset{OR}{|}}{\overset{\overset{OR}{|}}{Si}}-OR \quad \xrightarrow{H^+} \quad RO-\underset{\underset{OR}{|}}{\overset{\overset{OR}{|}}{Si}}-O-\underset{\underset{OR}{|}}{\overset{\overset{OR}{|}}{Si}}-OR \quad + \quad H_2O$$
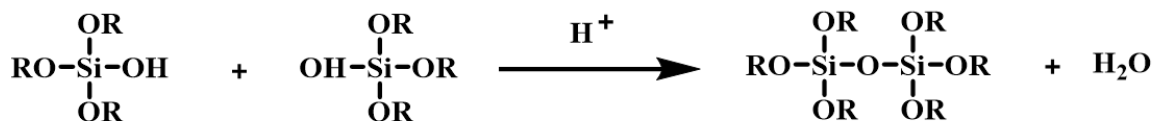
Condensation Reaction with alcohol formation

$$RO-\underset{\underset{OR}{|}}{\overset{\overset{OR}{|}}{Si}}-OH \quad + \quad RO-\underset{\underset{OR}{|}}{\overset{\overset{OR}{|}}{Si}}-OR \quad \xrightarrow{H^+} \quad RO-\underset{\underset{OR}{|}}{\overset{\overset{OR}{|}}{Si}}-O-\underset{\underset{OR}{|}}{\overset{\overset{OR}{|}}{Si}}-OR \quad + \quad ROH$$
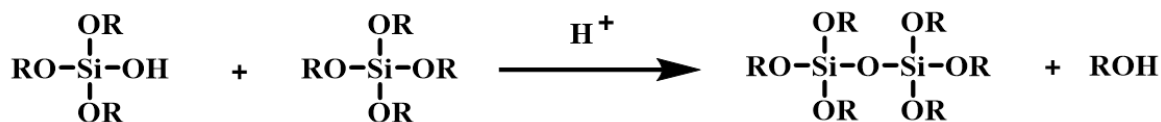
Fig. 1.7. Reactions involved during sol-gel process

Hydrolysis is the chemical reaction where two or more molecules join together to form a colloid or the *sol*. The sol then forms an inorganic network containing a liquid phase, which is the *gel*. Formation of a metal oxide involves connecting the metal centers with oxo (M-O-M) or hydroxo (M-OH-M) bridges, therefore generating metal-oxo or metal-hydroxo polymers in solution. Since the neutral reaction is extremely slow, the sol-gel process of silica is usually triggered by either acid or base catalysts to make it faster [26]. After the reaction is complete,

it can be used as a thin-film coating on metal substrates. Various techniques used for coating application are: dip-coating, spin-coating, spray-coating and electrodeposition. Irrespective of the coating method, the crucial step is the curing process, where the solvent or water evaporates and causes contraction, which could sometimes lead to cracks in the coating. As a result, heat treatment becomes a critical criterion in developing such thin film coatings. Thus, sol-gel coating is a more environmentally friendly alternative to traditional toxic conversion coatings for imparting corrosion resistance. Apart from corrosion resistance,

these coatings can also be abrasion, oxidation, and water resistant. Examples of some sol-gel precursors are shown in Fig. 1.8.
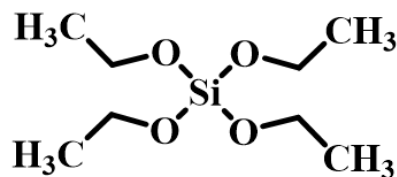
(a) Tetraethyl orthosilicate (TEOS)
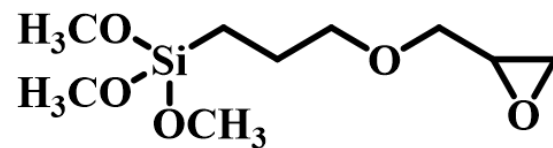
(b) (3-glycidyloxypropyl)trimethoxysilane (GPTMS)

(c) (3-aminopropyl)trimethoxysilane (APTMS)
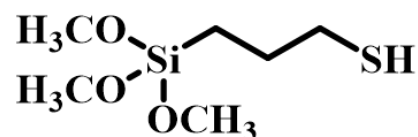
(d) (3-mercaptopropyl)trimethoxysilane (MPTMS)

Fig. 1.8. Structures of organic and inorganic sol-gel precursors

1.5.3. Literature review on sol-gel coating developed for steel

According to Quian et al. [28], coatings developed on carbon steel using pre-hydrolyzed amino-siloxanes provide excellent anti-corrosion properties in aggressive alkaline, acidic, or saline environments. Kannan et al. [29] generated a hybrid coating by copolymerizing 2-methacryloyloxyethyl-phosphate and methacryloxypropyl trimethoxysilane (MAPTS). Phosphate groups in the matrix improve interfacial bonding between the coating and the metal substrate, resulting in greater corrosion resistance. Chou et al. [30] described the use of copolymerized tetraethyl orthosilicate (TEOS) and MAPTS on stainless steel grades 304 and 316. The hybrid coating formed on the substrate was uniform and free of surface defects, resulting in excellent corrosion resistance. Jianguo and colleagues [31] investigated the effect of a hybrid silica gel/Dacromet composite coating on carbon steel under acid-catalyzed hydrolysis using TEOS and MAPTS in ethanol. The coating system exhibits improved corrosion-erosion resistance. Castro et al. [32] studied the effect of dip-coating and electrophoretic deposition (EPD) of base-catalyzed hybrid silica sols containing TEOS and methyltriethoxysilane (MTES) on steel. It was discovered that the corrosion resistance of coatings generated by EPD was two orders of magnitude higher than that of dip-coating, implying that the coating produced by EPD was uniform and defect-free. Guin et al. [33] used titanium-isopropoxide and N-phenyl-3-aminopropyltriethoxysilane in their work, which results in a hybrid nanotitania-silica composite coating after

polycondensation. It was concluded that the coating, when applied to steel sheets, provided hydrophobicity, which improved the coatings' corrosion resistance. Jeyaram et al. [34] generated a silane-based coating on mild steel substrates by using (3-glycidyloxypropyl) trimethoxysilane (GPTMS) as the precursor and (3-aminopropyl) trimethoxysilane (APTMS) as the cross-linking agent. Electrochemical studies and salt spray tests revealed that silane-based coatings were more corrosion resistant. Furthermore, these coatings have demonstrated low wettability and a higher contact angle. Duran et al. [35] used TEOS and MTES to create a hybrid sol-gel film under basic-catalyst conditions. The galvanised steel coating improves corrosion resistance for both the zinc layer beneath and the steel substrate.

Though sol-gel coatings have prominent barrier properties to withstand corrosive environment, but in order to provide active corrosion inhibition, use of corrosion inhibitors as an additive in the sol-gel coating is widely studied and practised.

1.6.   Corrosion Inhibitors

Complete elimination of corrosion is nearly impossible, but it can be mitigated or prevented to a large extent. The first step to control corrosion is using corrosion inhibitors. The choice of selecting best corrosion inhibitors depends on their compatibility with the metal surface, ease of availability, cost-effectiveness, environment friendly nature and non-toxic properties [36]. Corrosion inhibitors are classified into organic and inorganic corrosion inhibitors. Organic corrosion inhibitors slow down the corrosion process by adsorbing on the metal surface, whereas, inorganic corrosion inhibitors block or react with the anodic sites to prevent corrosion [37]. Some of the examples of organic corrosion inhibitors are shown in Fig. 1.9.
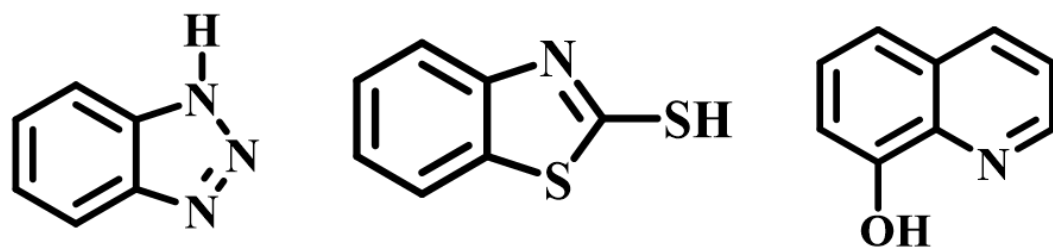
(a) Benzotriazole (BTA)   (b) Mercaptobenzothiazole (MBT)   (c) 8-Hydroxyquinoline (8-HQ)

Fig. 1.9. Structures of organic corrosion inhibitors

Organic corrosion inhibitors are composed of heteroatoms such as nitrogen, oxygen, and sulphur. The inhibition mechanism depends upon the donation of a lone pair of electrons present in these heterocyclic compounds to empty or vacant d-orbital of the metal [38, 39].

Because of the presence of these heteroatoms, a protective passive film is formed on the metal surface, which acts as a barrier to prevent further corrosion.

Inorganic corrosion inhibitors are composed of metallic compounds e.g., chromates, nitrates, acetates, molybdates, phosphates, etc [40]. In general, inorganic corrosion inhibitors show either cathodic or anodic reactions, whereas organic corrosion inhibitors show cathodic, anodic or mixed type.

To calculate inhibition efficiency (I.E) of the corrosion inhibitor, the following equation is used:

$$I.\,E\,\% = \frac{C.R_0 - C.R}{C.R_0} \times 100$$

where C. R_0 and C. R are corrosion rates in the absence and presence of corrosion inhibitors, respectively.

1.6.1. Literature review on corrosion inhibitors loaded sol-gel coatings for steel

Perrin et al. [41] created a hybrid sol-gel matrix with triethylenetetramine (TETA) as a catalyst for mild steel corrosion protection. TETA acted as an efficient basic catalyst for the condensation of GPTMS and TEOS, according to Si High-Resolution Magic Angle Spinning Nuclear Magnetic Resonance (HRMAS NMR) spectroscopy. Electrochemical impedance spectroscopic studies revealed that adding TETA to the sol-gel matrix improved the barrier property of the coatings. Victoria et al. [42] used the sol-gel technique to create a functionalized coating with Santa Barbara Amorphous-15 or SBA-15 (Silica) as the matrix and fluconazole as the corrosion inhibitor. After that, the prepared composite was dispersed in nitrocellulose resin and applied to MS. When exposed to NaCl and $(NH_4)_2SO_4$, EIS studies revealed that the coatings have good barrier properties. Acero-Gutiérrez et al. [43] used SnO_2 nanoparticles dispersed in SiO_2 coatings to develop a coating for A36 steel. Electrochemical tests in a 3 wt% NaCl solution revealed that the coating had improved barrier properties, as well as increased corrosion resistance. Tuan et al. [44] discussed the use of a hybrid sol-gel matrix dispersed with caffeine extracted from tea leaves to protect mild steel from corrosion. Caffeine-doped coatings were found to have greater inhibition efficiency. Tafel plots revealed that the inhibition was of the mixed type, which means that both anodic and cathodic reactions were suppressed at the same time. The coating was hydrophobic, according to water contact angle (WCA) analysis, preventing contact with a corrosive

medium. Samiee et al. [45] produced a silane-based coating with benzimidazole/cationic praseodymium inhibitors. Electrochemical studies and salt spray tests revealed that coatings dispersed with inhibitor mixtures have competent self-healing properties. Trabelsi et al. [46] used a bis-[triethoxysilylpropyl]tetrasulfide matrix containing cerium nitrate or zirconium nitrate in an effort to control galvanized steel corrosion. The inhibitor-doped film outperforms the neat coating due to reduced porosity and increased thickness. To protect 304 L stainless steel in a 3.5 % NaCl solution, Zandi Zand et al. [47] used a cerium-doped silane coating. The significant improvement in corrosion resistance when cerium ions were present was attributed to improved barrier properties and corrosion inhibition ability.

Coated substrates exposed to wet conditions for an extended period of time can affect inhibitor release and accelerate corrosion inhibitor depletion, compromising the coating barrier properties [48]. Encapsulation into nanocontainers becomes critical for ensuring long-term inhibition action and controlling the fast release of the corrosion inhibitors [49]. These intelligent nanocontainers serve as a repository for corrosion inhibitors [50, 51]. During corrosion, the local pH of the affected area rises, signaling the nanocontainers to release the corrosion inhibitor and heal the damaged area. Loading these encapsulated nanocontainers to the coating, which are capable of responding to external stimuli such as pH, temperature, pressure, and so on, can increase the durability of the coating while also improving its barrier properties [52]. The coatings thus obtained were termed "self-healing coatings," as they could both heal the affected area and prevent the underlying metal surface from corroding.

1.7. Self-healing Coatings

To understand self-healing coatings, it is necessary first to comprehend the definition of self-healing. Self-healing refers to the ability to repair damages on its own. The motivation or inspiration for developing these coatings came from the naturally occurring self-healing action of living organisms, in which a wound or cut heals or repairs itself over time. As a result, self-heal coatings are structurally designed engineered products in which corrosion

inhibitors encapsulated into nanocontainers release as a result of physical changes in its surrounding environment, healing the damaged area as represented in Fig. 1.10.
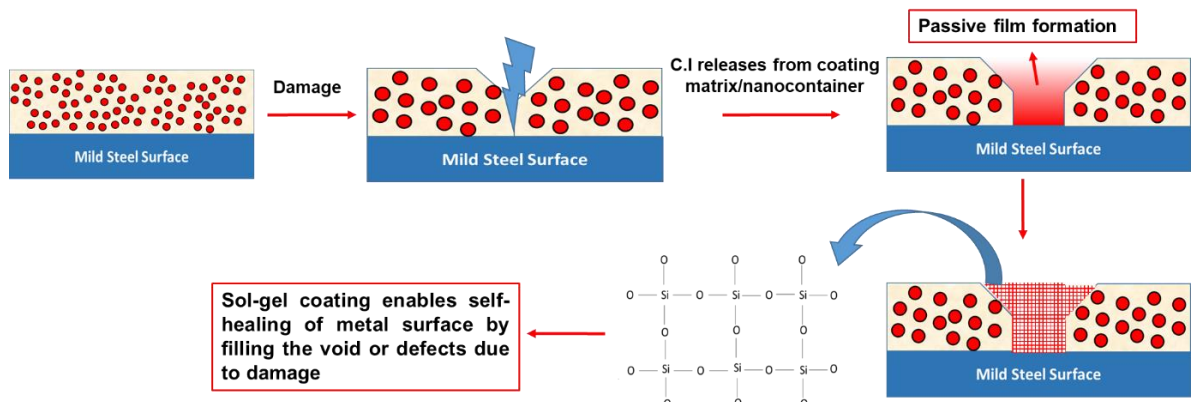
Fig. 1.10. Schematic representation of self-healing mechanism

There are two mechanisms for self-healing actions: intrinsic self-healing and extrinsic self-healing. The coatings with intrinsic self-healing capability are one of its design features. These coatings repair the damage and restore their original properties when exposed to external stimuli like temperature, light, chemicals, etc. The reversible reactions taking place during the process are induced via hydrogen bond [53, 54], urea bond [55], Diels-Alder reaction [56, 57], or disulphide bond [58]. The benefit of intrinsic self-healing is that it can go through multiple cycles of damage and repair. The extrinsic self-healing mechanism, in contrast, involves the release of healing agents or corrosion inhibitors from the micro/nano-containers. These micro/nano-containers are sensitive to any environmental changes occurring in their immediate vicinity, resulting in the release of corrosion inhibitors or self-healing agents to repair the damaged area [59].

1.7.1. Nanocontainers based self-healing coatings

Nanocontainers can be classified based on their size, dimension, morphology and chemical composition. The size of the nanocontainers ranges from 1 to 100 nm. Based on their dimensions, they are further categorized into four classes, namely zero dimension, e.g. quantum dots; one dimensional, e.g. nanotube, nanowire, nanofiber, etc.; two dimensional, e.g. crystalline or amorphous nanoplates, etc.; and three dimensional, e.g. fibers, carbon nanobuds, fullerenes, pillars, etc. Morphological classification includes nanorods, nanohooks, nanocubes, nanohelics, etc. Some of the nanocontainers widely used for encapsulation of corrosion inhibitors are described below:

1.7.1.1. *Nanotubes*

(a) <u>Halloysite nanotubes (HNTs):</u> Halloysite nanotubes are naturally occurring hydrated minerals consisting of layered structure of aluminosilicate sheets, with inner octahedron alumina sheet and outer silica tetrahedron sheet that has the ideal formula of $Al_2Si_2O_5(OH)_4 \cdot nH_2O$ as shown in Fig. 1.11.
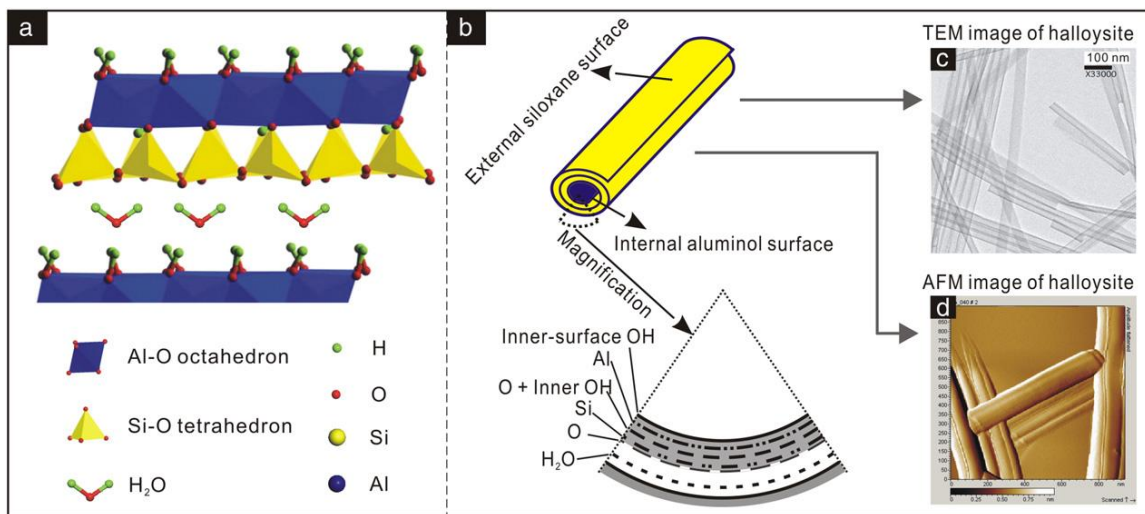
Fig. 1.11. (a) Schematic of Halloysite nanotube, (b) magnified image of rolled HNT, and (c and d) Transmission electron microscopy (TEM) and Atomic force microscopy (AFM) images of HNT (Reproduced from Ref. [61] with permission)

The morphology of HNTs is similar to that of kaolinite clay except for an additional water monolayer between the adjacent layers. When n = 2, the mineral is called halloysite-10 Å due to its layer periodicity of 10 Å. Heating halloysite-10 Å to 120 °C irreversibly dehydrates it to halloysite-7 Å with n = 0. They have internal diameter of 10 to 20 nm and external diameter of 50 to 60 nm with average length of 500 to 1000 nm [60]. HNTs possess negative charge on the outermost layer, and the inner alumina layer gives positive charge to the hollow lumen. Being highly porous in nature, HNTs are suitable nanocontainers for adsorption or intercalation of the molecules in the empty lumen. The hollow lumen can store and release the molecules in the presence of certain triggers in a controlled manner. HNTs are biocompatible, cost-effective and easily-available nanoclays [60].

Falcon et al. [62] have described the use of halloysite nanotubes (HNT) to encapsulate dodecylamine (DOC) as an effective corrosion inhibitor for carbon steel. 10 % of the inhibitor-loaded HNT was dissolved in the alkyd primer before it was applied to the carbon steel. The controlled release of the corrosion inhibitor from the HNT's lumen in

response to a pH change was observed by electrochemical impedance spectroscopy (EIS), scanning vibrating electrode technique (SVET), and salt spray tests, demonstrating the coatings self-healing behaviour. For loading into HNT, Joshi et al. [63] used three different kinds of corrosion inhibitors: benzotriazole (BTA), mercaptobenzothiazole (MBT), and mercaptobenzimidazole (MBI). To control the release of corrosion inhibitors, copper end stoppers were used to seal the tube ends. The as-loaded HNTs were mixed homogeneously with alkyd paint and applied on steel panels. The panels were submerged in a 0.5 M NaCl solution to observe the self-healing behaviour, and current density maps were obtained. The corrosion current scans obtained after SVET analysis, revealed that the mercaptobenzimidazole and benzotriazole loaded HNT with urea-formaldehyde microcapsules as end stoppers were more effective corrosion inhibiting materials for the protection of mild steel. According to Xing et al. [64], HNT loaded with $CaMoO_4$ end stoppers and Na_2MoO_4 as a corrosion inhibitor was used to control the corrosion inhibitor's release rate. Different loading percentages (5, 10 and 15 wt%) of the end stoppered-inhibitor loaded halloysite nanotube was mixed with an epoxy matrix and was deposited on Q235 steel. Before conducting electrochemical and immersion studies on the steel coupons, they were submerged in 3.5 % NaCl solution. The optimised loading of 10 wt% demonstrated the highest corrosion resistance and least amount of corrosion products on the surface, which suggested controlled release of the corrosion inhibitor to achieve the self-healing behaviour. According to Manasa et al. [65], HNT loaded with Ce^{3+}/Zr^{4+} and mixed into a sol-gel silica matrix was used to coat aluminum alloy A356.0. Using electrochemical studies, the coatings produced were then evaluated for their self-healing property. When exposed to corrosive media, such as 3.5 weight percent sodium chloride solution, the inhibitors are released into the scribe area, causing the damaged part to self-heal. Electrochemical studies showed that coatings with inhibitor-loaded HNT impart better corrosion resistance and self-healing properties when compared to uncoated substrates. Adsul et al. [66] performed similar experiments using Ce^{3+}/Zr^{4+} loaded HNT in a sol-gel matrix on magnesium alloy AZ91D. Weight loss experiments, potentiodynamic polarization, and electrochemical impedance spectroscopy were used to investigate the self-healing property and corrosion resistance behaviour. The scanning vibrating electrode technique (SVET) confirmed the self-healing mechanism of AZ91D substrates by the release of cationic corrosion inhibitors into the scribe area. Habib et al. [67] have developed multifunctional nanocomposite epoxy coatings on mild steel substrates using HNTs loaded with $NaNO_3$ and urea formaldehyde microcapsules

(UFMCs) loaded with linseed oil as self-healing component. The loading of HNTs with NaNO$_3$ and encapsulation of UFMCs with linseed oil was confirmed using Fourier-transform Infrared Spectroscopy, X-ray Photoelectron Spectroscopy and thermogravimetric (TGA) analyses. EIS studies indicated promising anticorrosive performance of novel nanocomposite coatings.

(b) <u>Titania nanotubes:</u> In past few years, titanium dioxide nanotubes (TNTs) have attracted more attention of researchers because of their structural modification, controllable size and advanced characteristics. TNTs are important nanomaterials as they possess excellent optical and electronic properties, biocompatibility, chemical stability and corrosion resistance. TNTs are classified as biocompatible material as they have a tendency to form stable oxide films of approx. 2 to 5 nm thickness, which is one of the possible reason that among all metal oxides, titanium oxide provides excellent corrosion resistance [68]. Figure 1.12 shows the schematic of TNTs.
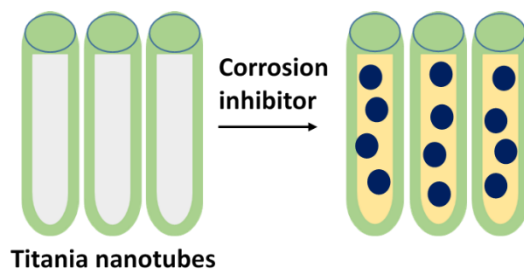
Fig. 1.12. Schematic representation of the incorporation of corrosion inhibitors into titania nanotubes

By using a hydrothermal process, Chen et al. [69] synthesized TNTs that were loaded with the Na$_2$MoO$_4$ inhibitor and had an average size of 6 to 9 nm. The inhibitor loaded TNTs were added to conducting polypyrrole coatings via electrochemical method for corrosion protection of 304 stainless steel. The corrosion behaviour of coatings with and without TNTs was examined after immersing the coated substrates in 3.5 wt% NaCl solution for 720 h. The coating with inhibitor loaded TNTs showed excellent corrosion resistance behaviour due to controlled release of the corrosion inhibitor from the nanotubes. Ubaid et al. [70], in their work, reported the use of titania nanotubes of average size of 20 nm for loading epoxy monomer as self-healing agent and dodecylamine as corrosion inhibitor. The loaded TNTs were mixed with an epoxy matrix and applied on steel substrates. Self-healing action of the coatings after the damage was examined via scanning electron microscopy. As per

electrochemical studies, the corrosion rate of coated steel substrates decreases after 5 days of immersion in salt water. Nawaz et al. [71] have reported the use of titania nanotubes (TNT) for loading dodecylamine (DOC) as corrosion inhibitor. The inhibitor encapsulated TNTs were dispersed into the epoxy coating before being submerged in corrosive media at two different pH levels, 2.0 and 5.0, to determine the coating's characteristics. The EIS investigation revealed that at pH 2, where the corrosion inhibitor's active release was effective, rather than at pH 5, the coatings displayed improved anti-corrosion performance. Another research work carried out by Arunchandran et al. [72] deals with the synthesis of titania nanotube powder by anodization process. The as-synthesized nanotubes were used for loading BTA inhibitors. Inhibitor-loaded TNTs were then dispersed in silane-titania coating. Electrochemical studies confirm that the coatings generated using inhibitor doped nanocontainers gave better corrosion resistance when compared to those generated using bare matrix sol and direct inhibitor added matrix sols.

(c) <u>Carbon nanotubes:</u>

Carbon nanotubes are cylindrical shapes composed of rolled-up graphite sheets. Carbon nanotubes (CNTs) are single molecules where each atom has its own conformation. They are composed of carbon fibres and fullerene molecules aligned in a hexagonal arrangement to form small tubes. CNTs are classified into two categories, namely, single-walled carbon nanotubes (SWCNTs) and multi-walled carbon nanotubes (MWCNTs) as shown in Fig. 1.13.

(b) SWCNTs

(a) Graphene (2-D) structure   (c) MWCNTs
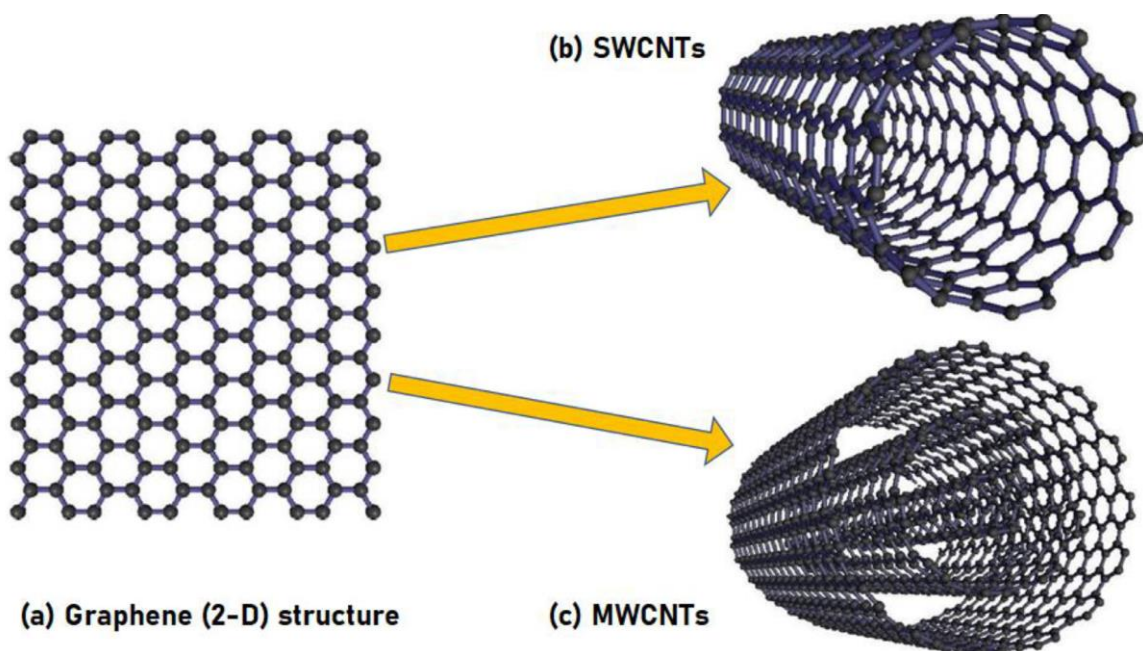
Fig. 1.13. Single-walled and multi-walled CNT (Reproduced from Ref. [75] with permission)

The average diameter of the single layer graphene carbon nanotubes is between 0.5 and 1.5 nm, whereas, it is $\geq$ 100 nm for multi-layered rolled graphene sheets [73]. CNTs are biocompatible in nature and are used as fillers to improve the mechanical strength of the coating matrix. They have hollow tubular structure with larger surface area, enhanced thermal and chemical stability [74].

Tannic acid-modified carbon nanotubes were used by Yang et al. [76] to reinforce with epoxy resin in order to prevent corrosion of NdFeB magnet. The modified coating was applied via cathodic electrophoretic deposition method. The corrosion resistance of the magnet improved due to the even dispersion of nanotubes within the resin. The nanocomposite coatings showed a corrosion potential of -0.207 V and a corrosion current of 5.281×10^{-11} Acm^{-2} in 3.5 wt% NaCl solution, respectively. Lorwanishpaisarn et al. [77] synthesized a nanocomposite coating comprising epoxy vitrimer with carbon nanotube for corrosion protection of steel surfaces. On exposure to 3.5 wt% NaCl solution, the corrosion resistance of the coating decreased to 3.12×10^{-5} MPY. It was concluded that addition of 5 % of nanofiller in the coating matrix provided 99.99 % corrosion protection efficiency. Using acetylene and the catalysts Fe-Ni/kaolin, Abdulrahaman et al. [78] developed multi-walled carbon nanotubes (MWCNTs). High resolution scanning electron microscopy (HRSEM), high resolution transmission electron microscopy (HRTEM), Brunauer-Emmett-Teller (BET), X-ray diffraction (XRD), differential thermogravimetry (DTG), and thermogravimetric analysis (TGA) techniques were used to characterize the MWCNTs. Using ultrasonication, the synthesized MWCNT was mixed with water and Arabic gum before being coated on mild steel panels. The first set of samples were heated at austenitic temperature of 900 °C whereas the second set of samples were heated to 950 °C for different periods (30, 60 and 90 min) followed by soaking. Similar findings were obtained from electrochemical measurements. Samples heated at 950 °C with a holding time of 90 min were found to have the best mechanical properties, such as hardness, tensile strength, and yield strength. The samples heated at 950 °C for 90 min have good anti-corrosion properties, indicating that increasing the heat treatment temperature and holding time significantly increased the corrosion protection efficiency of the coatings.

1.7.1.2.   *Nanofibers*

Nanofibers are widely used in various applications because of the advantages they possess. They have large surface area with high aspect ratio which helps in forming a structural network as represented in Fig. 1.14.
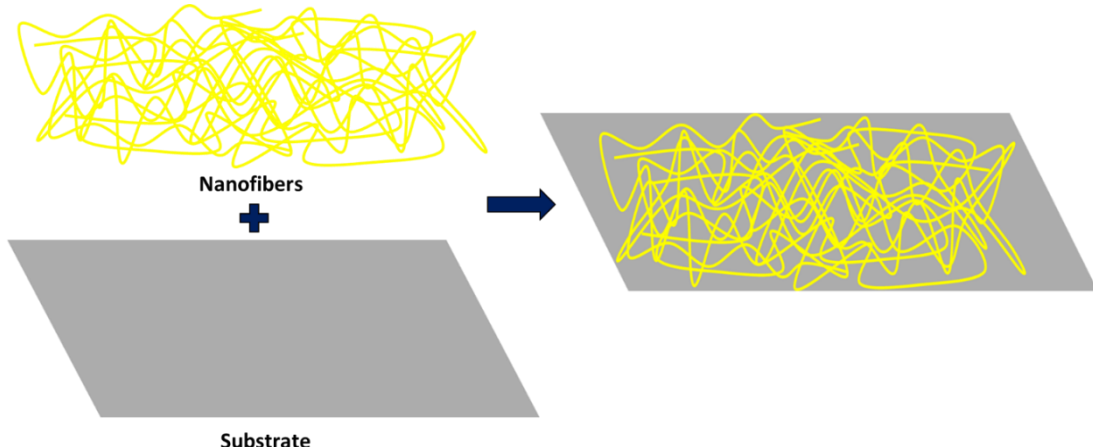
Fig. 1.14. Nanofiber synthesis and deposition on metal substrate

To fabricate nanofibers, various methods are used; among them, electrospinning and centrifugal spinning are most widely used. Different types of fibers with varying diameters can be obtained using different fabrication method. The one having a diameter of less than 1 μm are called as nanofibers. Most common form of fibers is polymer based as they are easy to fabricate and are in abundant in nature. Adding or coating specific multifunctional components onto these nanofibers helps in obtaining a structure possessing self-healing and anti-corrosion properties [79].

Ceria-doped polyvinyl chloride nanofibers were applied to an aluminum substrate by Gaballah et al. [80]. By using a nanofiber coating on the aluminium substrate, they could control the cathodic reaction and minimise the effect of electrochemical corrosion. The corrosion rate was determined using electrochemical impedance and polarization studies, where the highest inhibition efficiency was found at 5 % concentration of cerium oxide nanoparticles. The anti-corrosion performance of conductive poly(o-phenylenediamine) (POPD) nanofibers on stainless steel in 3.5 % NaCl solution was studied by Muthirulan et al. [81]. The potentiodynamic polarization data revealed that the POPD nanofiber coatings offer excellent corrosion protection for stainless steel. Aldabbagh et al. [82] reported the use of polyamide nanofiber coatings on aluminum surface via electrospinning technique. When exposed to 3.5 wt% NaCl solution, polyamide coated aluminum substrates show a decrease in corrosion rate and corrosion current with an increase in corrosion resistance compared to bare substrates. Yabuki et al. [83] used polymer coatings

containing cellulose nanofibers loaded with calcium nitrite, corrosion inhibitor to control the corrosion of carbon steel in alkaline solution. Polarization resistance of fiber-coated samples was higher when compared to only polymer coating consisting corrosion inhibitor. These nanofibers served as a pathway for the controlled release of the corrosion inhibitor. Using the interfacial polymerization method, Yao et al. [84] have created polyaniline (PANI) nanofibers. PANI nanofibers and aggregated PANI were used in two different coating formulations, which were then applied to carbon steel in order to observe the anti-corrosion behaviour of these materials. For the purpose of analyzing the electrochemical properties, coated steel samples were exposed to a 5 % NaCl solution. The findings indicated that PANI nanofibers exhibit greater corrosion resistance than aggregated PANI, which is attributed to the uniform and dense coating produced by PANI nanofibers due to their superior ethanol dispersivity. The chemical composition of the passive layer formed on the surface was further confirmed by Raman spectral analysis. The presence of α-Fe_2O_3 and Fe_3O_4 in the PANI nanofiber coated sample indicated the formation of a thin passive film, which in turn prevents further corrosion of the mild steel. In order to achieve a uniform and dense coating on mild steel, Zhang et al. [85] reported incorporating PANI nanofibers and epoxy microcapsules into traditional epoxy/polyamide coatings. After immersing the steel substrates in 12 wt% NaCl solution for 100 days at room temperature, EIS studies were conducted. The results show that while PANI fibres form a passive film acting as a barrier to protect the metal surface from corrosion, controlled release of epoxy fluid from the microcapsules imparts protection and autonomous-healing properties. Zhao et al. [86] in their work reported the synthesis of electrospun microfibers using a mixed solution of PANI and PMMA (polymethylmethacrylate). To evaluate the anti-corrosion performance, various coating formulations were prepared with different loading percentages of PANI (4, 8, 15, 25 and 35 wt%) and coated on Q235 steel. PANI/PMMA coating developed via the drop-casting technique was chosen as a reference for comparison studies. After placing the steel panels in 0.1 M H_2SO_4 solution, the electrochemical results revealed that the coating produced with 25 wt% loading had better protection when compared to other loading percentages and PANI/PMMA-coated substrates.

1.7.1.3. *Nanolayers*

(a) <u>Layer-by-layer nanocontainers:</u>

Layer-by-layer (LbL) method was initially based on alternate deposition of polyelectrolytes with opposite charges on flat surfaces. The deposition primarily takes place due to the electrostatic forces acting in between the oppositely charged layers. Therefore, this methodology is based on template or precursor molecule which acts as a building block for synthesizing the final material. Recent research has taken a step ahead and switched to different template material based on their shapes, chemical structures and sizes. Furthermore, tailoring of these LbL nanocontainers for achieving the desired properties is quite easy and thus becomes the promising material for encapsulation [87]. Figure. 1.15 shows the layer-by-layer deposition of polyelectrolyte layers on template molecule.
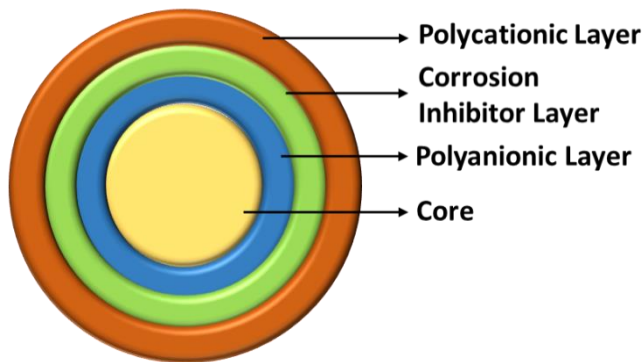
Fig. 1.15. Synthesis of layer-by-layer nanocontainer using different polyelectrolyte layers and inhibitor layer in between

Lanthanum cerium molybdate (LCM) nanoparticles produced using the sol-gel method were used by Arora et al. [88] to develop layer-by-layer (LbL) nanocontainers. The synthesized LCM nanoparticles were used as the template onto which two different combinations of polyelectrolyte layers were deposited as the shell, and a corrosion inhibitor was sandwiched between the layers. LCM nanoparticles/polypyrrole/benzotriazole/polyacrylic acid (abbreviated as LCM/PPY/BTA/PAA) were one type of nanocontainer that was used for mild steel substrates. The other type of nanocontainers were made up of LCM nanoparticles/polyethyleneimine/benzotriazole/polystyrene sulfonate combination, abbreviated as LCM/PEI/BTA/PSS, and were used for magnesium alloy. Electrochemical measurements show that coatings with nanocontainers exhibit higher corrosion resistance than substrates with only epoxy coated with dispersed nanoparticles. Multilayer polyelectrolyte coatings with effective stimuli response towards self-healing and barrier

property for SS430 have been reported by Syed et al. [89]. According to electrochemical studies carried out in 3 wt% NaCl solution, the multilayer polyelectrolyte coatings offered improved barrier properties. Kamburova et al. [90] synthesized nanocontainers by using layer-by-layer deposition of polyacrylic acid (PAA) and poly (diallyldimethylammonium chloride) (PDADMAC) with BTA on hematite particles in the presence of 0.1 M NaCl. Steel substrates were coated with the nanocontainer-dispersed galvanized coating. Cyclic voltammetry, potentiodynamic measurements, and scanning electron microscopy (SEM) were used to characterize the coatings, and it was found that composite coatings provided better corrosion protection than pure zinc coatings. Using layer-by-layer technique, Qian et al. [91] synthesized nanocontainers with a SiO_2 core and polyelectrolyte layers made of chitosan and alginate that contained polyaspartic acid (PASP) as a corrosion inhibitor. SVET was used to validate the self-healing capacity of the epoxy coating dispersed in nanocontainers that was applied to mild steel. Liu et al. [92] discuss the use of pH-responsive attapulgite (ATP) nanoparticles with PEI and PSS polyelectrolyte layers with a BTA layer sandwiched in between the polyelectrolyte layers. The 2 wt% of the obtained nanocontainers were mixed with epoxy resin and applied to Q235 carbon steel. TEM, SEM, XRD, and BET analysis confirmed the corrosion inhibitor loading and surface morphology of the coatings. The EIS results reveal that the coating acts as a barrier because of nanocontainers in the matrix. In addition, the corrosion inhibitor also gets released and heals the affected area by forming a passive film on the metal surface.

   (b) **<u>Montmorillonite:</u>**

Montmorillonite (MMT) is a type of layered nanocontainer that consists of hydrated cations which are intercalated in the interlayer spaces. The presence of these cations balances the negative charge of the layers. The chemical formula of montmorillonite is $M^+_y n H_2O (Al_{2-y} Mg_y) Si_4 O_{10}(OH)_2$ which consists of one octahedral layer sandwiched in between two tetrahedral sheets as shown in Fig. 1.16 [93].
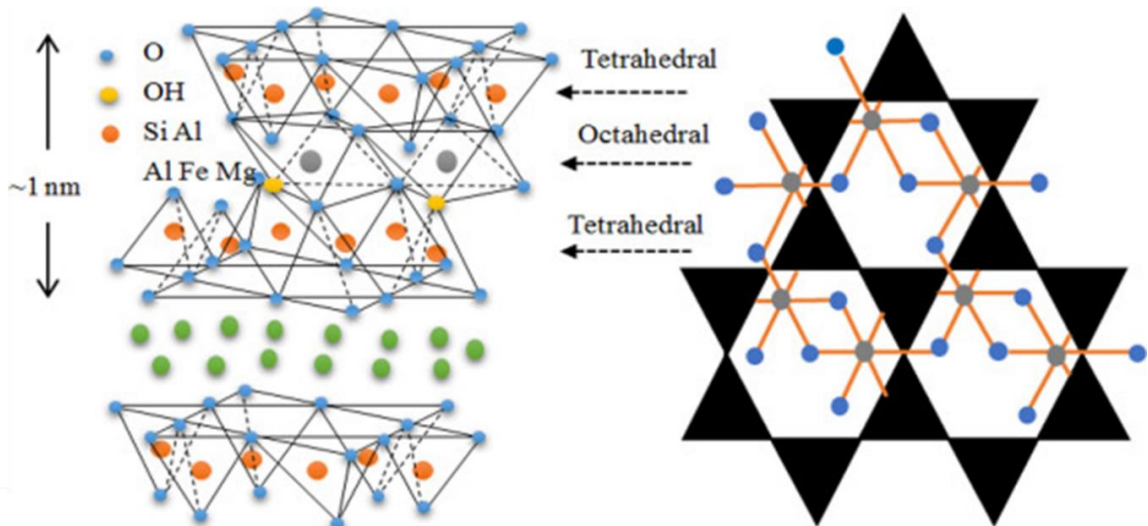
Fig. 1.16. Structure of Montmorillonite nanoclay (Reproduced from Ref. [95] with permission)

They have high cation exchanger capacity making it the most prominent nanocontainer for loading positively charged corrosion inhibitors. The structural design of this nanocontainer is ideal for loading both organic and inorganic cations. It is one of the abundant natural mineral clay which is easily available at cheaper prices [94].

Motte et al. [96] used Na-montmorillonite to load Ce^{3+} cations. For this, the clay mineral was dispersed in a solution of $CeCl_3$ under continuous stirring for 16 h at ambient temperature. The authors confirmed that the release of loaded cerium ions is only possible via ion-exchange mechanism. They compared the release in three different solutions, namely, water, NaCl, and $ZnCl_2$. The percentage release was bare minimum in water, 7 % in NaCl and 26 % in $ZnCl_2$ after 1 h of exposure in the media. Though the percentage release was fast, the chances of active corrosion inhibition was maximum in case of $ZnCl_2$. The loaded nanocontainer was then added to silane coating and applied on galvanized steel, followed by corrosion test in NaCl. The silane coating with Ce-MMT loading shows excellent corrosion resistance when compared to Na-MMT coatings, which is due to the accelerated release of Ce^{3+} ions during initial exposure. Similar work was reported by Mohammadi et al. [97], where they used Ce-MMT nanocontainer loaded in epoxy coating and applied on mild steel coupons. In order to obtain Ce-MMT nanocontainer from Na-MMT clay, the starting material used was $Ce(NO_3)_3$. Electrochemical studies reveal that the corrosion protection efficiency for Ce-MMT epoxy coating was better when compared to only epoxy coating. As discussed earlier, MMT nanocontainers are efficient in loading cations of organic corrosion inhibitors too, therefore, Ghazi et al. [98] have researched

loading benzimidazole (BIA) and Zn^{2+} into these nanocontainers using the traditional approach of ion-exchange mechanism. In order to incorporate BIA, the pH of the solution consisting of BIA was controlled so as to protonate the BIA. The protonation will thus help in generating positive charge on the BIA molecules enabling it to intercalate between the layers of MMT nanoclay. For corrosion studies, coating with Na-MMT, Zn-MMT and BIA-MMT was compared and investigated. It was found that the corrosion resistance of Zn-MMT and BIA-MMT was higher than that of Na^+-MMT due to controlled release of these corrosion inhibitors, in addition to the synergistic effect of BIA and Zn^{2+} on their release, which inhibits further corrosion of carbon steel. Similar example on the use of organic corrosion inhibitor, i.e., 8-hydroxyquinoline (8-HQ) was reported by Truc et al. [99]. Na^+-MMT was dispersed in acidic solution, so that the neutral 8-HQ molecule protonates and replaces the Na+ cations. XRD data confirms the cation-exchange reaction by an increase in the basal spacing. Release rate studies for 8-HQ-MMT nanoclay confirms the 100 % release of corrosion inhibitor in 24 h exposure in NaCl solution due to the weak bonding of 8-HQ cations when intercalated. The epoxy coating modified using 8-HQ intercalated MMT when applied on steel substrates shows excellent adhesion as well as anti-corrosion properties when compared to coatings having only MMT without inhibitor. To protect the surface of mild steel, Edraki et al. [100] reported the use of various ion exchange-based nanolayers. The investigation focuses on the intercalation of sodium montmorillonite clay (Na^+-MMT) layers with 2-mercaptobenzothiazole (MBT) and 2-mercaptobenzimidazole (MBI) as corrosion inhibitors. The mild steel samples were immersed into various solutions, including blank, MBT, MBI, MMT-MBT, MMT-MBI, and Na^+-MMT before the corrosion studies. When compared to just MBT, MBI, and Na^+-MMT, the corrosion protection efficiency observed for MMT-MBT and MMT-MBI was very high. The MMT-MBT absorbed surface has reportedly shown more uniform layer formation, which confirms the inhibition action of the corrosion inhibitor, according to the SEM images obtained after the samples were immersed for 24 h in the corresponding solutions. In order to create coatings on magnesium alloy, Swapnil et al. [101] intercalated Ce^{3+}/Zr^{4+} cations into Al pillared MMT and dispersed the loaded MMT into a hybrid silica matrix. XRD patterns and small angle X-ray scattering (SAXS) analysis verified the intercalation of cations into pillared clay. EIS/polarization and SVET were used, respectively, to assess the coating's anticorrosion abilities and capacity for self-healing.

(c) **Layered double hydroxides:**

In contrast to MMT nanoclay, the layered double hydroxides (LDHs) are anionic-exchanger nanocontainer. The structure of LDH comprises hydroxide layers of divalent (M^{2+}) and trivalent (M^{3+}) metal cations, where the positive charge on the layers is because of the trivalent cation which is balanced by hydrated anions i.e., A^{n-}. The metal ions present in the LDH nanocontainers are coordinated to hydroxide ligands octahedral ($M(OH)_6$) arranged in a distorted array sharing their edges as depicted in Fig. 1.17.
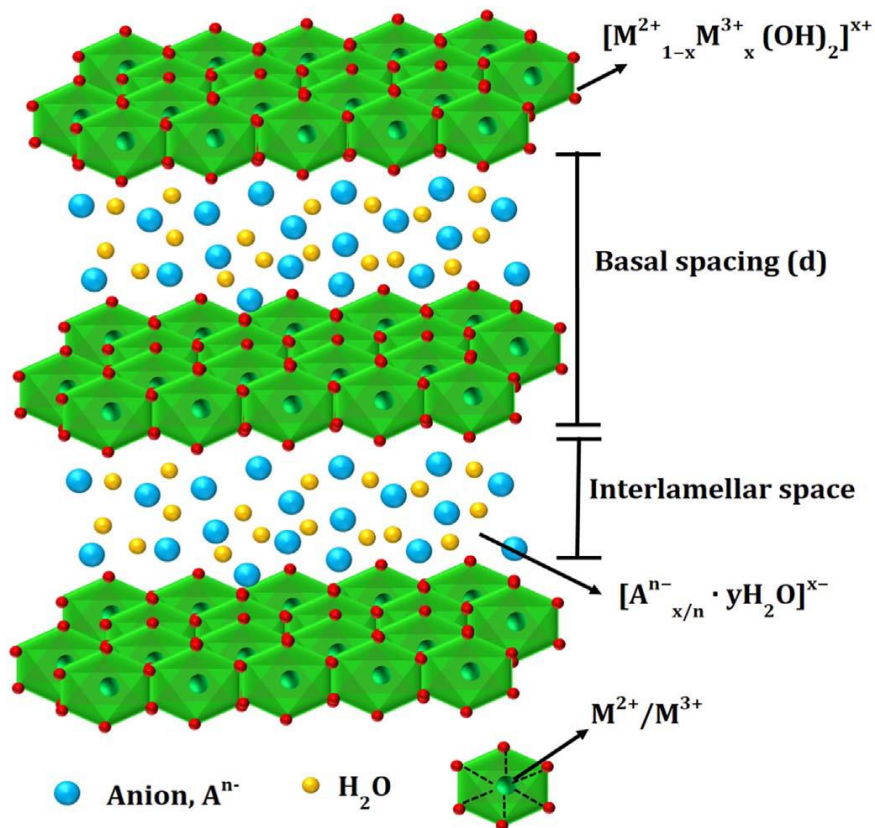
Fig. 1.17. Structure of Layered double hydroxide (Reproduced from Ref. [102] with permission)

The general formula of LDH is $[M^{2+}_{1-x} M^{3+}_x(OH)_2] (A^{n-})_{x/n} \cdot yH_2O$, where divalent metal cation can be Ca^{2+}, Zn^{2+}, Mg^{2+}, Ni^{2+}, Co^{2+}, Mn^{2+}, etc., whereas, trivalent metal cation can be Al^{3+}, Fe^{3+}, Cr^{3+}, In^{3+}, etc., and x usually varies from $0.33 < x < 0.80$. The presence of negative charge neutralizes the overall charge of the LDH nanocontainer and also helps in stacking of layers one above the other due to electrostatic forces [94].

In highly corrosive environments, the presence of chloride anions causes severe corrosion of the metal. Therefore, the use of LDH nanocontainers is advisable for the release of anionic corrosion inhibitors in addition to holding or intercalating aggressive ions such as

chloride ions, thereby inhibiting their direct contact with the metal surface [103]. In this manner, the LDH nanocontainers have dual functions. Rodriguez et al. [104] reported the generation of epoxy coating on Zn-Mg steel by intercalating BTA into Mg-Al LDH nanocontainers and adding these nanocontainers into the coating matrix. The release of BTA not only provides the active corrosion inhibition but also helps in intercalating aggressive corrosive species and thus imparting barrier properties to the coating. Another research work by Deip et al. [105] focuses on the effect of Zn-Al-BTA LDH nanocontainers when loaded into an epoxy coating containing zinc phosphate pigment. The corrosion studies were planned based on the requirements of industries. For this purpose, they have carried out corrosion tests for up to 75 days of exposure. The coatings have shown excellent corrosion protection due to the controlled release of BTA from the interlayers of LDH and the simultaneous intercalation of corrosive species during the corrosion process. Based on similar approach, different corrosion inhibitors intercalated into LDH nanocontainers were added to epoxy coating for corrosion protection of steel surfaces such as decavanadate/Zn-Al LDH [106], 2-benzothiazolylthiosuccinate (BTS)/Mg-Al LDH [107], and molybdate/Zn-Al LDH [108]. Subasri et al. [109] have carried out the detailed studies on the use five different corrosion inhibitors, namely, phytate, molybdate, vanadate, 2-mercaptobenzothiazole, and 8-hydroxyquinolinate and loading into Zn-Al LDH nanocontainers, followed by dispersing them into sol-gel matrix. The modified coating was then deposited on AA 2024-T3 aluminum alloy substrates using dip-coating method. On comparison with bare and chromate conversion coatings, all the inhibitor modified coatings exhibited better corrosion protection and good adhesion strength. Among all the corrosion inhibitors, the best corrosion protection was observed for 8-hydroxyquinoline and phytate. To effectively intercalate 2-benzothiazolylthio-succinic acid (BTSA) as a corrosion inhibitor, Duong et al. [110] explained the use of layered double hydroxides (LDH)/graphene oxide (GO) hybrid. The loading and surface morphology of GO, LDH-BTSA, and LDH/GO-BTSA layered nanocontainer was confirmed using FTIR spectra, XRD profiles, and SEM images. The carbon steel samples were immersed in corrosive media (0.1 M NaCl solution) containing LDH/BTSA and LDH/GO-BTSA at 1 g/l concentration for 2 h in order to analyse the corrosion protection performance. According to the polarization data, LDH/GO-BTSA had a 94.2 % inhibition efficiency, compared to LDH-BTSA having 85.5 % efficiency. The presence of GO, which in addition to BTSA exhibits corrosion inhibitive action, may account for the high inhibition efficiency of LDH/GO-BTSA.

1.7.1.4.   *Porous microstructures*

(a) **Zeolites:** Zeolites are micro-porous crystalline alumino-silicate crystals. Their structure comprises an array of SiO_4^{4-} or AlO_4^{5-} tetrahedrons, as shown in Fig. 1.18.
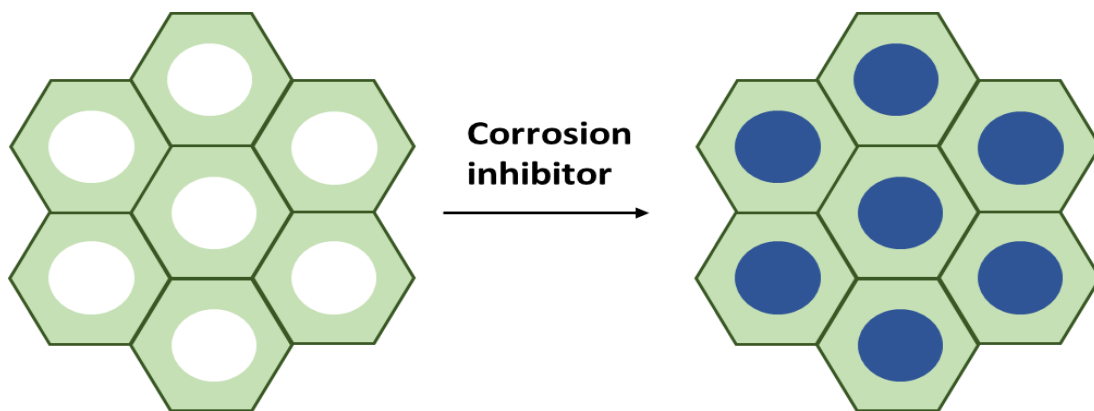
Fig. 1.18. Schematic of Zeolite nanocontainer

Tetrahedrons are made up of four atoms: four silicon or aluminium atoms at the centres, and four oxygen atoms at the vertex, which serve as a link between neighbouring tetrahedrons. The building blocks are arranged in a three-dimensional structure with channels and cavities to create a crystal with a very large specific surface area (typically about 300 m^2 g^{-1} with the volume of internal voids about 0.1 cm^3 g^{-1}) [111].

      An anticorrosive epoxy paint was modified with NaY zeolites exchanged with zinc metal ions by Padhy et al. [112]. The findings showed that mild steel can be sufficiently shielded against corrosion with Zn^{2+} ion-exchanged zeolite for up to 16 days of immersion in 3.5 wt% NaCl solution. In comparison to the unmodified coating, the impedance magnitude for as-prepared coating at low frequency was also three orders of magnitude higher. An epoxy coating functionalized with zeolite filler and used as a reservoir for active Ce^{3+} ions produced similar results [113]. The anti-corrosion capabilities of a silicoaluminophosphate-34 (SAPO-34) zeolite composite coating on an AA6061 aluminium alloy substrate were examined by Calabrese et al. [114]. The silane matrix's filler content, which ranged from 2000 to 8000 ppm, was examined. In comparison to the uncoated aluminum sample, the results showed that the corrosion current drops by up to three orders of magnitude. The use of SAPO-34 filler at a concentration of 4000 ppm gave better results. Roselli et al. [115] have reported the use of Cerium (III) ions as an effective corrosion inhibitor and loaded into the porous zeolite microstructure in order to replace the phosphate

based coatings on SAE 1010 steel panels. Two different zeolite compositions were used and were abbreviated as Z_1 and Z_2. XRD pattern obtained for both the rocks revealed that the concentration of mordenite was higher in case of Z_1 (more than 80 %) than Z_2 (50-80 %). SEM images obtained for zeolite rocks and zinc phosphate (PZ) showed that the average particle size was <10 μm. Five different coating formulations were prepared and following nomenclature was assigned: control alkyd coating (C), Ce-Z_1/coating (1A), Ce-Z_2/coating (1B), Ce-Z_1/PZ/coating (2A) and Ce-Z_2/PZ/coating (2B). Electrochemical studies were carried out after immersing the coated steel panels in 0.5 M NaCl solution for 1, 18 and 31 days. The results suggested that the modified zeolite based coatings could effectively replace the zinc phosphate coatings partially with the use of Z_2 or totally with the use of Z_1. The corrosion protection increased for the modified zeolite based coatings because of the presence of Ce (III) ions as corrosion inhibitor.

(b) **Mesoporous Silica:** Mesoporous silica (MeSi), a porous material, has been used as a host for corrosion inhibitors. This material has high surface area (700–1500 $m^2\ g^{-1}$), large pore volume (1 $cm^3\ g^{-1}$), high thermal and chemical stability, and ease of functionalization. It also has highly regular arrays of cylindrical pores of uniform size with a diameter in the range of 2–50 nm, as shown in Fig. 1.19.
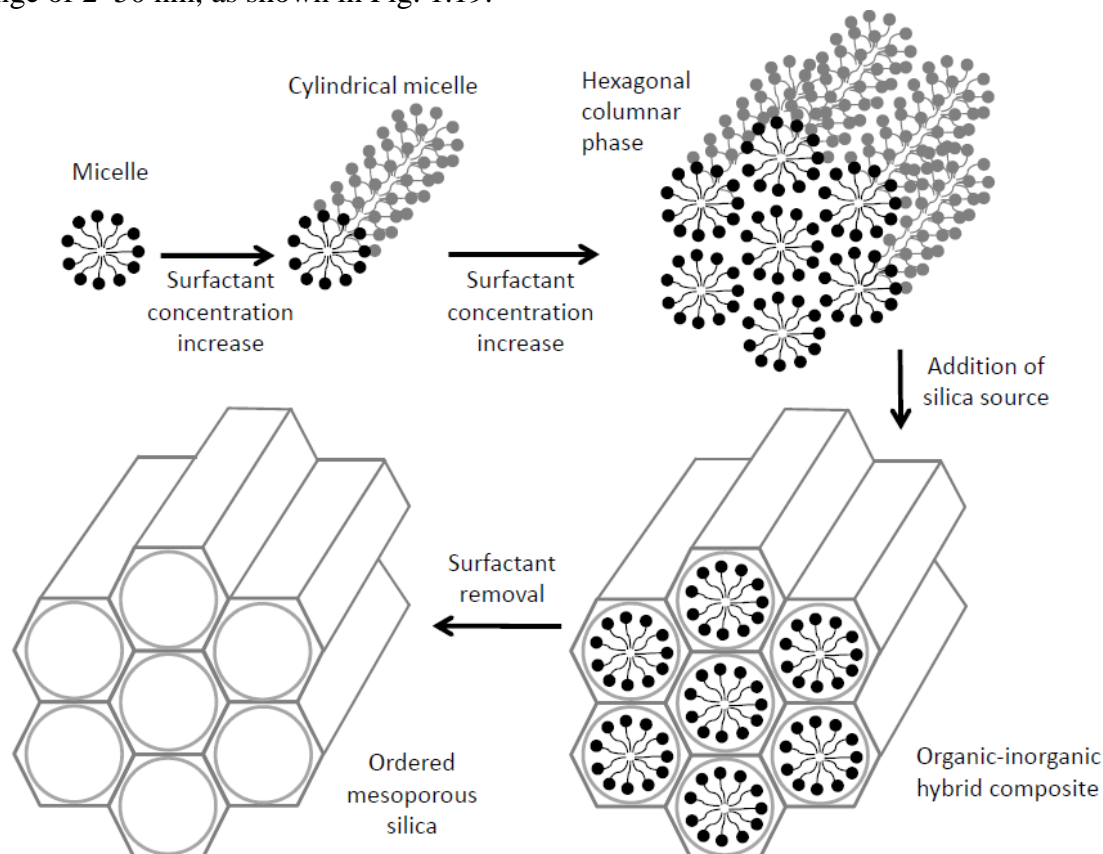
Fig. 1.19. Mesoporous Silica structure (Reproduced from Ref. [117] with permission)

Mesoporous silica may be used as an encapsulating material for the controlled release of corrosion inhibitors in protective coatings due to its well-controlled pore size, narrow pore size distribution, and controllable functionality [116].

According to Alipour et al. [118], the 3-Mercaptopropyltrimethoxysilane (MPTMS) functionalization of MeSi increases the coatings hydrophobicity additionally enhancing its adhesion to the metal substrate and improving the coating's barrier properties by decreasing its porosity. Furthermore, a hydrophobic functionalization can directly enhance the coating barrier qualities, lowering the rate of corrosion of the treated substrate. Hollamby et al. [119] functionalized the nanoparticles with octyltriethoxysilane (OTES) to enhance the MSN dispersion in a polyester-based coating. They further emphasized that the interactions between free dispersed BTA and the polymer network during the curing process make it ineffective at preventing corrosion phenomena. However, using corrosion inhibitor nanocarriers, like MSN, prevents BTA interactions with the polymer network and enhances corrosion protection. MSN functions as an intelligent inhibitor reservoir and has no impact on the coating's adhesion or barrier qualities. Yeganeh et al. [114] proposed the use of mesoporous silica (MeSi) based nanocontainer with Na_2MoO_4 (NMO) as corrosion inhibitor to be loaded into the nanocontainer. The composite coatings were generated by mixing Na_2MoO_4 loaded MS nanocontainers into the polypyrrole (Ppy) matrix and coating on steel substrates. FESEM images revealed that the MS powder has hexagonal pores, which was confirmed further from the observed XRD pattern relevant to the hexagonal structure of the powder. BET analysis indicated that the pore volume and diameter decreased after loading the corrosion inhibitor. The corrosion behaviour of the Ppy/MeSi(NMO) and Ppy/MeSi coated substrates was evaluated after immersing the substrates in 2 g.dm^{-3} NaCl solution at pH 8. Results of the electrochemical impedance and polarization studies indicate that the incorporation of the corrosion inhibitor NMO increased the coating functionality to a much higher extent as it protects the surface from corrosion attack. Further, the inhibitor restricts the formation of the corrosion products rather it helps in forming a passive layer as soon as the inhibitor is released in the vicinity of the damaged area.

Objective of the Research

The overall objective of this research work was to develop a smart self-healing sol-gel coating on mild steel which has excellent barrier and active inhibition properties. The coating formulation was designed in such a way that they should be environmental friendly, cheap and compatible for industries seeking replacement for toxic chromate conversion coating. The additives such as corrosion inhibitors with and without encapsulation was dispersed into the sol-gel silica matrix to be applied on mild steel surface for anti-corrosion performance and increasing the durability of the coating matrix. For this purpose, first set of experiments were planned to compare and investigate the effect of two different nanocontainers i.e., halloysite nanotubes and layer-by-layer polyelectrolyte nanocontainers loaded with benzotriazole, an organic corrosion inhibitor. The choice of organic corrosion inhibitor was based on its compatibility with the nanocontainers and tendency to form a stable complex with metal ion thus preventing the corrosion process. Another set of experiments were planned using inorganic corrosion inhibitors, i.e., zirconium, cerium, lanthanum, gadolinium and erbium, followed by loading them into the nanocontainers. The objective of using inorganic corrosion inhibitors was that they also act as a catalyst to polymerize the epoxide ring of the monomer present in the matrix coating formulation. In addition to this, these corrosion inhibitors provide excellent corrosion inhibition properties by forming a stable passive film on the metal surface during the corrosion process. The modified nanocontainers were added to sol-gel matrix and applied on mild steel via dip-coating method. Initial experiments based on optimization of inhibitor loaded HNTs was also performed to compare and analyse optimum loading of modified HNTs into the matrix sol.

The coatings thus obtained were examined for their self-healing action by electrochemical impedance spectroscopy, potentiodynamic polarization studies, and salt spray tests. To carefully examine the localized corrosion, the scanning vibrating electrode technique (SVET) was also used. In certain coatings, SEM images were also collected before and after salt spray to analyze the damaged area and confirm the self-healing action of the corrosion inhibitors. Further experiments were also performed on the release rate of benzotriazole from halloysite nanotubes to observe their controlled release with respect to time at different pH conditions.

The present research work is divided into seven chapters as follows:

1. **CHAPTER 1:** Introduction
2. **CHAPTER 2:** Experimental
3. **CHAPTER 3:** Benzotriazole encapsulated nanocontainer-based self-healing coatings for corrosion protection of mild steel
4. **CHAPTER 4:** Capped inhibitor-loaded halloysite nanoclay-based self-healing silica coatings for corrosion protection of mild steel
5. **CHAPTER 5: E**ffect of pH on the controlled release of benzotriazole from halloysite nanotubes for corrosion protection of mild steel
6. **CHAPTER 6:** Effect of transition metal and different rare-earth inhibitors-based sol-gel coatings on corrosion protection of mild steel
7. **CHAPTER 7:** Summary and Conclusions

1.8. References:

[1] Le, L., Sofi, M., Lumantarna, E., The Combined effect of stress and corrosion on mild steel, J. Constr. Steel Res. 185 (2021) 106805.

[2] Bilgic, S., Plant extracts as corrosion inhibitors for mild steel in H_2SO_4 and H_3PO_4 Media-Review II, Int. J. Corros. Scale Inhib. 11 (2022) 1-42.

[3] Open source: "https://worldsteel.org/steel-by-topic/steel-markets/".

[4] Zarras, P., Stenger-Smith, J. D., Corrosion processes and strategies for prevention: An Introduction, Handbook of Smart Coatings for Materials Protection. (2014) 3-28.

[5] Makhlouf, A. S. H., Chapter 15 - Intelligent stannate-based coatings of self-healing functionality for magnesium alloys, Intelligent Coatings for Corrosion Control, Butterworth-Heinemann. (2015) 537-555.

[6] Eliaz, N., Corrosion of Metallic Biomaterials: A Review, Materials. 12 (2019) 400-407.

[7] Michael, E., Pudji, P., Standard handbook of petroleum and natural gas engineering, Production Engineering. 2 (1996).

[8] Hoar, T. P., Agar, J. N., Factors in throwing power illustrated by potential-current diagrams, Discuss. Faraday Soc. (1947) 6-28.

[9] North, N. A., & Macleod, I., Corrosion of metals, Conservation of Marine Archaeological Objects. (1987) 68-98.

[10] Tan, Y. J., Bailey, S., Kinsella, B., Mapping non-uniform corrosion using the wire beam electrode method. II. Crevice corrosion and crevice corrosion exemption, Corros. Sci. 43 (2001) 1919-1929.

[11] Koch, G., Varney, J., Thompson, N., Moghissi, O., Gould, M., Payer, J., International measures of prevention, application, and economics of corrosion technologies study, NACE® Int 216 (2016).

[12] Jafar Mazumder, M.A., Global impact of corrosion: occurrence, cost and mitigation, Glob. J. Eng. Sci. 5 (2020) 0–4.

[13] Allam, I. M., Arlow, J. S., Saricimen, H., Initial stages of Atmospheric Corrosion of Steel in the Arabian Gulf, Corros. Sci. 32 (1991) 417-432.

[14] D. de la Fuente, Diaz, I., Alcantara, J., Chico, B., Simancas, J., Llorente, I., Garcia-Delgado, A., Jimenez, J. A., Adeva, P., Morcillo, M., Corrosion mechanisms of mild steel in chloride-rich atmospheres, Mater. Corros. 67 (2016) 227-238.

[15] Evans, U. R., The Corrosion and Oxidation of Metals: Second Supplementary Volume, Ch. 8. Edward Arnold, London (1976).

[16] Sahoo, P., Das, S. K., Paulo Davim, J., Surface Finish Coatings, Comprehensive Materials Finishing. 3 (2017) 38-55.

[17] Sun, M., Ma, Z., Effects of heat-treatment and hot-dip galvanizing on mechanical properties of RHS, J. Constr. Steel Res. 153 (2019) 603-617.

[18] Muthukumar, N., Petroleum Products Transporting Pipeline Corrosion-A Review, The Role of Colloidal Systems in Environmental Protection. (2014) 527-571.

[19] Sankara Narayanan, T. S. N., Surface Pre-treatment by phosphate conversion coatings-A Review, Rev. Adv. Mater. Sci. 9 (2005) 130-177.

[20] Figueria. R. B., Fontinha, I. R., Silva, C. J. R., Pereira, E. V., Hybrid sol-gel coatings: Smart and Green Materials for Corrosion Mitigation, Coatings. 6 (2016) 1-19.

[21] Zhao, J., Xia, L., Sehgal, A., Lu, D., McCreery, R. L., Frankel, G. S., Effects of chromate and chromate conversion coatings on corrosion of aluminum alloy 2024-T3, Surf. Coat. Technol. 140 (2001) 51-57.

[22] Commission Regulation (EU) No 301/2014 of 25 March 2014 amending Annex XVII to Regulation (EC) No 1907/2006 of the European Parliament and of the Council on the Registration, Evaluation, Authorisation and Restriction of Chemicals (REACH) as regards chromium VI compounds, Retrieved September 21, 2022

[23] Ebelmen, J. J., Sur une production artificielle de silice diaphane, Comptes Rendus Acad. Sci. Fr. 19 (1844) 398.

[24] Dimitriev, Y., Ivanova, Y., Iordanova, R., History of Sol-gel Science and Technology-Review, J. Chem. Technol. Metall. 43 (2008) 181-192.

[25] Dislich, H., Glassy and crystalline systems from gels: Chemical basis and technical application, J. Non Cryst. Solids. 57 (1983) 371–388.

[26] Danks, A. E., Hall, S. R., Schnepp, Z., The evolution of 'sol–gel' chemistry as a technique for materials synthesis, Mater. Horiz. 3 (2016) 91–112.

[27] Wang, D., Bierwagen, G. P., Sol-gel coatings on metals for corrosion protection - Review, Prog. Org. Coat. 64 (2009) 327-338.

[28] Qian, M., Mcintosh Soutar, A., Tan, X.H., Zeng, X.T., Wijesinghe, S.L., Two-part epoxy-siloxane hybrid corrosion protection coatings for carbon steel, Thin Solid Films. 517 (2009) 5237–5242.

[29] Kannan, A. G., Choudhury, N. R., Dutta, N. K., Electrochemical performance of sol-gel derived phospho-silicate-methacrylate hybrid coatings, J. Electroanal. Chem. 641 (2010) 28–34.

[30] Chou, T., Chandrasekaran, C., Cao, G. Z., Sol-gel-derived hybrid coatings for corrosion protection, J. Sol-Gel Sci. Technol. 26 (2003) 321–327.

[31] Jianguo, L., Gaoping, G., Chuanwei, Y., Enhancement of the erosion–corrosion resistance of Dacromet with hybrid SiO_2 sol-gel, Surf. Coat. Technol. 200 (2006) 4967–4975.

[32] Castro, Y., Ferrari, B., Moreno, R., Duran, A., Corrosion behaviour of silica hybrid coatings produced from basic catalysed particulate sols by dipping and EPD, Surf. Coat. Technol. 191 (2005) 228–235.

[33] Guin, A. K., Nayak, S. K., Rout, T. K., Bandyopadhyay, N., Sengupta, D. K., Corrosion behavior of nanohybrid titania–silica composite coating on phosphated steel sheet, J. Coat. Technol. Res. 9 (2011) 97–106.

[34] Jeyaram, R., Elango, A., Siva, T., Ayeshamariam, A., Kaviyarasu, K., Corrosion protection of silane based coatings on mild steel in an aggressive chloride ion environment, Surf. Interfaces. 587 (2020) 18:100423.

[35] Duran, A., Castro, Y., Aparicio., Conde, A., Damborenea, J. J., Protection and surface modification of metals with sol-gel coatings, Int. Mater. Rev. 52 (2007) 1-18.

[36] Thakur, A., Kumar, A., Sustainable inhibitors for corrosion mitigation in aggressive corrosive media: A comprehensive study, J. Bio- Tribo-Corros. 7 (2021) 1-48.

[37] Tamalmani, K., Husin, H., Review on corrosion inhibitors for oil and gas corrosion issues, Appl. Sci. 10 (2020) 1-16.

[38] Bhawsar, J., Jain, P. K., Jain, P., Experimental and computational studies of Nicotiana tabacum leaves extract as green corrosion inhibitor for mild steel in acidic medium. Alex. Eng. J. 54 (2015) 769–775.

[39] Ramdani M., Ramdani M., Elmsellem H., Elkhiati N., Benyounes, H., Aouniti, A., Ghazi, Z., Chetouani, A., Hammouti, B., Caulerpa prolifera green algae using as eco-friendly corrosion inhibitor for mild steel in 1 M HCl media, Der Pharma Chem. 7 (2015) 67–76.

[40] Refaey, S. A. M., Abd El-Rehim, S. S., Taha, F., Saleh, M. B., Ahmed, R. A., Inhibition of chloride localized corrosion of mild steel by PO_4^{3-}, CrO_4^{2-}, MoO_4^{2-}, and NO_2^- anions, Appl. Surf. Sci. 158 (2000) 190-196.

[41] Perrin, F. X., Ziarelli, F., Dupuis, A., Relation between the corrosion resistance and the chemical structure of hybrid sol-gel coatings with interlinked inorganic-organic network, Prog. Org. Coat. 141 (2020) 105532.

[42] Bustos-Terrones, V., Uruchurtu, J., Rochin-Medina, J. J., Ramirez, K., Rangel-Peraza, J. G., Romero-Romo, M. A., Bustos-Terrones, Y., Synthesis, characterisation and electrochemical evaluation of a functionalised coating for mild steel corrosion protection, Surf. Eng. 35 (2019) 360–369.

[43] Acero-Gutierrez, A. K., Perez-Flores, A. L., Godinez-Salcedo, J. G., Moreno-Palmerin, J., Morales-Ramirez, A. de J., Corrosion protection of A36 steel with SnO_2 nanoparticles integrated into SiO_2 coatings, Coatings. 10 (2020) 385.

[44] Hamidon, T. S., Hussin, M. H., Susceptibility of hybrid sol-gel (TEOS-APTES) doped with caffeine as potent corrosion protective coatings for mild steel in 3.5 wt.% NaCl, Prog. Org. Coat. 140 (2020) 105478.

[45] Samiee, R., Ramezanzadeh, B., Mahdavian, M., Alibakhshi, E., Assessment of the smart self-healing corrosion protection properties of a water-base hybrid organo-silane film combined with non-toxic organic/inorganic environmentally friendly corrosion inhibitors on mild steel, J. Clean. Prod. 220 (2019) 340–356.

[46] Trabelsi, W., Triki, E., Dhouibi, L., Ferreira, M.G.S., Zheludkevich, M.L., Montemor, M.F., The use of pre-treatments based on doped silane solutions for improved corrosion resistance of galvanised steel substrates, Surf. Coat. Technol. 200 (2006) 4240–4250.

[47] Zandi Zand, R., Verbeken, K., Adriaens, A., Corrosion resistance performance of cerium doped silica sol-gel coatings on 304L stainless steel, Prog. Org. Coat. 75 (2012) 463–473.

[48] Ashrafi-Shahri, S. M., Ravari, F., Seifzadeh, D., Smart organic/inorganic sol-gel nanocomposite containing functionalized mesoporous silica for corrosion protection, Prog. Org. Coatings. 133 (2019) 44−54.

[49] Ding, C., Fu, J., Smart anticorrosion coatings based on nanocontainers, Elsevier Inc. 413 (2020).

[50] Zheludkevich, M. L., Tedim, J., Ferreira, M. G. S., 'Smart' coatings for active corrosion protection based on multi-functional micro and nanocontainers, Electrochim. Acta. 82 (2012) 314−323.

[51] Yeganeh, M., Marashi, S. M., Mohammadi, N., Smart corrosion inhibition of mild steel using mesoporous silica nanocontainers loaded with molybdate, Int. J. Nanosci. Nanotechnol. 14 (2018) 143−151.

[52] Nazeer, A. A., Madkour, M., Potential use of smart coatings for corrosion protection of metals and alloys: A review, J. Mol. Liq. 253 (2018) 11−22.

[53] Song, Y., Liu, Y., Qi, T., Li, G. L., Towards dynamic but super tough healable polymers through biomimetic hierarchical hydrogen-bonding interactions, Appl. Organomet. Chem. 57 (2018) 13838–13842.

[54] Blight, B. A., Hunter, C. A., Leigh, D. A., McNab, H., Thomson, P. I., An AAAA–DDDD quadruple hydrogen-bond array, Nat. Chem. 3 (2011) 244–248.

[55] Ying, H., Zhang, Y., Cheng, J., Dynamic urea bond for the design of reversible and self-healing polymers, Nat. Commun. 5 (2014) 1–9.

[56] Schafer, S., Kickelbick, G., Double reversible networks: improvement of self-heal- ing in hybrid materials via combination of Diels–Alder cross-linking and hydrogen bonds, Macromolecules. 51 (2018) 6099–6110.

[57] Gandini, A., Coelho, D., Silvestre, A. J. D., Reversible click chemistry at the service of macromolecular materials. Part 2. Thermoreversible polymers based on the Diels-Alder reaction of an A-B furan/maleimide monomer, J. Polym. Sci. Part A: Polym. Chem. 48 (2010) 2053–2056.

[58] Canadell, J., Goossens, H., Klumperman, B., Self-healing materials based on disulfide links, Macromolecules. 44 (2011) 2536–2541.

[59] Makhlouf, A. S. H., Abu-Thabit, N. Y., Advances in smart coatings and thin films for future industrial and biomedical engineering applications, Elsevier, Netherlands. 2019.

[60] Lvov, Y., Wang, W., Zhang, L., Fakhrullin, R., Halloysite Clay Nanotubes for Loading and Sustained Release of Functional Compounds, J. Adv. Mater. 28 (2015) 1227-1250.

[61] Yuan, P., Tan, D., Annabi-Bergaya, F., Properties and applications of halloysite nanotubes: recent research and future prospects, Appl. Clay Sci. 112 (2015) 75-93.

[62] Falcon, J. M., Sawczen, T., Aoki, I. V., Dodecylamine-loaded halloysite nanocontainers for active anticorrosion coatings, Front. Mater. 2 (2015) 1–13.

[63] Joshi, A., Abdullayev, E., Vasiliev, A., Volkova, O., Lvov, Y., Interfacial Modification of Clay Nanotubes for the Sustained Release of Corrosion Inhibitors, Langmuir (2012) 2–11.

[64] Xing, X., Zhou, D., Tang, E., Liu, S., Chu, X., Xu, X., Xu, Y., A novel method to control the release rate of halloysite encapsulated Na_2MoO_4 with Ca^{2+} and corrosion resistance for Q235 steel, Appl. Clay Sci. 188 (2020) 105492.

[65] Manasa, S., Jyothirmayi, A., Siva, T., Sathiyanarayanan, S., Gobi, K. V., Subasri, R., Effect of inhibitor loading into nanocontainer additives of self-healing corrosion protection coatings on aluminum alloy A356.0, J. Alloys Compd. 726 (2017).

[66] Adsul, S. H., Siva, T., Sathiyanarayanan, S., Sonawane, S. H., Subasri, R., Self-healing ability of nanoclay-based hybrid sol-gel coatings on magnesium alloy AZ91D, Surf. Coat. Technol. 309 (2017).

[67] Habib, S., Khan, A., Nawaz, M., Sliem, M. H., Shakoor, R. A., Kahraman, R., Abdullah, A. M., Zekri, A., Self-healing performance of multifunctional polymeric smart coatings, Polymers (Basel). 11 (2019) 1–19.

[68] Batool, S. A., Maqbool, M. S., Javed, M. A., Niaz, A., Atiq Ur Rehman, M., a review on the fabrication and characterization of titania nanotubes obtained via electrochemical anodization, Surface. 5 (2022) 456-480.

[69] Chen, Z., Yang, W., Yin, X., Chen, Y., Liu, Y., Xu, B., Corrosion Protection of 304 stainless steel from a smart conducting polypyrrole coating doped with pH-sensitive molybdate-loaded TiO_2 nanocontainers, Prog. Org. Coat. 146 (2020) 105750.

[70] Ubaid, F., Radwan, A. B., Naeem, N., Shakoor, R. A., Ahmad, Z., Montemor, M. F., Kahraman, R., Abdullah, A. M., Soliman, A., Multifunctional self-healing polymeric nanocomposite coatings for corrosion inhibition of steel, Surf. Coat. Technol. 372 (2019) 121-133.

[71] Nawaz, M., Yusuf, N., Habib, S., Shakoor, R. A., Ubaid, F., Ahmad, Z., Kahraman, R., Mansour, S., Gao, W., Development and properties of polymeric nanocomposite coatings, Polymers (Basel). 11 (2019) 852.

[72] Arunchandran, C., Ramya, S., George, R. P., Kamachi Mudali, U., Self-healing corrosion resistive coatings based on inhibitor loaded TiO_2 nanoconatiners, J. Electrochem. Soc. 159 (2012) 552-559.

[73] Bhong, S. Y., More, N., Choppadandi, M., Kapusetti, G., Review on carbon nanomaterials as typical candidates for orthopaedic coatings, SN Applied Sciences, 1: 76 (2019) 1-16.

[74] Najmi, P., Keshmiri, N., Ramezanzadeh, M., Ramezanzadeh, B., Synthesis and application of Zn-doped polyaniline modified multi-walled carbon nanotubes as stimuli-responsive nanocarrier in the epoxy matrix for achieving excellent barrier-self-healing corrosion protection potency, J. Chem. Eng. 412 (2021) 128637.

[75] Onyancha, R. B., Aigbe, U. O., Ukhurebor, K. E., Muchiri, P. W., Facile synthesis and applications of carbon nanotubes in heavy-metal remediation and biomedical fields: A comprehensive review, J. Mol. Struct. 1238 (2021) 130462.

[76] Yang, H., Duan, L., Zhang, P., Xu, G., Cui, J., Lv, J., Sun, W., Li, B., Wang, D., Wu, Y., Corrosion resistance of functionalized carbon nanotubes enhanced epoxy coatings on sintered NdFeB magnets, J. Coat. Technol. Res. 19 (2022) 1317–1329.

[77] Lorwanishpaisarn, N., Srikhao, N., Jetsrisuparb, K., Knijnenburg, J. T. N., Theerakulpisut, S., Okhawilai, M., Kasemsiri, P., Self-healing ability of epoxy vitrimer nanocomposites containing bio-based curing agents and carbon nanotubes for corrosion protection, J. Polym. Environ. 30 (2022) 472–482.

[78] Abdulrahaman, M.A., Abubakre, O. K., Abdulkareem, S.A., Tijani, J. O., Aliyu, A., Afolabi, A. S., Effect of coating mild steel with CNTs on its mechanical properties and corrosion behaviour in acidic medium, Adv. Nat. Sci. Nanosci. Nanotechnol. 8 (2017) 015016.

[79] Yabuki, A., Fathona, I. W., Recent trends in nanofiber-based anticorrosion coatings, Handbook of Nanofibers, Springer International Publishing, (2018) 2-27.

[80] Soha, G., Nader, S., Mohamed, S., Nosier, S., Hefnawy, A., Hamed, A., Samir, E., Corrosion inhibition of aluminum in hydrochloric acid solution using ceria doped polyvinyl chloride nanofiber. Int. J. Electrochem. Sci. 12 (2017) 1094–1105.

[81] Muthirulan, P., Kannan, N., Meenakshi, S. M., Synthesis and corrosion protection properties of poly(o-phenylenediamine) nanofibers. J. Adv. Res. 4 (2013) 385–392.

[82] Aldabbagh, B. M., Alshimary, H. J., Polyamide nanofibers coating by electrospinning technique for anti-corrosion behavior. J. Eng. Technol. 35 (2017) 987–991.

[83] Yabuki, A., Kawashima, A., Fathona, I. W., Self-healing polymer coatings with cellulose nanofibers served as pathways for the release of a corrosion inhibitor. Corros. Sci. 85 (2014) 141–146.

[84] Yao, B., Wang, G., Ye, J., Li, X., Corrosion inhibition of carbon steel by polyaniline nanofibers, Mater. Lett. 62 (2008) 1775–1778.

[85] Zhang, H., Wang, J., Liu, X., Wang, Z., Wang, S., High performance self-healing epoxy/polyamide protective coating containing epoxy microcapsules and polyaniline nanofibers for mild carbon steel, Ind. Eng. Chem. Res. 52 (2013) 10172–10180.

[86] Zhao, Y., Zhang, Z., Yu, L., Tang, Q., Electrospinning of polyaniline microfibers for anticorrosion coatings: An avenue of enhancing anticorrosion behaviours, Synth. Met. 212 (2016) 84–90.

[87] Guzman, E., Mateos-Maroto, A., Ruano, M., Ortega, F., Rubio, R. G., Layer-by-layer polyelectrolyte assemblies for encapsulation and release of active compounds, Adv. Colloid Interface Sci. 249 (2017) 290-307.

[88] Arora, S., Mestry, S., Singh, H. K., Mhaske, S. T., Sol–gel based layer-by-layer deposits of lanthanum cerium molybdate nanocontainers and their anticorrosive attributes, Iran. Polym. J. 29 (2020) 133–146.

[89] Syed, J.A., Tang, S., Lu, H., Meng, X., Smart PDDA / PAA multilayer coatings with enhanced stimuli responsive self-healing and anti-corrosion ability, Colloids Surf. A: Physicochem. Eng. Asp. 476, (2015) 48–56.

[90] Kamburova, K., Boshkova, N., Boshkov, N., Radeva, T., Design of polymeric core-shell nanocontainers impregnated with benzotriazole for active corrosion protection of galvanized steel, Colloids Surf. A: Physicochem. Eng. Asp. 499 (2016) 24–30.

[91] Qian, B., Song, Z., Hao, L., Wang, W., Kong, D., Self-healing epoxy coatings based on nanocontainers for corrosion protection of mild steel, J. Electrochem. Soc. 164 (2017) 54–60.

[92] Liu, X., Zhang, D., Hou, P., Pan, J., Zhao, X., Hou, B., Preparation and characterization of polyelectrolyte-modified attapulgite as nanocontainers for protection of carbon steel, J. Electrochem. Soc. 165 (2018) 907–915.

[93] Uddin, F., Clays, nanoclays, and montmorillonite minerals, Metall. Mater. Trans. A 39 (2008) 2804–2814.

[94] Leal, D. A., Kuznetsova, A., Silva, G. M., Tedim, J., Wypych, F., Marino, C. E. B., Layered materials as nanoconatiners for active corrosion protection: A brief review, Appl. Clay Sci. 225 (2022) 106537.

[95] Zhou, C., Tong, D., Yu, W., Chapter-7-Smectite Nanomaterials: Preparation, Properties and Functional Applications, Nanomaterials from Clay Minerals (2019) 335-364.

[96] Motte, C., Poelman, M., Roobroeck, A., Fedel, M., Deflorian, F., Olivier, M. G., Improvement of corrosion protection offered to galvanized steel by incorporation of lanthanide modified nanoclays in silane layer. Prog. Org. Coat. 74 (2012) 326-333.

[97] Mohammadi, I., Izadi, M., Shahrabi, T., Fathi, D., Fateh, A., Enhanced epoxy coating based on cerium loaded Na-montmorillonite as active anti-corrosive nanoreservoirs for corrosion protection of mild steel: synthesis, characterization, and electrochemical behaviour. Prog. Org. Coat. 131 (2019) 119–130.

[98] Ghazi, A., Ghasemi, E., Mahdavian, M., Ramezanzadeh, B., Rostami, M., The application of benzimidazole and zinc cations intercalated sodium montmorillonite as smart ion exchange inhibiting pigments in the epoxy ester coating. Corros. Sci. 94 (2015) 207–217.

[99] Truc, T. A., Thuy, T. T., Oanh, V. K., Hang, T. T. X., Nguyen, A.S., Causse, N., Pebere, N., 8-hydroxyquinoline-modified clay incorporated in an epoxy coating for the corrosion protection of carbon steel, Surf. Interfaces. 14 (2019) 26–33.

[100] Edraki, M., Zaarei, D., Azole derivatives embedded in montmorillonite clay nanocarriers as corrosion inhibitors of mild steel, Int. J. Miner. Metall. Mater. 26 (2019) 86–97.

[101] Adsul, S. H., Siva, T., Sathiyanarayanan, S., Sonawane, S. H., Subasri, R., Aluminum pillared montmorillonite clay-based self-healing coatings for corrosion protection of magnesium alloy AZ91D, Surf. Coat. Technol. 352 (2018) 445–461.

[102] Mishra, G., Dash, B., Pandey, S., Layered double hydroxides: A brief review from fundamentals to application as evolving biomaterials, Appl. Clay. Sci. 153 (2018) 172-186.

[103] Verma, C., Ebenso, E. E., Bahadur, I., Quraishi, M. A., An overview on plant extracts as environmental sustainable and green corrosion inhibitors for metals and alloys in aggressive corrosive media, J. Mol. Liq. 266 (2018) 577–590.

[104] Rodriguez, J., Bollen, E., Nguyen, T. D., Portier, A., Paint, Y., Olivier, M. G., Incorporation of layered double hydroxides modified with benzotriazole into an epoxy resin for the corrosion protection of Zn-Mg coated steel, Prog. Org. Coat. 149 (2020) 105894.

[105] Deip, A. R., Leal, D. A., Sakae, G. H., Maia, F., Berton, M. A. C., Ferreira, M. G. S., Marino, C. E. B., Performance of commercial LDH traps for chloride ion in a commercial corrosion protection primer for petrochemical industry, Corros. Eng. Sci. Technol. 55 (2020) 66–74.

[106] Granizo, N., Vega, J. M., de la Fuente, D., Chico, B., Morcillo, M., Ion-exchange pigments in primer paints for anticorrosive protection of steel in atmospheric service: anion-exchange pigments, Prog. Org. Coat. 76 (2013) 411-424.

[107] Hang, T. T. X., Truc, T. A., Duong, N. T., Pebre, N., Olivier, M. G., Layered double hydroxides as containers of inhibitors in organic coatings for corrosion protection of carbon steel, Prog. Org. Coat. 74 (2012) 343–348.

[108] Shkirskiy, V., Keil, P., Hintze-Bruening, H., Leroux, F., Vialat, P., Lefevre, G., Ogle, K., Volovitch, P., Factors affecting MoO_4^{2-} inhibitor release from Zn2Al based layered

double hydroxide and their implication in protecting hot dip galvanized steel by means of organic coatings, ACS Appl. Mater. Interfaces. 7 (2015) 25180–25192.

[109] Subasri, R., Soma Raju, K. R. C., Reddy, D. S., Jyothirmayi, A., Ijeri, V. S., Prakash, O., Gaydos, S. P., Environmentally friendly Zn–Al layered double hydroxide (LDH)-based sol–gel corrosion protection coatings on AA 2024-T3, J. Coat. Technol. Res. 16 (2019) 1447–1463.

[110] Duong, N. T., An, T. B., Thao, P. T., Son, N. A., Oanh, V. K., Truc, T. A., Thi, T., Hang, X., Corrosion inhibition of carbon steel by LDH/GO hybrid intercalated with 2-benzothiazolythio-succinic acid, Vietnam J Sci Technol. 55 (2017) 119–125.

[111] Zagorodni, A. A., Ion Exchange Materials: Properties and Applications; Elsevier: Oxford, UK, 2006; ISBN 9780080467535.

[112] Padhy, R. R., Shaw, R., Tiwari, S., Tiwari, S. K., Ultrafine nanocrystalline mesoporous NaY zeolites from fly ash and their suitability for eco-friendly corrosion protection. J. Porous Mater. 22 (2015) 1483–1494.

[113] Wang, J., Zhang, T., Zheng, X., Zhu, Y., Yan, Y., Zhang, M., Shchukin, D. G., Li, C., Wang, Y., Song, D., Smart epoxy coating containing Ce-MCM-22 zeolites for corrosion protection of Mg-Li alloy, Appl. Surf. Sci. 369 (2016) 384–389.

[114] Calabrese, L., Bonaccorsi, L., Proverbio, E., Corrosion protection of aluminum 6061 in NaCl solution by silane-zeolite composite coatings, J. Coat. Technol. Res. 9 (2012) 597–607.

[115] Roselli, S., Deya, C., Revuelta, M., Di Sarli, A. R., Romagnoli, R., Original article Zeolites as reservoirs for Ce (III) as passivating ions in anticorrosion paints, Corros. Rev. (2018) 1–18.

[116] Keyvani, A., Yeganeh, M., Rezaeyan, H., Application of mesoporous silica nanocontainers as an intelligent host of molybdate corrosion inhibitor embedded in the epoxy coated steel, Prog. Nat. Sci.: Mater. Int. 27 (2017) 261-267.

[117] Seljak, K. B., Kocbek, P., Gasperlin, M., Mesoporous silica nanoparticles as delivery carriers: An overview of drug loading techniques, J. Drug Deliv. Sci. Technol. 59 (2020) 101906.

[118] Alipour, K., Nasirpouri, F., Smart anti-corrosion self-healing Zinc metal-based molybdate functionalized-mesoporous-silica (MCM-41) nanocomposite coatings, RSC Adv. 7 (2017) 51879–51887.

[119] Hollamby, M. J., Fix, D., Donch, I., Borisova, D., Möhwald, H., Shchukin, D., Hybrid polyester coating incorporating functionalized mesoporous carriers for the holistic protection of steel surfaces, Adv. Mater. 23 (2011) 1361–1365.

[120] Yeganeh, M., Saremi, M., Rezaeyan, H., Corrosion inhibition of steel using mesoporous silica nanocontainers incorporated in the polypyrrole, Prog. Org. Coatings. 77 (2014) 1428–1435.

CHAPTER-2

Experimental

CHAPTER-2

Experimental

In our study, we have used two types of nanocontainers, i.e., Halloysite nanotube (HNT) and Layer-by-Layer assembled polyelectrolyte nanocontainers, for the loading of different corrosion inhibitors. The sections below are divided accordingly.

2.1. Corrosion Inhibitor loading into Halloysite Nanotubes

0.357 g of Benzotriazole (BTA) as an organic corrosion inhibitor; 2.17 g each of Zirconium n-propoxide, Cerium nitrate ($Ce(NO_3)_3$), Lanthanum nitrate ($La(NO_3)_3$), Gadolinium acetate ($Gd(CH_3COO)_3$) and Erbium nitrate ($Er(NO_3)_3$), all as inorganic corrosion inhibitors were added individually to 100 ml of iso-propyl alcohol (IPA) and stirred for 15 to 20 min. To the above individual solutions, 5 g of HNT was added with continuous stirring for 15 min. The resultant mixtures were kept in vacuum desiccator for approximately 1 h. Upon application of vacuum, slight fizzing is observed which means removal of air bubbles from the lumen of empty HNTs. The removal of air causes the loading of individual corrosion inhibitors into empty lumen of halloysite nanotube. The individual mixtures were kept in vacuum condition for 3 cycles each of 1 h duration to ensure complete loading of corrosion inhibitors into HNTs. The sign of less or no fizzing in the solution confirms the complete loading of corrosion inhibitors into tubes. The obtained mixtures were then centrifuged at 5000 rpm for 15 min followed by drying at 60 °C for 10 h. The procedure for encapsulation of the corrosion inhibitor into the empty lumen of HNTs is shown in Fig. 2.1.
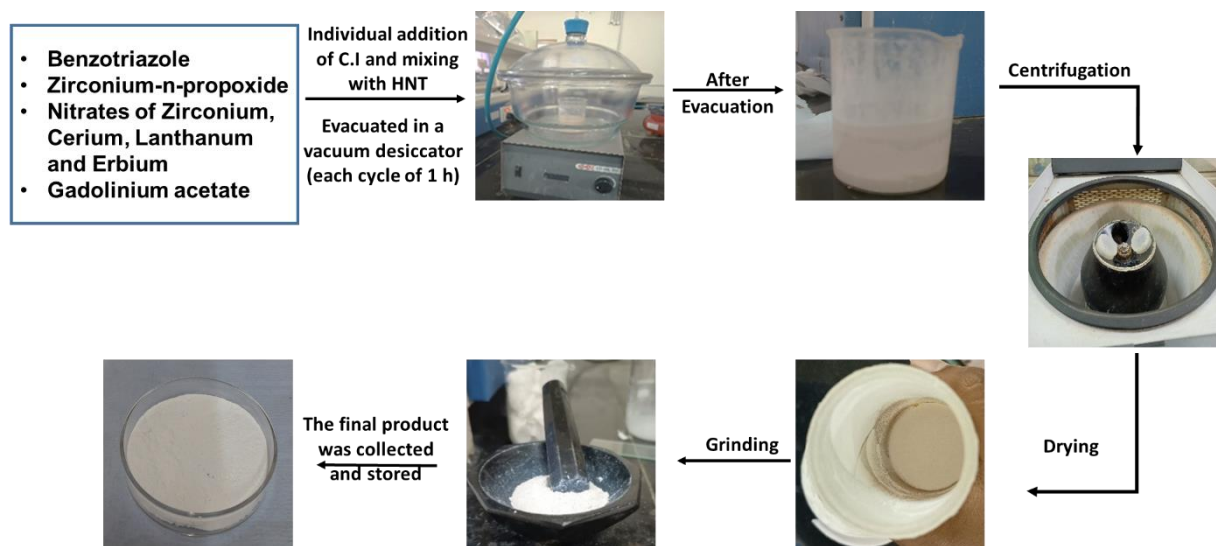
Fig. 2.1. Steps involved during the encapsulation of corrosion inhibitors into halloysite nanotube

BTA loaded HNTs were capped using urea-formaldehyde nanocapsules (UFNCs) for its controlled release [1, 2]. For this purpose, 5 g of polyvinyl alcohol was dissolved in 100 ml of deionized water. In another beaker, 5 ml of this solution was diluted with 130 ml of DI water, followed by addition of 5 g of urea, 0.5 g of resorcinol and 0.5 g of ammonium chloride, respectively. With the help of 0.1 N HCl, the pH of the above mixture was adjusted to 3. In second beaker, 27 g of (3-Glycidyloxypropyl) trimethoxysilane (GPTMS), 0.86 g of 0.1 N HCl and 2.54 g of water were mixed together while keeping the mixture on stirrer. The contents of beaker 2 were slowly added to beaker 1 by keeping the mixture of beaker 1 on continuous stirring. Further, 12.68 g of 37 % formaldehyde was added to the resultant mixture and stirred for 15 to 20 min to stabilize the emulsion. The mixture was kept on a hot plate at 60 °C for 4 h under continuous stirring. Presence of a slightly pale pink precipitate confirms the formation of urea-formaldehyde nanocapsules. The solution was then centrifuged at 6000 rpm for 10 min by washing with DI water first and later with isopropanol to separate the nanocapsules from the suspension. The obtained nanocapsules were then stored in IPA and kept in refrigerator for further use.

2.2. Corrosion Inhibitor loading into Layer-by-Layer Nanocontainers

2.2.1. Synthesis of iron oxide nanoparticles

For BTA as corrosion inhibitor, commercially purchased iron oxide nanoparticles (as-procured from Sigma Aldrich, USA) was used as core or template. In later experiments, it was synthesized in-situ and used for developing layer-by-layer (LbL) nanocontainers.

7 g of iron nitrate was dissolved in 40 ml of DI water and 21 g of sodium hydroxide (NaOH) was dissolved in 100 ml of DI water. The $Fe(NO_3)_3$ solution was added slowly to NaOH solution under continuous stirring. The mixture was then kept for stirring for another 1 h at 500 rpm. The obtained mixture was centrifuged twice and was washed thoroughly using DI water. The precipitate was kept for drying at 60 °C for 2 h followed by calcination at 500 °C for 3 h using Nabertherm Furnace.

2.2.2. Synthesis of bulk solutions of polyelectrolyte layers and corrosion inhibitor layers

Bulk solutions of polyelectrolyte layers and inhibitor layers were prepared initially. 1 g of poly (acrylic acid) (PAA) and 1 g of poly (diallyldimethyl ammonium chloride) (PDADMAC) were added separately to 100 ml of DI water, these layer acts as polyanionic and polycationic layers, respectively. To prepare the bulk solutions of the corrosion inhibitors, 0.0167 moles of BTA, $Ce(NO_3)_3$, $La(NO_3)_3$ and Zirconyl nitrate, $Zr(NO_3)_4$ was added individually to 100 ml of DI water.

2.2.3. Synthesis of layer-by-layer nanopowder

To 100 ml of 0.1 M NaCl solution, 1 g of iron oxide nanoparticles were added and sonicated to ensure proper dispersion. To this mixture, 100 ml of the prepared PAA solution was added and pH was adjusted to 5.5 to 6 using 0.1 N HCl. The whole mixture was then centrifuged and dried to obtain dry powder. The powder obtained was collected and redispersed in a minimum amount of 0.1 M NaCl solution, followed by the addition of a corrosion inhibitor layer. For this, 100 ml of each inhibitor layer (i.e., BTA, $Ce(NO_3)_3$, $La(NO_3)_3$, and $Zr(NO_3)_4$) was deposited individually when synthesizing the LbL nanopowders, and pH was adjusted to 5.5 to 6. Again the mixture was centrifuged and dried. Similar steps were followed while depositing second layer of PAA and PDADMAC, the final terminating layer having positive charge [3, 4].

2.3. Sol Synthesis

To synthesize the hybrid silica sol, 3-(Glycidoxypropyl) trimethoxysilane, GPTMS (from Alfa Aesar, United States of America (USA) with purity 97%) and tetraethylorthosilicate, TEOS (from Sigma Aldrich, USA with purity 98%) were used as precursors. To prepare standard matrix sol, 56.5 g of GPTMS and 26.12 g of TEOS were mixed together to obtain 3.1:1.0 molar ratio. To catalyse the above mixture of sols, 1.72 g of 0.1 N HCl was added dropwise while keeping the solution on stirrer [5]. The sol was then stirred for 1 h to obtain a homogeneous transparent hybrid matrix sol.

The above prepared matrix sol was used as the base formulation for preparing the inhibitor modified sols. The inhibitor modified matrix sol can be further categorized into different categories, namely, (i) direct addition of corrosion inhibitor into matrix sol, where 2 wt% of pure inhibitor was added directly to the matrix sol; (ii) corrosion inhibitor encapsulated into HNT, 2 wt% of encapsulated HNT was added to matrix sol, and (iii) corrosion inhibitor based LbL nanocontainer, followed by addition into matrix sol (2 wt%).

For BTA encapsulated into HNT, different sets of experiments were carried out on the basis of loading amount corrosion inhibitor encapsulated into HNT, followed by addition in matrix sol and comparative study of capping the ends of HNT using urea-formaldehyde nanocapsules. The amount of capping agent added into the matrix sol is ten times that of inhibitor encapsulated HNTs. For better understanding, the detailed discussion of each type of sol synthesized and their abbreviations used throughout the text is well described in the introduction section of each "Chapter".

2.4. Sample Preparation and Coating Deposition

Mild steel coupons of dimensions 2.5 cm × 2.5 cm × 0.3 cm and 5 cm × 2.5 cm × 0.3 cm were used for different coating characterization and salt spray tests, respectively. Prior to coating deposition, the samples were polished and cleaned to obtain a perfect finish. Polishing of the samples was carried out using different grades of abrasive paper, i.e., 400, 600, 800 and 1000. After polishing thoroughly, the samples were immersed in the 2-propanone and ultra-sonicated for 15 min. The process was repeated twice to ensure the complete removal of impurities and grease from the sample surface. The cleaned substrates were then coated with different sols using a dip-coater (EPG GmbH, Germany) at a withdrawal speed of 1 mm/s and cured at 130 °C for 1 h in a drying oven. The process of dip-coating is illustrated in Fig. 2.2.

<mark>**Fig. 2.2.** Dip-coating setup used for coating mild steel substrates</mark>

2.5. Characterization Techniques

2.5.1. Electron microscopic analysis

The field emission scanning electron microscopy is equipped with an electron source emitting an electron beam on the surface which is scanned by electromagnetic lenses. The reflection or interaction of the electrons with the sample surface is recorded by these electromagnetic lenses and an image is created. This technique helps in visualising the structures and topography of the surface as low as 1 nanometre [6, 7]. Field emission scanning electron microscopy/energy dispersive X-ray spectroscopy (FESEM/EDS-Zeiss Gemini 500, as shown in Fig. 2.3) was used for observing and analysing the morphology of the nanopowders, cross-sectional coating thickness and recording the images before and after salt spray test and elemental analysis. Prior to the analysis, the nanopowders were dispersed in a minimum amount of IPA followed by ultra-sonication for 5 min. Fine drops of the solution were dropped on the stubs containing carbon tape and were dried for 10 to 15 min at room temperature to evaporate the solvent completely. The as-prepared stubs and the sol-gel coated mild steel samples were subjected to gold sputtering for 45 to 60 sec in order to avoid the charging of the samples and to obtain a sharp image without any haziness during the analysis. During the analysis, images were recorded at different magnifications, starting from 350 X to 20 kX.
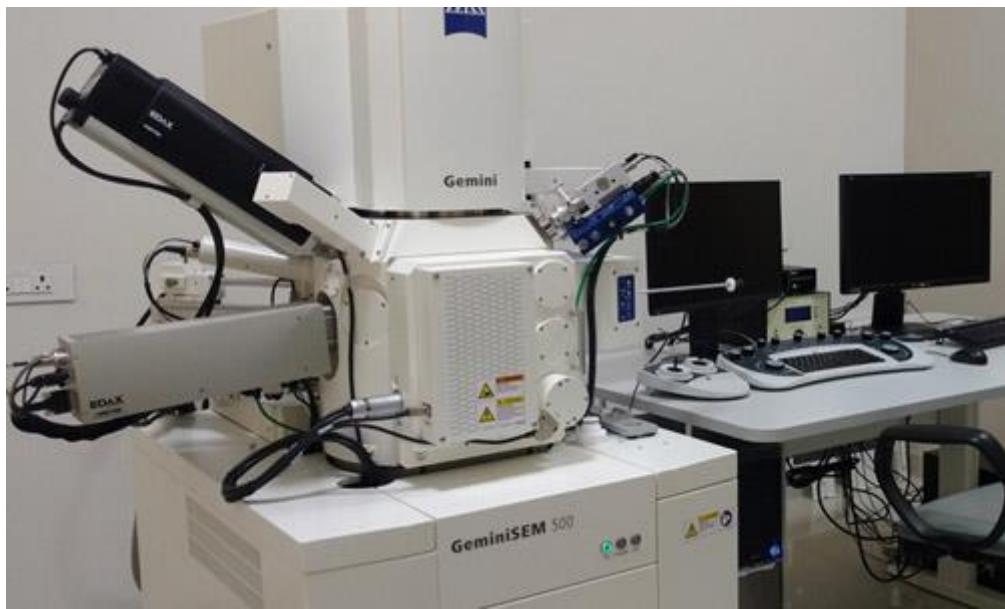
Fig. 2.3. Field Emission Scanning Electron Microscopy-Zeiss Gemini 500

To compare and analyse the as-received HNT, inhibitor loaded HNT and capped inhibitor loaded HNT, transmission electron microscopy (TEM, Tecnai 200 G2, FEI, Netherlands) was used. The TEM analysis was carried out to obtain the in-depth analysis of the nanopowders, where it can provide high resolution images from which the user can extract information such as morphology, size, crystal structure of the samples, etc. For the analysis, only a small amount of powder sample was dispersed in ethyl alcohol and ultra-sonicated for 5 min to ensure good dispersion. The suspension was dropped on the Cu grids consisting the carbon tape onto it with the help of micro-pipette. In our research work, we could extract the information about the empty and loaded lumen of HNTs, their diameter and length, respectively. Later, the next set of experiments where inorganic corrosion inhibitors were encapsulated into HNTs was characterized using a different instrument (JEOL JEM F200).

2.5.2. Brunauer-Emmett-Teller (BET) surface area and pore volume analysis

The BET analysis of the as-received HNTs, BTA encapsulated HNTs and capped BTA encapsulated HNTs were carried out to confirm the pore volume and surface area of the nanopowders. The instrument used for the analysis was Micromeritics Tristar 3000 from USA (shown in Fig. 2.4a). The characterization was carried out to compare and analyse the change in pore volume and surface area after loading the corrosion inhibitor into HNTs w.r.t pristine HNTs. BET analysis relies on multilayer adsorption, which primarily uses an adsorbate gas that does not react chemically with the material for analysis. Nitrogen is one of the most commonly used adsorbate gas which adsorbs and desorbs at 77 K. Prior to the analysis, all the samples

were degassed under vacuum at 300 °C for 6 h. Later the experiments were performed using Quantchrome Autosorb iQ, Anton Paar, USA (as shown in Fig. 2.4b) for inorganic corrosion inhibitors encapsulated into HNTs.
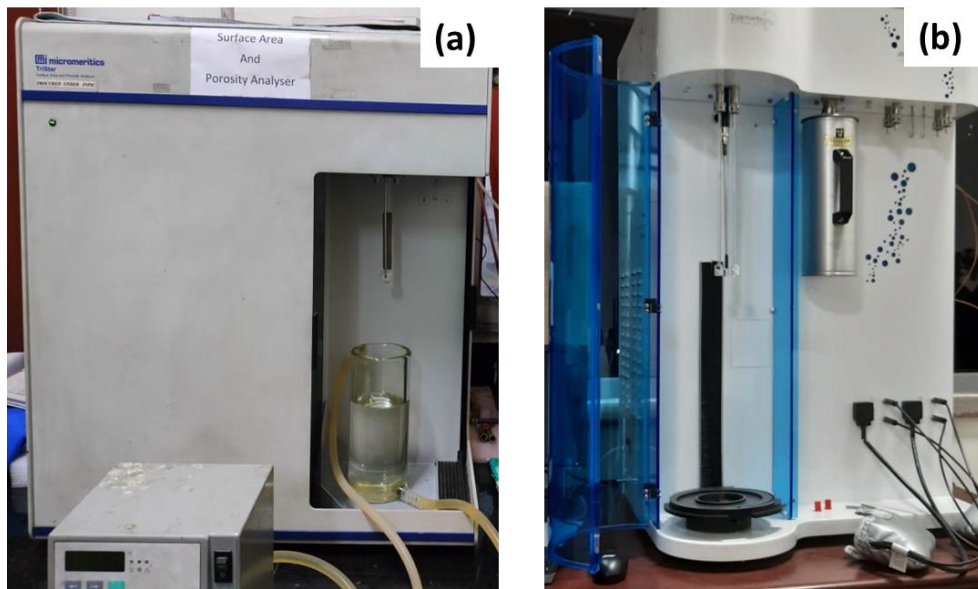
Fig. 2.4. BET Surface area and pore volume analysers (a) Micromeritics Tristar 3000 and (b) Quantchrome Autosorb iQ, Anton Paar

2.5.3. X-ray diffraction (XRD) analysis

The crystalline or amorphous nature of as-received iron oxide nanoparticles, in-situ synthesized iron oxide nanoparticles, HNTs, different corrosion inhibitor loaded HNTs, and modified layer-by-layer nanocontainers were confirmed using XRD, Bruker AXS D8 Advance, USA as shown in Fig. 2.5. The XRD was performed in 2θ range from 5° to 100° with a step size of 0.1°.

Fig. 2.5. Bruker AXS D8 Advance- X-ray Diffractometer

It is one of the non-destructive techniques used for analysing materials at its atomic or molecular level. It is generally carried out for crystalline materials but can also give information about the amorphous material too. It was used to determine the arrangements of each atom in the crystal, phase analysis and lattice parameters of the material. In XRD, the material is subjected to X-rays, which when passed through the crystal diffracts off into two different planes to form a constructive interference pattern. This pattern then helps in deducing the crystal structure of the material. X-ray diffraction is based on Bragg's law,

$$n\lambda = 2d\sin\theta$$

Where, *n = order of reflection*

λ = wavelength of incident X-rays

d = interplanar distance

θ = angle of incidence

The experimental principle for X-ray Diffraction is shown in Fig. 2.6.
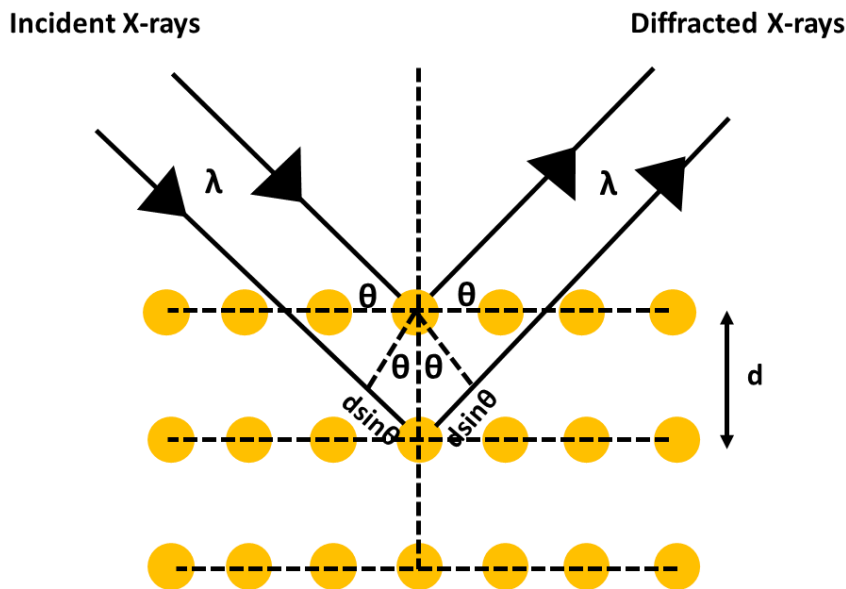
Fig. 2.6. Schematic representation of the principle involved in X-ray Diffraction

The International Centre for Diffraction Data (ICDD) is a database that maintains the record of powder diffraction patterns. The qualitative phase analysis obtained via diffraction pattern of XRD for the powder material is compared with the standard crystallographic database. The files stored in the database are called Powder Diffraction Files (PDF), which include different parameters such as d-spacing, unit cell and intensity of diffraction, which helps in matching and identification of the material. The XRD profiles were analysed using Match$^{®}$ software.

2.5.4. Fourier transform infra-red (FTIR) spectroscopy

Sample preparation becomes an important criterion for FTIR technique. The solid sample to be characterized via FTIR is prepared using KBr. Nearly, 1 mg of the sample is added to 100 mg of KBr powder, which is then grinded homogenously into fine powder. The obtained mixture is then compressed into transparent pellets for further use. One must be extra careful while preparing the sample, as the hygroscopic nature of KBr can cause solidifying of the samples and hence making it look more opaque rather than transparent [9]. After this, the KBr pellet was placed in the sample holder and analyzed.

FTIR is an analytical technique used for characterizing organic or polymeric materials. The fundamental principle of FTIR relies on atomic vibrations of a molecule which can absorb at a certain frequency in the infrared region. A black body source is used for emitting IR

radiation in the range of 400-4000 cm^{-1}, a beam splitter, and two mirrors: one moving and one fixed type. As IR beam passes from the source to splitter, the beam reflects into two parts, which are transmitted to the two mirrors, respectively. Again the two beams are reflected from the mirrors and recollected at the beam splitter giving an interference pattern, which is transmitted through the sample compartment to the detector giving a spectrum. FTIR spectra were recorded using Vertex 70, Bruker Optik GmbH, Germany (shown in Fig. 2.7) for as-received HNT and different corrosion inhibitor encapsulated HNTs.
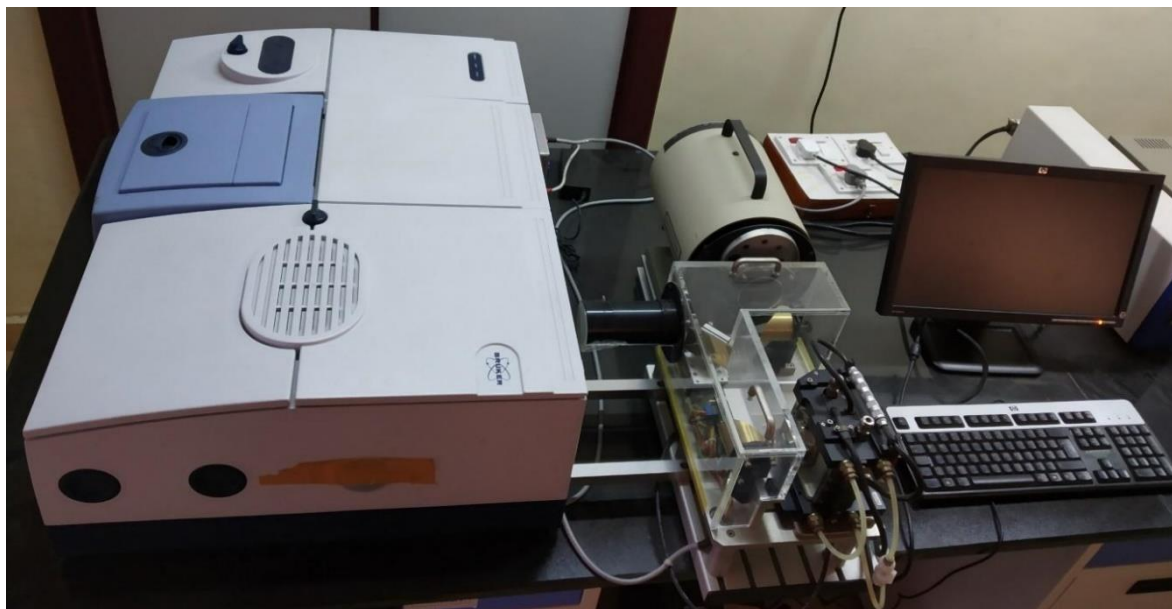
Fig. 2.7. Fourier Transform Infrared Spectroscopy-Vertex 70, Bruker Optik GmbH, Germany

2.5.5. Zeta potential measurements

On application of electric field, the particles tend to move due to the interaction between the applied electric field and charged particle. The particle velocity is measured by Doppler shift in the scattered light. The motion of particle is directly proportional to the electrical potential near the shear plane which is termed as "Zeta potential". It is a technique that helps in measuring the electrochemical equilibrium at the particle-electrolyte interface. It usually measures the magnitude of electrostatic attraction and repulsion between the particles, and helps in determining the stability of the colloidal particles. Figure 2.8 shows the schematic of zeta potential measurement principle.
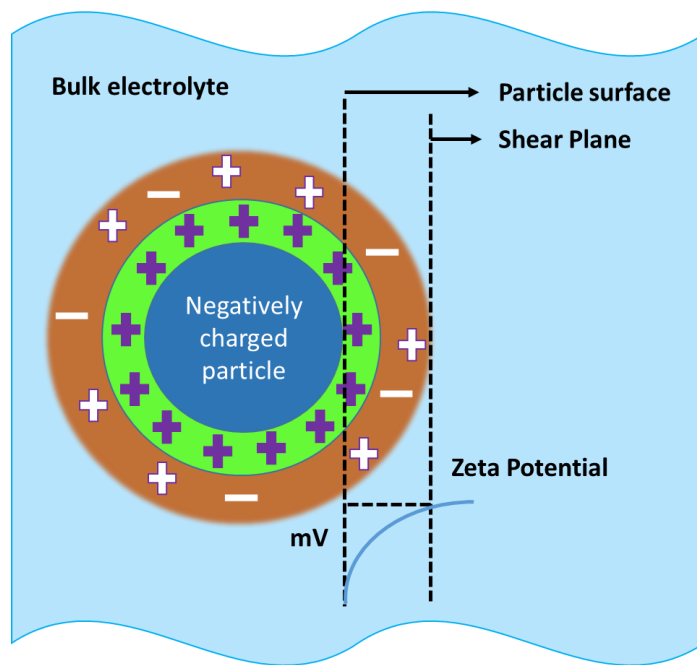
Fig. 2.8. Schematic representation of Zeta potential measurement principle

  Zeta potential measurements were carried out after deposition of each polyelectrolyte layer and inhibitor layer during the layer-by-layer nanocontainer synthesis using Zetasizer (MALVERN AT-0050007) instrument, as shown in Fig. 2.9.
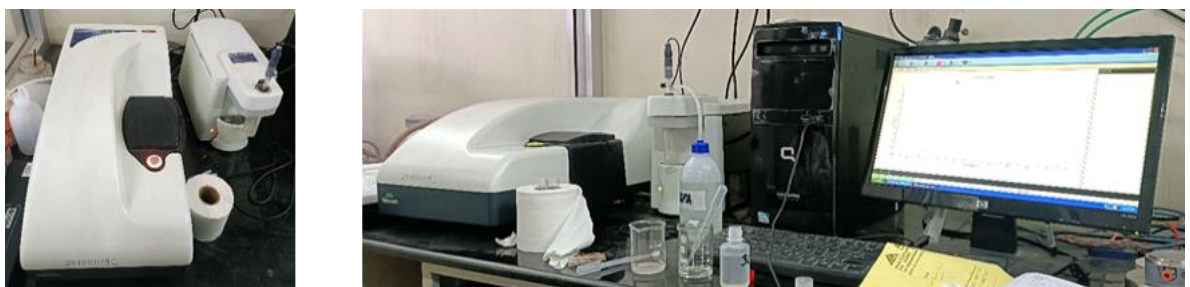
Fig. 2.9. Zetasizer (MALVERN AT-0050007) instrument

2.5.6. Ultraviolet Visible Near Infrared (UV-Vis-NIR) spectroscopy

  UV-Vis-NIR spectroscopy is a technique that is used to determine the optical properties such as reflectance, absorbance, and transmittance of liquid or solid samples at a specific wavelength. It is broadly divided into three regions, covering a wavelength range from 200 to 3000 nm. The UV-Vis-NIR spectroscopy is based on Beer Lambert's Law, where the amount of light coming from the source transmits through the sample and is then detected by the detectors. The presence of detectors in the instrument helps in converting the light signal to

electrical signal and data is analysed. Figure 2.10 shows the working principle of UV-Vis spectroscopy.
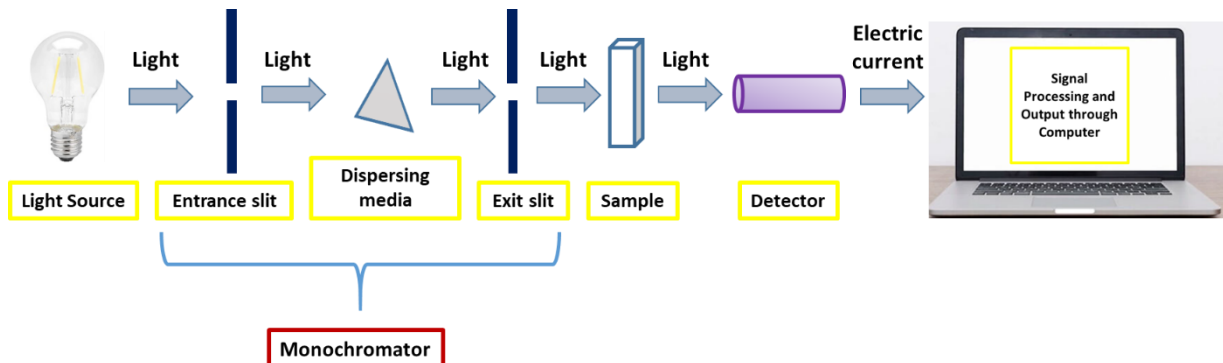
Fig. 2.10. Schematic representation of the working principle of UV-Vis Spectroscopy

The release rate of benzotriazole from halloysite nanotube at different pH w.r.t different time intervals was measured using UV-Vis-NIR spectroscopy (Shimadzu, Japan UV-3600 plus, shown in Fig. 2.11).

Fig. 2.11. UV-Vis-NIR Spectrophotometer-Shimadzu, Japan UV-3600 plus

2.5.7. Viscosity of the sol

Viscosity of the sols used for coating on MS substrates was measured with respect to time. The Rotational viscometer, RheolabQC by Anton Paar, shown in Fig. 2.12 was used for the measurements.

Fig. 2.12. Rotational viscometer, Rheolab QC, Anton Paar

The rheometer measures the torque and deflection angle of the rotating spindle. The speed is obtained with the help of deflection angle and time. The rheological parameters such as shear stress, deformation, shear rate and viscosity are usually deduced from the torque, deflection angle and speed.

2.5.8. Coating thickness and Tape adhesion test

Coating thickness gauge measures the thickness of the coating on metal surfaces using magnetic and eddy current principle. The data obtained using Positector® is reliable, accurate and precise. The instrument (Positector® 6000, De Felsko Corporation, USA as shown in Fig. 2.13) is calibrated using the known film thickness by placing the probe on the surface. Further, the thicknesses of all the coatings generated on the mild steel substrates were measured.
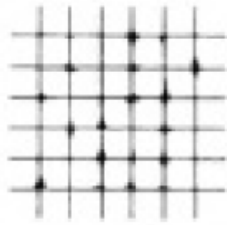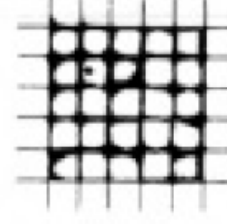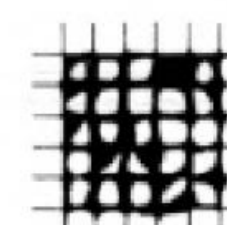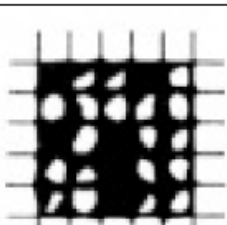
Fig. 2.13. Coating thickness gauge - Positector® 6000, De Felsko Corporation

Tape adhesion test or cross cut adhesion test was carried out using multi-hatch gauge, BEVS 2203, China (as shown in Fig. 2.14 a and b) for different mild steel coated samples. The images were recorded using optical microscope (BX51M, shown in Fig. 2.14 c) before and after the test to compare and analyse the data.
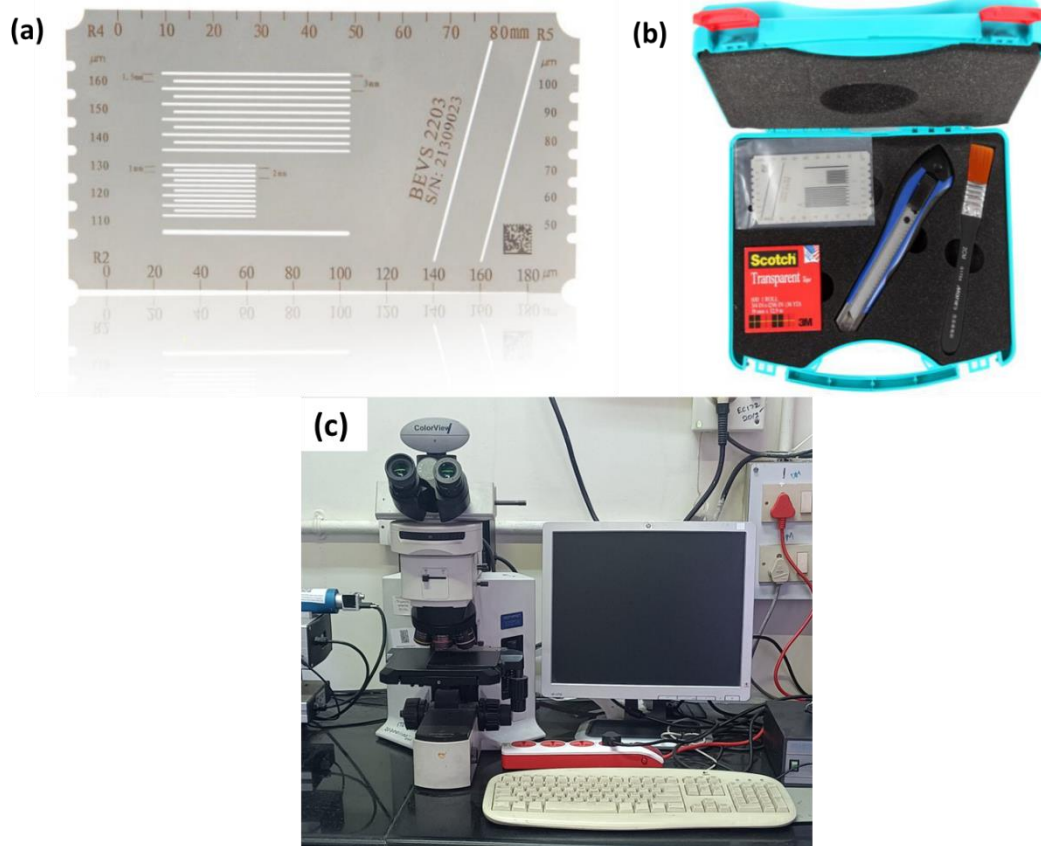
Fig. 2.14. (a) Scale used for making cross-hatch pattern on the substrates, (b) Cross-hatch kit consisting of necessary tools used during the test, and (c) optical microscope (BX51M).

As per ISO 2409 standards [10], using a knife and scale, a grid-like or cross-cut pattern was incised on the coating surface and images were collected. Further, a piece of tape was applied onto the incised surface and was peeled-off forcefully. The images were recorded again after the pull-off test and were evaluated as per the scale provided below (Fig. 2.15):

Class	Description	Performance
0	The edges of the cuts are completely smooth; none of the squares of the lattice is detached	
1	Detachment of small flakes of the coating at the intersections of cuts. A cross-cut area not significantly greater than 5% is affected	
2	The coating has flaked along the edges and/or at the intersections of the cuts. A cross-cut area significantly greater than 5%, but not significantly greater than 15%,is affected	
3	The coating has flaked along the edges of the cuts partly or wholly in large ribbons, and or it has flaked partly or wholly on different parts of the squares. A cross-cut area significant greater than 35%,is affect	
4	The coating has flaked along the edges of the cuts in large ribbons and/or same square have detached parity or wholly. A cross-cut area significantly greater than 35%, but not significantly greater than 60%, is affected	
5	Any degree of flaking that cannot even be classified by classified buy classification	

Fig. 2.15. Classification of ranks as per ISO 2409 after tape adhesion test

2.5.9. Water contact angle measurements

A Krüss GmbH drop shape analyser as shown in Fig. 2.16 was used to measure the water contact angle (WCA).

Fig. 2.16. Water Contact Angle measurement instrument

The contact angle was calculated using the tangent method and the DSA II software. The WCA measurement is a qualitative technique to identify whether the surface is having hydrophobic or hydrophilic properties. It is based on the intermolecular interactions between the sessile drop and the surface, giving the indication about the wettability of the sample surface. If the water drop makes an angle less than 90°, it means that the surface is wetting and hence termed as hydrophilic surface. If the WCA is greater than 90°, it means the surface is non-wetting, which is called as a hydrophobic surface. In this research work, we have measured the water contact angle for the inorganic corrosion inhibitor-based coatings on mild steel surface.

2.5.10. Electrochemical impedance spectroscopy (EIS) and potentiodynamic polarization studies (PPS)

An electrochemical system from CH instruments (Model CHI 604E, USA) was used to perform EIS and PPS of bare and coated MS substrates. A three electrode-based electrochemical cell assembly was used to measure the electrochemical and polarization data, where the saturated calomel electrode as the reference electrode, the Pt plate electrode as the auxiliary electrode, and bare and coated MS substrates as the working electrode.

Electrochemical impedance data was recorded in the frequency range from 100 kHz to 0.01 Hz by applying an AC signal of 0.01 V amplitude. Open-circuit potential (OCP) and polarization data were recorded after immersing the bare and coated MS substrates in 3.5 wt% NaCl solution at different durations. For polarization measurements, a potential of +300 mV to -300 mV was applied with reference to OCP at a scanning speed of 1 mV/s. The experimental values of polarization resistance were calculated by considering a small overpotential of ±30 mV with respect to OCP. ZSimpWin® and CH604E® software were used to examine the electrochemical impedance and polarization data, respectively. Capacitance values were determined using ZSimpWin® software. As some of the electrochemical data were fitted using constant phase elements (CPEs), the pseudo-capacitance or capacitance (C) was calculated in the software, which uses the equation given below to convert the CPE into C.

$$C = (CPE, Yo * R)^{\frac{1}{n}} / R$$

where, CPE, Yo is the pre-factor of CPE, R is ohmic resistance, and n is the surface heterogeneity factor i.e., deviation from the ideal capacitive behaviour ($0.5 < n < 1$). To establish the reproducibility of the data for each uncoated/coated system, four individual experiments ($n = 4$) were carried out. The CH instrument set up is shown in Fig. 2.17, where the right hand side image shows the electrochemical cell used for the studies.

Fig. 2.17. CH instrument electrochemical workstation along with the electrochemical cell

2.5.11. Scanning vibrating electrode technique (SVET)

To analyse the localized corrosion and autonomic-healing property of the coated MS coupons, scanning vibrating electrode technique (SVET) analysis was performed using a Biologic SCV 470 control unit as depicted in Fig. 2.18.
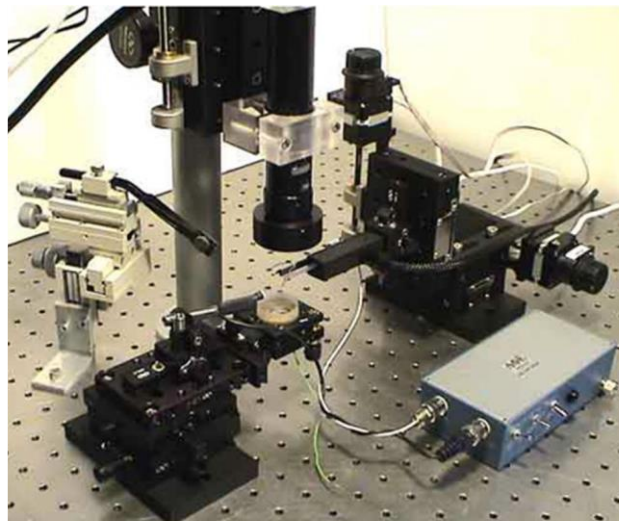
Fig. 2.18. Scanning vibrating electrode technique apparatus

For measurement, samples of 10 mm × 10 mm and a scan area of $4000 \times 4000 \ \mu m^2$ were considered. An artificial defect ranging from 0.1 to 0.3 mm^2 was made on coated substrates before the measurements. Samples were dipped in 3.5 wt% NaCl solution for the analysis. Initial scans were obtained immediately after 5 min exposure to 3.5 wt% NaCl solution and lasted for 30 min to obtain a complete scan. The current density maps were obtained in 3D format.

2.5.12. Salt spray test

The salt spray test (SST) was carried out on the scribed coated and bare MS coupons. Samples were scribed using knife with sharp edge. It was ensured that the edges of the samples were completely insulated using cellophane tape in order to prevent corrosion from the ends. The samples were exposed to 5 wt% NaCl solution in a salt spray chamber as per ASTM B117 standard for different time durations [11]. After salt spray tests, all the exposed samples were rinsed with DI water and dried at room temperature. Elemental analysis of the scribed area was also carried out before and after SST. EDS was carried out to confirm the presence of corrosion inhibitors in the scribed area. The salt spray chamber (Khushboo Scientific Pvt. Ltd., India) used for the accelerated corrosion test is shown in Fig. 2.19.

(a)   (b)

Fig. 2.19. (a) Salt spray cabinet and (b) sample holder containing the mild steel substrates for corrosion test

2.5.13. Micro-Raman spectroscopic analysis

Micro Raman Spectroscopy technique was also employed (WI Tec Alpha 300, Germany-Micro Raman Spectrometer, shown in Fig. 2.20) to confirm the presence of inhibitor and self-healing action of the corrosion inhibitor in the scribed area.
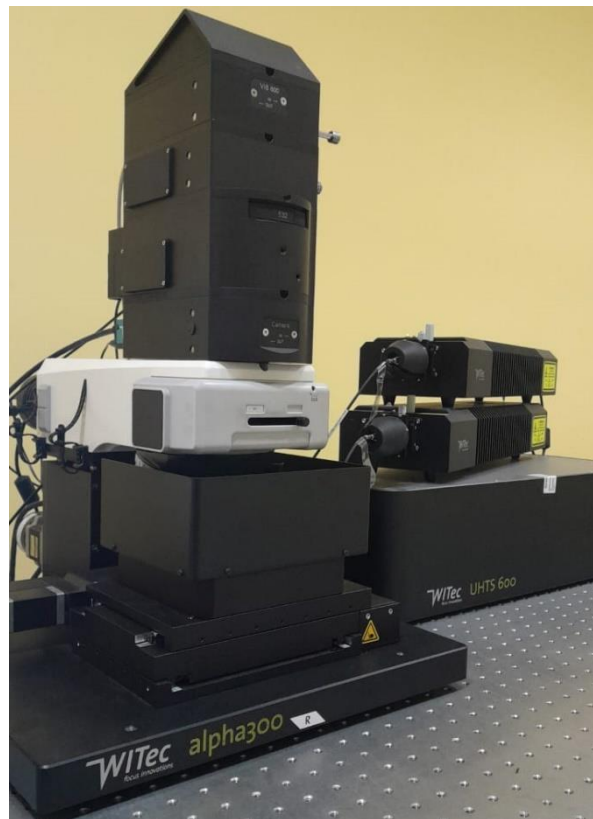
Fig. 2.20. Image of Micro-Raman Spectrophotomer apparatus

The photons from the laser source interact with the molecules of the sample subjected for the analysis. These photons on their interaction scatter inelastically and are collected to give a spectrum from which the data is analysed. The advantage of performing the Raman spectroscopy is that only small amount of sample is required, and data can be collected for selective or localized areas. Note that the molecules with low polarizability, which determines the intensity of the Raman scattering, are the only ones that can be subjected to Raman analysis. Increased molecular polarizability corresponds to increased Raman spectra intensity.

2.6. References:

[1] Abdullayev, E., Lvov, Y., Clay nanotubes for corrosion inhibitor encapsulation: Release control with end stoppers, J. Mater. Chem. 20 (2010) 6681–6687.

[2] Katoueizadeh, E., Zebarjad, S. M., & Janghorban, K., Investigating the effect of synthesis conditions on the formation of urea-formaldehyde microcapsules, J. Mater. Res. Technol. 8 (2019) 541–552.

[3] Rydzek, G., Ji Q., Li M., Schaaf P., Hill J, P., Boulmedais, F., Ariga, K., Electrochemical nanoarchitectonics and layer-by-layer assembly: From basics to future, Nano Today. 10 (2015) 138–167.

[4] Kamburova, K., Boshkova, N., Boshkov, N., Radeva, T., Design of polymeric core-shell nanocontainers impregnated with benzotriazole for active corrosion protection of galvanized steel, Colloids Surf. A: Physicochem. Eng. 499 (2016) 24–30.

[5] Sowntharya, L., Gundakaram, R, C., Soma Raju, K. R. C., Subasri, R., Effect of addition of surface modified nanosilica into silica-zirconia hybrid sol-gel matrix, Ceramics International. 39 (2013) 4245–4252.

[6] Nada, M. H., Scanning electron microscopy, BAOJ Microbiol. 1 (2015) 1-8.

[7] Carter, M., Shieh, J., Chapter-5 Microscopy, Guide to Research Techniques in Neuroscience, Science Direct. (2015) 117–144.

[8] Bragg, W. H. Bragg, W. L., The Reflexion of X-rays by Crystals, Proc. R. Soc. Lond. A. 88 (1913) 428–38.

[9] Salzer, R., Siesler, W. H., Infrared and Raman Spectroscopic Imaging, 2nd Edition, John Wiley & Sons. (2014) 1-180.

[10] ISO 2409, International Standard for Cross-cut test. (2020-08) 1-11.

[11] ASTM B117-16, Standard Practice for Operating Salt Spray (Fog) Apparatus, (2011) 1-12.

CHAPTER-3

Benzotriazole Encapsulated Nanocontainer-based Self-healing Coatings for Corrosion Protection of Mild Steel

CHAPTER-3

Benzotriazole Encapsulated Nanocontainer-based Self-healing Coatings for Corrosion Protection of Mild Steel

3.1. Introduction

Chapter 3 focuses on the anticorrosion and self-healing behavior of an eco-friendly hybrid sol-gel matrix into which benzotriazole (BTA) encapsulated into two different types of nanocontainers (NCs), namely HNT and LbL polyelectrolyte shell is dispersed. The experimental work in this chapter is designed so that a comparison between the performance of BTA encapsulated in two nanocontainers can be made and the best suitable nanocontainer for encapsulating BTA, an organic corrosion inhibitor, can be concluded. The encapsulation of BTA into different types of nanocontainers depends on the charge of the BTA molecule. Being an anionic inhibitor, it can bind easily with the hollow lumen of HNT, which is positively charged because of the alumina layer inside, as shown in Fig. 3.1a. Similarly, BTA is entrapped in between the polyelectrolyte layers based on the charge difference, shown in Fig. 3.1b. The effects of encapsulation of corrosion inhibitors in different nanocontainers followed by dispersion into the sol-gel matrix on the barrier and mechanical properties of the derived coatings were analyzed and discussed.
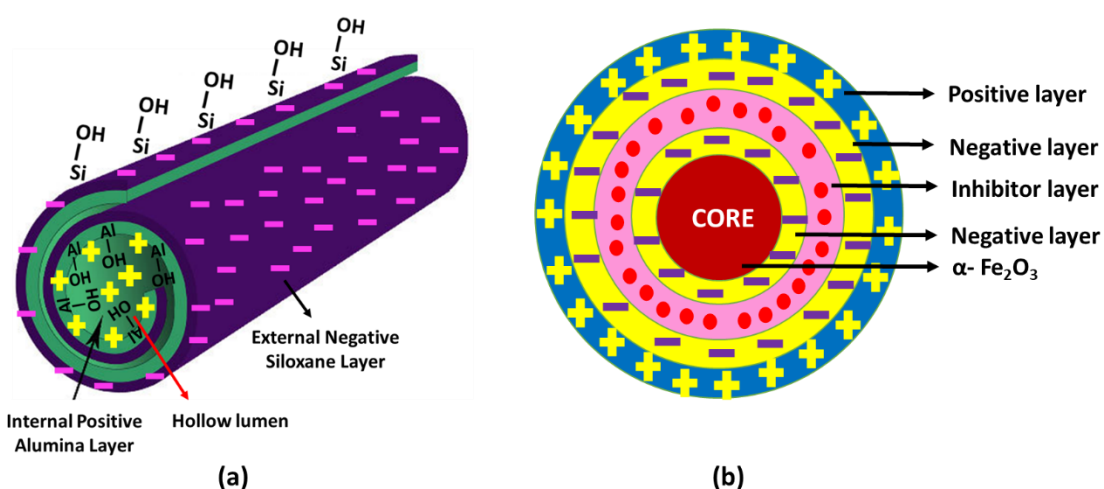
Fig. 3.1. Schematic representation of (a) Halloysite nanotube and (b) Layer-by-layer nanocontainer

3.1.1. Coating deposition and nomenclature of different sols coated on mild steel substrates

The bare mild steel substrate was coated with only matrix sol and corrosion inhibitor encapsulated into different nanocontainers followed by homogenizing in the matrix sol. Table 3.1 shows the nomenclature of different sols with their description.

Table 3.1. Nomenclature of different sols with their description

S. No.	Description of Sol	Sample ID
1.	Matrix sol	**Matrix**
2.	2 wt% BTA added directly to matrix sol	**BS**
3.	2 wt% BTA-encapsulated into LbL NC added to matrix sol	**BLLS**
4.	2 wt% BTA-encapsulated into HNT added to matrix sol	**BHS**

3.2. Results and discussion

3.2.1. Scanning electron microscopy (SEM) and transmission electron microscopy (TEM) analyses

SEM analysis for as-received α-Fe_2O_3 nanoparticles, corrosion inhibitor loaded LbL nanocontainers, bare halloysite nanotube and inhibitor loaded halloysite nanotube was carried out. Elemental composition was determined using EDS. The FESEM image shown in Fig. 3.1 for as-received α-Fe_2O_3 nanoparticles reveals that the particles are in clusters having spherical structures with an average diameter of 30 ± 5 nm. Fe and O were found as constituent elements from the EDS data as depicted in Fig. 3.1. The polyelectrolyte layer deposited α-Fe_2O_3 nanoparticles shows large agglomerates of approximately 200 nm diameter, and EDS analysis indicates the presence of Fe, O, C, Na, Cl and N, confirming the formation of BTA entrapped polyelectrolyte layers on α-Fe_2O_3 nanoparticles [1]. FESEM analysis of as-received HNT shows that the nanoclay has a tubular structure with transparent hollow lumen, and the elemental analysis reveals the presence of Al and Si elements in larger proportions. The inhibitor-loaded HNT shows denser and darker tubular structures, confirming the loading of BTA in the hollow lumen of HNT. Further, the elemental composition determined by EDS analysis shows the presence of Al, Si, C and N, confirming the entrapment of BTA in HNT [2].
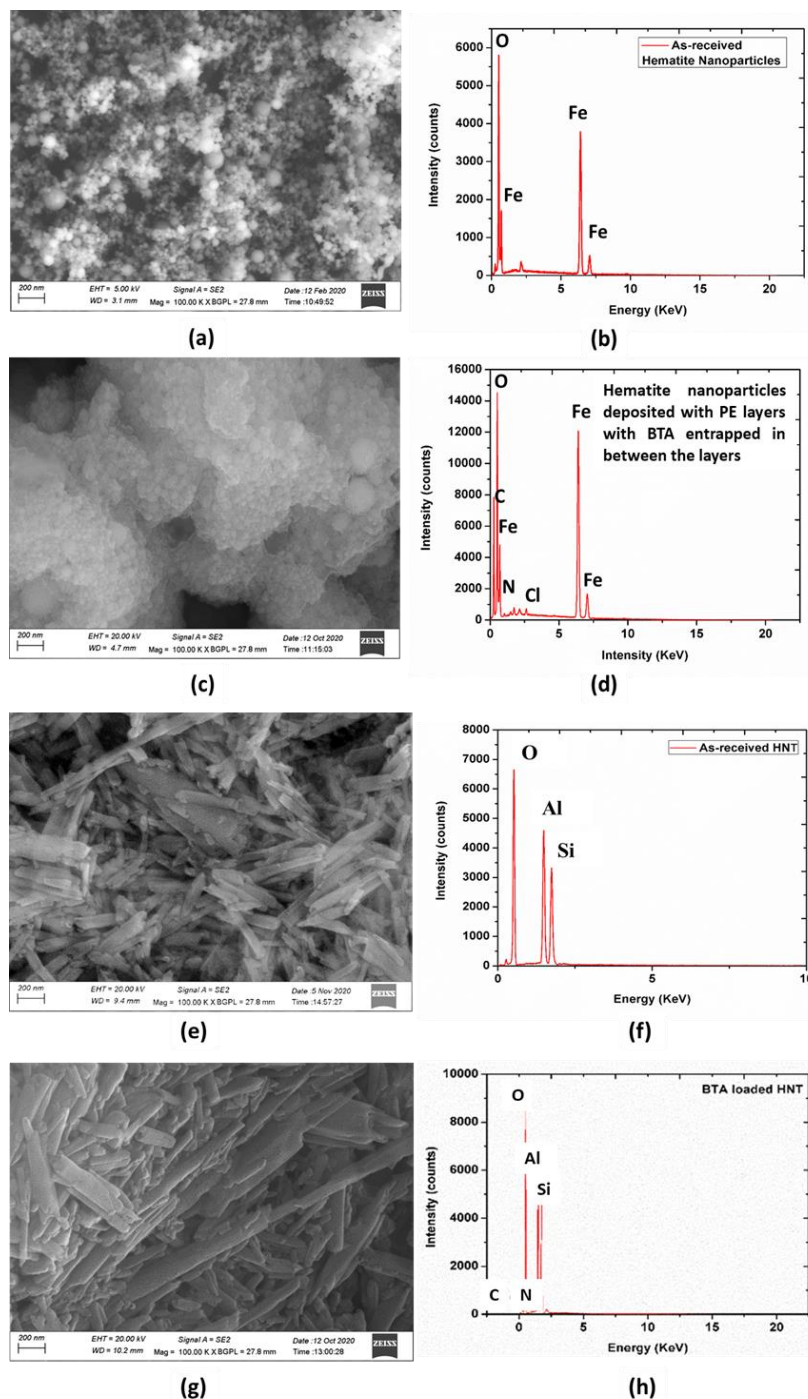
Fig. 3.1. FESEM images and EDS profiles: (a, b) α-Fe$_2$O$_3$ nanoparticles; (c, d) Benzotrizole entrapped polyelectrolyte layers deposited α-Fe$_2$O$_3$ nanoparticles; (e, f) Halloysite nanoclay; (g, h) Benzotriazole encapsulated Halloysite nanoclay

TEM images further confirmed the morphological changes after loading the corrosion inhibitor. TEM image of bare HNT (Fig. 3.2a) confirms the tubular structure of HNT with empty lumen. The internal diameter varied from 15 to 20 nm, and the length of the nanotube was in

the range of 0.5 to 1.0 μm. The morphology of HNT was intact even after loading of BTA, as shown in Fig. 3.2b. However, the lumen appears dense with some depositions, confirming the successful loading of BTA into the empty lumen of HNT. Schematic of only HNT and BTA loaded HNT is shown in Fig. 3.2c.
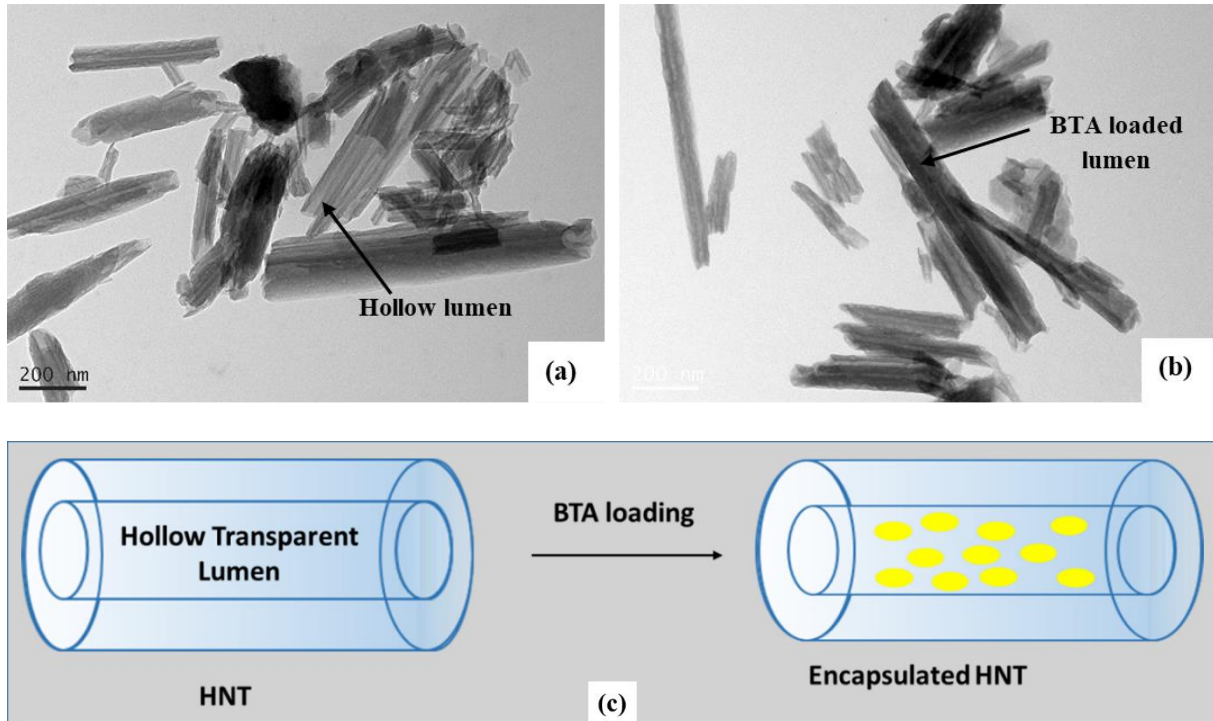
Fig. 3.2. TEM images of (a) as-received halloysite (HNT) nanoclay, (b) Benzotriazole (BTA)-encapsulated HNT, and (c) schematic representation of HNT showing empty hollow lumen and after loading BTA into HNT

3.2.2. X-ray diffraction

The XRD pattern for as-received α-Fe_2O_3 nanoparticles is shown in Fig. 3.3. The XRD analysis shows the intense peak at 2θ value of 35°, indicating that the crystal structure of α-Fe_2O_3 was tetragonal, according to the International Centre for Diffraction Data (**ICDD File no. 04-014-7214**) [3].
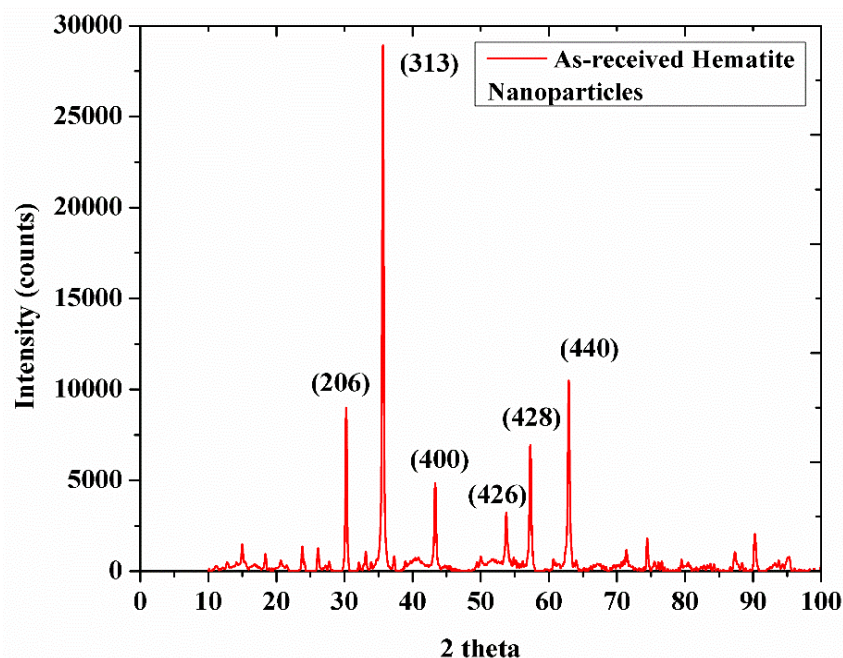
Fig. 3.3. XRD pattern for as-received α-Fe$_2$O$_3$ nanoparticles

3.2.3. Zeta potential and electrophoretic mobility measurements

Zeta potential and electrophoretic mobility measurements were carried out for α-Fe$_2$O$_3$ nanoparticles during the several stages of stepwise depositions of polyelectrolyte layers using Zetasizer instrument. Zeta potential values of α-Fe$_2$O$_3$ nanoparticles at all stages were found to be in the range of $\pm$ 15 to $\pm$ 30 mV, thereby confirming that the particles are highly stable without the formation of any agglomerates. The electrophoretic mobility values confirmed that the α-Fe$_2$O$_3$ nanoparticles were positively charged (Fig. 3.4).
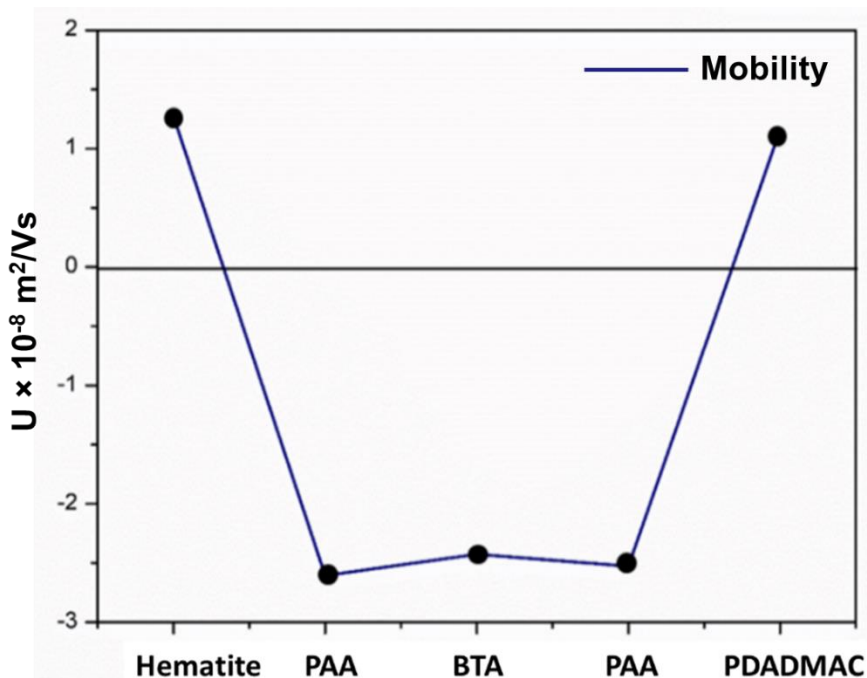
Fig. 3.4. Comparison of electrophoretic mobilities of each deposited layer

The negative electrophoretic mobility for PAA layer deposited nanoparticles confirmed that the negative surface charge surrounds the nanoparticles, confirming the firm deposition of PAA layer on α-Fe$_2$O$_3$ nanoparticles. Entrapment of BTA on the PAA layer decreased the negative charge mobility values. The loosely bound particles of BTA were removed by depositing a second negatively charged layer of PAA. On further deposition of a second PAA layer, the electrophoretic mobility value became a little more negative. The nanocontainers were terminated using the cationic polyelectrolyte layer of PDADMAC, and hence the electrophoretic mobility for this layer was found to be positive, as depicted in Fig. 3.4. The zeta potential measurements confirmed that the surface charge of each deposited layer was in accordance with the charge of each layer and the particles are stable in nature. The observed results of zeta potential and electrophoretic mobility studies supported the stepwise deposition of polyelectrolyte layers and the fabrication of LbL nanocontainers, and the results are in good agreement with those reported in the literature [4].

3.2.4. Thickness and adhesion measurements

The thicknesses of matrix, BS, BLLS and BHS sol-gel coatings were found to be in the range of 6-8 micron. An adhesion test was carried out using a multi-hatch gauge where cross-hatches were marked manually. The images obtained using an optical microscope before and after the

adhesion test are shown in Fig. 3.5. For all the coatings, the adhesion test showed that no coating was removed from the corners of each intersection point of the cross hatch. The corners and edges of the squares were smooth. Hence, the observations confirm that all the coatings possess good adhesion properties with the substrate in accordance with the ISO standard 2409 [5], where such types of coatings are classified into 0 class (means 0% removal).
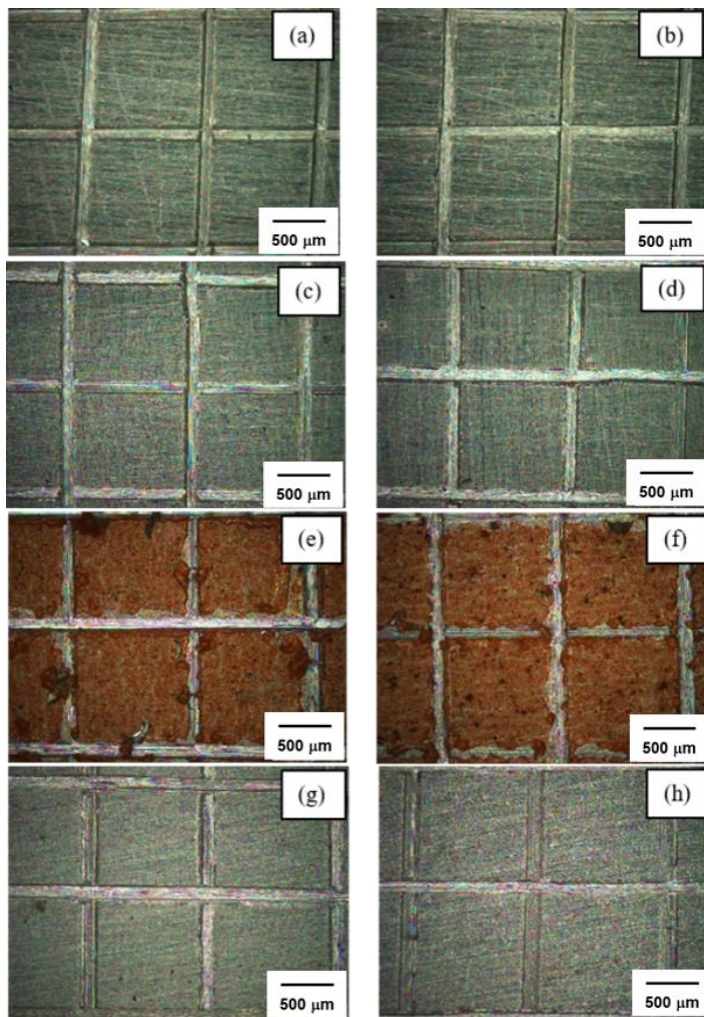
Fig. 3.5. Tape Adhesion test images of different coatings (a, b) matrix sol, (c, d) BTA added into matrix sol, (e, f) BTA encapsulated into layer-by-layer nanocontainer added into matrix sol and (g, h) BTA encapsulated into halloysite nanotubes added into matrix sol MS coated substrates.

3.2.5. Electrochemical impedance spectroscopy (EIS) and potentiodynamic polarization studies (PPS)

EIS and PPS were carried out for bare and coated MS substrates exposed to 3.5 wt% NaCl solution for 1 h. The data obtained after the electrochemical measurements were analyzed using two different equivalent electric circuits, as shown in Fig. 3.6. The equivalent circuit impedance parameters are R_s (resistance due to solution), CPE_{coat} (capacitance due to coating) R_{coat}, (resistance due to coating), C_{dl} (capacitance due to double layer) and R_{ct} (resistance due to charge transfer).

(a)   (b)
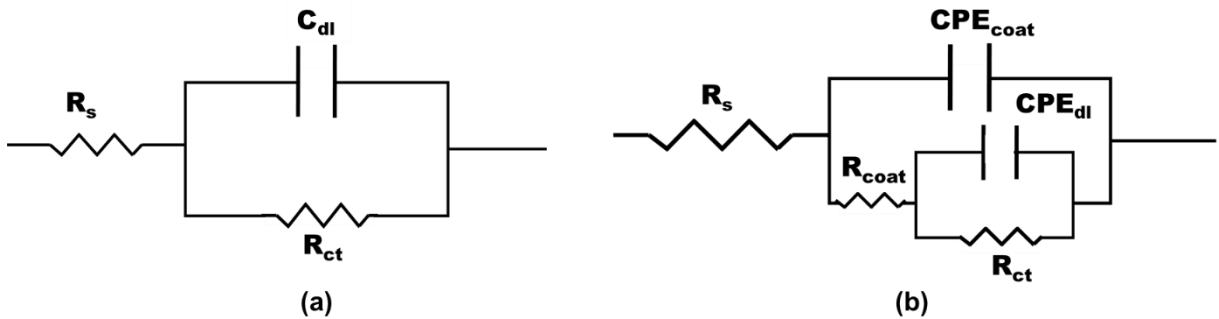
Fig. 3.6. Equivalent electric circuits used for fitting impedance data for (a) bare MS and (b) coated MS susbtrates

 Figure 3.6a conveys the equivalent electric circuit that fits best for bare substrate, where R_s is connected in series with CPE_{dl} and R_{ct} which are in parallel with each other. In order to obtain the EIS fit parameters for coated substrates with and without encapsulating BTA into the nanocontainers, the equivalent electric circuit shown in Fig. 3.6b fitted best. Here, the R_s is in series with CPE_{coat} parallel to R_{coat}, which are in series with C_{dl} parallel to R_{ct}. Since the Nyquist plot obtained deviates from the standard semi-circle shape, the CPE (constant phase element) was used instead of pure capacitor for all the circuit fittings. The presence of intrinsic surface non-uniformity in mild steel is responsible for the non-ideal nature of electrical double layer. The pseudo capacitance can be obtained using the formula:

$$C = (Qo * R)^{1/n}\left(1/R\right)$$

where, C is pseudo capacitance in F/cm^2, Q_o is constant phase element in $S\text{-}sec^n/cm^2$, n is frequency factor and R is resistance in Ω.

The Nyquist plots obtained after 1 h exposure to a NaCl solution of concentration 3.5 wt% are displayed in Fig. 3.7.
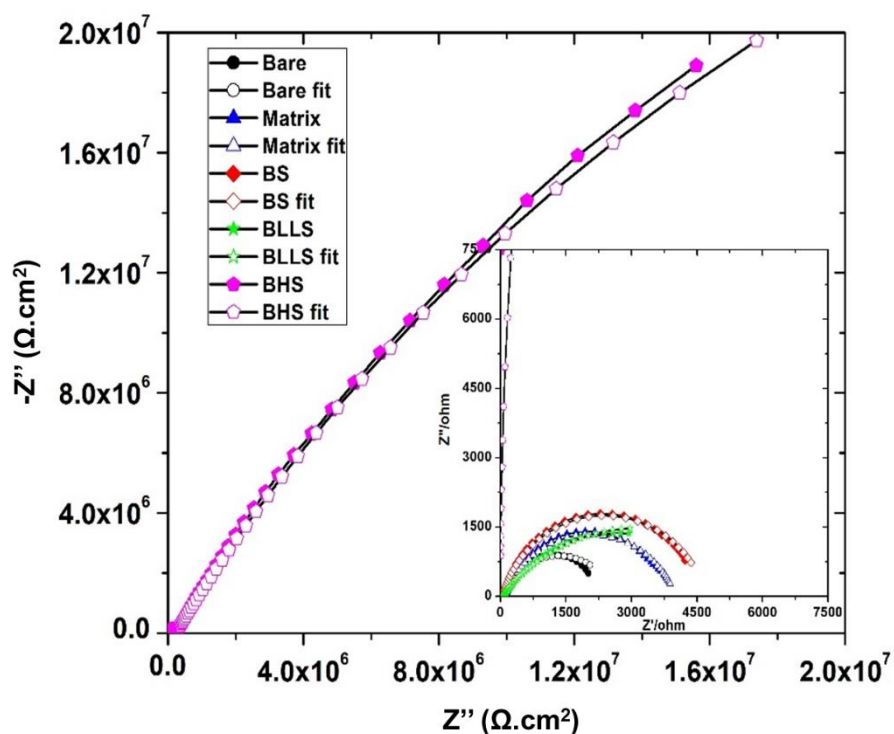
Fig. 3.7. Nyquist plots for bare MS and coated MS substrates after immersing in 3.5 wt% NaCl solution

The plots obtained for bare and coated coupons are nearly semicircular in shape, showing good corrosion resistance properties. The impedance value for bare substrate was found to be very low, from which it can be inferred that it has very low corrosion resistance. Hybrid sol-gel coating and the presence of corrosion inhibitors in the sol-gel matrix can be responsible for increased impedance values of matrix and BTA-loaded matrix coated substrates, attributing to the larger diameter of the semicircle. The sol-gel coating consisting of BTA-encapsulated LbL nanocontainers (BLLS) showed higher impedance values and larger semicircles compared to only matrix-coated and BS-coated substrates, thereby exhibiting higher corrosion resistance and lower corrosion rate. The BTA-HNT-sol coated substrates (BHS) exhibited enhanced corrosion resistance with impedance values several orders higher than those of all other coatings, indicating the extremely superior corrosion resistance and barrier properties of BHS coatings. The electrochemical impedance data along with charge transfer resistance values are shown in Table 3.2.

Table 3.2. EIS fit data for bare and coated substrates after 1 h exposure to 3.5 wt% NaCl solution

Substrate	R_{coat} $\Omega.cm^2$	R_{ct} $\Omega.cm^2$	C_{coat} F/cm^2	C_{dl} F/cm^2	CHI^2
Bare	-	2558	-	4.280×10^{-4}	5.369×10^{-3}
Matrix	158.1	3813	1.599×10^{-5}	5.614×10^{-5}	3.579×10^{-3}
BS	726.8	3955	1.012×10^{-4}	1.11×10^{-5}	3.076×10^{-3}
BLLS	438.4	5954	7.343×10^{-5}	1.189×10^{-5}	4.801×10^{-3}
BHS	2.287×10^5	1.033×10^8	2.178×10^{-10}	7.478×10^{-7}	6.490×10^{-3}

The data obtained shows that the capacitance value for BLLS coated substrates has increased when compared to only matrix-coated substrates, which can be because of the presence of polyelectrolyte layers, which swell upon absorption of water and act as a barrier by blocking the entry of foreign species. With time, these polyelectrolyte layers may burst with an increase in water uptake, initiating the release of an encapsulated corrosion inhibitor which self-heals the damage on the metal surface, thereby confirming the coating resistance value [6]. The BS coated substrates have shown an increase in coating capacitance because of the uptake of water along with an increase in coating resistance, which can be attributed to the presence of freely loaded BTA into the matrix sol, which adsorbs on the mild steel surface at the sites where Cl⁻ ions of electrolyte solution were attached. This results in the formation of a protective film, which restricts the entry of water molecules to some extent. The BHS-coated substrates have shown decreased capacitance values, suggesting that the coating is more compact, which blocks further penetration of water molecules. This barrier film formation protects the metal surface from corrosion. The coating and charge transfer resistance values have increased drastically for BHS-coated substrates when compared to other coatings. The corrosion inhibitor molecules get protonated in the presence of an electrolyte solution, which forms a bond with the negatively charged surface of metal. This interaction helps in corrosion mitigation by self-healing the defects on the metal surface [7].

Potentiodynamic polarization profiles of bare and coated substrates after 1 h exposure to 3.5 wt% NaCl solution were recorded and are shown in Fig. 3.8. The values of corrosion potential and corrosion current after Tafel fitting of the PPS data are shown in Table 3.3.
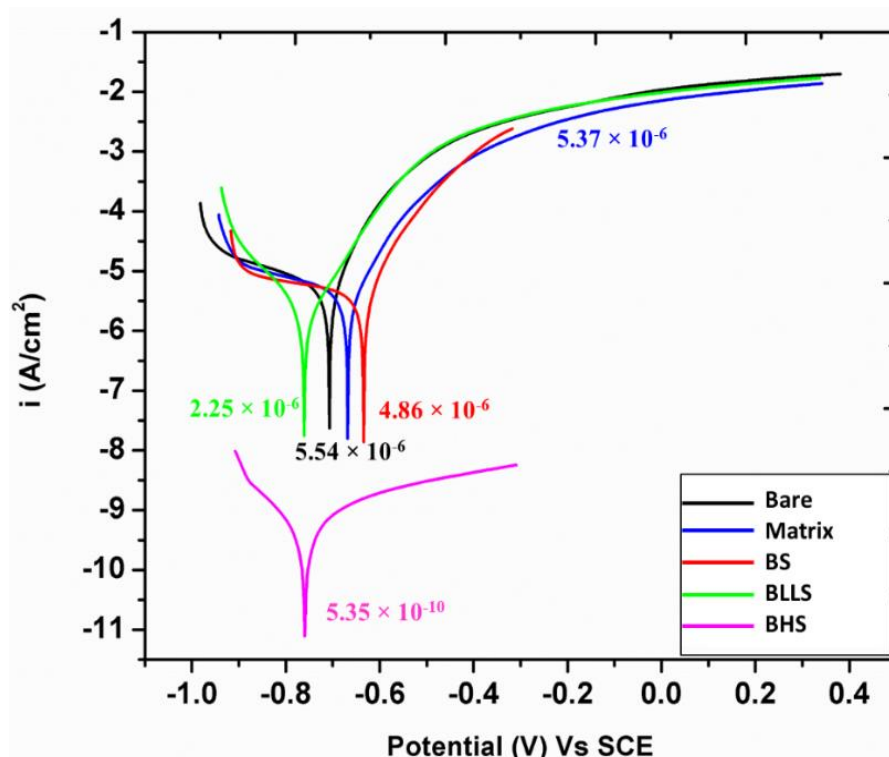
Fig. 3.8. Tafel plots for bare MS and coated MS substrates after immersing in 3.5 wt% NaCl solution

Table 3.3. Electrochemical polarization data for bare MS and coated MS substrates after immersing in 3.5 wt% NaCl solution

Sample ID	E_{corr} (V vs. SCE)	I_{corr} (A/cm^2)	R_p ($\Omega.cm^2$)
Bare	-0.707	5.54×10^{-6}	45.7×10^2
Matrix	-0.668	5.37×10^{-6}	61.0×10^2
BS	-0.634	4.86×10^{-6}	60.4×10^2
BLLS	-0.761	2.25×10^{-6}	10.5×10^3
BHS	-0.760	5.35×10^{-10}	64.7×10^6

The above data reveal that the corrosion potential values changed by a meager 60 mV from bare electrodes and became more positive for sol-get coatings (Matrix and BS) and more negative for nanocontainer encapsulated substrates (BLLS and BHS). However, the value of corrosion current was high for bare, matrix and BS substrates, but the nanocontainer encapsulated coatings

85

(BLLS and BHS) exhibited low corrosion currents. This extreme decrease in the corrosion current established the enhanced self-healing ability provided by the BTA-entrapped HNT sol coating. The encapsulated BTA-HNT sol (BHS) coated substrates exhibited extremely low corrosion current density and hence very low corrosion rate, indicating that the controlled release of BTA from HNT provided better self-healing properties and good corrosion resistance when compared to uncoated and other coated substrates [8].

3.2.6. Salt spray test

Photographs of uncoated and coated substrates after the salt spray test are shown in Fig. 3.9. Artificial scribes were created on the coated substrates before the salt spray test to visualize the self-repairing nature of the coatings. The substrates were kept in a salt spray compartment and exposed to 5 wt% NaCl solution as per ASTM B117 standard for different durations namely, 1, 2, 4, 6 and 24 h [9]. The images obtained after 1 h exposure show that the corrosion products are formed on the bare substrate, whereas, for the coated substrates, no significant change was observed. After 2 h exposure, the bare substrate was 50% corroded but the matrix-coated substrate showed rust formation at the edges of the defect and nearby area. The BTA-encapsulated coatings still possessed good corrosion inhibition properties. Images obtained after 4 and 6 h exposure clearly showed that the bare substrate got corroded completely, whereas matrix, BS and BHS coated substrates were nearly 50% corroded, which indicates that the loading of BTA into the sol caused the self-healing behavior as the inhibitor is released from the scribed area. Images obtained after 24 h exposure illustrate that all the substrates corroded completely, but the BLLS-sol coated substrate showed enhanced barrier properties because of the layered structure, where the polyelectrolyte layers swell up on absorbing the electrolyte solution, imparting protection for longer durations when compared to other coatings. In addition, BTA acts as a next step protection by self-healing the surface defects [10].

The information obtained from SST differs from EIS and PPS. The reason behind this difference is that the SST is an accelerated test where artificial defects are made on the coatings to observe the self-healing mechanism of bare and coated substrates, whereas, in EIS technique, no such damage occurs and information is retrieved based on the adhesion of coatings onto the metal surface. The PPS measures the stability of the system when polarized with respect to the open circuit potential. Therefore, the BLLS coated substrates have shown enhanced barrier properties when compared to other coatings because of the presence of a layered structure where the polyelectrolyte layers swell upon the uptake of water. These polyelectrolyte layers may burst

on an increase in pressure, which in turn releases the corrosion inhibitor, imparting the self-healing behavior for longer durations. A similar effect was observed where the capacitance values increased because of the water uptake.
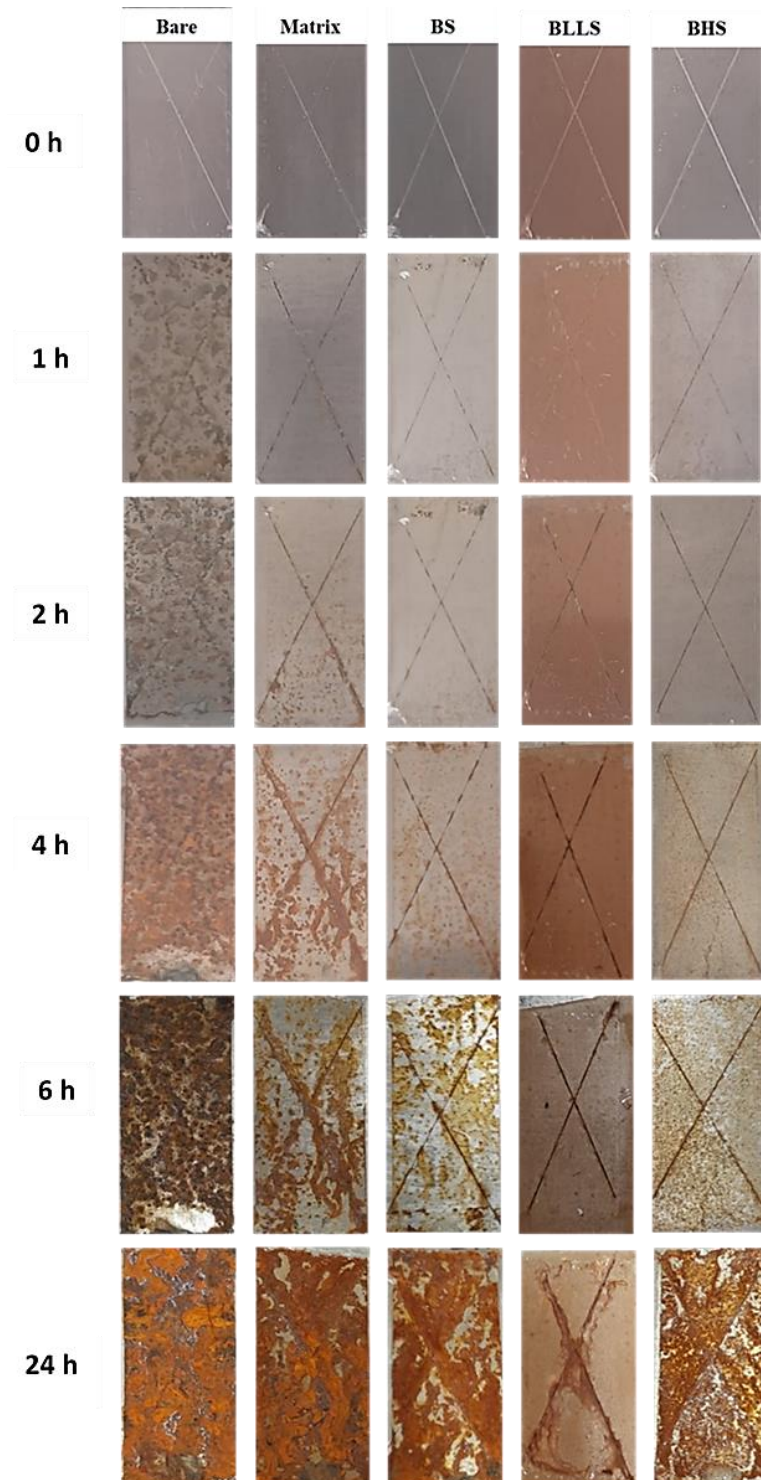
Fig. 3.9. Images of bare and coated MS substrates when exposed to salt spray

A schematic of the mechanism of self-healing in the case of corrosion inhibitors encapsulated into halloysite nanotubes and layer-by-layer nanocontainers is shown in Fig. 3.10. Due to any damage, either mechanical or electrochemical polarization, the inhibitor encapsulated into the nanocontainers releases at the corrosion site forming a passive film in the damaged area. This passive film is formed as a result of the interaction of corrosion inhibitor molecule, BTA, with the metal ion, i.e., Fe^{+2}. The resulting complex forms a self-healing layer in the damaged area, thereby decreasing the corrosion rate and increasing the durability of the coating as well as of the metal substrate. The advantage of loading these corrosion inhibitors into the nanocontainers is to prevent the unwanted leaching of corrosion inhibitors, thereby, providing excellent barrier properties.
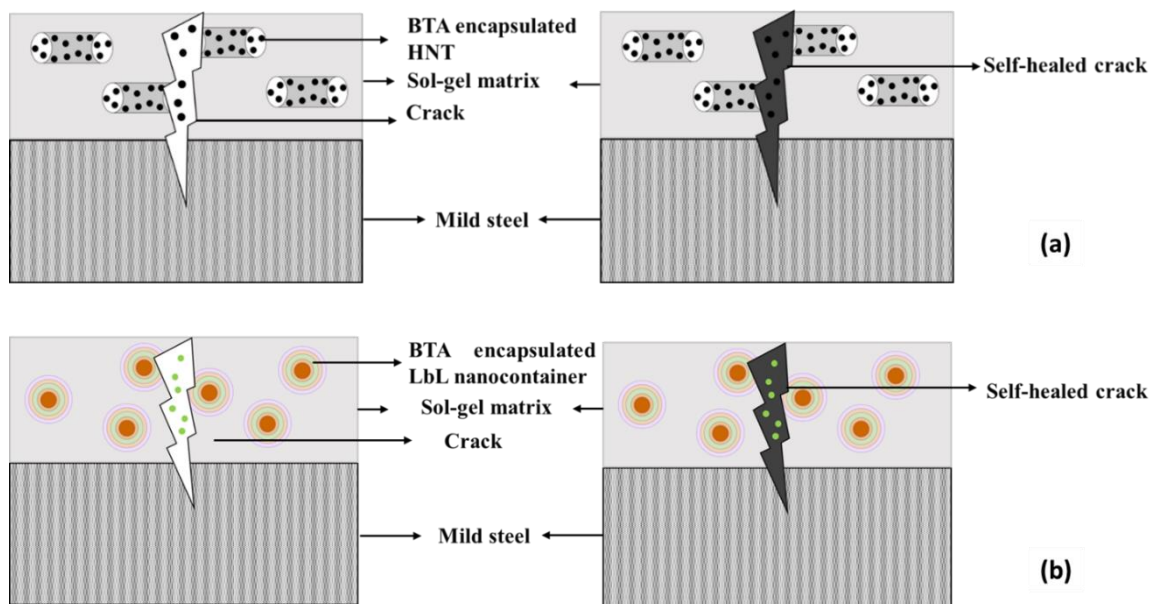
Fig. 3.10. Schematic of expected autonomic-healing process: (a) Benzotriazole encapsulated into halloysite nanotubes (b) Benzotriazole encapsulated into layer-by-layer nanocontainers

3.3.   Conclusions

- Hybrid sol-gel coatings exhibited good barrier properties by forming homogenous coatings on substrates.
- BTA-encapsulated halloysite nanotubes mixed in a sol-gel matrix showed enhanced corrosion protection properties when exposed to 3.5 wt% NaCl solution.
- Electrochemical impedance and polarization studies show that the encapsulation of BTA into the halloysite nanoclay showed higher corrosion resistance and lower corrosion rate among all coated substrates.

- The salt spray analysis confirmed the self-healing behavior of encapsulated BTA into HNT for up to 6 h. The BLLS sol coated substrates showed good barrier properties up to 24 h when subjected to SST (salt spray test) because of the presence of polyelectrolyte layers. which swell up and restricts the entry of water molecules. In addition to this, the encapsulated BTA provides protection by self-healing the damage.

3.4. References:

[1] Kongsat, P., Kudkaew, K., Tangjai, J., A. O'Rear, E., Pongprayoon, T., Synthesis of structure-controlled hematite nanoparticles by a surfactant-assisted hydrothermal method and property analysis, J. Phys. Chem. Solids. 148 (2021) 1-12.

[2] Yang, Y., Chen, Y., Leng, F., Huang, Li., Wang, Z., Tian, W., Recent advances on surface modification of halloysite nanotubes for multifunctional applications, Appl. Sci. 7 (2017) 1-9.

[3] Rasheed, R. T., Al-Algawi, S. D., Kareem, H. H., Mansoor, H, S., Preparation and characterization of hematite iron oxide (α-Fe$_2$O$_3$) by sol-gel method, Chem. Sci. J. 9 (2018) 1-7.

[4] Kamburova, K., Boshkova, N., Boshkov, N., Radeva, T., Design of polymeric core-shell nanocontainers impregnated with benzotriazole for active corrosion protection of galvanized steel, Colloids Surf. A: Physicochem. Eng. 499 (2016) 24–30.

[5] ISO 2409, International Standard for Cross-cut test. (2020-08) 1-11.

[6] Sonawane, S. H., Bhanvase, B. A., Jamali, A. A., Dubey, S. K., Kale, S. S., Pinjari, D. V., Kulkarni, R. D., Gogate, P. R., Pandit, A. B., Improved active anticorrosion coatings using layer-by-layer assembled ZnO nanocontainers with benzotriazole, Chem. Eng. J. 189 (2012) 464–472.

[7] Njoku, D. I., Cui, M., Xiao, H., Shang, B., Li, Y., Understanding the anticorrosive protective mechanisms of modified epoxy coatings with improved barrier, active and self-healing functionalities: EIS and spectroscopic techniques, Sci. Rep. 7 (2017) 1–15.

[8] Abdullayev, E., Lvov, Y., Halloysite clay nanotubes for controlled release of protective agents, J. Nanosci. Nanotechnol. 11 (2011) 10007–10026.

[9] ASTM B117-16, Standard Practice for Operating Salt Spray (Fog) Apparatus, (2011) 1-12.

[10] Guzman, E., Mateos-Maroto, Ana., Ruano, M., Ortega, F., Rubio, R., Layer-by-layer polyelectrolyte assemblies for encapsulation and release of active compounds, Adv. Colloid Interface Sci. 249 (2017) 290-307.

CHAPTER-4

Capped Inhibitor-loaded Hallosyiste Nanoclay-based Self-healing Silica Coatings for Corrosion Protection of Mild Steel

CHAPTER-4

Capped Inhibitor-Loaded Halloysite Nanoclay-based Self-healing Silica Coatings for Corrosion Protection of Mild Steel

4.1. Introduction

It was concluded in the previous chapter that halloysite nanotube is an appropriate nanocontainer for the organic corrosion inhibitor, BTA. Therefore, the objective of the upcoming experimental work plan is to control the release of the corrosion inhibitor and optimize the loading of these nanocontainers into the silica sol. Recent studies in the literature are more focused on increasing the duration of release of the encapsulated corrosion inhibitors by using capping agents/end stoppers. These end stoppers block the ends of the halloysite nanotube and cover the surface, which in-turn controls the release of the corrosion inhibitors. Polyelectrolyte shell, urea-formaldehyde nanocapsules (UFNCs) [1], calcium hydroxide [2], $CoCO_3$ [3], 8-hydroxyquinoline-Cu complex [4], benzotriazole-Cu complex [5], etc. are various types of end stoppers that have been investigated. So far, there are no studies on benzotriazole-incorporated HNT with UFNCs as the capping agent. The choice of UFNCs as end stoppers is found to be quite promising as the release of the self-healing material is based on mechanical stimuli. These nanocapsules provide good mechanical stability, increased shelf-life, good adhesion and compatibility with different coating matrices [6, 7].

Recently, the development of corrosion protection coatings using low-cost and environmentally friendly compounds, such as corrosion inhibitors in combination with naturally available nanocontainers has gained interest. The inhibitors are required in low concentrations and give excellent inhibitive performance by forming strong bonds with the metal surface. Thin-film coatings consisting of nanocontainers are investigated to reduce the quantity of inhibitors and also to extend the efficient lifetime of the protective coatings with the controlled release of inhibitors on-demand only. Here, the novelty of our work is to analyze the effect of benzotriazole (BTA) encapsulated in halloysite nanotube followed by the capping of loaded HNTs using urea-formaldehyde nanocapsules. Different weight fractions of BTA-encapsulated and capped HNTs were dispersed into matrix sol, followed by their dip-coating on mild steel substrates. The coatings generated from capped and uncapped HNTs were analyzed systematically for their anti-corrosion performance with the help of electrochemical impedance

spectroscopy (EIS) and potentiodynamic polarization studies (PPS), salt-spray test and scanning vibrating electrode technique (SVET).

4.1.1. Coating deposition and nomenclature of different sols coated on mild steel substrates

To realize the capping of the halloysite nanotube, BTA encapsulated HNT and UFNCs were added in the weight ratio of 1:10 into the matrix sol. The proportions of matrix sol, BTA-encapsulated HNT and UFNCs for uncapped and capped matrix sols are detailed in Tables 4.1 a and b, and the details of various samples prepared along with their labels are listed in Table 4.1 c.

Table 4.1. a. Chemical composition of different sols consisting of varying percentages of inhibitor-loaded nanocontainers and matrix sol.

Sample ID	BTA-encapsulated HNT (g)	Matrix sol (g)	Wt% of BTA-encapsulated HNT
Sample 1	0.25	25	1 wt%
Sample 2	0.50	25	2 wt%
Sample 3	0.75	25	3 wt%
Sample 4	1.00	25	4 wt%
Sample 5	1.25	25	5 wt%

Table 4.1. b. Chemical composition of different sols consisting of varying percentages of inhibitor-loaded nanocontainers, capping agents, and matrix sol

Sample ID	BTA-HNT (g)	Urea-formaldehyde nanocapsules (UFNCs) (g)	Matrix sol (g)	Wt% of capped BTA-encapsulated HNT
Sample 8	0.25	2.5	25	1 wt%
Sample 9	0.50	5.0	25	2 wt%
Sample 10	0.75	7.5	25	3 wt%
Sample 11	1.00	10	25	4 wt%
Sample 12	1.25	12.5	25	5 wt%
Sample 13	1.50	15.0	25	6 wt%

Table 4.1. c. Nomenclature of different sols with their description to be coated on mild steel substrates

S. No.	Description of Sol	Sample ID
1.	Uncapped 1 wt% BTA-encapsulated HNT	1
2.	Uncapped 2 wt% BTA-encapsulated HNT	2
3.	Uncapped 3 wt% BTA-encapsulated HNT	3
4.	Uncapped 4 wt% BTA-encapsulated HNT	4
5.	Uncapped 5 wt% BTA-encapsulated HNT	5
6.	Matrix sol	6
7.	BTA directly dispersed into matrix sol (2 wt%)	7
8.	Capped 1 wt% BTA encapsulated HNT	8
9.	Capped 2 wt% BTA encapsulated HNT	9
10.	Capped 3 wt% BTA encapsulated HNT	10
11.	Capped 4 wt% BTA encapsulated HNT	11
12.	Capped 5 wt% BTA encapsulated HNT	12
13.	Capped 6 wt% BTA encapsulated HNT	13

4.2. Results and discussion

4.2.1. Characterization of nanoreservoirs

4.1.1.1. Scanning electron microscopy, Transmission electron microscopy and BET analysis

The surface morphology of HNTs and inhibitor-loaded HNTs along with EDS elemental mapping were already reported in Chapter 3. The SEM image (Fig. 4.1a) of urea-formaldehyde nanocapsules confirms that the nanocapsules have sphere-like structures with average size of 150 ± 50 nm. SEM image for capped BTA-encapsulated HNT (Fig. 4.1b) shows the presence of microsphere structure and at the ends and on the surface of HNT, inferring the firm binding of UFNCs on HNTs.
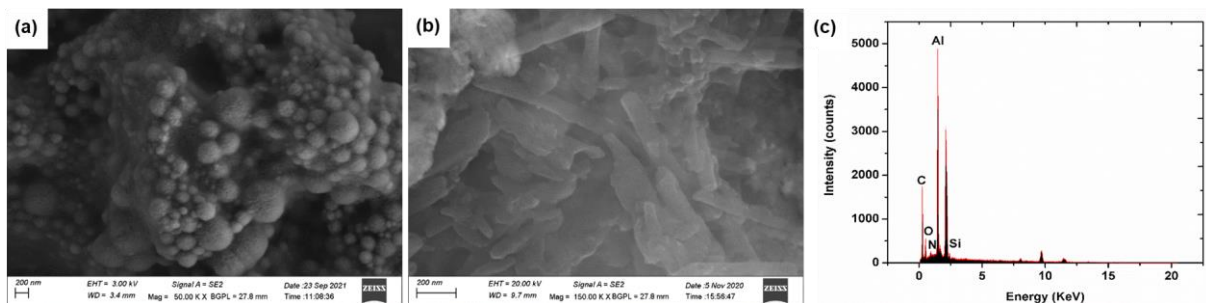
Fig. 4.1. FESEM image and EDS profile of benzotriazole-encapsulated and capped halloysite nanotube

The elemental analysis (Fig. 4.1c) further confirms the presence of Al, Si and O with increased amounts of C and N because of the addition of UFNCs, which may have completely covered the surface of HNT. Because of the presence of UFNC coating on HNTs, the electron beam had not penetrated deep within to give an in-depth analysis thereby showing less amounts of O, Al and Si when compared to raw HNT and BTA-encapsulated HNT [8-10].

TEM image of capped BTA-encapsulated HNT (Fig. 4.2a) shows that the nanocapsules used for capping have blocked the ends and covered the walls of HNT for the controlled release of BTA. SEM image of UFNCs shown in Fig. 4.1b confirms that the average size of the nanocapsules was 150 ± 50 nm, which further explains the blocking of tube ends completely as the diameter of HNTs is in the range of mere 15 to 20 nm. EDS analysis (Fig. 4.2b) shows all the constituent elements involved in synthesizing UFNCs.
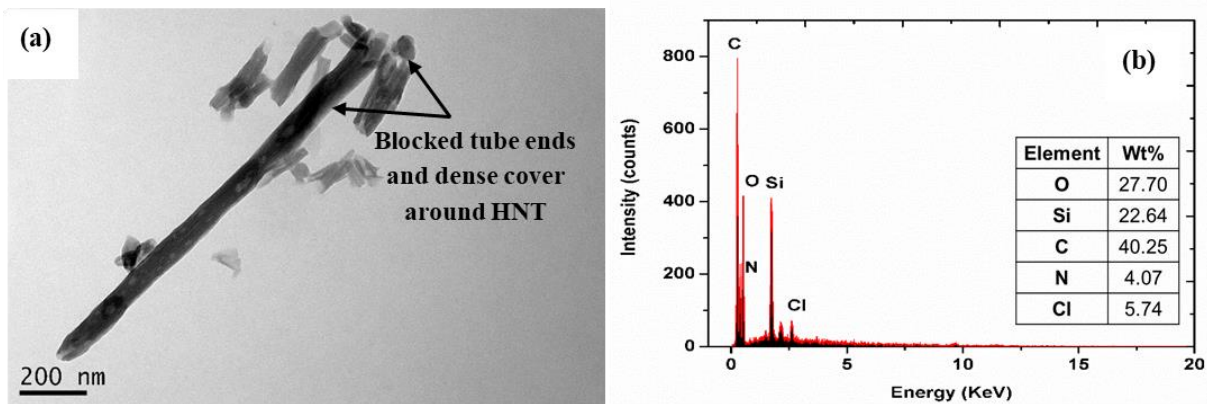
Fig. 4.2. TEM image (a) capped benzotriazole-encapsulated halloysite nanotube, and (b) EDS profile of urea-formaldehyde nanocapsules.

Figure 4.3 shows the plot of pore volume as a function of pore diameter for as-received HNT, BTA-encapsulated and capped BTA-encapsulated HNT. BET data confirms the decrease in pore volume for capped and inhibitor-loaded HNT. The decrease in pore volume is attributed to the loading of the inhibitor into the hollow lumen of HNT. Therefore, TEM and BET data concluded that the loading and capping of HNT had successfully taken place.
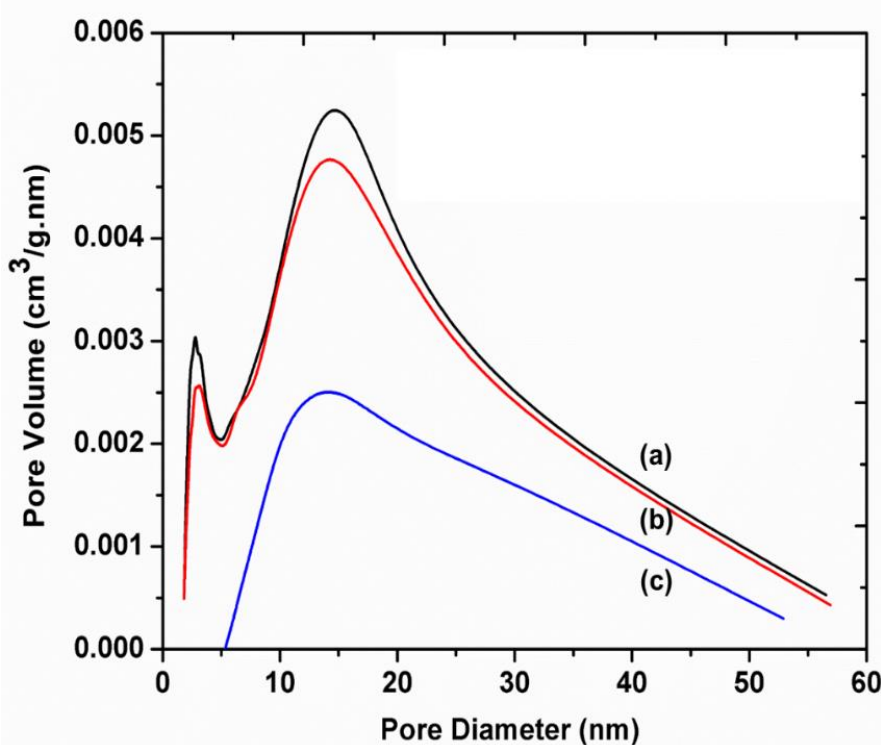
Fig. 4.3. BET pore volume as a function of pore diameter for (a) as-received halloysite nanotube (HNT), (b) Benzotriazole (BTA)-encapsulated HNT, and (c) BTA-encapsulated capped HNT

4.1.1.2. FTIR analysis

The FTIR spectra obtained for HNT, BTA-encapsulated HNT, and capped BTA-encapsulated HNT are shown in Fig. 4.4.
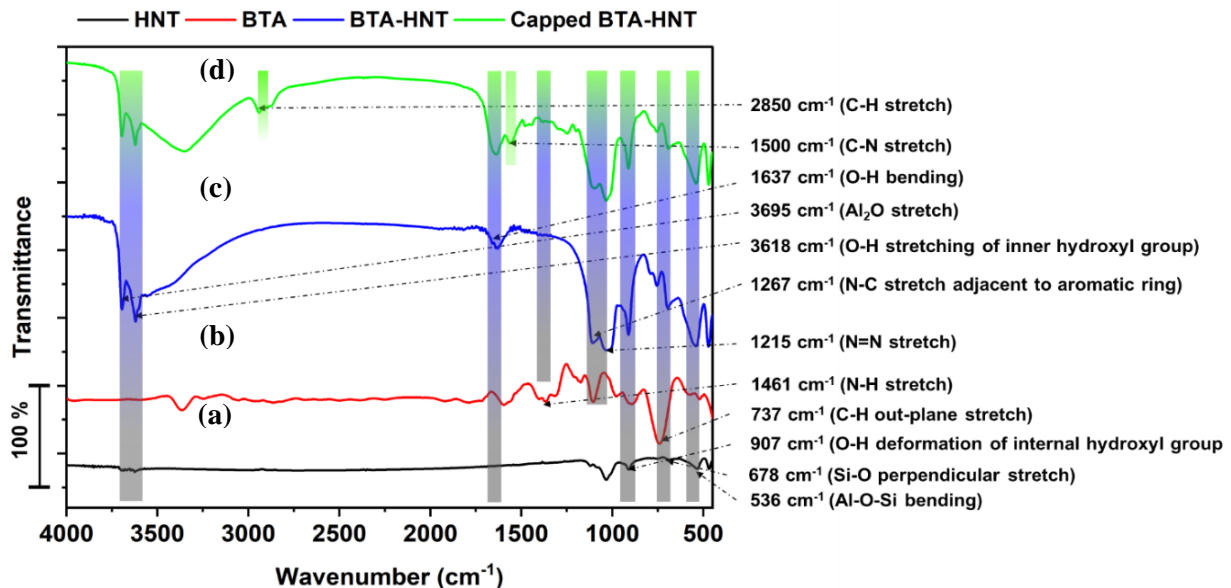
Fig. 4.4. FTIR spectra of (a) as-received halloysite nanotube (HNT), (b) benzotriazole (BTA), (c) BTA-encapsulated HNT, and (d) BTA-encapsulated capped HNT

The halloysite nanoclay shows the most prominent peaks at 3695, 3618, 1637, 792, 678 cm^{-1}, and 536 cm^{-1}, corresponding to Al$_2$O stretching vibration, OH stretching of inner hydroxyl group, O-H bending vibration, Si-O symmetric stretching vibration, Si-O perpendicular stretching vibration and Al-O-Si deformation respectively [11-15]. All these peaks are also well distinguished in the spectrum of BTA-encapsulated HNT and capped BTA-encapsulated HNT, confirming that no peak shift occurred after loading the corrosion inhibitor and that the morphology of the halloysite nanotube was not disturbed. The vibrational peak observed at 1267 cm^{-1} corresponds to the stretching N-C bond adjacent to the aromatic ring of BTA. The peaks located at 1215 and 1461 cm^{-1} are attributed to N=N and N–H stretching vibrations, respectively [15-17]. The peaks at 2850 and 1500 cm^{-1} confirm C-H stretching of formaldehyde and C-N stretching vibration of urea, which confirms the capping of HNT with UFNCs [18,19]. A thorough analysis of FTIR spectra also confirmed that the lumen of the halloysite nanotube was filled with BTA and the ends of the tube are capped with the help of urea-formaldehyde nanocapsules.

4.1.1.3. X-ray diffraction

XRD patterns of HNT, BTA-encapsulated HNT, and capped BTA-encapsulated HNT are shown in Fig. 4.5. The XRD pattern of HNT has shown diffractions at 12°, 21°, 28°, 34°, and 37° corresponding to (002), (111), (004), (113), (020) and (022), respectively, which correspond to the interlayer spacing of 7.34 Å between the alumina and silica layers, indicating that the crystal structure of HNT was monoclinic, according to the International Centre for Diffraction Data (ICDD File no. 01-077-4776). Similar XRD patterns were observed for both BTA-encapsulated HNT and capped BTA-encapsulated HNT without any shift in the peak positions. This observation suggests that, even after loading and capping, the interlayer spacing between the alumina and silica layers of HNT did not change, which confirms that the inhibitor was loaded only inside the lumen of the nanotube and that no intercalation had taken place in between the layers of HNT [20].
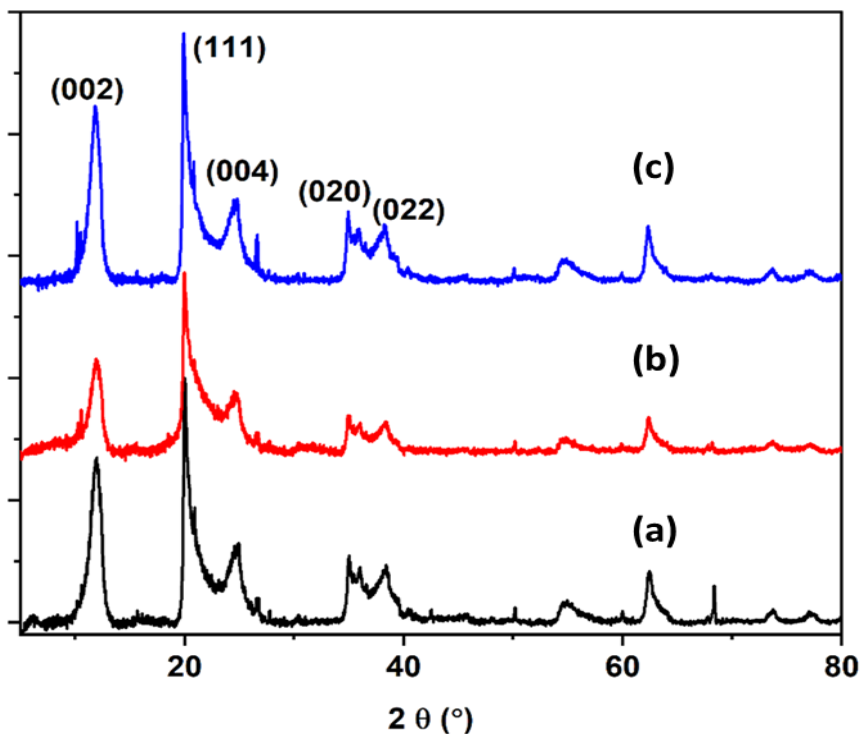
Fig. 4.5. XRD profiles of (a) as-received halloysite nanotube (HNT), (b) benzotriazole-encapsulated HNT, and (c) BTA-encapsulated capped HNT matched with ICDD File no. 01-077-4776

4.2.2. Characterization of coatings derived from HNT and inhibitor-modified HNTs in combination with sol-gel matrix

4.1.1.4. Thickness and tape adhesion measurements

The thicknesses of coatings of samples 1 to 7 were in the range of 6-8 µm. For samples 8 to 10, the thicknesses of the coatings were in the range of 5-6 µm, whereas the thicknesses of samples 11, 12 and 13 are found to be 11, 22 and 22 µm, respectively. The thickness measured using PosiTector® was confirmed from FESEM cross-sectional images, as shown in Fig. 4.6. The thicknesses for uncapped 2 wt% BTA-encapsulated HNT and capped 5 wt% BTA-encapsulated HNT were 6 and 22 microns, respectively.

| (a) | (b) |
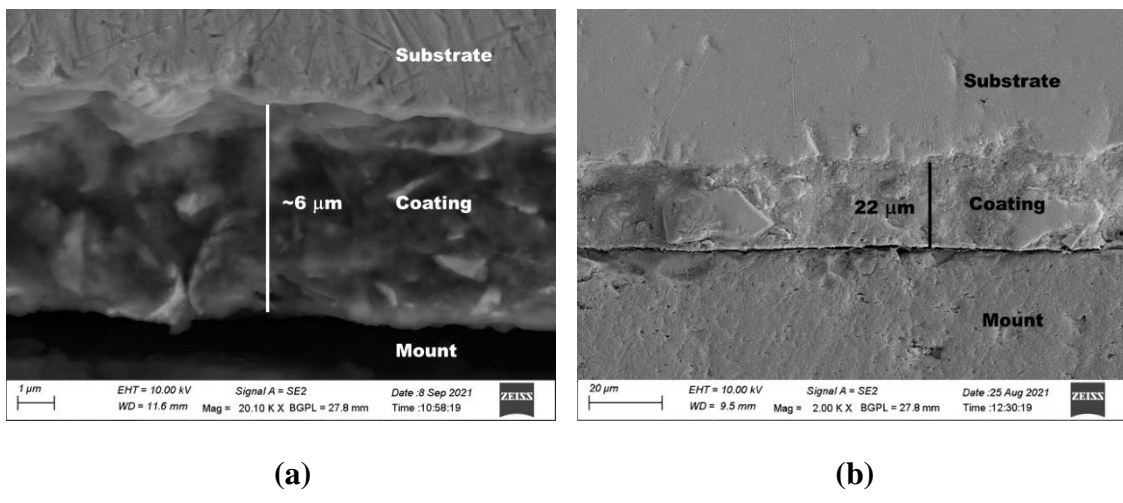
Fig. 4.6. Cross-sectional coating thickness measurement from SEM images: (a) uncapped 2 wt% benzotriazole (BTA)-encapsulated halloysite nanotube (HNT), and (b) capped 5 wt% BTA-encapsulated HNT

The images of coated MS substrates obtained using an optical microscope before and after the adhesion test are shown in Fig. 4.7. The adhesion test showed that no coating was removed even from the corners of each intersection point of the cross-hatch for all the coatings. The corners and edges of the squares were firm and smooth. Hence, the observations confirm that all the coatings possessed suitable adhesion properties with the substrate as per the ISO standard 2409, where such types of coatings are classified into 0 class (means 0% removal).
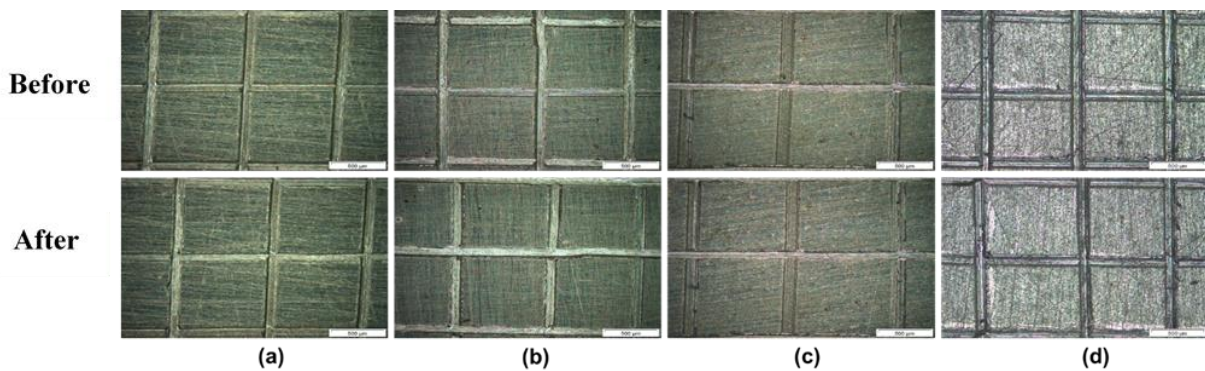
Fig. 4.7. Tape adhesion test images: (a) matrix sol, (b) 2 wt% benzotriazole (BTA) directly dispersed into matrix sol, (c) uncapped 2 wt% BTA-encapsulated halloysite nanotube (HNT), and (d) capped 5 wt% BTA-encapsulated HNT

4.1.1.5. Electrochemical impedance spectroscopy (EIS) and potentiodynamic polarization studies (PPS)

EIS is a quantitative technique used to evaluate the corrosion performance of coatings. It provides fast and reliable data, making it one of the crucial methods in predicting the durability and adhesion of the coatings. The polarization technique helps in measuring the corrosion resistance during the electrochemical process, which is advantageous for examining the corrosion-inhibiting behaviour [21]. The actual behaviour of the charge transfer and corrosion resistance is examined at equilibrium potential only. Therefore, the scan range should not exceed much from the equilibrium potential as applying larger potentials can adversely change the surface of the substrates, which is not ideal to completely extrapolate the Tafel plot [21]. The plots thus obtained help in determining the reaction kinetics by observing the cathodic and anodic branches obtained [22]. Further, it helps in identifying the coating adhesion and its resistance to the breakdown [23]. In the case of thick organic coatings like epoxy or acrylic coatings, where thicknesses are several microns, polarization creates a high drop in voltage, which may not be significant. Polarization experiments give valuable information like current passing through the coating, autonomic-healing behaviour and shift in corrosion potentials, and potentiodynamic polarization studies of thin sol-gel coatings are widely explored to give insights on the corrosion protection efficiency of thin-film coatings.

(a) Optimization study to evaluate the optimum loading percentage of the nanocontainers

EIS and PPS were carried out on samples 1 to 5 to evaluate the optimum loading of HNT into the matrix sol. Nyquist plots obtained after submerging the coated substrates in 3.5 wt% NaCl solution for 1 h are shown in Fig. 4.8.
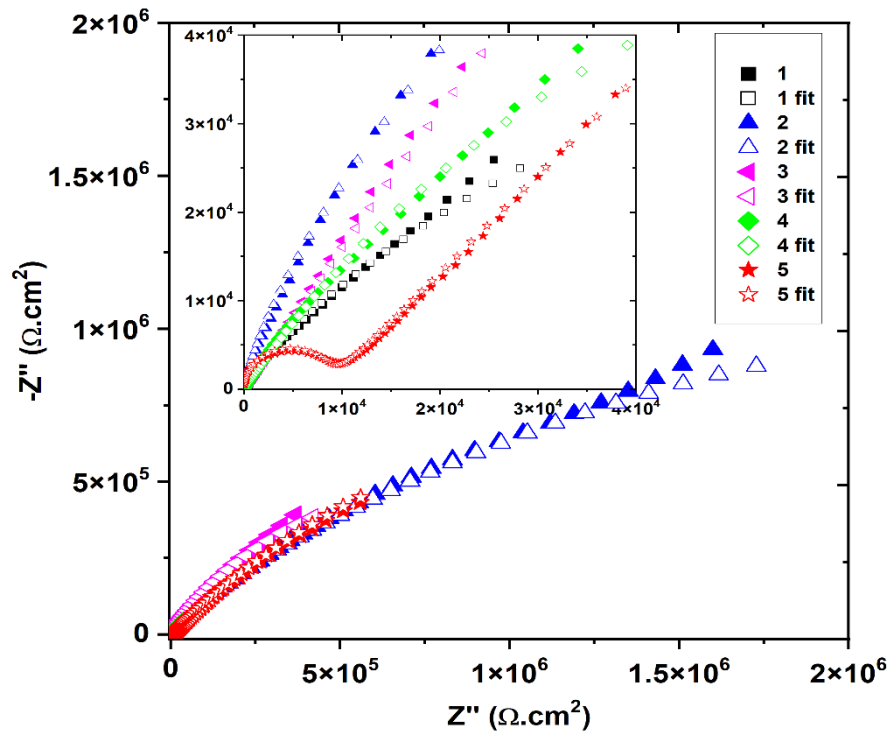
Fig. 4.8. Nyquist plots for samples 1 to 5 (uncapped 1 to 5 wt% benzotriazole-encapsulated halloysite nanotubes) obtained after immersion in 3.5 wt% NaCl solution for 1 h.

The equivalent electric circuits used for the best fitting of EIS results are depicted in Fig. 4.9, where R_s is solution resistance, R_{coat} and C_{coat} are coating resistance and capacitance, respectively, C_{dl} is electrical double layer capacitance and R_{ct} is charge transfer resistance.
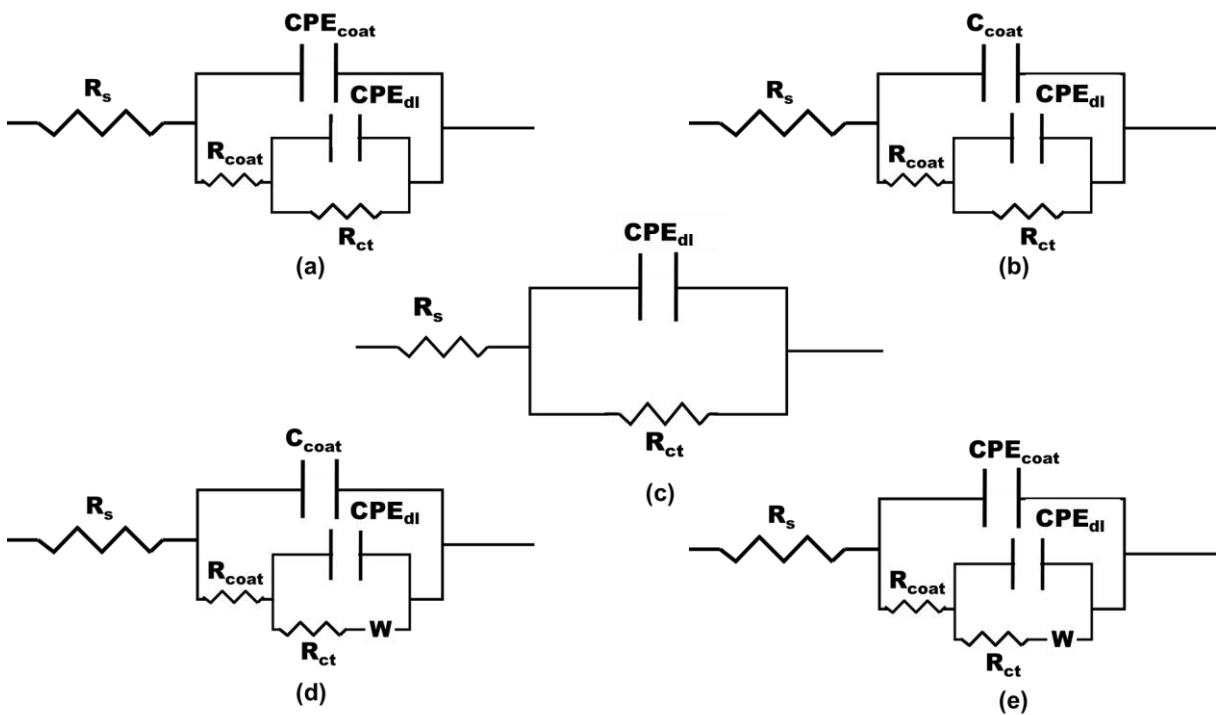
Fig. 4.9. Equivalent circuits used for fitting EIS data of bare MS and different coated samples as mentioned in the respective tables

Enhanced high impedance value was observed in the Nyquist plot of sample 2, suggesting a better corrosion resistance for sample 2 coatings. Results of EIS fit data shown in Table 4.2 confirm that the charge transfer resistance was highest for sample 2, i.e., 5.769×10^6 $\Omega.cm^2$. In contrast, all the other coatings have shown remarkably low charge transfer resistance values, which means that the electrolyte solution penetrated the coating matrix, leading to a decrease in barrier properties as well as corrosion resistance.

Table 4.2. EIS fit data obtained after immersing the samples 1 to 5 (uncapped 1 to 5 wt% benzotriazole-encapsulated halloysite nanotubes) obtained after immersion in 3.5 wt% NaCl solution for 1 h.

Sample ID	R_{coat} ($\Omega.cm^2$)	C_{coat} (F/cm^2)	R_{ct} ($\Omega.cm^2$)	C_{dl} (F/cm^2)	CHI^2	Fitted circuit
1	54.49	8.508×10^{-6}	0.321×10^6	2.827×10^{-4}	4.295×10^{-3}	a
2	63.84×10^2	1.642×10^{-10}	5.760×10^6	1.212×10^{-6}	1.630×10^{-3}	a
3	11.58×10^1	2.839×10^{-9}	1.710×10^6	3.589×10^{-5}	2.406×10^{-3}	b
4	10.43×10^1	1.390×10^{-6}	0.208×10^6	2.763×10^{-4}	5.267×10^{-3}	a
5	86.45×10^2	4.122×10^{-10}	3.160×10^6	2.550×10^{-6}	5.939×10^{-3}	b

The corrosion potential, current and polarization resistance values for samples 1 to 5 are shown in Table 4.3.

Table 4.3. Tafel Fit parameters of potentiodynamic polarization data obtained after immersing the samples 1 to 5 (uncapped 1 to 5 wt% benzotriazole-encapsulated halloysite nanotubes) in 3.5 wt% NaCl solution for 1 h.

Sample ID	E_{corr} (V vs. SCE)	i_{corr} ($\mu A/cm^2$)	βc (mV/dec)	βa (mV/dec)	R_p ($\Omega.cm^2$)
1	-0.58 ± 0.014	0.39 ± 0.051	98.0	205	0.0700×10^6
2	-0.76 ± 0.069	$(0.53 \pm 0.034) \times 10^{-3}$	134	196	64.7×10^6
3	-0.43 ± 0.028	0.027 ± 0.058	112	213	1.17×10^6
4	-0.45 ± 0.071	0.36 ± 0.065	106	237	0.0800×10^6
5	-0.64 ± 0.036	0.078 ± 0.0045	174	213	3.25×10^6

The Tafel plots for different loading percentages are shown in Fig. 4.10.
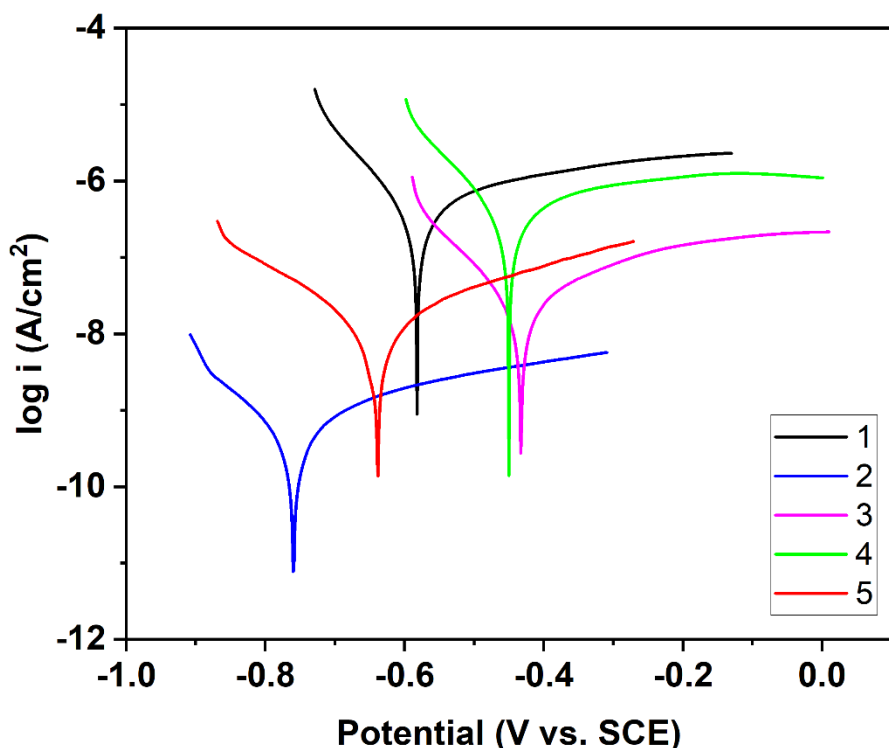
Fig. 4.10. Tafel plots for samples 1 to 5 (uncapped 1 to 5 wt% benzotriazole-encapsulated halloysite nanotubes) obtained after immersion in 3.5 wt% NaCl solution for 1 h.

It was found that the current density for sample 2 coatings was the least and was nearly two to three orders of magnitude less when compared with the other sol-coated substrates. The decrease in i_{corr} value for sample 2 suggests that the coating possessed improved barrier properties and autonomic healing properties by releasing BTA from HNT. Figure 4.11 shows the surface morphology for samples 2 and 4, corresponding to 2 and 4 wt% loading. The SEM images (Fig. 4.11 a, b) show that the coating was well adherent and uniform in the case of 2 wt% loading, whereas coating defects were seen on the surface for 4 wt% loading.
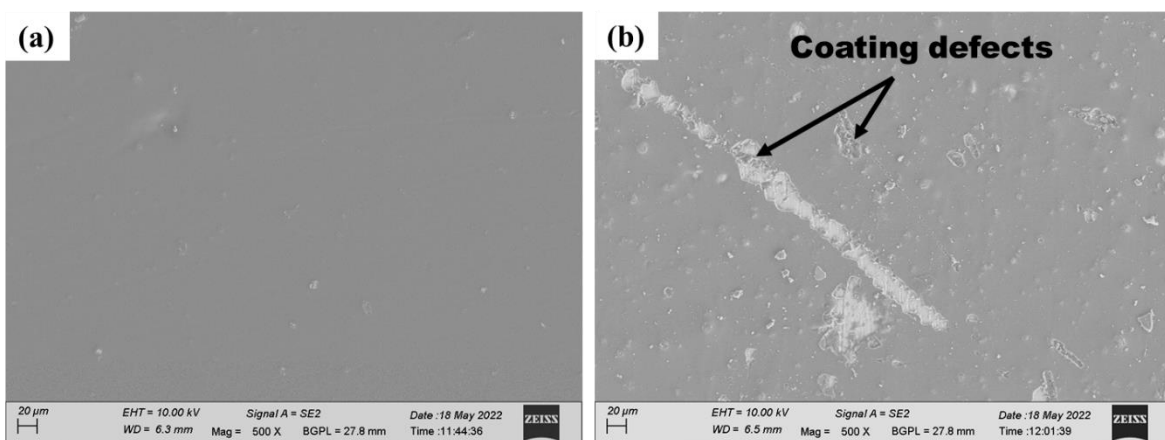
Fig. 4.11. Surface morphology: (a) sample 2 and (b) sample 4, where sample 2 and 4 correspond to uncapped 2 and 4 wt% benzotriazole-encapsulated halloysite nanotubes sol coated mild steel substrates

The reason behind these surface defects is the addition of more and more halloysite nanotubes in the coating matrix. Addition of HNTs more than its optimum concentration causes random orientation of the nanotubes, because of which the coating defects are not completely filled, leaving behind some unfilled pores and voids [24,25]. The coating with 4 wt% loading thus would have an increase in water uptake, leading to a decrease in barrier and corrosion resistance properties. Hence, it can be concluded from the above results that the 2 wt% was the optimum loading percentage for BTA-encapsulated HNT in the coating formulation to achieve both high barrier and autonomic healing properties.

(b) Autonomic healing behaviour of corrosion inhibitor loaded HNT

EIS and PPS were performed for bare MS, samples 6, 7, and 2 after immersing the substrates in 3.5 wt% NaCl solution for 1 h to observe the effect of loading corrosion inhibitor into the halloysite nanotube. Electrochemical impedance data of coated and bare MS coupons were the best fit with the equivalent electrical circuits shown in Fig. 4.9 a, b, and c.

It is to be noted that the data was fitted using two-time constants, and the Bode plots obtained are shown in Fig. 4.12. At lower frequencies, the time constant corresponds to the interface, whereas at higher frequencies, it is because of the coating matrix. The Bode magnitude plot (Fig. 4.12a) for sample 2 has shown an increase in impedance magnitude, suggesting the combined effect of a self-healing agent and sol-gel coating to provide better corrosion protection. From the Bode phase angle plots given in Fig. 4.12b, it could be seen that the phase angle maximum is 50° for the uncoated mild steel substrates, whereas all coated substrates have shown an increased phase angle than the bare substrate.
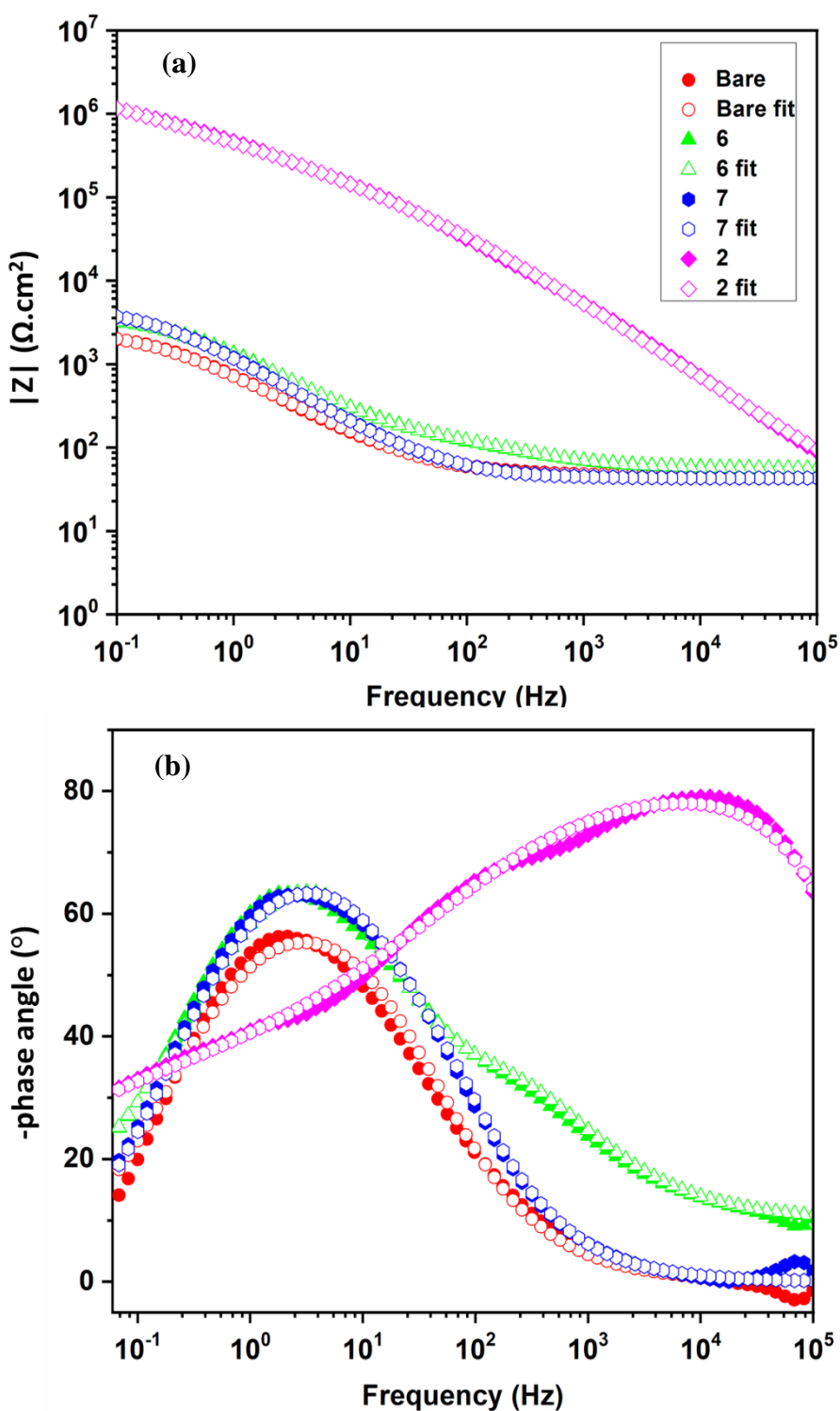
Fig. 4.12. Bode plots for bare MS and samples 6, 7 and 2 obtained after immersion in 3.5 wt% NaCl for 1 h, where samples 6, 7 and 2 correspond to matrix sol, 2 wt% benzotriazole directly dispersed into matrix sol, and uncapped 2 wt% benzotriazole-encapsulated halloysite nanotubes matrix sol, respectively.

The Bode phase angle plot has shown a high phase angle maximum of ~80° for sample 2 alone, which indicates the presence of an effective insulation film at the interface in sample 2. This is due to the presence of timely autonomous-healing corrosion inhibitors in the coating. Sample 7 coating has shown a phase angle maximum nearly equal to that of sample 6 (~64°), suggesting that the corrosion resistance of these coatings was minimal when compared to sample 2, where the protective layer on the metal is reinforced time-to-time because of the release of corrosion inhibitors from the loaded nanocontainers. The EIS fit parameters for bare and coated substrates are shown in Table 4.4.

Table 4.4. EIS fit data obtained after immersing the bare and sample 6, 7 and 2 in in 3.5 wt% NaCl solution for 1 h, where samples 6, 7 and 2 correspond to matrix sol, BTA (2 wt%) dispersed into matrix sol and uncapped 2 wt% BTA encapsulated into HNT, respectively.

Sample ID	R_{coat} ($\Omega.cm^2$)	C_{coat} (F/cm^2)	R_{ct} ($\Omega.cm^2$)	C_{dl} (F/cm^2)	CHI^2	Fitted circuit
Bare	-	-	2558	4.283×10^{-4}	5.369×10^{-3}	c
6	158.1	1.599×10^{-5}	3813	5.521×10^{-5}	3.579×10^{-3}	a
7	23.2	4.414×10^{-9}	4750	1.713×10^{-4}	8.058×10^{-4}	b
2	638.4×10^1	1.642×10^{-10}	576×10^4	1.212×10^{-6}	1.630×10^{-3}	a

Bare MS substrate has shown the least charge transfer resistance value among all the electrodes (Table 4.4), whereas the R_{ct} values of samples 6 and 7 were a little higher than that of bare MS substrate. The R_{ct} values of both 6 and 7 are nearly equal, indicating that the direct addition of BTA into the coating did not increase the barrier property of the coating significantly. However, the BTA-encapsulated HNT-coated substrates (sample 2) have shown an enormous increase in the charge transfer resistance, and the R_{ct} of sample 2 is at least three orders of magnitude higher than all the other substrates.

Polarization measurements were carried out in order to evaluate the coating resistance. Tafel plots thus obtained for bare and coated substrates are shown in Fig. 4.13.
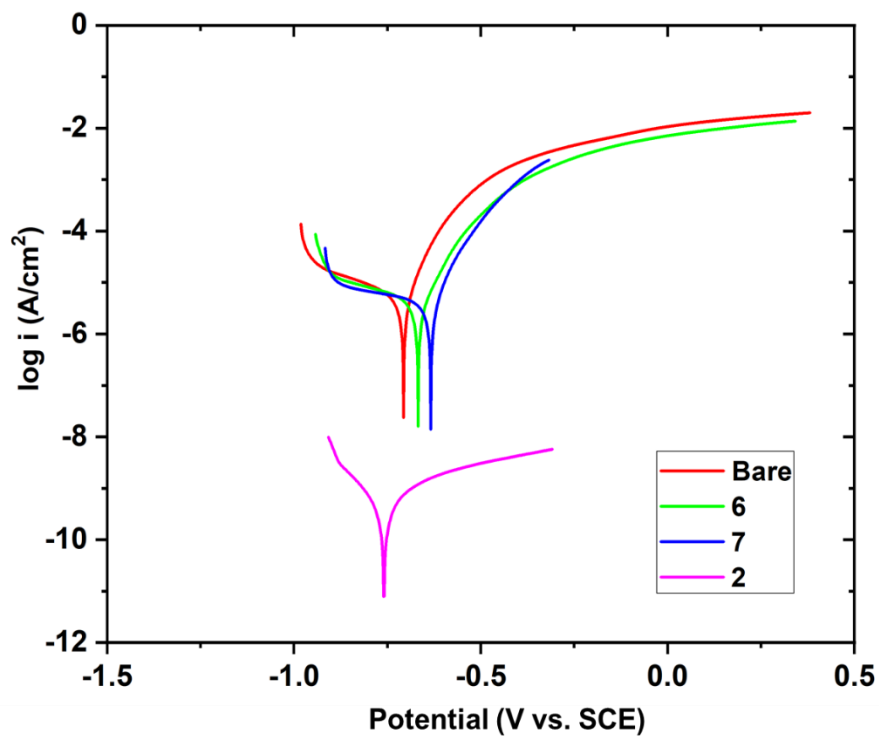
Fig. 4.13. Tafel plots for bare MS and samples 6, 7 and 2 obtained after immersion in 3.5 wt% NaCl solution for 1 h, where samples 6, 7 and 2 correspond to matrix sol, 2 wt% benzotriazole directly dispersed into matrix sol, and uncapped 2 wt% benzotriazole-encapsulated halloysite nanotubes matrix sol, respectively.

The curves indicate that the current density for sample 2 was the least of all. The E_{corr}, i_{corr} and R_p values are tabulated in Table 4.5.

Table 4.5. Tafel Fit parameters of potentiodynamic polarization data obtained after immersing the bare and samples 6, 7 and 2 in 3.5 wt% NaCl solution for 1 h, where samples 6, 7 and 2 correspond to matrix sol, BTA (2 wt%) dispersed into matrix sol and uncapped 2 wt% benzotriazole-encapsulated halloysite nanotubes, respectively.

Sample ID	E_{corr} (V vs. SCE)	i_{corr} (μA/cm^2)	βc (mV/dec)	βa (mV/dec)	R_p/(Ω.cm^2)
Bare	-0.707 ± 0.013	5.54 ± 0.117	327	70	45.7×10^2
6	-0.668 ± 0.019	5.37 ± 0.295	439	91	61.0×10^2
7	-0.634 ± 0.024	4.86 ± 0.092	577	76	60.4×10^2
2	-0.760 ± 0.069	$(0.53 \pm 0.034) \times 10^{-3}$	134	196	64.7×10^6

PPS results show that the polarization resistance was high for sample 2. Therefore, it can be affirmed that the polarization data is in good agreement with the electrochemical impedance spectroscopy measurements. This observation clearly indicates the controlled release of BTA from loaded HNT nanocontainers, which enhanced corrosion resistance and improved the self-healing behaviour when compared to bare MS substrate and samples 6 and 7.

(c) Optimization studies for inhibitor-loaded and capped HNT

To optimize the loading percentage of BTA-encapsulated and capped HNT into the sol, six different sols were prepared with 1 to 6 wt% loadings and coated on mild steel substrates with sample IDs 8 - 13. The capping of HNTs enables a controlled release of the corrosion inhibitors from the nanocontainers. As the tube ends are stoppered with the help of capping agents, the corrosion inhibitors are released only if any crack or damage occurs. The capping agents will slow down the release process to increase the durability of the coating matrix and to avoid excessive loss of the corrosion inhibitor.

The capped BTA-encapsulated HNT coated substrates were dipped in 3.5 wt% NaCl solution for 1 h before performing the electrochemical impedance and potentiodynamic polarization studies. Nyquist plots of samples 8 to 13 shown in Fig. 4.14 illustrate that all the coated substrates possess higher impedance as the capacitive loop is a perfect semi-circle.
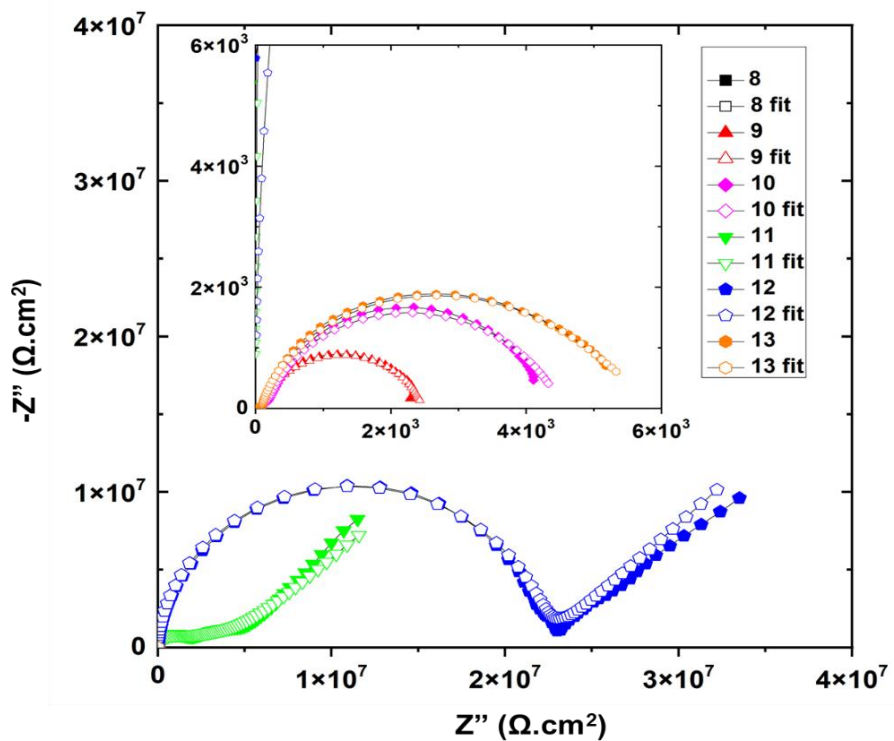
Fig. 4.14. Nyquist plots for samples 1 to 5 (capped 1 to 5 wt% benzotriazole-encapsulated halloysite nanotubes) obtained after immersion in 3.5 wt% NaCl solution for 1 h

The electrochemical circuit used for fitting the data obtained for 8 to 10 and 13 is the same as that shown in Fig. 4.9 a and b. In contrast, the equivalent circuit used for 11 and 12 is the same as that of other coatings but with an additional fit parameter i.e., Warburg impedance denoted as W in series with R_{ct}. EIS fit parameters are shown in Table 4.6, where the charge transfer resistance of sample 12 was higher than all other loading percentages.

Table 4.6. EIS fit data obtained after immersing the samples 8 to 13 (capped 1 to 6 wt% benzotriazole-encapsulated halloysite nanotubes) in 3.5 wt% NaCl solution for 1 h.

Sample ID	R_{coat} ($\Omega.cm^2$)	C_{coat} (F/cm^2)	R_{ct} ($\Omega.cm^2$)	C_{dl} (F/cm^2)	W ($\Omega.s^{-1/2}$)	CHI^2	Fitted circuit
8	34.30	2.79×10^{-3}	69	7.34×10^{-3}	-	1.11×10^{-3}	a
9	74.18	9.88×10^{-10}	2404	1.92×10^{-4}	-	1.74×10^{-3}	a
10	280.30	1.09×10^{-5}	4222	4.18×10^{-5}	-	4.82×10^{-3}	a
11	1.08×10^{6}	2.15×10^{-10}	4.82×10^{6}	3.64×10^{-8}	3.07×10^{-7}	7.14×10^{-3}	d
12	1.48×10^{6}	1.59×10^{-10}	21.95×10^{6}	5.86×10^{-11}	2.78×10^{-7}	5.85×10^{-3}	d
13	92.14	1.41×10^{-5}	5939	8.90×10^{-5}	-	1.67×10^{-3}	a

The current densities of different capped BTA-encapsulated HNT coatings were recorded after immersion in 3.5 wt% NaCl solution for 1 h as shown in the Tafel plot in Fig. 4.15.
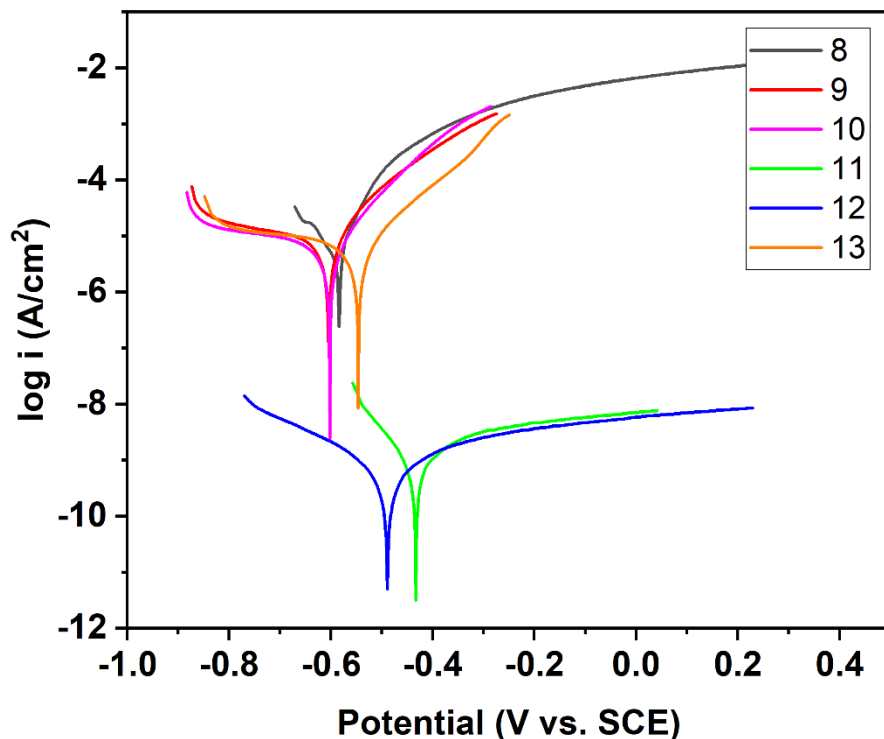
Fig. 4.15. Tafel plots for samples 8 to 13 (capped 1 to 6 wt% benzotriazole-encapsulated halloysite nanotube) obtained after immersion in 3.5 wt% NaCl solution for 1 h.

The current densities of all the capped substrates except 11 and 12 were high, implying that the coating is porous and the electrolyte species have entered through the pores, having higher access to the metal surface. The current densities of samples 11 and 12 were nearly equal, and a similar trend was observed from the polarization data shown in Table 4.7.

Table 4.7. Tafel fit parameters of potentiodynamic polarization data obtained after immersing the samples 8 to 13 (capped 1 to 6 wt% benzotriazole-encapsulated halloysite nanotube) obtained after immersion in 3.5 wt% NaCl solution for 1 h.

Sample ID	E_{corr} (V vs. SCE)	i_{corr} ($\mu A/cm^2$)	βc (mV/dec)	βa (mV/dec)	R_p ($\Omega.cm^2$)
8	-0.584 ± 0.026	7.12 ± 0.626	98	45	0.189×10^4
9	-0.605 ± 0.005	10.10 ± 1.38	520	105	0.380×10^4
10	-0.602 ± 0.016	7.25 ± 0.322	454	101	0.495×10^4
11	-0.433 ± 0.039	$(0.82 \pm 0.039) \times 10^{-3}$	81	121	2.595×10^7
12	-0.489 ± 0.047	$(0.69 \pm 0.042) \times 10^{-3}$	173	218	6.088×10^7
13	-0.548 ± 0.065	7.53 ± 0.059	441	121	0.550×10^4

The polarization resistance for sample 12 was the highest among all the samples. Therefore, it can be concluded from the impedance and polarization data that the corrosion resistance of sample 12 was highest, which corresponds to 5 wt% loading.

In the case of sample 13, adding more inhibitors and capping agents into the sol was found to decrease the barrier property of the coating. The coating performance decreases with the increase in the amount of nanocontainers which in turn affects the coating adhesion suggesting that the loading percentage should not exceed the optimal concentration [26,27]. Surface morphology, as shown in Fig. 4.16(a), shows that the coating is quite dense for sample 12, whereas the coating seems to delaminate from the mild steel surface for sample 13 due to poor adhesion strength. When the concentration of the capped BTA-encapsulated HNT was increased from 1 to 5 wt%, the coating thickness and compatibility of the capping agent with the coating matrix also increased, which in turn helped to fill all the voids and surface defects of the coating. Further increase in the amount of loading beyond an optimum level, the coating seemed to peel off from the substrate for sample 13, as shown in Fig. 4.16(b).
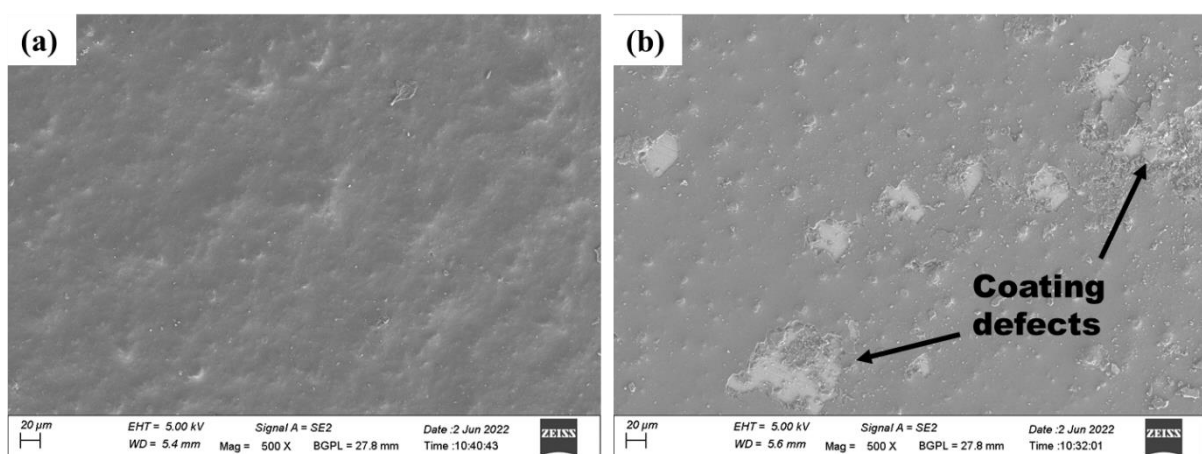
Fig. 4.16. Surface morphology: (a) sample 12, and (b) sample 13, where sample 12 and 13 correspond to capped 5 and 6 wt% benzotriazole-encapsulated halloysite nanotube sol coated mild steel substrates.

It should be noted that in the case of uncapped HNT, the optimum loading was only 2 wt%, whereas, in the case of capped HNT, the optimum loading was found to be 5 wt%. This difference in the optimum loadings could be due to enhanced compatibility of the capping agent, UFNCs, with the silica gel coating matrix, which helps to disperse more amount of capped HNT into the coating matrix. Therefore, it can be concluded from all the above results that the 5 wt% loading was found to be the optimized loading percentage in the case of capped HNTs for achieving good barrier properties with high R_{ct}, perfect semi-circular capacitive loop and efficient self-healing property.

(d) Self-healing behaviour of capped BTA-encapsulated HNT sols at different exposure intervals

Based on the optimization studies, sample 12 was considered the most efficient to obtain the best coating with prominent self-healing and barrier properties for mild steel. Electrochemical impedance analysis of sample 12 was carried out after immersing it in 3.5 wt% NaCl for different time periods, 1 h, 5 h and 10 h, and the equivalent electrical circuit for obtaining the best fit for the EIS results is similar to the one in Fig. 4.9 d and e, however with an additional fit parameter, i.e. Warburg impedance 'W' in series with R_{ct}. All the Nyquist plots of sample 12 dipped in 3.5 wt% NaCl solution for different times (1- 10 h) have shown a perfect semi-circular pattern, as shown in Fig. 4.17, confirming that the coating possessed good anti-corrosion and adhesion properties for the extended period in corrosive 3.5 wt% NaCl.
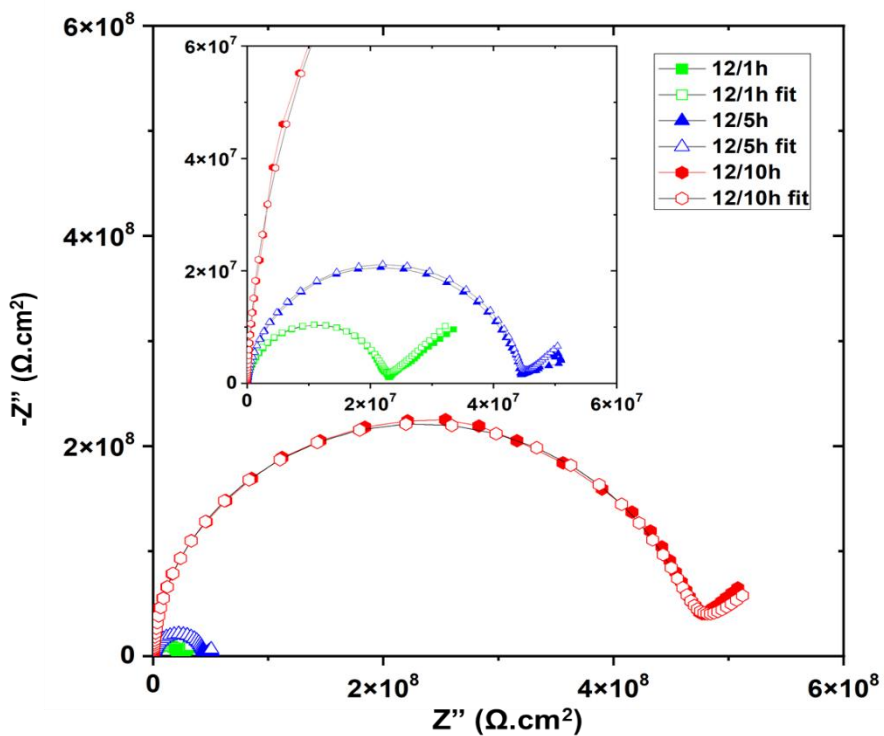
Fig. 4.17. Nyquist plots for sample 12 after exposing it to 3.5 wt% NaCl solution at varying time intervals, where sample 12 corresponds to capped 5 wt% benzotriazole-encapsulated halloysite nanotube

Nyquist plots have shown an inclination at 45° in the diffusion region for all the immersion periods, confirming that the coating possessed minute cracks or channels leading to diffusion of electrolyte species which is termed the Warburg impedance effect. The results of Nyquist plot analysis obtained with the best fit are given in Table 4.8.

Table 4.8. EIS fit data obtained after immersing sample 12 in 3.5 wt% NaCl solution at different time intervals, where sample 12 corresponds to capped 5 wt% BTA encapsulated into HNT

Immersion Period	R_{coat} ($\Omega.cm^2$)	C_{coat} (F/cm^2)	R_{ct} ($\Omega.cm^2$)	C_{dl} (F/cm^2)	W ($\Omega.s^{-1/2}$)	CHI^2	Fitted circuit
1 h	1.48×10^6	1.59×10^{-10}	0.22×10^8	5.87×10^{-11}	2.78×10^{-7}	5.85×10^{-3}	d
5 h	2.05×10^7	2.11×10^{-10}	0.23×10^8	7.77×10^{-11}	3.94×10^{-7}	5.76×10^{-3}	e
10 h	4.55×10^6	1.35×10^{-10}	4.55×10^8	2.48×10^{-11}	4.78×10^{-7}	4.12×10^{-3}	d

The initial value of Warburg impedance was lower because of the uptake of water and electrolyte diffusion, whereas the Warburg impedance was found to increase with an increase in exposure time in 3.5 wt% NaCl solution, which suggests that the corrosion inhibitor has been

released, due to which the permeability of the film has decreased, increasing both the coating resistance and charge transfer resistance [28,29]. Despite the diffusion of electrolyte species initially, the coating remained intact at all the immersion periods and improved with time, resulting in higher impedance values. The plausible reason for this trend is the polymeric nature of the urea-formaldehyde nanocapsules. For initial exposure to a corrosive environment, these polymeric nanocapsules will swell up with the water uptake and act as a barrier to avoid the penetration of the electrolyte. The charge transfer resistance values increased with the increase in immersion time. The increase in R_{ct} is due to the infiltration of loaded halloysite nanotubes and urea-formaldehyde nanocapsules into the micro and nanopores of the sol coatings as fillers. These pore fillers could either conceal the voids in the coating or cover and insulate with the loaded inhibitors, making the coatings more homogenous and thus providing an excellent barrier property.

Potentiodynamic polarization studies for sample 12 were carried out at different immersion periods to examine the self-healing behaviour of the coatings, and the resulting Tafel plots are shown in Fig. 4.18.
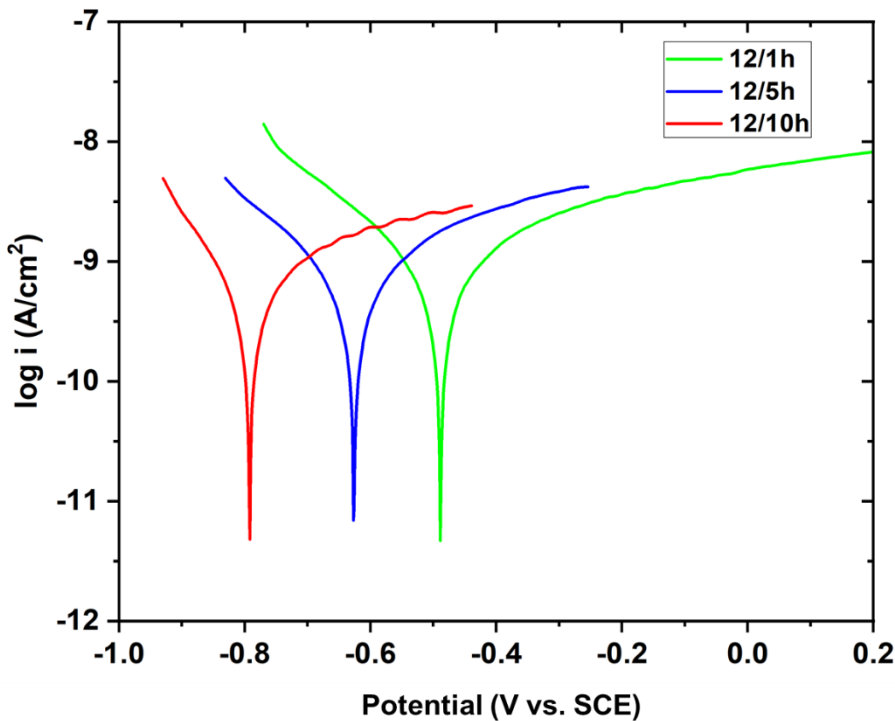
Fig. 4.18. Tafel plots for sample 12 after exposing it to 3.5 wt% NaCl solution at varying time intervals, where sample 12 corresponds to capped 5 wt% benzotriazole-encapsulated halloysite nanotube

The polarization data obtained matched well with the outcomes of electrochemical impedance analysis. Sample 12 exposed to 3.5 wt% NaCl solution for 10 h possessed the least current, inferring that the coating improves and withstands extremely corrosive conditions for a longer duration after immersing in the aggressive medium. As the external voltage is applied during the potentiodynamic polarization measurements, these nanocapsules open and allow the corrosion inhibitor to be released, thereby self-healing the damaged area. The current density and potential values obtained from the Tafel plots are given in Table 4.9.

Table 4.9. Tafel fit parameters of potentiodynamic polarization data obtained after immersing sample 12 in 3.5 wt% NaCl solution, different time intervals, where sample 12 corresponds to capped 5 wt% bezotriazole encapsulated into HNT

Sample ID	E_{corr} (V vs. SCE)	i_{corr} (μA/cm^2)	βc (mV/dec)	βa (mV/dec)	R_p (Ω.cm^2)
1 h	-0.489 ± 0.047	(6.9 ± 0.42) × 10^{-4}	173	218	6.08 × 10^7
5 h	-0.627 ± 0.019	(6.3 ± 0.84) × 10^{-4}	175	216	6.63 × 10^7
10 h	-0.792 ± 0.095	(5.5 ± 0.89) × 10^{-4}	130	206	6.79 × 10^7

The EIS and potentiodynamic polarization studies suggest that the loaded inhibitors were released in a controlled manner due to the capping of halloysite nanotubes, similar to our previous work on Mg alloy AZ91D [30]. The higher impedance values and increase in the polarization resistance also confirmed the release of corrosion inhibitor, thereby imparting autonomic healing property to the coatings even after 10 h of exposure to 3.5 wt% NaCl solution.

4.1.1.6. *Scanning vibrating electrode technique (SVET) analysis*

Current density plots obtained in SVET analysis of bare MS substrate and sample 2 are shown in Fig. 4.19.
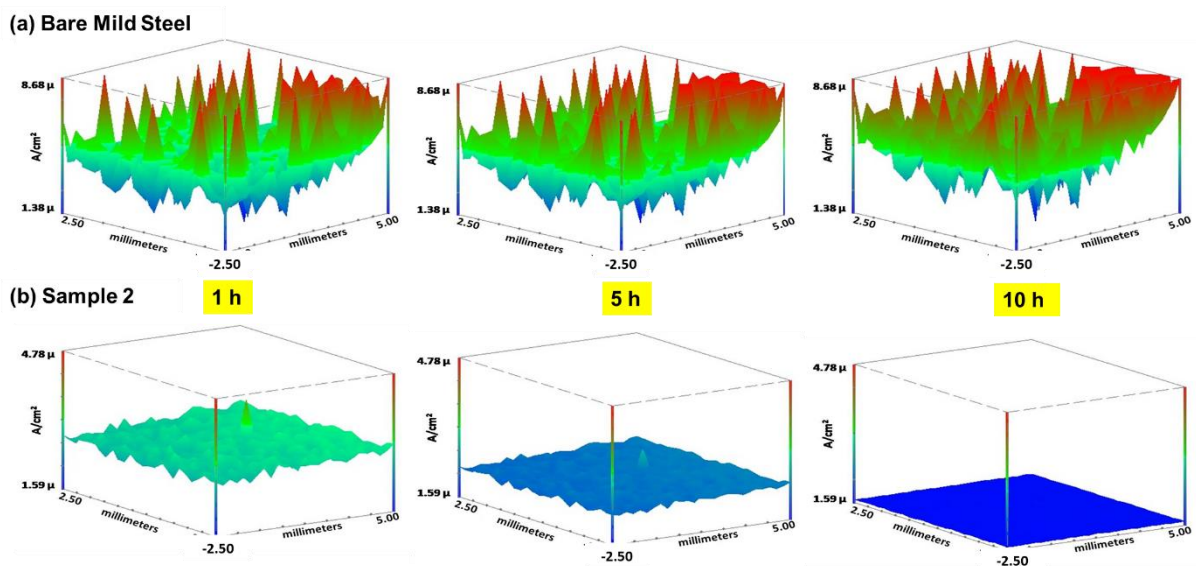
Fig. 4.19. Current density maps for bare and sample 2 (2 wt% benzotriazole-encapsulated halloysite nanotube matrix sol) after immersing in 3.5 wt% NaCl solution at different time intervals.

The plots show the localized current density maps resulted after immersing the substrates in 3.5 wt% NaCl solution for different periods, 1, 5 and 10 h. Mild steel substrate, when exposed to a neutral solution, will undergo a redox reaction as follows:

$$Fe \longrightarrow Fe^{2+} + 2e^- \quad \text{Oxidation}$$
$$O_2 + 2H_2O + 4e^- \longrightarrow 4\,OH^- \quad \text{Reduction}$$

Oxidation and reduction reactions, as shown above, occur simultaneously at the metal surface. From SVET measurements, bare MS substrate (Fig. 4.19a) shows an increase in anodic current with the immersion time at the scribed area, which could be attributed to the increase in the corrosion rate of bare substrate. Figure 4.19b depicts the localized current density maps of sample 2 observed after immersing in 3.5 wt% NaCl solution for different time periods. The localized current densities observed for the beginning 1 h immersion period are considerably less at sample 2 than those at bare MS substrate (Fig. 4.19a). Furthermore, the anodic currents decreased step-by-step with the increase in the exposure time from 1 h to 10 h, which could be attributed to the release of corrosion inhibitor molecules which in turn passivate the metal surface. The anodic behaviour of sample 2 reduces, and eventually, the anodic reaction is entirely blocked, as seen in the plot after 10 hours of immersion, which shows no spikes (Fig.

4.19b), inferring the autonomic healing capability. The observations show that sample 2 possessed barrier properties initially; after an exposure to a corrosive environment, the corrosive ions penetrate through the pinholes present on the surface of the coated metal and initiate the localized corrosion phenomenon. At the same time, the HNTs release the corrosion inhibitor and heal the damaged area. SVET analysis confirmed that the self-healing properties occur only in the BTA-encapsulated HNT coated mild steel substrates and not on the bare mild steel. Previous investigations carried out in our laboratory for different substrates and matrix coatings have shown that the anodic current has decreased with exposure time, suggesting the partial recovery of the barrier property [31,32]. Thus, it can be concluded that the sols prepared using corrosion inhibitor-encapsulated HNT exhibited better self-healing properties than bare mild steel substrates, even after exposing the coated specimens for 10 h.

4.1.1.7. Salt spray test

Photographs of uncoated and coated substrates after the salt spray test are shown in Fig. 4.20. Artificial scribes were created on the coated substrates to visualize the self-repairing ability of coatings. The substrates were kept in a salt spray compartment and exposed to 5 wt% NaCl solution for different time durations, namely 5 h, 10 h and 24 h. The images obtained for bare mild steel substrate after 5 h exposure show corrosion product formation throughout the surface. In contrast, for the coated substrates, the onset of corrosion was observed only near the scribed mark. Images obtained after 10 h of exposure to salt spray reveal that the bare substrate corroded completely. A similar observation was seen for sample 7, corresponding to the direct dispersion of BTA into the matrix sol. Images for sample 2 and sample 12 show minimum corrosion, maintaining the coating integrity even after 10 h exposure. This can be explained by the self-healing action of BTA released from HNT nanocontainers. Encapsulation of BTA into HNT becomes more prominent and efficient as it prevents excessive leaching of the corrosion inhibitor, thereby ensuring its sustained release. Images obtained after 24 h of exposure illustrate that samples 2 and 12, although corroded throughout, show the presence of small coating patches that are still visible, confirming that the coating is still well adherent to the metal surface. BTA-encapsulated HNT or capped BTA-encapsulated HNT coatings have shown enhanced protection for a longer duration, as the release of corrosion inhibitor depends on timely demand of the coating. This phenomenon, in turn, increases the durability of the coating and maintains its intactness for a longer period. Another reason to explain the corrosion

protection of capped coatings, sample 12 is the usage of UFNCs which are polymeric in nature. These UFNCs form a layer on HNT, thus forming a layered structure, which had the added advantage of providing a barrier effect against the electrolyte species that penetrate into the coating matrix. Self-healing action of BTA starts as soon as the electrolyte enters the coating matrix, thus protecting for a longer period compared to other coatings. The SST images are in well agreement with the electrochemical studies, which also confirms that the corrosion resistance of capped BTA-encapsulated HNT was highest among all other coating types investigated.
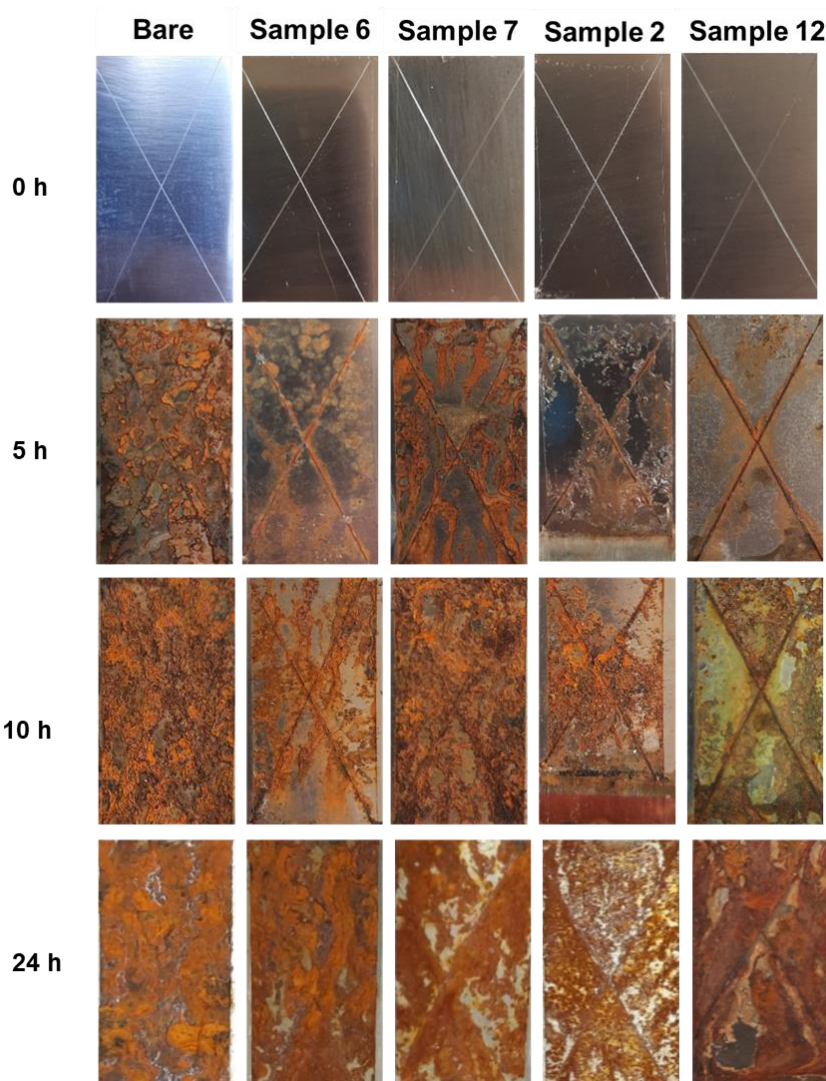
Fig. 4.20. Salt spray test images for bare MS, samples 6, 7, 2 and 12 after exposing them to 5 wt% NaCl solution at different time intervals, where samples 6, 7, 2 and 12 correspond to matrix sol, 2 wt% BTA directly dispersed into matrix sol, uncapped 2 wt% BTA-encapsulated HNT, capped 5 wt% BTA-encapsulated HNT, respectively

A schematic representation of loaded and capped halloysite nanotubes and the autonomic-healing of the damage by a corrosion inhibitor is shown in Fig. 4.21.

(a) Encapsulation and capping of HNT
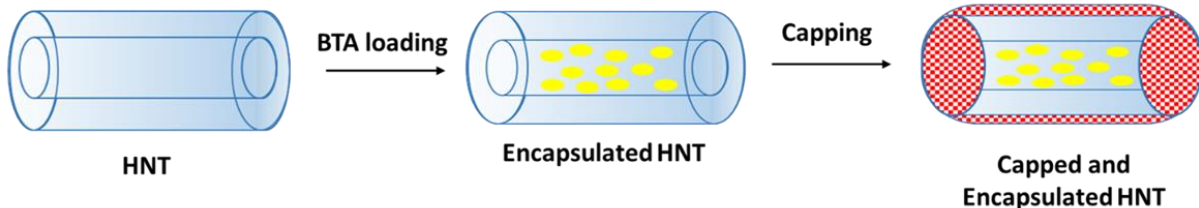
(b) Self-healing action of capped BTA-loaded HNT
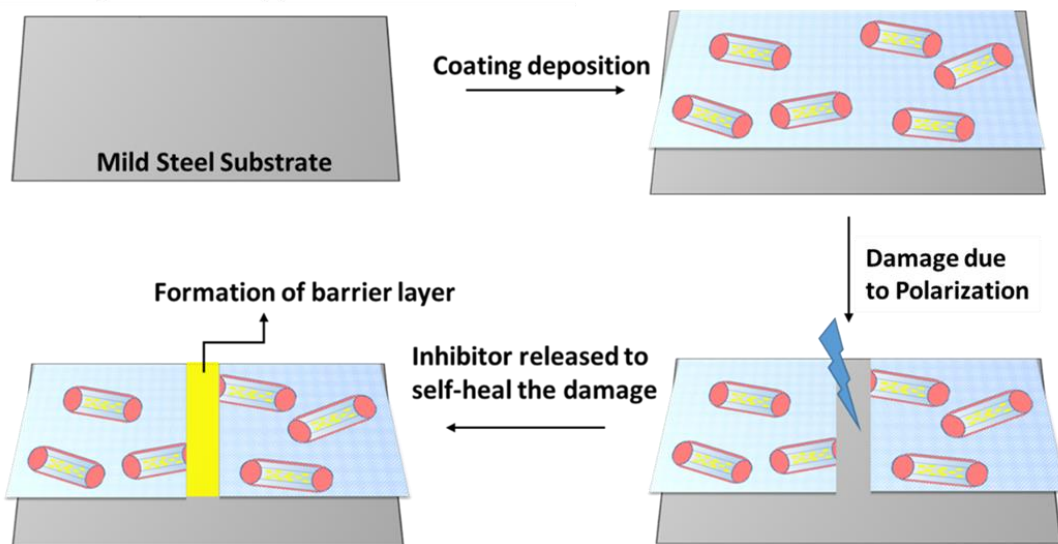
Fig. 4.21. Proposed mechanism of (a) Encapsulation and capping of HNT and (b) Autonomic-healing of the surface defects after release of the corrosion inhibitor

MS substrate is coated with a thin film of capped BTA-encapsulated HNT sol. When the protective film is damaged by mechanical or electrochemical polarization, the inhibitor molecules entrapped in the HNTs get released at the site, and the complex between the inhibitor BTA molecules and metal ions forms a passive protective layer. In the potentiodynamic polarization studies, the externally applied potential induces micro-cracks or breaks in the film, which results in the rupturing of nanocapsules to release the entrapped corrosion inhibitors. Eventually the released corrosion inhibitors prompt self-healing action. Hence, capping and encapsulation of corrosion inhibitor into the nanocontainers i.e., HNT, prevents unwanted leaching of the corrosion inhibitor, providing an enhanced barrier and self-healing properties, thereby prolonging the corrosion protection.

4.3. Conclusions

- Present investigation on the protection of mild steel against corrosion using thin sol-gel films consisting of inhibitor-loaded HNTs with/without capping demonstrated the autonomic-healing of the coated substrates when damage occurred.

- Optimization studies of uncapped BTA-encapsulated HNT coatings revealed that sample 2, corresponding to 2 wt% loading of BTA encapsulated into HNT, was significant in achieving better anti-corrosion properties. The corrosion current density decreased from 10^{-7} A/cm^2 to 10^{-10} A/cm^2 compared to other loading levels.

- BTA, when encapsulated into HNTs and dispersed into an organic-inorganic hybrid sol corresponding to sample 2 showed better anti-corrosion performance due to the encapsulation of corrosion inhibitor when compared to bare and direct addition of BTA into the matrix sol. Sample 2 showed a substantial increase in Rct value from 10^3 Ω/cm^2 to 10^8 Ω/cm^2 with respect to bare MS, matrix sol-coated and BTA directly dispersed-sol coated substrates.

- Optimization studies for capped inhibitor-loaded HNT revealed that the coating with 5 wt% capped BTA-encapsulated HNT sol (sample 12) provided excellent corrosion resistance in contrast with the other loading percentages.

- Coatings based on BTA-encapsulated HNTs capped with polymeric nanocapsules have shown improved corrosion resistance on MS substrates compared to sol coatings generated from uncapped BTA-encapsulated HNT.

- Electrochemical impedance spectroscopy and potentiodynamic polarization studies showed that sample 12 possessed excellent barrier and self-healing behaviour even after exposing them to 3.5 wt% NaCl solution for 10 h. The charge transfer resistance at the end of 10 h exposure was 10 times higher compared to that at the end of 1 and 5 h exposure to 3.5 wt% NaCl solution.

- The localized corrosion and self-healing properties of sample 2 coated substrates were confirmed using SVET analysis compared to bare MS substrates. The localized current densities of sample 2 at the scribed area decreased gradually with the increase in exposure time to 3.5 wt% NaCl solution. They became negligible at the end of 10 h, demonstrating the self-healing action of the coating.

4.4. References:

[1] Samadzadeh, M., Boura, S. H., Peikari, M., Ashrafi, A., Kasiriha, M., Tung oil: An autonomous repairing agent for self-healing epoxy coatings, Prog. Org. Coat. 70 (2011) 383–387.

[2] Cavallaro, G., Danilushkina, A., Evtugyn, V., Lazzara, G., Milioto, S., Parisi, F., Rozhina, E., Fakhrullin, R., Halloysite nanotubes: Controlled access and release by smart gates, Nanomaterials. 7 (2017) 1–12.

[3] Zheng, Z., Huang, X., Shchukin, D., A Cost-effective pH-sensitive release system for water source pH detection, Chem. Commun. 50 (2014) 13936–13939.

[4] Wang, M., Wang, J., Hu, W., Preparation and corrosion behavior of Cu-8-HQ@HNTs/epoxy coating, Prog. Org. Coat. 139 (2020) 105434.

[5] Abdullayev, E., Lvov, Y., Clay nanotubes for corrosion inhibitor encapsulation: Release control with end stoppers, J. Mater. Chem. 20 (2010) 6681–6687.

[6] Katoueizadeh, E., Zebarjad, S. M., Janghorban, K., Investigating the effect of synthesis conditions on the formation of urea-formaldehyde microcapsules, J. Mater. Res. Technol. 8 (2019) 541–552.

[7] Yan, X., Han, Y., Yin, T., Synthesis of urea-formaldehyde microcapsule containing fluororesin and its effect on performances of waterborne coatings on wood surface, Polymers (Basel). 13 (2021) 1674.

[8] Haruna, K., Saleh, T., N,N′-Bis-(2-aminoethyl)piperazine functionalized graphene oxide (NAEP-GO) as an effective green corrosion inhibitor for simulated acidizing environment, J. Environ. Chem. Eng. 9 (2021) 104967.

[9] Suleiman, R. K., Saleh, T., Al Hamouz, O, C., Ibrahim, M, B., Sorour, A, A., El Ali, B., Corrosion and fouling protection performance of biocide-embedded hybrid organosiloxane coatings on mild steel in a saline medium, Surf. Coat. Technol. 324 (2017) 526–535.

[10] Dhenadhayalan, N., Lin, K. C., Saleh, T. A., Recent advances in functionalized carbon dots toward the design of efficient materials for sensing and catalysis applications, Small. 16 (2020) 1–24.

[11] Saleh, T. A. Nanocomposite of carbon nanotubes/silica nanoparticles and their use for adsorption of Pb(II): from surface properties to sorption mechanism, Desalin. Water Treat 57, 10730–10744 (2016).

[12] Talib, N. N. A., Bakar, N. H. H. A., Bakar, M. A., Iqbal, A., Yusof, N. H., Depolymerisation of liquid epoxidized natural rubber (LENR) using lanthanum hydroxide

(La(OH)$_3$)-HNT Catalyst, IOP Conf Ser Mater Sci Eng. 509 (2019) 1-9.

[13] Saleh, T. A., Simultaneous adsorptive desulfurization of diesel fuel over bimetallic nanoparticles loaded on activated carbon, J. Clean. Prod. 172 (2018) 2123–2132.

[14] Xu, D., Lou, C., Huang, J., Lu, X., Xin, Z., Zhou, C., Effect of inhibitor-loaded halloysite nanotubes on active corrosion protection of polybenzoxazine coatings on mild steel, Prog. Org. Coat. 134 (2019) 126–133.

[15] Yuan, P., Southon, P. D., Liu, Z., Green, M, E, R., Hook, J, M., Antill, S. J., Kepert, C, J., Functionalization of halloysite clay nanotubes by grafting with γ-aminopropyltriethoxysilane, J. Phys. Chem. C. 112 (2008) 15742-15751.

[16] Gao, B., Tan, B., Liu, Y., Wang, C., He, Y., Huang, Y., A study of FTIR and XPS analysis of alkaline-based cleaning agent for removing Cu-BTA residue on Cu wafer, Surf. Interface Anal. 51 (2019) 566–575.

[17] Barreto, L. S., Tokumoto, M. S., Guedes, I. C., Gomes de Melo, H., Amado, F., Capelossi, V. R., Study and assessment of the efficiency of the cocoa bark extracted from the theobroma cacao as an inhibitor of the corrosion of carbon steel in substitution of benzotriazole, Mater Res. 21 (2018) 1-9.

[18] Yan, J., Lin, S., Wang, M., Zhao, W., Preparation and characterization of metatitanic acid/urea-formaldehyde microcapsules as wear-reducing additives, Propellants Explos. Pyrotech. 45 (2020) 1805–1812.

[19] Popović, M., Miljković, J., Simendić, J. B., Pavlićević, J., Ristić, I., Curing characteristics of low emission urea-formaldehyde adhesive in the presence of wood, Wood Res. 56 (2011) 589–600.

[20] Joshi, A., Abdullayev, E., Vasiliev, A., Volkova, O., Lvov, Y., Interfacial Modification of Clay Nanotubes for the Sustained Release of Corrosion Inhibitors, Langmuir. 29 (2012) 7439-7448.

[21] Popov, B. N., Chapter-5: Basics of Corrosion Measurements, Corrosion Engineering. (2015) 181–237.

[22] Sravanthi, M., Manjunatha, K. G., Khan, S., Sunitha, N., Tafel Polarization and Impedance Studies of Al-7075 Alloy and Its Composites in Different Medium, Int. J. Adv. Res. 7 (2019) 779–794.

[23] Sowa, M., Simka, W., Electrochemical impedance and polarization corrosion studies of tantalum surface modified by DC Plasma electrolytic oxidation, Materials (Basel). 11 (2018) 545.

[24] Manasa, S., Jyothirmayi, A., Siva, T., Sathiyanarayanan, S., Gobi, K. V., Subasri, R., Effect of inhibitor loading into nanocontainer additives of self-healing corrosion protection coatings on aluminum alloy A356.0, J. Alloys Compd. 726, 969–977 (2017).

[25] Huttunen-Saarivirta, E., Vaganov, G. V., Yudin, V. E., Vuorinen, J., Characterization and corrosion protection properties of epoxy powder coatings containing nanoclays, Prog. Org. Coat. 76 (2013) 757–767.

[26] Shchukina, E., Wang, H., Shchukin, D. G., Nanocontainer-based self-healing coatings: Current progress and future perspectives, Chem. Commun. 55 (2019) 3859–3867.

[27] Shchukin, D. G., Möhwald, H., Self-repairing coatings containing active nanoreservoirs, Small. 3 (2007) 926–943.

[28] Skale, S., Doleček, V., Slemnik, M., Electrochemical impedance studies of corrosion protected surfaces covered by epoxy polyamide coating systems, Prog. Org. Coat. 62 (2008) 387–392.

[29] Volmajer, N. K., Steinbücher, M., Berce, P., Venturini, P., Gaberscek, M., Electrochemical Impedance Spectroscopy Study of Waterborne Epoxy Coating Film Formation, Coatings. 9 (2019) 1–14.

[30] Adsul, S. H., Bagale, U. D., Sonawane, S. H. & Subasri, R. Release rate kinetics of corrosion inhibitor loaded halloysite nanotube-based anticorrosion coatings on magnesium alloy AZ91D, J. Magnes. Alloy 9 (2021) 202–215.

[31] Manasa, S., Jyothirmayi, A., Siva, T., Sarada, B. V., Ramakrishna, M., Sathiyanarayanan, S., Gobi, K. V., Subasri, R., Nanoclay-based self-healing, corrosion protection coatings on aluminum, A356.0 and AZ91 substrates, J. Coat. Technol. Res. 14 (2017) 1195–1208.

[32] Adsul, S. H., Siva, T., Sathiyanarayanan, S., Sonawane, S. H., Subasri, R., Self-healing ability of nanoclay-based hybrid sol-gel coatings on magnesium alloy AZ91D, Surf. Coat. Technol. 309 (2017) 609–620.

CHAPTER-5

Effect of pH on the Controlled Release of Benzotriazole from Halloysite Nanotubes for Corrosion Protection of Mild Steel

CHAPTER-5

Effect of pH on the Controlled Release of Benzotriazole from Halloysite Nanotubes for Corrosion Protection of Mild Steel

5.1. Introduction

In the previous chapter, it was concluded that the coatings based on the loading of benzotriazole (BTA) into halloysite nanotubes showed excellent anti-corrosion behaviour. The SVET maps obtained for BTA-encapsulated HNT sol-coated mild steel (MS) substrate on exposure to 3.5 wt% NaCl showed enhanced self-healing behaviour. In this context, the present chapter is designed to analyze the release behaviour of BTA from halloysite nanotubes at different pH. UV-Vis spectroscopy was used to determine the absorbance of BTA released under different pH conditions, which was then converted into the amount or percentage release data subsequently fitted with different kinetic models. The kinetic models probed here are used widely for determining the drug release from certain nanocarriers at different conditions such as pH, temperature etc. The controlled drug release from these nanocarriers helps in the self-healing of tissues in the human body and enhances therapeutic efficacy. Based on this mechanism, similar experiments were performed to analyze the release of corrosion inhibitor from the nanocontainer to observe the corrosion inhibition process and self-healing behaviour due to the released corrosion inhibitor. Salt immersion test at different pH was also carried out for bare and BHS coated MS substrates to visually observe and confirm the release of BTA, which self-heals the scribed area by forming passive film of BTA-Fe complex.

5.2. Experimental

The release assays were conducted by UV–Vis absorption spectroscopy using a UV-Vis spectrophotometer (Shimadzu, Model: UV-3600 plus, Japan). Approximately 0.2 g of BTA-encapsulated HNT sample was added to 100 mL of 3.5 wt% NaCl solution at three different pH (3.0, 7.0 and 10.0) in different beakers. The pH of 3.5 wt% NaCl was adjusted using 0.1 M HCl and 0.1 M NaOH solution. The solution of BTA-encapsulated HNT was then stirred for different time intervals at 600 rpm. At each time interval, 5 ml of supernatant was collected, and then 5 ml of fresh NaCl solution was added to the BTA-encapsulated HNT sample. For first 1 hour, the aliquot was collected at an interval of 10 minutes followed by every 1 hour, maximum up to 10 h duration. The as-collected aliquots were then analysed using UV-Vis spectroscopy.

5.3. Results and discussion

5.3.1. Release study of BTA from HNT

The standard UV-Vis absorption spectra of BTA at different concentrations in 3.5% NaCl solution are shown in Figure 5.1a. Intensity of the UV-Vis absorption peak was found to increase with the increase in concentration of BTA solution, and there was no UV-Vis characteristic peak observed for only 3.5 wt% NaCl solution, thereby confirming no absorption interference from NaCl solution. Hence, the intensity of the characteristic UV-Vis peak of BTA at 258 nm was used to quantify the concentration of BTA. The correlation between the BTA concentration and the absorbance of the characteristic peak is presented in Figure 5.1b, and the data could be fitted to a linear relationship as given below:

$$Y = 0.6126\,X \quad \text{-------- (i)}$$

where, Y = Characteristic absorbance value of BTA solution at 258 nm

    X = Concentration of BTA solution in mg/100 ml

    Slope (m) = 0.6126

From this equation, the concentration (X) of the BTA solution corresponding to a particular absorbance value (Y) can be determined by using the following equation:

$$X = Y/0.6126 \quad \text{-------- (ii)}$$

The amount of benzotriazole released at three different pHs was monitored via UV-Vis spectroscopy. Since benzotriazole has equilibrium structures that are dependent on the environmental pH [1-2], analytical curves were constructed at the appropriate pH. Azo heterocyclic compounds are well-known for their performance as corrosion inhibitors. Benzotriazole (BTA) is a well-known corrosion inhibitor for mild steel. When adsorbed on metal surface, it forms bonds involving the lone pair of electrons from the nitrogen atom of the triazole ring, which are further stabilized by the presence of the benzene ring. It can exist in its neutral (BTAH), negatively charged (BTA$^-$) or protonated (BTAH$_2^+$) forms, according to the environmental pH, as follows:

$$BTAH_2^+ \leftrightarrows BTAH + H^+$$
$$BTAH \leftrightarrows BTA^- + H^+$$
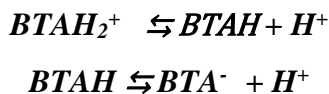
Figure 5.1 c and d shows the cumulative release and percentage release profile for BTA-encapsulated HNTs sample at the different pH values in 3.5 wt% NaCl solution, monitored for 600 min. The highest amount of total BTA released at the end of 10 h was taken as 100% of the amount released, since the total amount of BTA released attained a saturation level at the end of 10 h of release. In the initial 30 min of time, there was a sharp increase in the release of BTA at all the pH values. At pH 3, 7 and 10, the extent of BTA released in the medium was 48 %, 30 % and 20 %, respectively. After 1 h, the BTA release at pH 3 was maximum, whereas, for pH 7 and 10, the percentage of BTA release was nearly same. At pH 3, there was a sharp increase in the release rate of BTA, indicating that it could provide better self-healing action and protect the mild steel substrate from corrosion at its onset. As time passes, the amount of corrosion inhibitor released at pH 3 is at its peak; therefore, the inhibitor is consumed very fast when compared to pH 7 and 10. Though the release rate for pH 7 is steady, it can be concluded that the amount of BTA released has become constant with time. Therefore, the amount of BTA released at pH 7 may not be sufficient for corrosion protection, whereas, an optimum BTA release was observed at pH 10. Hence, among all the pH, the release rate at pH 10 has shown sustained and prolonged release of benzotriazole and, therefore, shows the self-healing action for a longer time duration. Salt immersion test analysis in the following section will help in understanding the inhibition action of BTA at different pH levels.
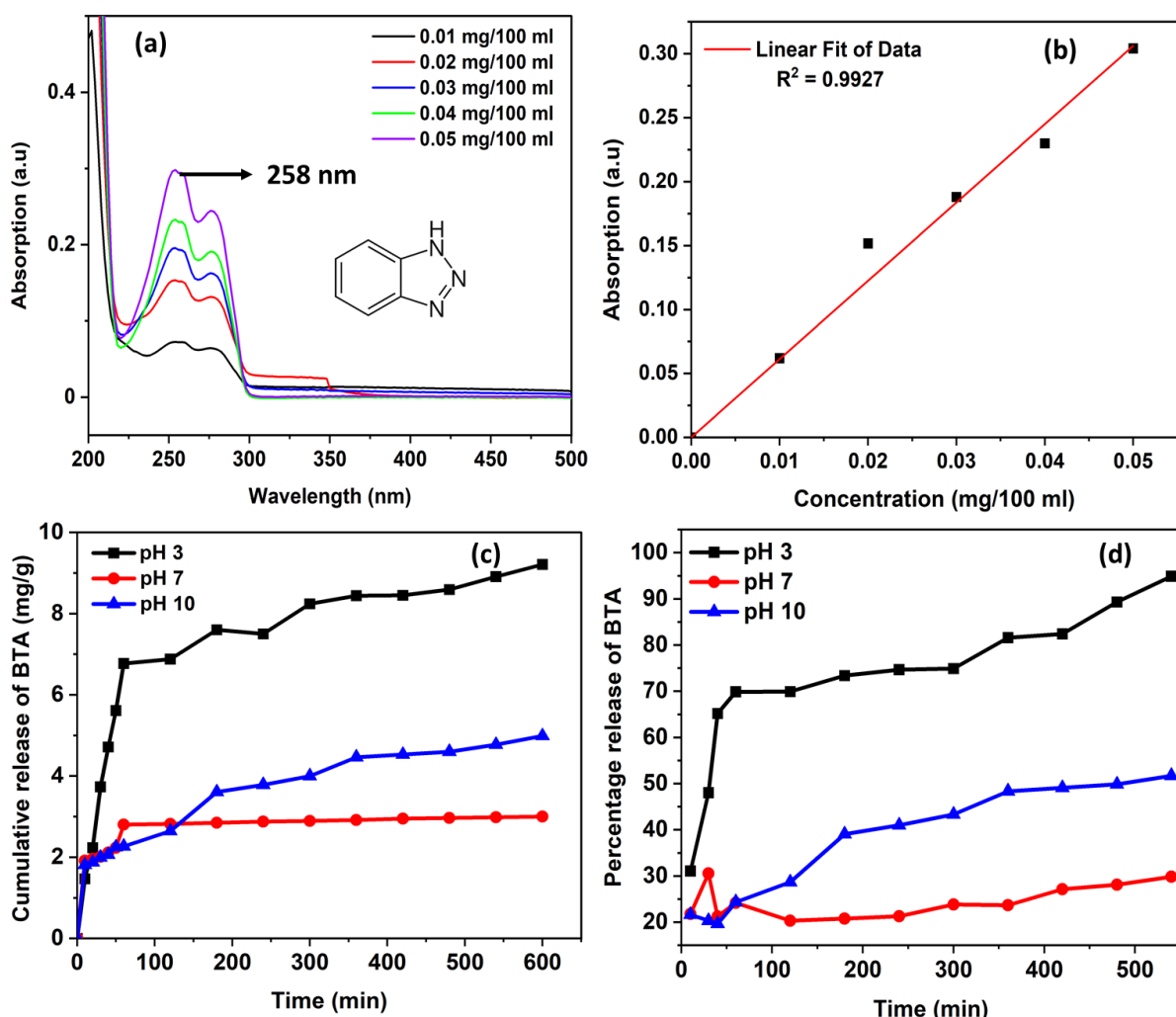
Fig. 5.1. (a) UV-Vis absorption spectra of benzotriazole (BTA) solution in 3.5 % NaCl solution at different concentrations. (b) Linear relationship between absorbance at 258 nm and the concentration of BTA (c) Cumulative release, and (d) Percentage release of BTA from halloysite nanotube at different pH.

5.3.2. Release models

The release profiles as discussed above was fitted using different mathematical models reported in literature to evaluate the release of BTA at different pH.

1. Zero order release kinetics

It refers to the process of constant corrosion inhibitor released from a nanocarrier independent of the concentration. In its simplest form, zero order release can be represented as

$$Q_t = Q_0 + K_0 t$$

where Q_t is the amount of corrosion inhibitor released or dissolved, Q_0 is the initial amount of corrosion inhibitor in solution (it is usually zero), and K_0 is the zero order release constant. Graphical representation of the fraction of corrosion inhibitor dissolved versus time will be linear. The slope of the curve gives the value of K in zero-order release kinetics [3].

2. First order release kinetics

The first order equation describes the release from a system where the release rate is concentration-dependent, expressed by the equation:

$$dC / dt = - K_t$$

where K is the first-order rate constant expressed in units of $time^{-1}$.
This equation can be expressed as:

$$Log\ A_t = Log\ A_0 – kt / 2.303$$

where A_0 is the initial concentration of corrosion inhibitor, and A_t is the concentration of corrosion inhibitor in solution at time t. The equation predicts a first-order dependence on the concentration gradient (A_0 - A_t) between the static liquid layer next to the solid surface and the bulk liquid. The plot is constructed between log cumulative of percentage of BTA released from HNT vs. time which would yield a straight line with a slope of –K/2.303 [4].

3. Higuchi model

The first example of a mathematical model aimed to describe drug release from a matrix system was proposed by Higuchi in 1963. This model is applicable to study the release of water-soluble and low soluble compounds incorporated in semisolid and solid matrices [5]. Simplified Higuchi model describes the release of corrosion inhibitor from an insoluble matrix as a square root of time-dependent process based on the Fickian diffusion Equation.

$$Q_t = K_H t^{1/2}$$

Following this model, the data obtained in the present study were plotted as cumulative percentage corrosion inhibitor release versus square root of time. The slope of the plot gives the Higuchi dissolution constant K_H. Despite the complexity of the involved mass transport processes, Higuchi derived a very simple equation, which is easy to use. Based on a pseudo steady-state approach, a direct proportionality between the cumulative amount of corrosion

inhibitor released and the square root of time can be demonstrated [6]. The Higuchi and zero-order models are used to describe the limits for transport and drug release.

4. Hixson-Crowell cube root law

The cube root law was first proposed by Hixson and Crowell (1931) as a means of representing the dissolution rate that is normalized for the decrease in solid surface area as a function of time [7]. Hixson-Crowell cube root law describes the release from systems where there is a change in surface area and diameter of particles. Provided there is no change in shape as a suspended solid dissolves, its surface area decreases as the two-thirds power of its weight. This relation has been used by Hixson and Crowell in the derivation of the cube root law. For corrosion inhibitor loaded nanocontainers consisting of uniformly sized particles, it is possible to derive an equation that expresses the weight of BTA remaining at time t. When sink conditions are applied, the cube root law can be written as:

$$W_0^{1/3} - W_t^{1/3} = \kappa t$$

where Wt denotes the remaining weight of BTA at time t, Wo is the initial weight of BTA at time $t = 0$, and 'κ' represents the rate constant.

5. Korsmeyer-Peppas Model

Korsmeyer et al (1983) derived a simple relationship that described corrosion inhibitor release from a nanocontainer [8]. Ritger and Peppas [9, 10] and Korsmeyer and Peppas [11] developed an empirical equation to analyze both Fickian and non-Fickian release of corrosion inhibitor from nanocontainers or coating matrix.
To find out the mechanism of corrosion inhibitor release, the first 60% corrosion inhibitor release data was fitted in Korsmeyer-Peppas model.

$$Mt / M_\infty = Kt^n$$

where Mt / M_∞ is the fraction of corrosion inhibitor released at time t, k is the rate constant (having units of t^n) incorporating structural and geometric characteristics of the delivery system, and n is the release exponent indicative of the mechanism of transport of corrosion inhibitor through the sol-gel matrix. The *n* value is used to characterize different release mechanisms [12]. To find out the exponent *n*, the portion of the release curve Mt / M_∞

< 0.6 should only be used. The model is plotted as log cumulative percentage corrosion inhibitor release *versus* log time [13].

5.3.3. Release rate kinetics using different fitting models

The BTA release data obtained at different pH for the total time duration studied were fitted using different kinetic models. Initially, Zero-order model was chosen to fit all the data obtained at different pH. Figure 5.2 (a-c) shows the release profiles of BTA from HNT at pH 3, 7 and 10. For pH 3 and 7, the regression coefficient or goodness of fit was in the range of 0.62 to 0.66, as tabulated in Table 5.1. For pH 10, the R^2 value is above 0.93, but the linear fit was not good enough to conclude that the zero-order kinetic model fits well for pH 10. Hence, one single model cannot fit the entire data to give a specific conclusion regarding which kinetic model best suits the BTA released. Therefore, to fit the data with more accuracy and make a meaningful interpretation, the fitting was carried out individually for two different time zones or two-stages, i.e., 0 to 60 minutes-first time zone (fast release stage) and 120 to 600 minutes-second time zone (slow release stage). Figure 5.2d shows schematic representation of the data divided into two-time zones.
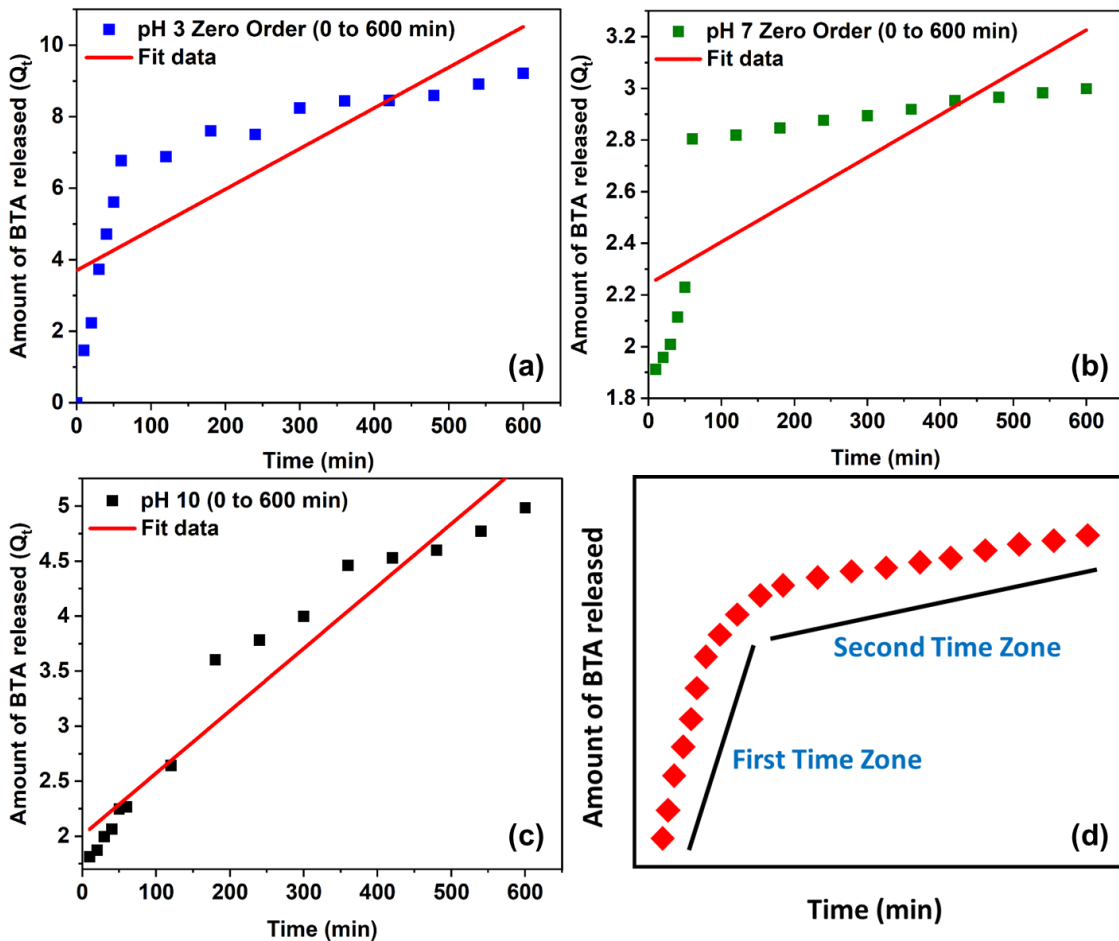
Fig. 5.2 (a-c) Zero-order model fitting for data obtained at pH 3, 7 and 10, respectively, and **(d)** a schematic representation showing that the data is divided into two time zones for fitting.

Table 5.1. Kinetic fit parameters obtained at different pH using zero-order model

pH	K_0 (mg/g.min)	R^2
3	0.0114	0.6629
7	0.0016	0.6238
10	0.0056	0.9384

Though the fitting was performed using all the kinetic models at all the three pH, the kinetic model that best fits the data is only shown in Fig. 5.3. Kinetic parameters obtained using Zero-order, First Order, Higuchi, Kormeyer-Peppas and Hixson-Crowell models are tabulated and shown in Table 5.2. It can be seen that up to 60 minutes at all pH values, the rate of BTA released was very fast, which can be inferred from the rate constant or the slope of each fit data. The slope tends to decrease for the second time zone i.e., 120 to 600 min. On close observation, it can be concluded that all the kinetic models fit well for entire time duration at all concentration as the regression coefficient values are more than 0.9 for all the cases. The experimental data fits the Zero-order and First-order efficiently as the regression coefficient approaches the linear fit condition ($R^2 \geq 0.96$) i.e., towards 1.
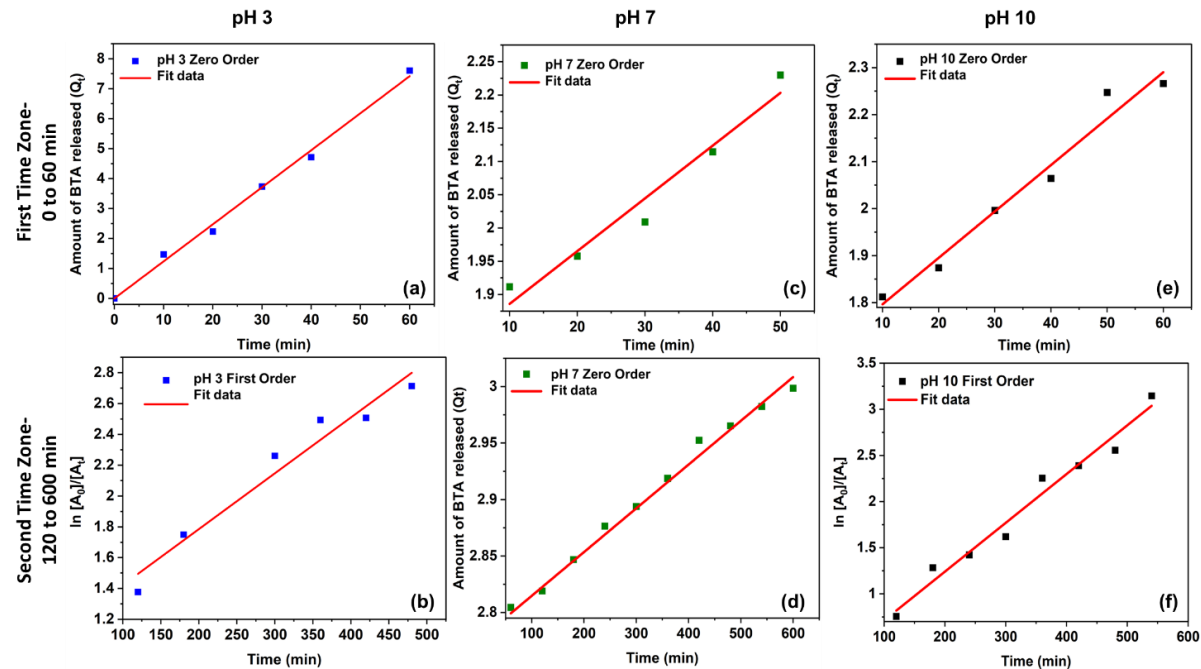
Fig. 5.3. Best fit graphs (a-b) zero order and first order at pH 3, (c-d) zero order at pH 7, and (d-e) zero and first order for pH 10

Table 5.2. Kinetic fit parameters obtained after fitting different mathematical models

pH	Zero Order		First Order		Higuchi model		Korsmeyer-Peppas Model			Hixson-Crowell Model	
	K_0 (mg/g.min)	R^2	K (min^{-1})	R^2	K_H (mg/g.min$^{1/2}$)	R^2	K_t (min^{-n})	N	R^2	K (mg$^{1/3}$/g$^{1/3}$ min)	R^2
3 (0 to 60 min)	0.1236	0.9980	0.0213	0.9723	0.8724	0.9305	0.02106	0.8760	0.9939	0.0119	0.9883
3 (120 to 600 min)	0.0043	0.9285	0.0036	0.9566	0.1578	0.9503	0.00116	0.8760	0.9359	0.0016	0.9426
7 (0 to 60 min)	0.0079	0.9576	0.0085	0.9384	0.0791	0.9027	1.2780	0.0667	0.9218	0.0027	0.9451
7 (120 to 600 min)	0.0038	0.9829	0.0042	0.9390	0.0124	0.9813				0.0007	0.9679
10 (0 to 60 min)	0.0098	0.9704	0.0033	0.9676	0.1074	0.9488	0.5540	0.157	0.9605	0.0014	0.9685
10 (120 to 600 min)	0.0033	0.9573	0.0052	0.9733	0.1541	0.9361				0.0015	0.9657

The rate of a zero-order reaction is unaffected by the reactant's concentration. According to the rate constant values, the corrosion inhibitor BTA exhibits a rapid release at the beginning of the experiment for zero-order kinetics, reaching its maximum release at pH 3, followed by pH 10 and pH 7. The regression coefficient value at pH 3 in the first time zone was maximum in the case of zero-order compared to all the other mathematical models. At the same pH, the data fits well with first order kinetics in the second time zone. At pH 7, for both time-zones, the data best fits using zero-order kinetics with R^2 values ranging from 0.95 to 0.98, which was the maximum among all the kinetic models. Fit data obtained for pH 10 was similar to pH 3 in the context of model fittings. For the first time zone, i.e., 0 to 60 min, the data best fits using zero-order, whereas, in the second time zone, the data best fits with first-order kinetics with R^2 value 0.97 in both cases.

BTA release from HNT was very fast at all pH during the first 30 minutes with maximum release in the case of pH 3 followed by pH 7 and 10. Here, the BTA release is independent of the concentration of the solution, whereas in the second time-zone for pH 3 and 10, the first-order kinetics is favourable, suggesting that the BTA release depends on the concentration of BTA in the surrounding environment. As the maximum amount of BTA is released in the first 30 minutes, the release rate constant was very high, but in the later time zone, the release rate values are very low. Hence, an extended release of BTA from HNT was observed for a maximum of up to 10 h duration.

Acid etching is the process by which the inner alumina layer tends to etch under extremely acidic conditions, increasing the specific surface area and maximising the loading efficiency of corrosion inhibitors [14]. Abdullayev et al. [15] found that the loading efficiency after acid etching increases 4 times compared to conventional encapsulation method. Manasa et al. [16] reported that the etched HNTs showed an increased pore volume than both inhibitor-loaded and as-received HNTs, indicating that the corrosion inhibitor was effectively encapsulated into the empty lumen of halloysite nanotubes. Adsul et al. [17] controlled the release of Ce^{3+}-Zr^{4+}, 2-mercaptobenzothiazole, and 8-hydroxyquinoline by using acid etching to increase the loading of corrosion inhibitors and polymeric microcapsules as end-capping agents for HNTs. During exposure to a highly acidic environment at pH 3, thinning of the inner alumina layer of halloysite nanotubes (as shown in Fig. 5.4) takes place, which could be one possible reason for the spontaneous release of BTA in acidic media. On exposure to an alkaline environment (as shown in Fig. 5.4), the thinning of halloysite nanotubes does occur, leading to

the degradation of the nanotube and forming flake-like structures. Hence, at both extremities during initial exposure at all pH, the change in morphological structure is the prime reason for the fast release of BTA, whereas the controlled and extended release was observed for a longer period of time thereafter [18-19]. The initial rate of dissolution of HNT at pH 3 and pH 10 is due to pseudo-first order kinetics as per White et al., which is in agreement with our fit data [19]. As per the release rate experiments, an optimum amount of BTA is required to initiate the corrosion inhibition process. Based on the literature, it is clear that at acidic pH 3, the excessive leaching of BTA from halloysite nanotubes takes place, causing it to be consumed very fast, but at pH 7, the BTA release has attained a saturation state, where the released BTA concentration is not sufficient to inhibit the corrosion process. At pH 7, the H^+ and OH^- ions are in equilibrium, which means that there is less chance of any trigger for BTA to release from HNT and thus a saturation state is attained after a certain duration. In the case of alkaline pH, the BTA released may be fast compared to pH 7, but to obtain the best corrosion inhibition efficiency, the BTA release at this pH was regarded as optimum.

BTA loaded into HNT dispersed 3.5 wt% NaCl at different pH

Dissolution of HNT caused burst release of BTA at extreme pH conditions

Thinning of inner tube diameter due to acid etching

Flake formation occurs due hydroxylation
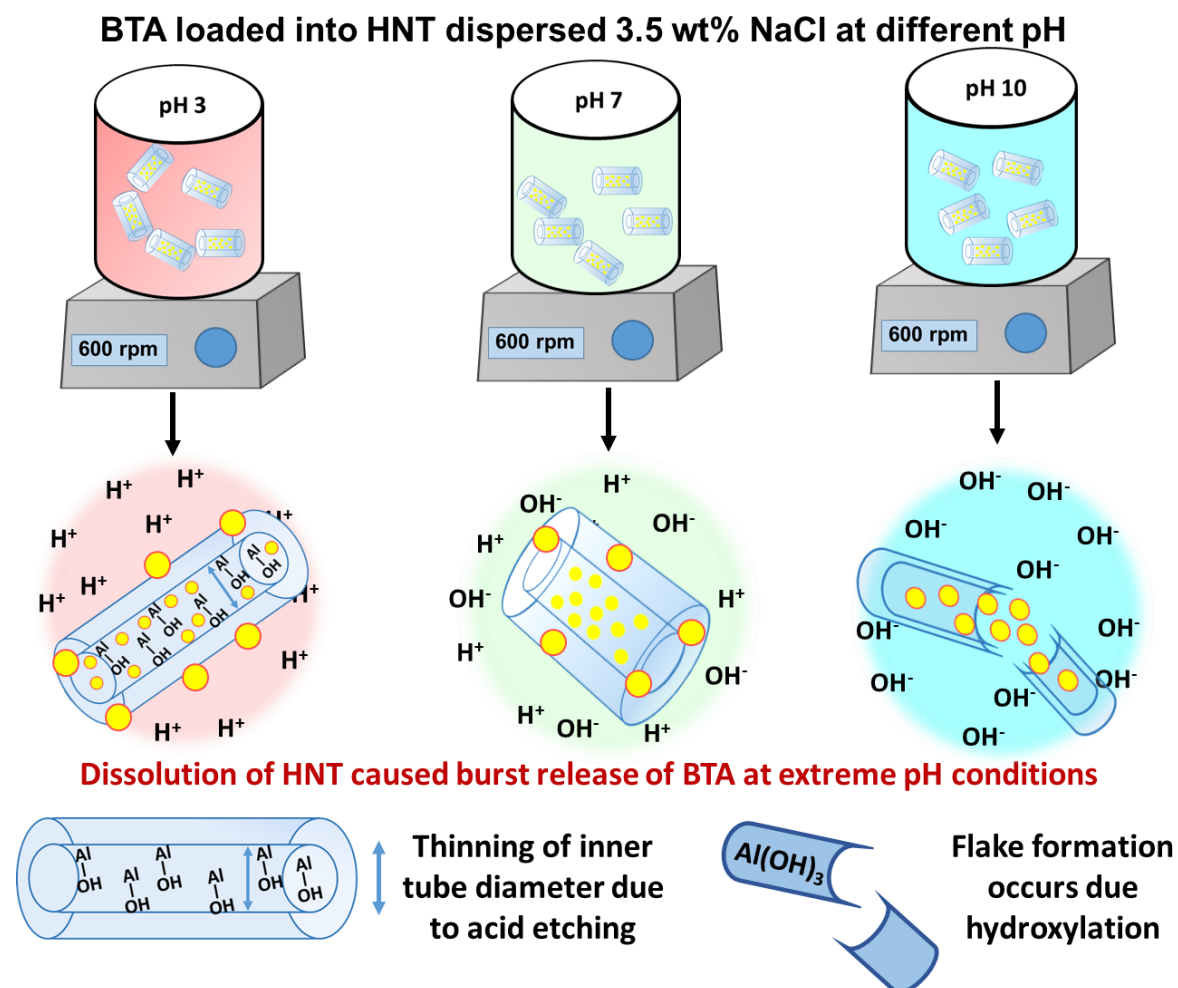
Fig. 5.4. Schematic representation of benzotriazole release from halloysite nanotubes at different concentrations.

Higuchi model is generally used to describe the sustained release from a semi-solid or solid matrix. The fitting degree in the extreme conditions for the first time zone, i.e., acidic or alkaline medium, was not very high, which could be due to the morphological changes in the nanocontainer leading to a sudden outburst of corrosion inhibitor at initial stages [20]. In the second time-zone, the R^2 values tend to increase and approach linearity with a decrease in rate constant values, confirming the sustained release of BTA. The Korsmeyer-Peppas model fits well for acidic pH and displays excellent fit data, but the regression coefficient at pH 7 was very poor with rate constant value increasing up to 1.2780 min^{-n}. For pH 10, the regression coefficient value was 0.9605, but the rate constant value was too high for a favourable reaction to occur, suggesting that this model was best suited for acidic pH rather than neutral or alkaline pH and hence, was ruled out for this experimental analysis.

On comparison of the actual data with mathematical models, it was concluded that the corrosion inhibitor works efficiently in the wide spectrum starting from pH 3 to highly alkaline pH 10 with excellent performance at alkaline pH. The salt immersion test was also performed to examine the coating behaviour at different pH to confirm the self-healing behaviour in the later section.

5.3.4. Salt immersion test (SIT)

The bare and BHS coated mild steel substrates were immersed in 3.5 wt% NaCl solution at pH 3, 7 and 10 for different time durations. At different time intervals, the samples were withdrawn and examined under an optical microscope to carefully analyse the rate of corrosion. Optical images as shown in Fig. 5.5 confirmed that at all pH, the bare mild steel sample corroded extensively, whereas for BHS coated MS substrates, at pH 10 the surface near to the scribe area is not affected much as compared to the other two pH i.e., 3 and 7.

The reason for better corrosion protection at pH 10 is attributed to the controlled and steady release of BTA from the halloysite nanotube, which is well in agreement with the percentage release data and also in alignment with the kinetic model fitting. Though at highly acidic and neutral condition, the corrosion inhibition property of BTA is evident, but the percentage release of BTA was very fast. In that case, the coating may be protected at the onset of corrosion by releasing maximum BTA at once. But to prolong the protection efficiency of

the BHS coating, the BTA should release in a sustained manner. The images below thus confirm that the BHS coating at pH 10 with an increase in exposure time shows enhanced self-healing as well as barrier properties when compared to coatings immersed in salt solution at pH 3 and 7.
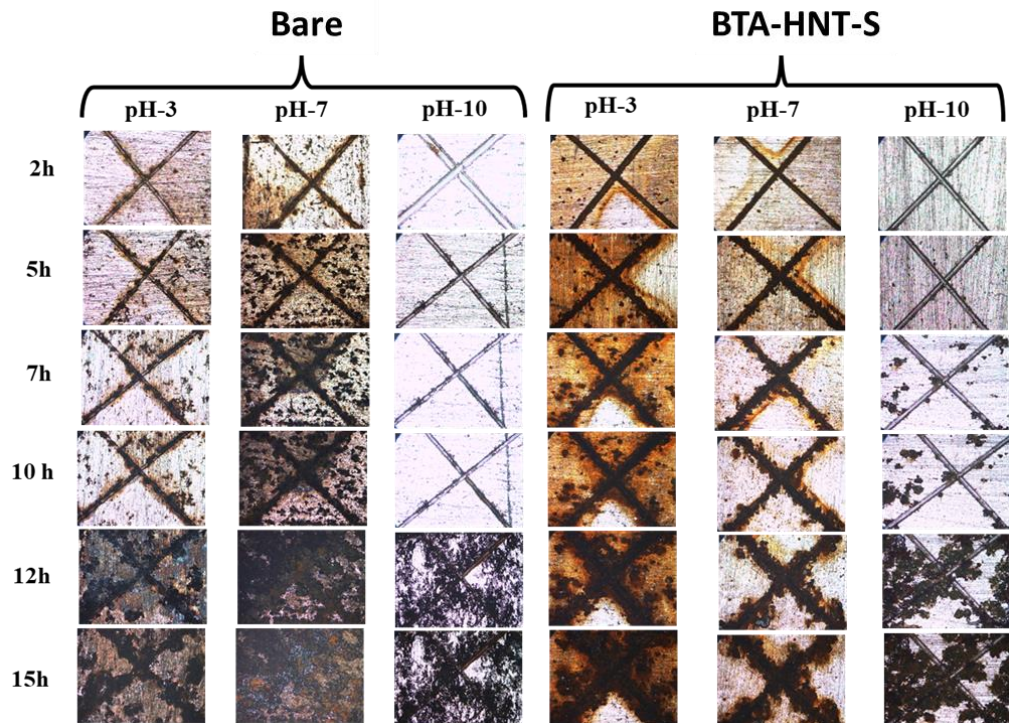
Fig. 5.5. Optical images of bare and BTA-HNT sol-coated mild steel substrates at pH (3, 7, 10) at different intervals of time

Similar results were obtained when bare mild steel substrates were exposed to 3.5 wt% NaCl solution containing BTA encapsulated HNT nanopowder at different pH i.e., 3, 7, and 10. From the SEM images (Fig. 5.6), it is evident that bare mild steel exposed at pH 3 shows more corrosion pits with larger surface area compared to pH 7 and 10.

From FESEM images, it is clear that BTA release works well at alkaline condition showing its maximum protection efficiency. For pH 3, it was expected that more amount of BTA being released will protect or passivate the mild steel surface, but the behaviour is quite opposite of that. More amount of BTA release will open the path for the corrosive species i.e., chloride ions to penetrate and form precipitate with the BTA thus causing more corrosion. At neutral condition, the samples are in equilibrium state, meaning that corrosion and self-healing action go hand in hand. For pH 10, the BTA released will protect the surface from corrosion and thus shows self-healing action. Therefore, the order of corrosion protection is pH 10 > pH 7 > pH 3.
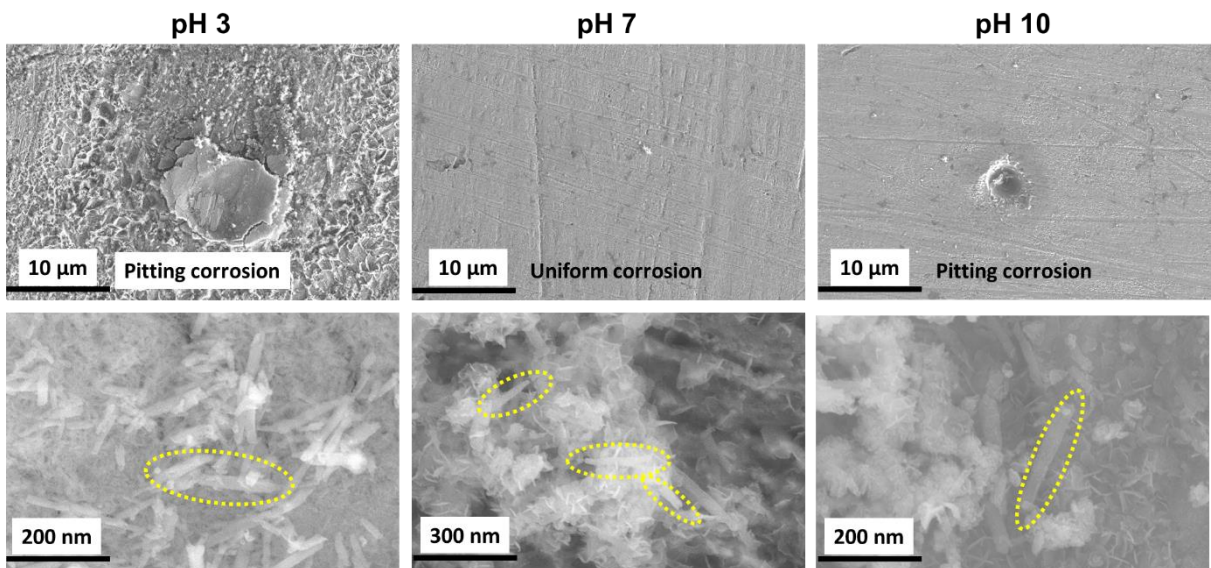
Fig. 5.6. FESEM images for bare mild steel after exposing to 3.5 wt% NaCl solution containing BTA encapsulated HNT nanopowder at different pH i.e., 3, 7, and 10

Comparison of salt spray test (SST) and salt immersion test (SIT) for same exposure time

Salt spray test as per ASTM B117 was carried out for bare, benzotrizaole directly added to the matrix (BS), and benzotriazole encapsulated into halloysite nanotube added to the matrix (BHS). After 10 h of salt spray exposure to 5 wt% NaCl, the BHS coating exhibited excellent corrosion protection with very less corrosion products on the surface, whereas, for BS coating, the corrosion products were visible in the scribe area as well as on the coated surface (fig. 5.6). Hence, it could be concluded that the loading of BTA provided prolonged active corrosion inhibition. The results of the salt immersion test for BHS coating at different pH for 10 h exposure are shown in Fig. 5.7. It is evident that at pH 3, the rate of corrosion is maximum which can be due to acidic corrosion or due to water caused by the abrupt benzotriazole release causing coating damage to permit entry of the corrosive species. The BHS coating at pH 3 in SIT behaves more or less similar to BS coating exposed to SST, which means that at pH 3, the burst release of BTA happens, which is similar to a direct addition of benzotriazole into the coating matrix or solution media (here in 3.5 wt% NaCl solution). Our earlier electrochemical experiments where direct addition of BTA either in the coating or corrosive medium showed

that the corrosion resistance was not substantially improved when compared to addition of BTA after encapsulation in a nanocontainer.
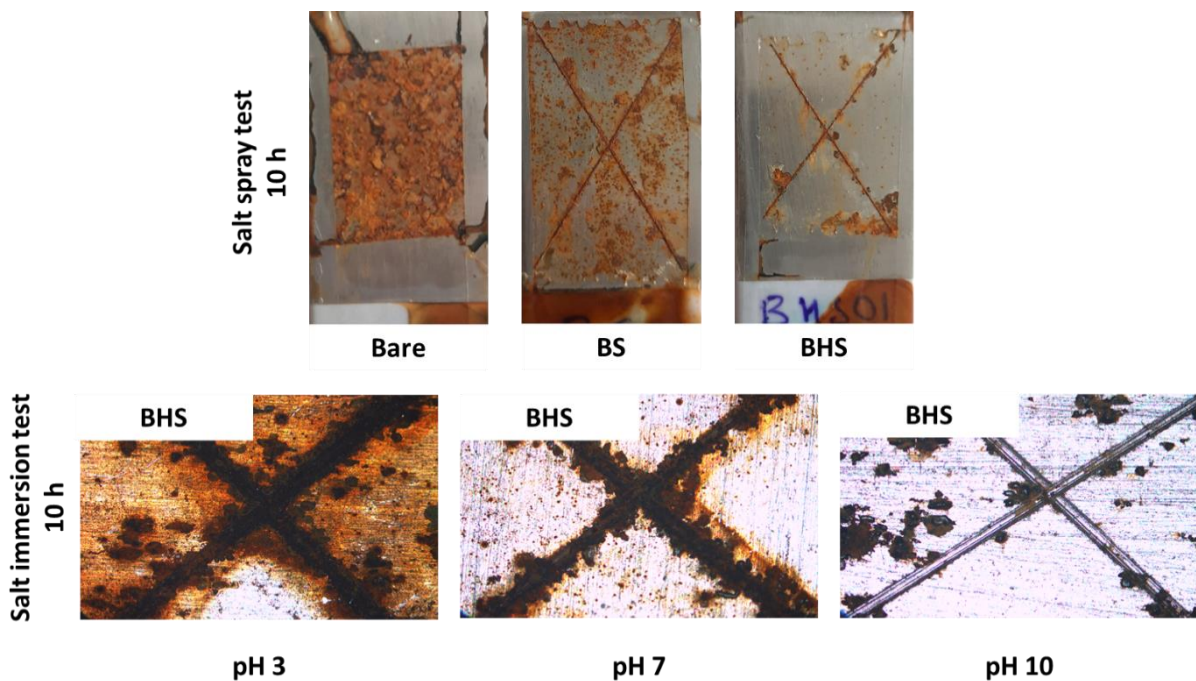
Fig. 5.7. Comparison of salt spray test images of direct addition of BTA into coating (BS) and BTA encapsulated into halloysite nanotube coating (BHS) with salt immersion test carried out for BHS coating at different pH

To compare the corrosion inhibition process, electrochemical studies were carried out for different coating types after immersing in neutral 3.5 wt% NaCl solution. Fig. 5.8 depicts the i_{corr} plot for bare and different coatings. The corrosion current density for BHS coating was lowest when compared to BS or only matrix-coated mild steel substrates. Thus, it can be inferred from SIT, SST, and electrochemical studies that, BTA must always be encapsulated into nanocontainers in order to have improved self-healing action and controlled, extended release to prevent excessive leaching.
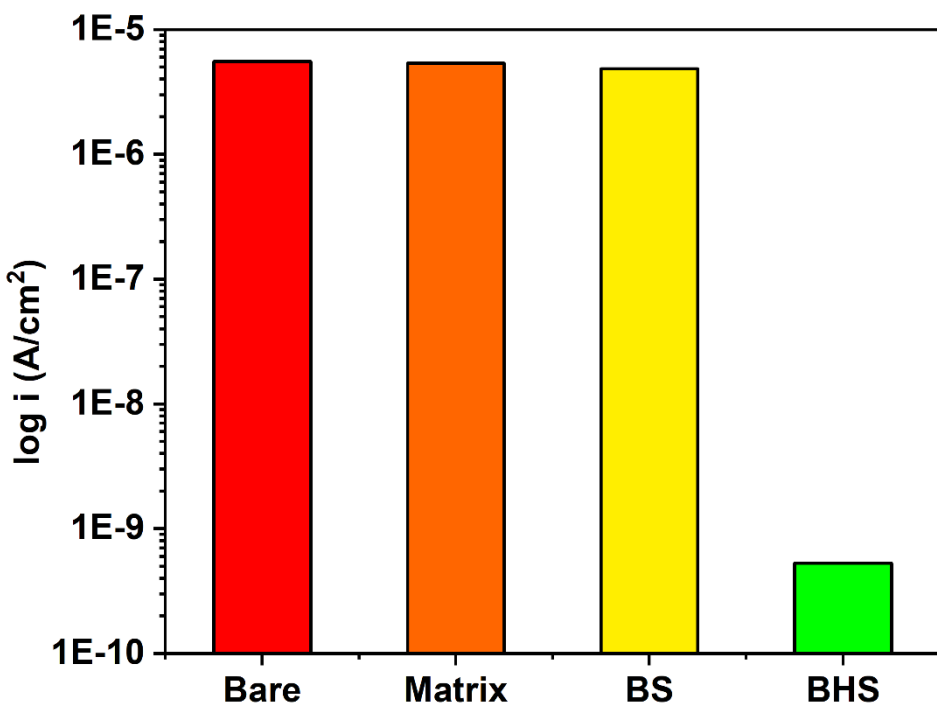
Fig. 5.8. Comparison of i_{corr} data for different coatings after exposure to neutral 3.5 wt% NaCl solution.

From the literature, it is reported that the cracks and water absorption affect the coating resistance and capacitance, because chloride ion makes its way to enter inside the coating through water as it is soluble in water. Higher water absorption by the coatings causes chloride ions to penetrate and partially damage the coating [21]. Therefore, more amount of BTA is released at pH 3 and 7 to repair the coating damage. With more release of BTA, the probability of freely available BTA after occupying the adsorbing site also increases. As a result, the coating takes in more water when the BTA concentration increases. This facilitates the entry of Cl⁻ ion into the coating, resulting in a poor anti-corrosion performance at pH 3 and 7. Therefore, the optimum condition for BTA to work efficiently is at pH 10, where the coating integrity, as well as the excessive leaching of BTA is controlled.

5.4. Conclusions

In this work, release rate tests demonstrated at different pH show different release behaviours. Within 0-60 min, higher amount of corrosion inhibitor (BTA) releases at pH 3.0 followed by pH 7 and 10. In all the cases, the percentage release in the second time zone was quite slow, with release rate constant values decreasing with a marginal difference. The order

of rate of inhibitor release within the first 60 min was pH 3 > pH 7 > pH 10. Zero-order and first-order kinetic models fit well with the actual data at all pH. Therefore, the corrosion inhibitor benzotriazole can potentially protect metal substrates against corrosion over a wide range of pH (3 to 10). The mild steel substrate coated with BHS exhibited better anti-corrosion performance than the bare substrate when exposed to 3.5 wt% NaCl solution at different pH. Moreover, the coatings showed an enhanced anti-corrosion ability when damaged by mechanical scratch, due to the instant release of BTA from BHS in the scratched area. Enhanced self-healing behaviour was observed at alkaline pH when compared to pH 3 and 7 due to the controlled release of BTA, which helps in achieving anti-corrosion properties for an extended duration.

5.5. References:

[1] Berden, G., Jalviste, E., Meerts, W. L., Rotationally resolved UV spectroscopy of the 2H-tautomer of benzotriazole in a molecular beam, 226 (1994) 305–309.

[2] Borin, A. C., Serrano-Andres, L., Ludwig, V., Canuto, S., Theoretical absorption and emission spectra of 1H- and 2H-benzotriazole, Phys. Chem. Chem. Phys. 5 (2003) 5001.

[3] Varles, C. G., Dixon, D. G., Steiner, C., Zero-order release from biphasic polymer hydrogels, J. Cont. Rel. 34 (1995) 185- 192.

[4] Suvakanta, D., Murthy, P.N., Lilakanta, N., Prasanta, C., Kinetic modelling on drug release from controlled drug delivery systems, Acta Pol. Pharm. 67 (2010) 217-223.

[5] Higuchi, T., Mechanism of sustained action medication: Theoretical analysis of rate of release of solid drugs dispersed in solid matrices, J. Pharm. Sci. 52, (1963) 1145-1149.

[6] Costa, P., Ferreira, D. C., Sousa Lobo, J. M., In vitro evaluation of the lioequivalence of pharmaceutical formulations, Rev. Port. Farm. 46 (1996) 4-8.

[7] Hixson, A. W., Crowell, J. H., Dependence of reaction velocity upon surface and agitation (I) theoretical consideration, Ind. Eng. Chem. 23 (1931) 923-931.

[8] Korsmeyer, R. W., Gurny, R., Doelker, E., Buri, P., Peppas, N. A., Mechanisms of solute release from porous hydrophilic polymers, Int. J. Pharm. 15 (1983) 25-35.

[9] Ritger, P. L., Peppas, N. A., A simple equation for description of solute release 1. Fickian and non-fickian release from non-swellable devices in the form of slabs, spheres, cylinders or discs, J. Cont. Rel. 5 (1987) 23-36.

[10] Ritger, P. L., Peppas, N. A., A simple equation for description of solute release II. Fickian and anomalous release from swellable devices, J. Cont. Rel. 5 (1987) 37-42.

[11] Korsmeyer, R. W., Peppas, N. A., Solute and penetrant diffusion in swellable polymers. III. Drug release from glassy poly(HEMA-co-NVP) copolymers, J. Cont. rel. 1 (1984) 89-98.

[12] Peppas, N. A., Sahlin, J. J., A simple equation for the description of solute release. III. Coupling of diffusion and relaxation, Int. J. Pharm. 57 (1989) 169-172.

[13] Singh, J., Gupta, S., Kaur, H., Prediction of in vitro drug release mechanisms form extended release matrix tablets using SSR/R2 technique, Trends in App. Sci. Res. 6 (2011) 400 – 409.

[14] Setter, O. P., Dahan, L., Hamad, H. A., Segal, E., Acid-etched halloysite nanotubes as superior carriers for ciprofloxacin, Appl. Clay Sci. 228 (2022) 106629

[15] Abdullayev, E., Joshi, A., Wei, W., Zhao, Y., Lvov, Y., Enlargement of halloysite clay nanotube lumen by selective etching of aluminum oxide, ACS Nano. 6 (2012) 7216–7226.

[16] Manasa, S., Jyothirmayi, A., Siva, T., Sarada, B. V., Ramakrishna, M., Sathiyanarayanan, s., Gobi, K. V., Subasri, R., Nanoclay-based self-healing, corrosion protection coatings on aluminum, A356.0 and AZ91 substrates, J. Coat. Technol. Res. 14 (2017) 1195-1208.

[17] Adsul, S. H., Bagale, U. D., Sonawane, S. H., Subasri, R., Release rate kinetics of corrosion inhibitor loaded halloysite nanotube-based anticorrosion coatings on magnesium alloy AZ91D, J. Magnes. Alloy. 9 (2021) 202-215.

[18] Singh, A. P., Siddiqui, J., Diosady, L. L., Characterizing the pH-dependent release kinetics of food-grade spray drying encapsulated iron microcapsules for food fortification, Food Bioproc. Tech. 11 (2018) 435-446.

[19] White, R. D., Bavykin, D. V., Walsh, F. C., The stability of halloysite nanotubes in acidic and alkaline aqueous suspensions, Nanotechnol. 23 (2012) 065705.

[20] Du, P., Wang, J., Zhao, H., Liu, G., Wang, L., Graphene oxide encapsulated by mesoporous silica for intelligent anticorrosive coating: studies on release models and self-healing ability, Dalton Trans. 48 (2019) 13064.

[21] Sharifiyan, M. S., Sanaghi, A., Moradi, H., Chu, P. K., Effects of high concentration of benzotriazole on corrosion behavior of nanostructured titania-alumina composite coating deposited on Al 2024 by sol-gel method, Surf. Coat. Technol. 321 (2017) 36-44.

CHAPTER-6

Effect of Transition metal and Different Rare-Earth Inhibitors-based Sol-gel Coatings on Corrosion Protection of Mild Steel

CHAPTER 6

Effect of Transition metal and Different Rare-Earth Inhibitors-based Sol-gel Coatings on Corrosion Protection of Mild Steel

6.1. Introduction

In the previous chapters, organic corrosion inhibitor, BTA, was studied extensively for its corrosion protection and self-healing action. The release rate experiments were also carried out to confirm the percentage release of BTA from halloysite nanotubes. In this chapter, corrosion protection efficiency of inorganic corrosion inhibitors i.e., rare-earth and transition metal based corrosion inhibitors is studied broadly. So far, there are no reports on the use of the wide range of RE as well as a comparison of their protection efficiency among themselves and with the transition metal-based corrosion inhibitor, Zr^{4+}. In addition, due to the emerging importance of self-healing coatings based on encapsulating inhibitors into nanocontainers, effects of the direct addition and the encapsulation into HNT and LbL nanocontainers followed by homogenizing in the sol-gel matrix were investigated. Hence, in the current study, we have loaded different inorganic corrosion inhibitors such as Zr^{4+}, La^{3+}, Ce^{3+}, Er^{3+} and Gd^{3+} into nanocontainers and compared the corrosion protection efficiency of coatings based on direct addition and encapsulated inhibitors into the matrix sol using various electrochemical and spectroscopic techniques.

6.1.1. Coating deposition and nomenclature of different sols coated on mild steel substrates

The synthesized matrix sol was used to prepare various sols containing different corrosion inhibitors (Zr^{4+}, Ce^{3+}, La^{3+}, Gd^{3+}, and Er^{3+}). For this, 2 wt% of each corrosion inhibitor was added into 25 g of matrix sol individually. For the study of encapsulation, 2.17 g of the above-mentioned corrosion inhibitors were individually encapsulated into HNTs. For encapsulation into LbL NCs, 0.0167 moles of Zr^{4+}, Ce^{3+}, and La^{3+} was added individually to 100 ml of DI water followed by sandwiching the inhibitor layer in between the polyelectrolyte layers as discussed in Chapter-2. Subsequently 2 wt % loaded NCs were mixed into matrix sol and coated on mild steel substrates. Table 6.1.

Table 6.1. Nomenclature of different sols used for coating MS substrates with their description

S. No.	Description of Sol	Sample ID
1.	Matrix sol	**Mat**
2.	2 wt% Zr^{4+}, Ce^{3+}, La^{3+}, Gd^{3+} and Er^{3+} individually added to matrix sol	**ZS, CS, LS, GS, and ES**
3.	2 wt% Zr^{4+}, Ce^{3+}, La^{3+}, Gd^{3+}, and Er^{3+}- encapsulated into HNT and added individually to matrix sol	**ZHS, CHS, LHS, GHS, and EHS**
4.	2 wt% Zr^{4+}, Ce^{3+}, and La^{3+} -encapsulated into LbL NC and added individually to matrix sol	**Zr-LbL, Ce-LbL, and La-LbL**

6.2. Results and discussion

6.2.1. Characterization of inhibitor loaded nanocontainers

6.2.1.1 FESEM/EDS analysis:

(a) Corrosion inhibitor encapsulated into halloysite nanotubes

Surface morphology of the as-procured HNT and inhibitor loaded HNT was confirmed from SEM analysis. Elemental mapping of bare HNT and modified HNT confirmed the presence of Al, Si, O and respective elements of each corrosion inhibitor, thereby confirming the encapsulation of corrosion inhibitor into HNTs. Figure 6.1 (a) corresponds to bare HNT, where the morphology of HNT appears to be tubular and cylindrical. Figure 6.1 (b-e) corresponds to different corrosion inhibitors encapsulated into HNT along with their EDS spectra.

Figure 6.2 corresponds to the TEM images obtained for as-received HNTs, Er^{3+}-HNT, Ce^{3+}-HNT and Zr^{4+}-HNT. The morphological changes were further confirmed by TEM images. The TEM image of bare HNT (Fig. 6.2a) reveals a transparent hollow structure in the middle of the nanotubes, confirming the presence of an empty lumen. The halloysite nanotube length ranged from 0.5 to 1.0 µm, while its internal diameter varied between 15 and 20 nm. As observed from Fig. 6.2 (b-c), the morphology of HNT remained intact even after loading different corrosion inhibitors. However, the lumen seems to be dense with some depositions,

indicating that the corrosion inhibitors were successfully encapsulated into the HNTs empty lumen. Elemental mapping confirmed the presence of corrosion inhibitors into HNTs.
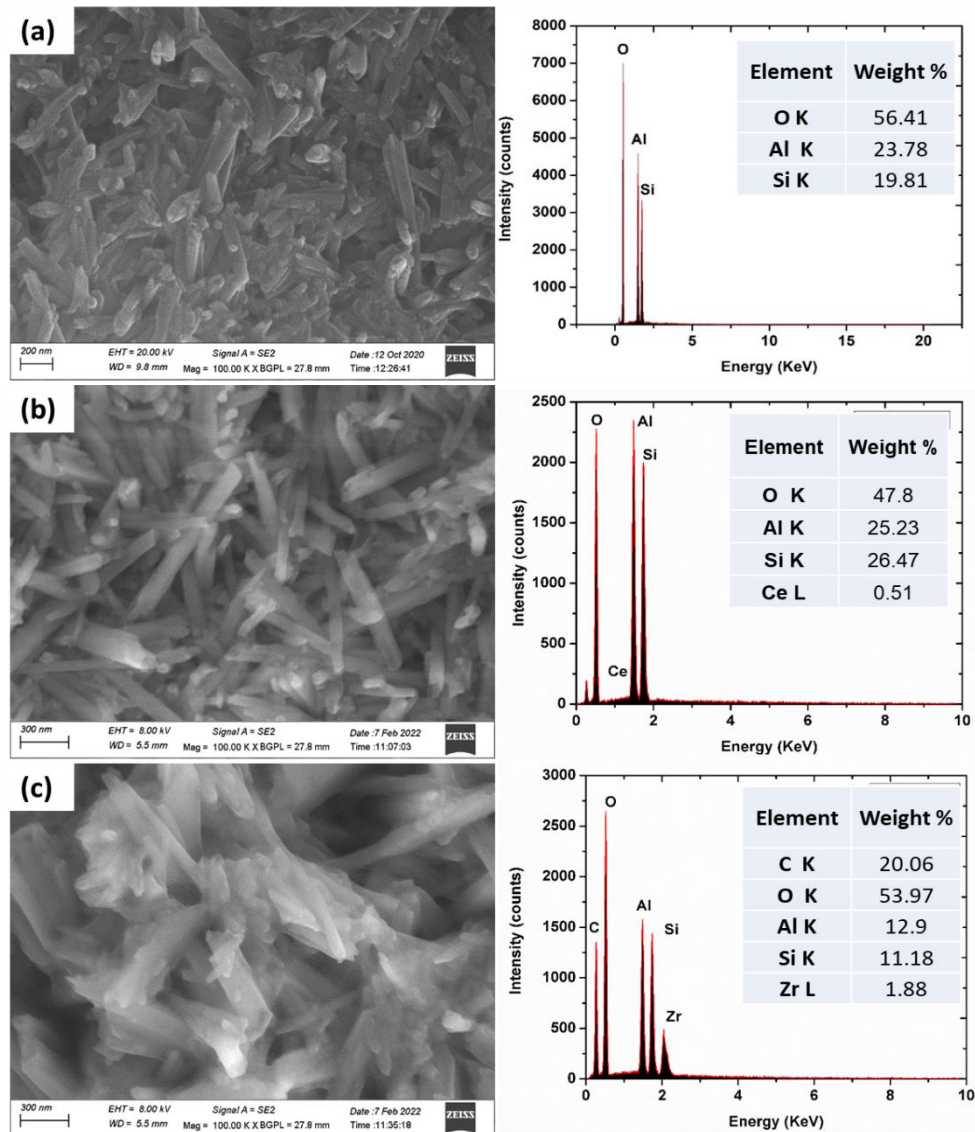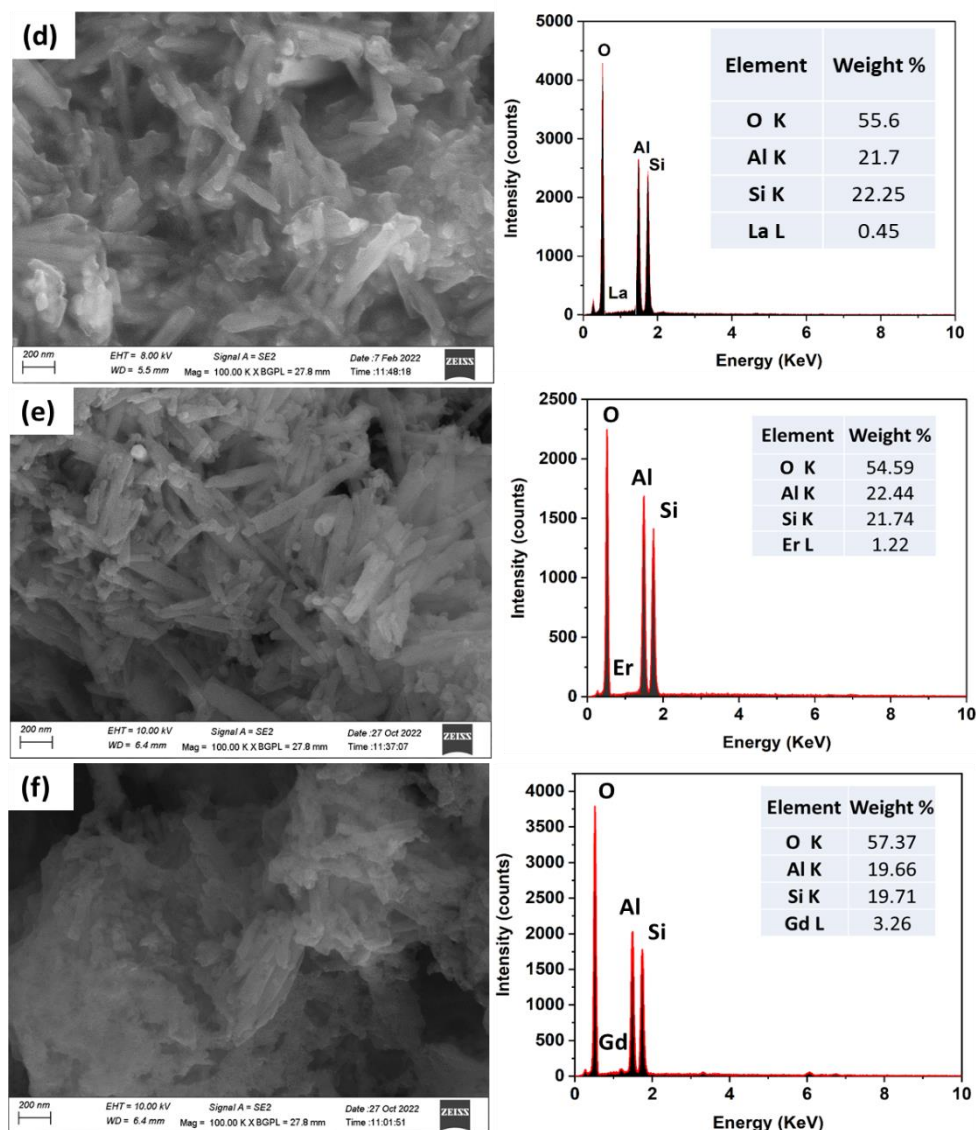
Fig. 6.1. Surface morphology and EDS analysis of (a) as-received halloysite nanotubes (HNT) powder, (b) Ce^{3+} loaded, (c) Zr^{4+} loaded, (d) La^{3+} loaded, (e) Er^{3+} loaded, and (f) Gd^{3+} loaded HNT powders
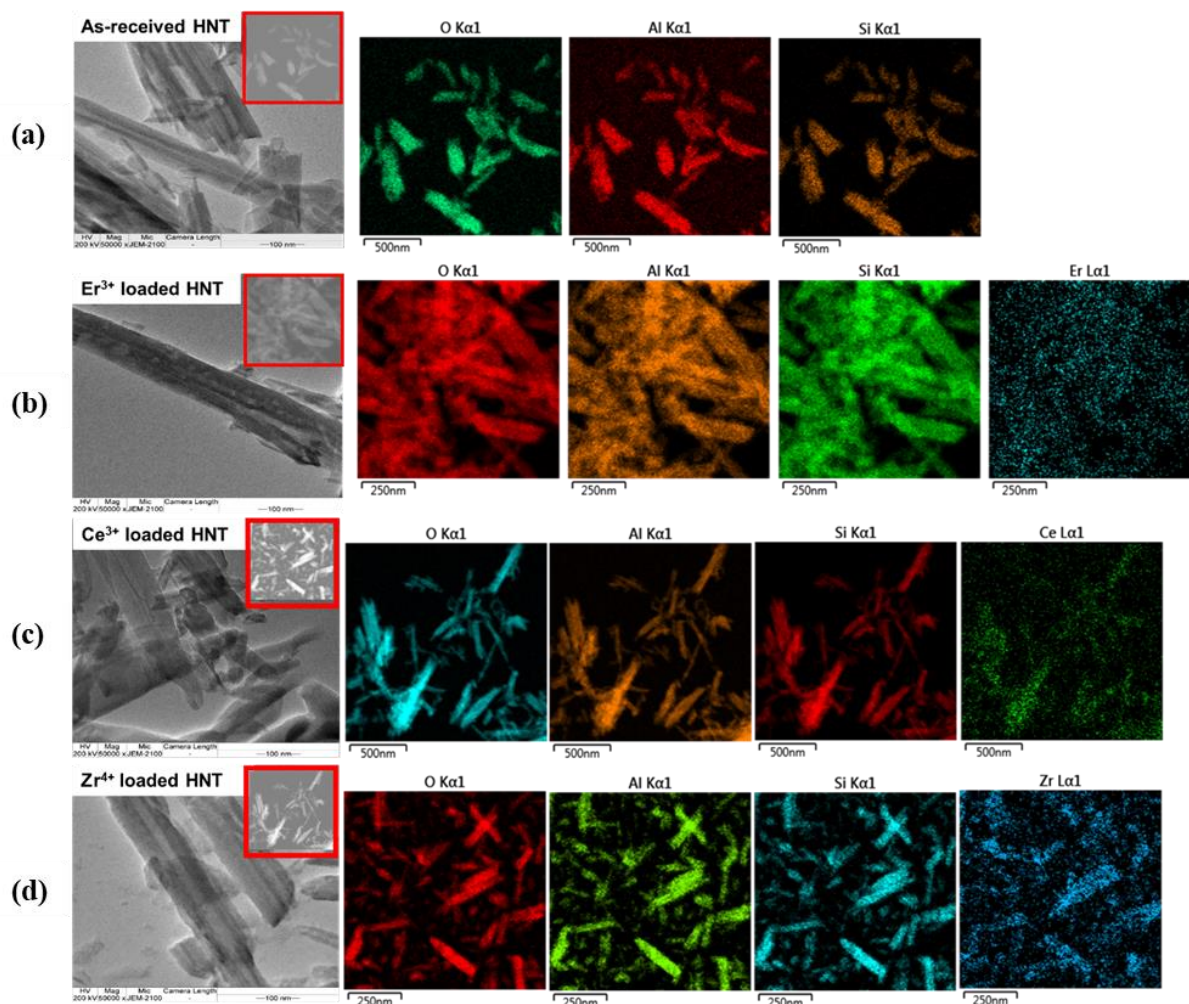
Fig. 6.2. TEM images for (a) as-received halloysite nanotube (HNT) powder, (b) Er^{3+} loaded, (c) Ce^{3+} loaded, and (d) Zr^{4+} loaded HNT powders

(b) Corrosion inhibitor encapsulated into layer-by-layer (LbL) nanocontainers (NC)

Figure 6.3(a) shows the SEM image of Fe_2O_3 nanoparticles (NPs), in which the particles appear to be around 100-300 nm in size, and the shape of the particles is rhombohedral. Figure 6.3(b-d) shows the SEM images of LbL NC powder with Ce^{3+}, La^{3+} and Zr^{4+} as the corrosion inhibitors, respectively, at the magnification of 150 KX. After the deposition of polyelectrolyte layers and corrosion inhibitor layers onto Fe_2O_3 NPs, the shape and size of the crystal have not changed significantly. In the case of Zr-LbL, particles are covered with a very thin film, which can be due to the reaction of Zr^{4+} with the polyelectrolyte layers. After modification, the particles appear to be more porous in nature rather than crystalline. To confirm the deposition of each constituent layer, elemental analysis was carried out. For Fe_2O_3 NPs, the presence of Fe and O was eminent; for only LbL, the major elements were C, O and Fe. For other inhibitor

loaded LbL NCs, the constituent corrosion inhibitor, i.e., Ce^{3+}, La^{3+} and Zr^{4+}, was present in the Ce-LbL, La-LbL and Zr-LbL NCs, respectively.
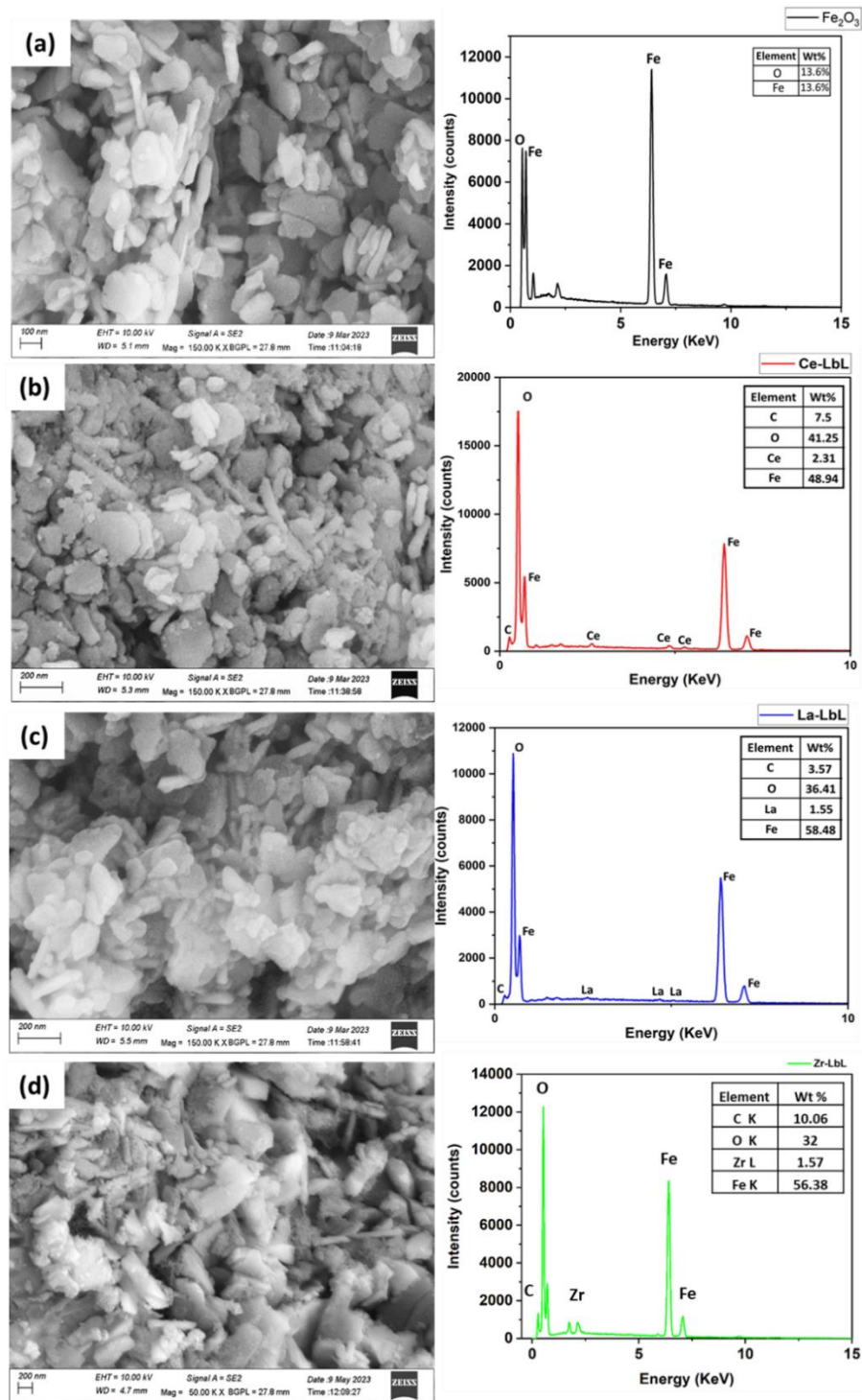
Fig. 6.3. Surface morphology and EDS analysis of (a) as-synthesized layer-by-layer (LbL) nanocontainers, (b) Ce-LbL, (c) La-LbL, and (d) Zr-LbL nanopowders

6.2.1.2. FTIR and BET analyses for HNTs and different corrosion inhibitors loaded HNTs:

FTIR spectra for bare HNT and inhibitor loaded HNTs are shown in Fig. 6.4. The spectra of all the inhibitor-modified HNTs show a similar pattern as that of bare HNT. The characteristic peaks at 3695, 3618, 1637, 907, 792, 678, and 536 cm^{-1} can be assigned to O-H stretching of inner surface hydroxyl groups, O-H stretching of inner hydroxyl groups, O-H bending of water, O-H deformation of inner hydroxyl groups, symmetric Si-O stretching, perpendicular Si-O stretching and Al-O-Si bending, respectively [1]. The peak at 1300 cm^{-1} is due to the bidentate nitrate present in RE(NO$_3$)$_3$ [2]. The evolved band at 1550 cm^{-1} is due to the bonding between the carbonyl group of MAA and Zr-O [3]. Comprehensively, FTIR analysis confirms the loading of corrosion inhibitors into the empty lumen of HNT.
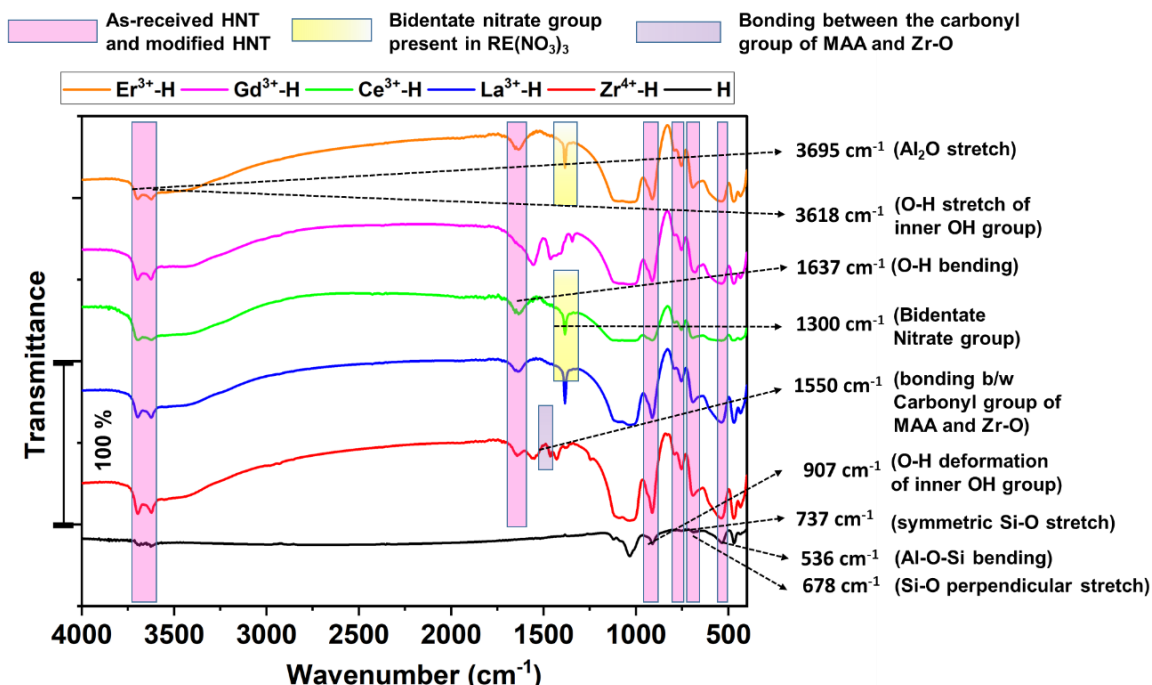
Fig. 6.4. FTIR spectra of as-received HNT (denoted as H) and modified inhibitor loaded HNTs (M^{3+}/M^{4+}-H)

BET analysis also confirmed the loading of corrosion inhibitors into HNTs as the pore volume decreases for inhibitor loaded HNTs when compared to as-received HNTs, **HNT-** 0.38 cc/g, **Zr-HNT-** 0.27 cc/g, **Ce-HNT-** 0.28 cc/g, and **Er-HNT-** 0.31 cc/g.

6.2.1.3. XRD analysis:

(a) Corrosion inhibitor encapsulated into halloysite nanotubes

Figure 6.5 depicts the XRD patterns of bare HNT and inhibitor-loaded HNT powders. The XRD patterns for inhibitor-modified HNT are in good agreement with that of the as-received HNT. The diffraction peaks for bare HNT are obtained at 12°, 21°, 24°, 25°, 28°, 34° and 37°, which are assigned to (002), (111), (004), (202), (113), (020) and (022) diffractions, respectively. According to ICDD file no. 01-77-4776, the crystal structure of bare HNT was found to be monoclinic. The similar XRD pattern for all the inhibitor-loaded HNTs confirms that there is no change in the interlayer spacing between silica and alumina layers of HNT. However, the diffraction peaks of inhibitor-loaded HNTs are broad compared to those of HNTs. The reason behind the peak broadening is due to the loading of corrosion inhibitors inside the HNT lumen. Full-width at half-maximum (FWHM) values for the prominent and symmetric basal peak at 12° are shown in Table 6.1. It may be noted that the FWHM values are higher for inhibitor-loaded HNTs when compared to as-received HNT, confirming the loading inside the nanotube instead of intercalating in between the layers [4].
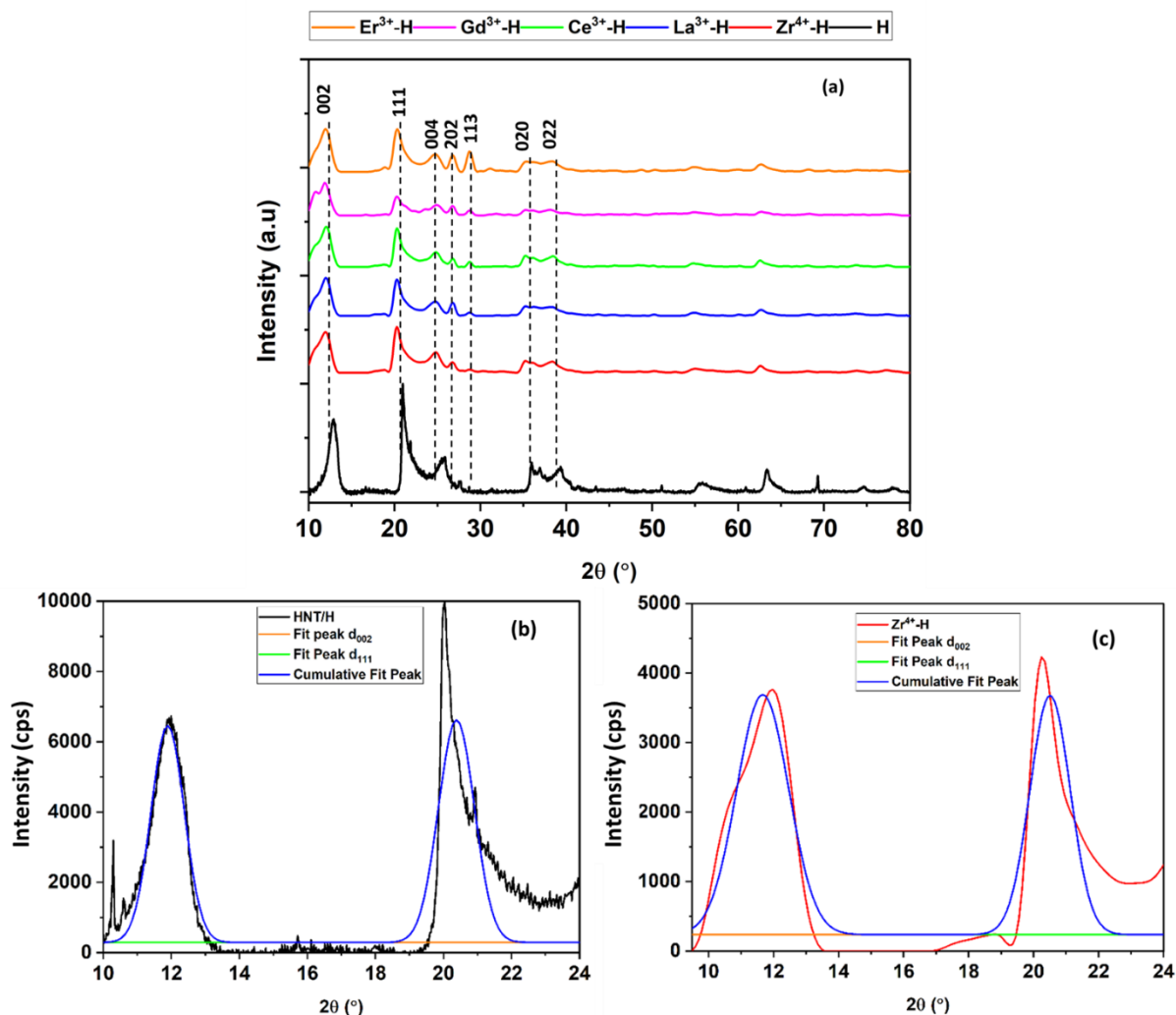
Fig. 6.5. (a) XRD patterns for as-received halloysite nanotubes (HNT) and different inhibitor-loaded HNTs; Normalized XRD peaks of d_{002} and d_{111} planes of (b) as-received and (c) inhibitor loaded halloysite nanotubes for the calculation of FWHM values

Crystallite size of materials could be determined using XRD. XRD patterns widened when the size of the crystallites decreased and was in the range of ≤100 nm. The crystallite size could be determined using Debye-Scherrer equation.

$$D = 0.9\lambda/\beta \cos \theta$$

where D = Average size of the crystallite (in diameter)

λ = Wavelength of the monochromatic X-ray

β = Full width at half maximum FWHM (in radians)

θ = XRD angle

The prominent and symmetric peak observed at 12° for HNT and loaded HNTs was analyzed to determine the size of the crystallites.

Table 6.1 FWHM and crystallite size values of (002) peak of as-received and inhibitor-loaded HNTs

Sample Name	FWHM of (002) peak (deg)	Crystallite size (nm)
As received HNT (H)	1.127°	7.005
Zr^{4+}-H	1.836°	4.302
La^{3+}-H	1.854°	4.261
Ce^{3+}-H	1.700°	4.645
Gd^{3+}-H	1.928°	4.092
Er^{3+}-H	1.677°	4.709

XRD angle of (002) = 6°

It was observed clearly that the crystallite size of all the transition metal or rare earth element loaded HNT particles was in the range of 4.1 to 4.7 nm and was lower compared to that of free HNT (7.0 nm). This observation indicates that the loading of transition metal or rare earth elements seemed to influence and increase the dispersion of HNT particles substantially.

(b) Corrosion inhibitor encapsulated into layer-by-layer nanocontainers

Analyzing the XRD pattern of the synthesized Fe_2O_3 NPs (Fig. 6.6), the diffractions at 25˚, 32˚, 35˚, 41˚, 50˚, 55˚, 63˚ and 65˚ correspond to (012), (104), (110), (113), (024), (116), (214) and (300) hkl values, respectively, among which, the peak at 32˚ of the 2θ value is the most intense peak, which indicates that the crystal structure of α-Fe_2O_3 was rhombohedral, according to the International Centre for Diffraction Data (ICDD File no. 01-080-5409). Similarly, the XRD patterns of only LbL NC, LbL NC encapsulated with Ce^{3+}, La^{3+} and Zr^{4+} as corrosion inhibitor were analysed. The XRD patterns for all the LbL nanocontainers were similar to iron oxide nanoparticles, suggesting that the inhibitors are well compacted in between the layers during the synthesis process. After the deposition of polyelectrolyte layers onto α-Fe_2O_3, no new peak or any peak shift was observed, confirming that the inhibitors are in their amorphous state without forming any crystalline stable oxide during the synthesis.
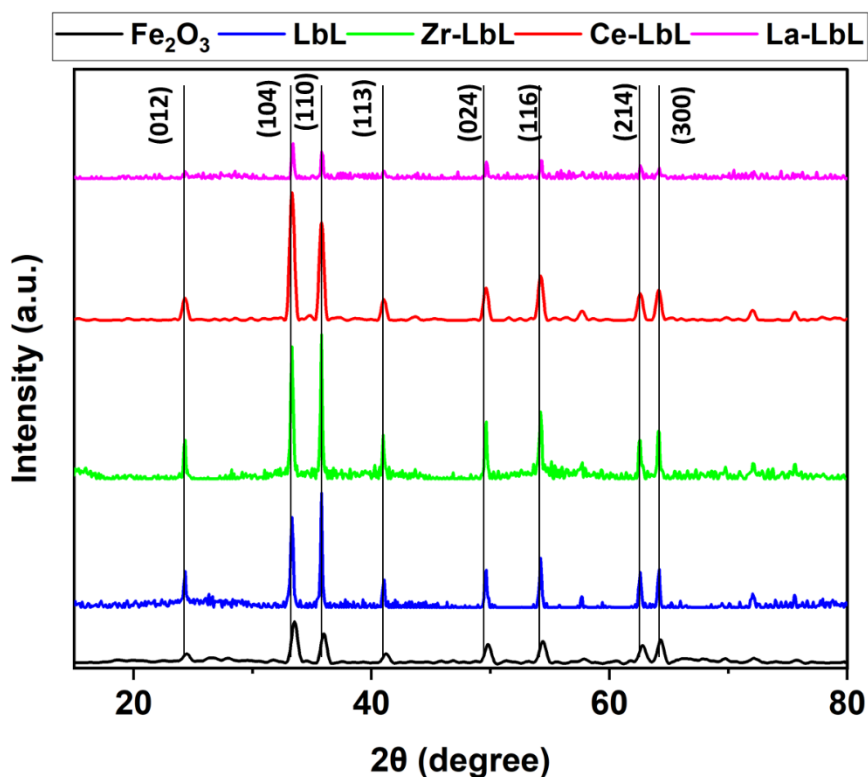
Fig. 6.6. XRD pattern of synthesized Fe_2O_3 nanoparticles, only-layer-by-layer nanocontainers (LbL), Ce-LbL, La-LbL and Zr-LbL

6.2.1.4. Zeta Potential Measurements

The zeta potential values of α-Fe_2O_3 nanoparticles at all layers were observed to be in the range of ±20 to ±40 mV, demonstrating their extreme stability, devoid of any agglomeration. The α-Fe_2O_3 nanoparticles were found to be positively charged, and this was confirmed by the electrophoretic mobility. The negative electrophoretic mobility for nanoparticles with a PAA layer indicated that the nanoparticles have a negative surface charge surrounding them, implying that the PAA layer was firmly deposited on the α-Fe_2O_3 nanoparticles. The addition of a second negatively charged layer of PAA helped to eliminate the corrosion inhibitor particles that were loosely bound. The electrophoretic mobility value somewhat decreased after the addition of a second PAA layer. The cationic polyelectrolyte layer of PDADMAC was used as the final outer layer of nanocontainers, and as a result, the electrophoretic mobility of the fabricated nanocontainers was found to be positive, as shown in Fig. 6.7. The solubility factor is prevalent in zeta potential measurements. When compared to Ce^{3+} and La^{3+}, the Zr^{4+} particles are less stable, as confirmed by the decrease in zeta potential and the electrophoretic mobility. Zr^{4+} is more likely to exist as free ions as a result of the decreased stability, which also causes poor solubility in the medium. Therefore, deposition of Zr^{4+}-layer onto the PAA shows poor adherence as seen in Fig. 6.7 (e and f). In order to confirm this, the viscosity of sols was evaluated with respect to time.
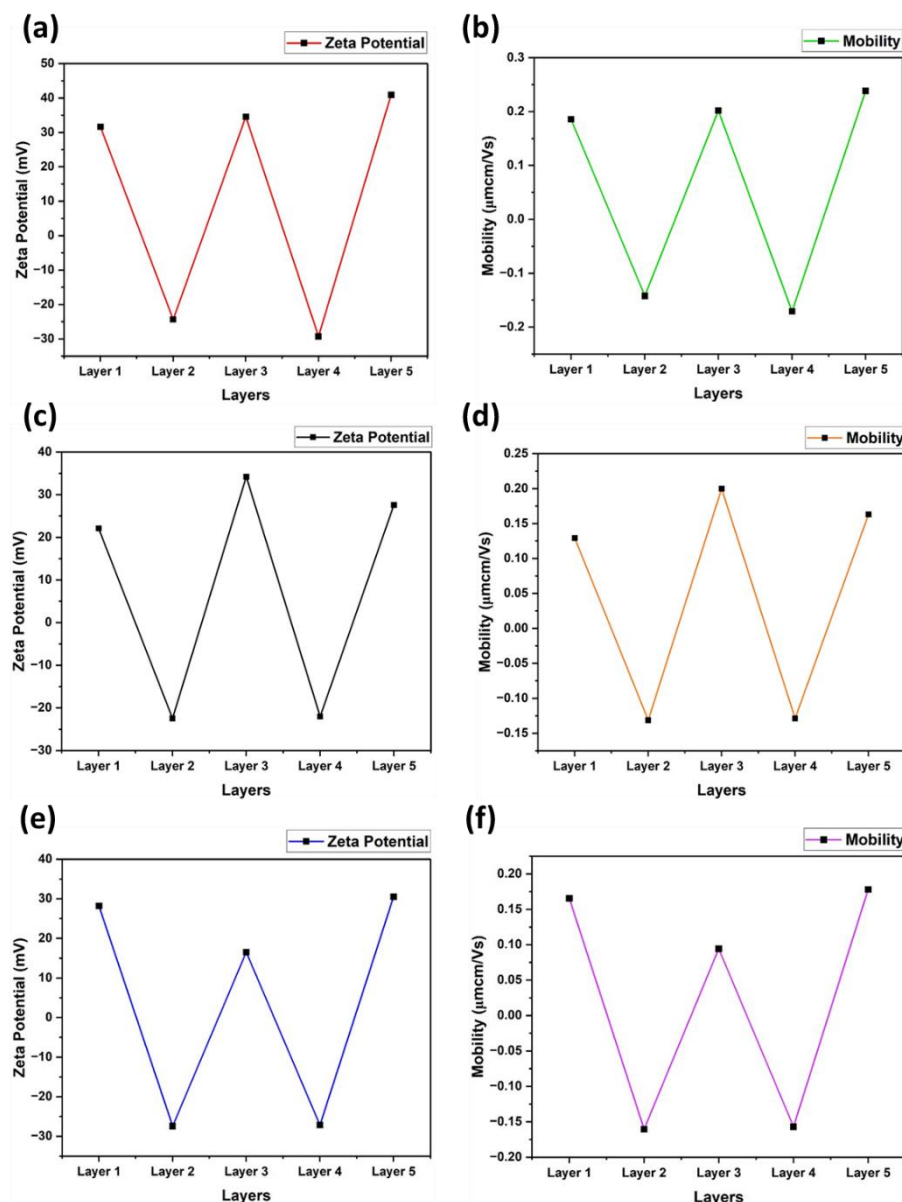
Fig. 6.7. Comparison of zeta potentials and electrophoretic mobilities of **(a, b)** Ce-LbL, **(c, d)** La-LbL and **(e, f)** Zr-LbL.

The zeta potential measurements confirmed that the surface charge of each deposited layer was in accordance with the charge of each layer and the particles are stable in nature. The observed results of zeta potential and electrophoretic mobility studies supported the stepwise deposition of polyelectrolyte layers and the fabrication of LbL nanocontainers [5].

6.2.2. Viscosity measurement of different sols

Viscosity of the sols that was prepared for the coatings on MS substrates was measured with respect to time. Metal-based precursors have high activity for epoxide ring opening of GPTMS. Addition of metal cations promotes the formation of more amorphous Si-O-Si network and thereby increases the organic crosslinking. The epoxide of GPTMS polymerizes into polyethylene oxide to form a polymer as shown in equation 1 [6].
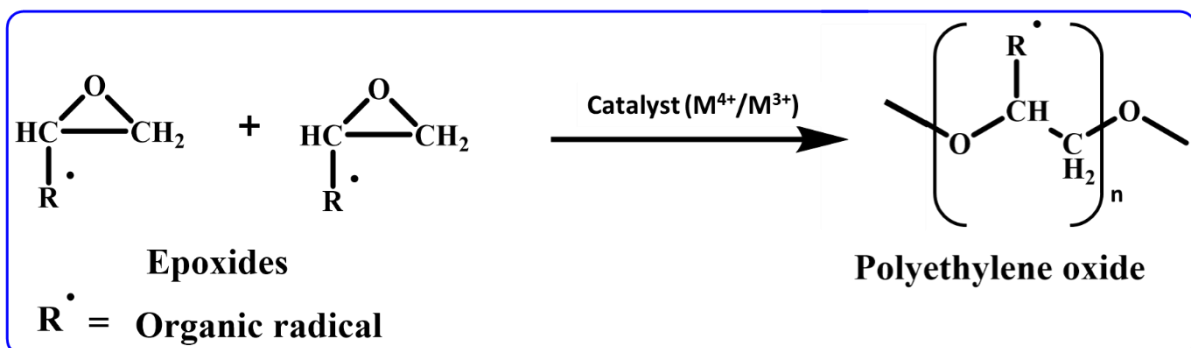
Equation 1: Ring opening of epoxide to form polyethylene oxide

Viscosity data for Zr^{4+}, La^{3+}, and Ce^{3+} either added directly or encapsulated into HNTs or LbL nanocontainers are shown in Fig. 6.8.
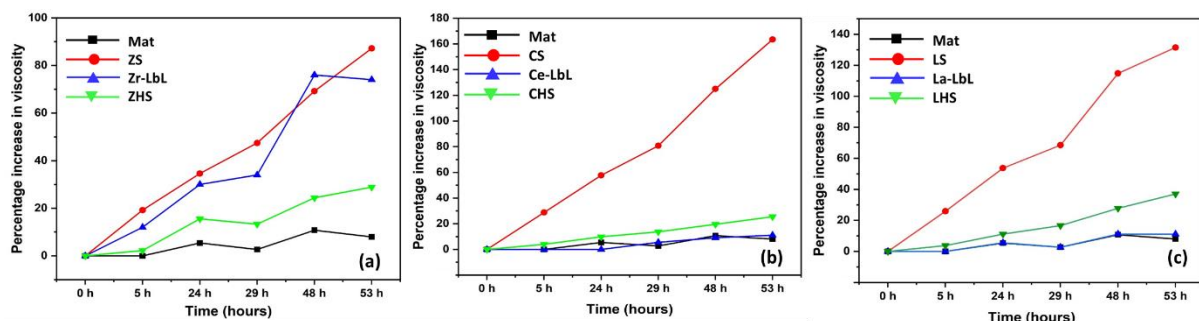
Fig. 6.8. Plots showing the change in viscosity of different sols synthesized with time; **(a)** Zr-based sols, **(b)** La-based sols, and **(c)** Ce-based sols

The graph is plotted between the change in viscosity (%) with respect to time. From zeta potential measurements, it was clear that among Zr^{4+}, Ce^{3+} and La^{3+}, Zr^{4+} ion shows less solubility and hence these ions are free to participate in the hydrolysis/condensation steps of sol-gel synthesis. The sol viscosity for Zr^{4+}, when directly added or sandwiched in between the LbL NCs, is nearly the same, confirming that the Zr^{4+} ions are readily available to participate in the reaction and help in catalyzing the polymerization of the sol with respect to time. In the case of Ce^{3+} and La^{3+}, the increase in the percentage of viscosity with time was relatively high

when directly added (existing as free ions) to the sol compared to loading them into LbL NCs and HNTs, where the sol viscosity is nearly the same as that of the matrix sol, thereby confirming that the cationic catalysed polymerization process either does not take place or takes place at a very slow rate. Therefore, the conclusions derived from zeta potential measurements are found to be in alignment with the viscosity data.

6.2.3. Characterization of HNT-based coatings

6.2.3.1. Thickness and tape peel-off test

The thicknesses of all the coatings measured using PosiTector® ranged from 4 to 8 µm. A tape peel-off test was performed to confirm the adhesion of the coatings. Representative results pertaining to direct addition of corrosion inhibitor into sol coatings, corrosion inhibitors loaded HNT based coatings and corrosion inhibitors loaded LbL nanocontainer based coatings in the form of optical microscope images are shown in Fig. 6.9 (a-c). The images confirmed that all the coatings possess excellent adhesion and are categorized under 0 class, meaning 0 % removal or no removal as per ISO standard 2409.

(a)

(b)

(c)
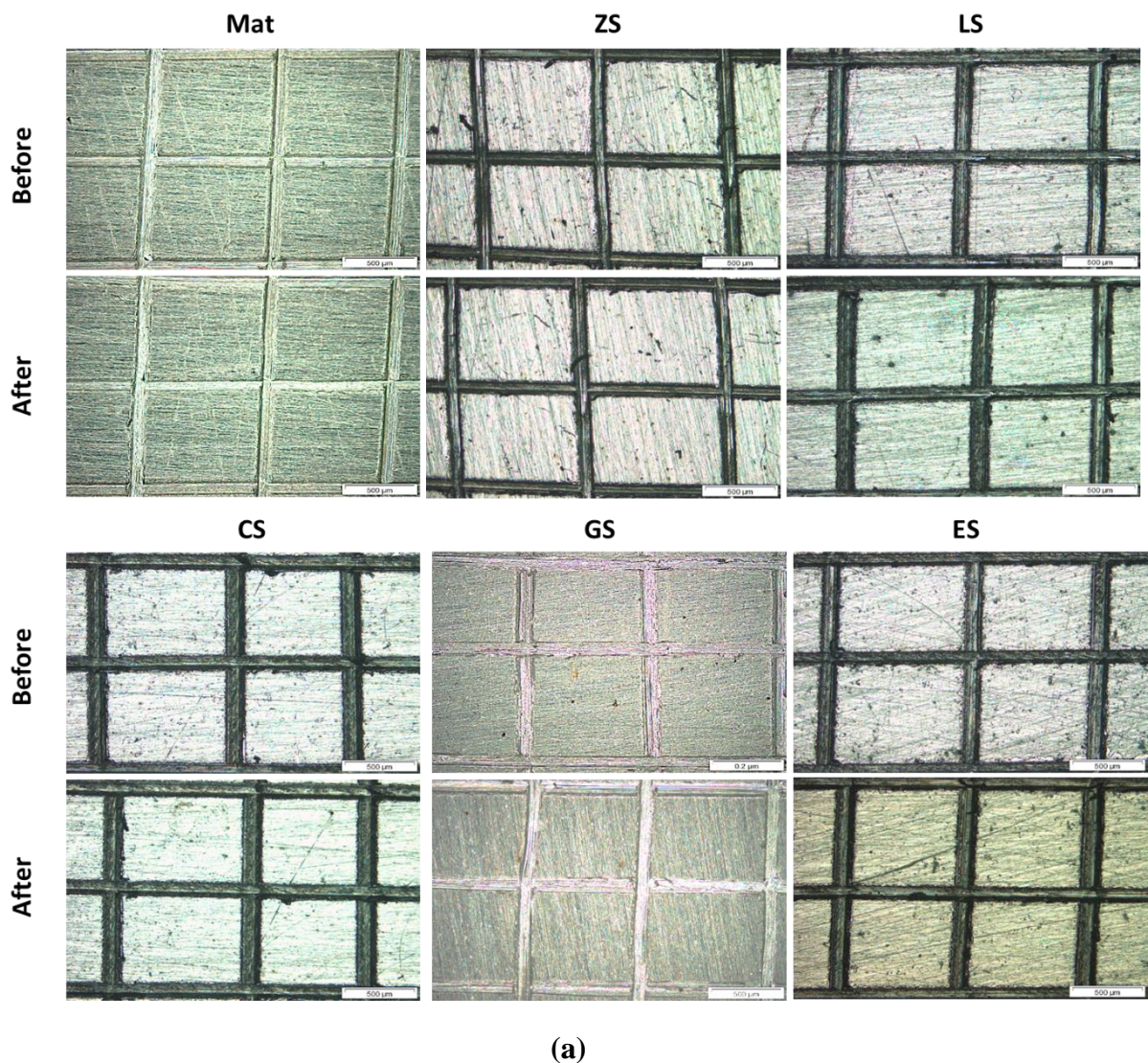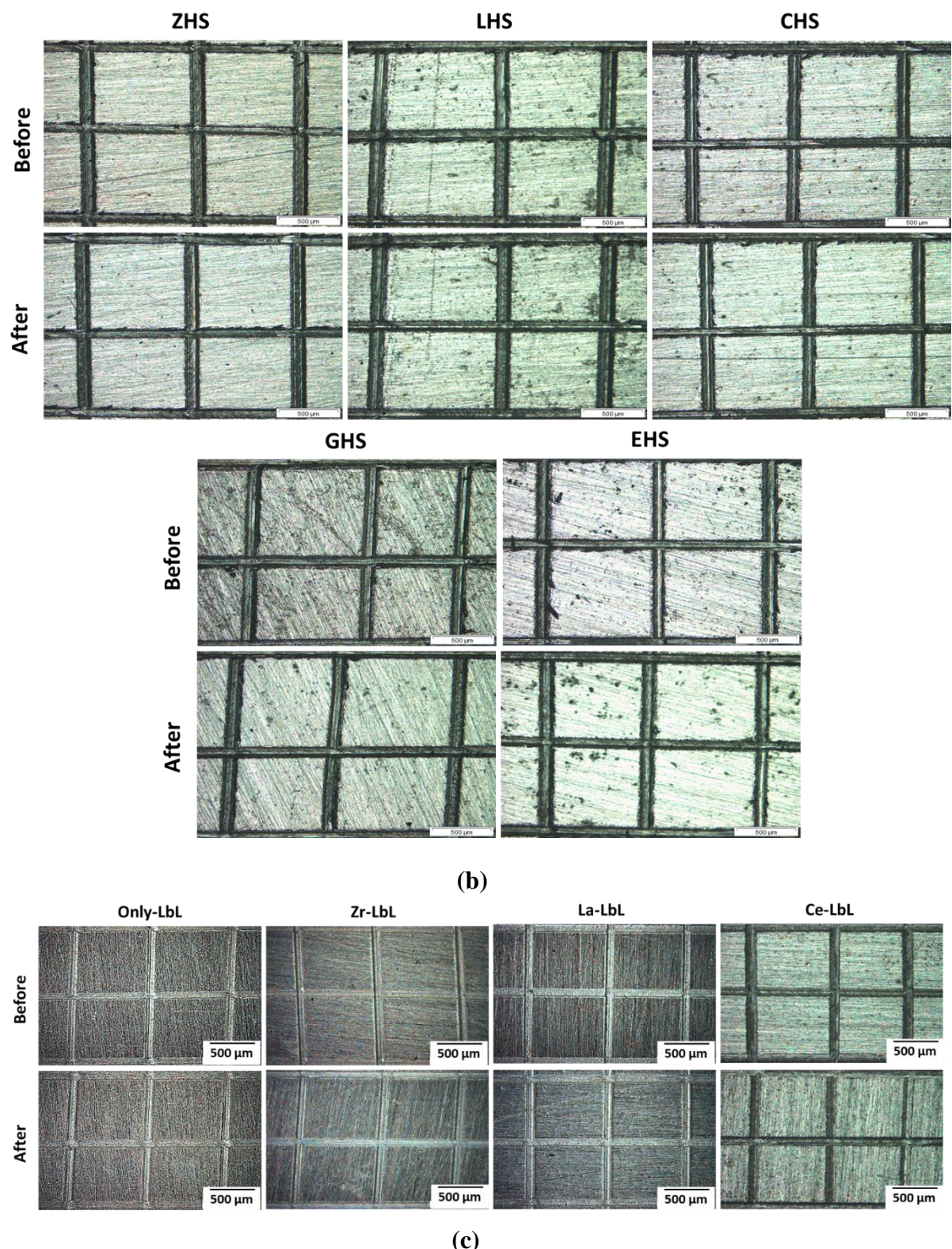
Fig. 6.9. Optical images of before and after tape adhesion test for MS substrates coated with (a) direct addition of corrosion inhibitors into matrix-sol, (b) corrosion inhibitors encapsulated into halloysite nanotubes, and (c) corrosion inhibitors encapsulated into layer-by-layer nanocontainers.

6.2.3.2. Water contact angle (WCA) measurements

The water contact angle measurement was carried out for both Z/RE and Z/REH-coated MS substrates. Researchers around the globe have reported different extents of wettabilities for RE-based coatings. Recently, a group of researchers have carried out significant experiments and confirmed that the coatings based on RE are initially hydrophilic, which later become hydrophobic. The increase in hydrophobicity was explained as due to the absorption of hydrocarbons from the surrounding environment [7]. Similar results were obtained in our measurements. The water contact angle was found to decrease for all the RE-based coatings when compared to matrix sol-coated substrates, as shown in Fig. 6.10 a and b. The WCA for Zr^{4+} based coating was comparatively high for direct addition and encapsulation. The reason behind this increase is the presence of MAA in the coatings, which leads to the formation of long organic chains at the time of curing. Among the inhibitor-loaded HNT coatings, ZHS substrate possessed maximum WCA (77.5°), suggesting increased hydrophobic nature of the coating. The increased hydrophobicity in the case of ZHS, as shown in Fig. 10 b, can be due to the surface modification of HNT caused during the loading of zirconium-n-propoxide into HNT, which has adsorbed more on the surface rather than loading into the lumen. As the outer surface of HNT is negatively charged, the adsorption of Zr^{4+} ions outside is relatively more when compared to the loading into HNT. A detailed explanation for this behaviour is provided in the forthcoming section on electrochemical testing 6.2.3.3 [8].

(a)

(b)
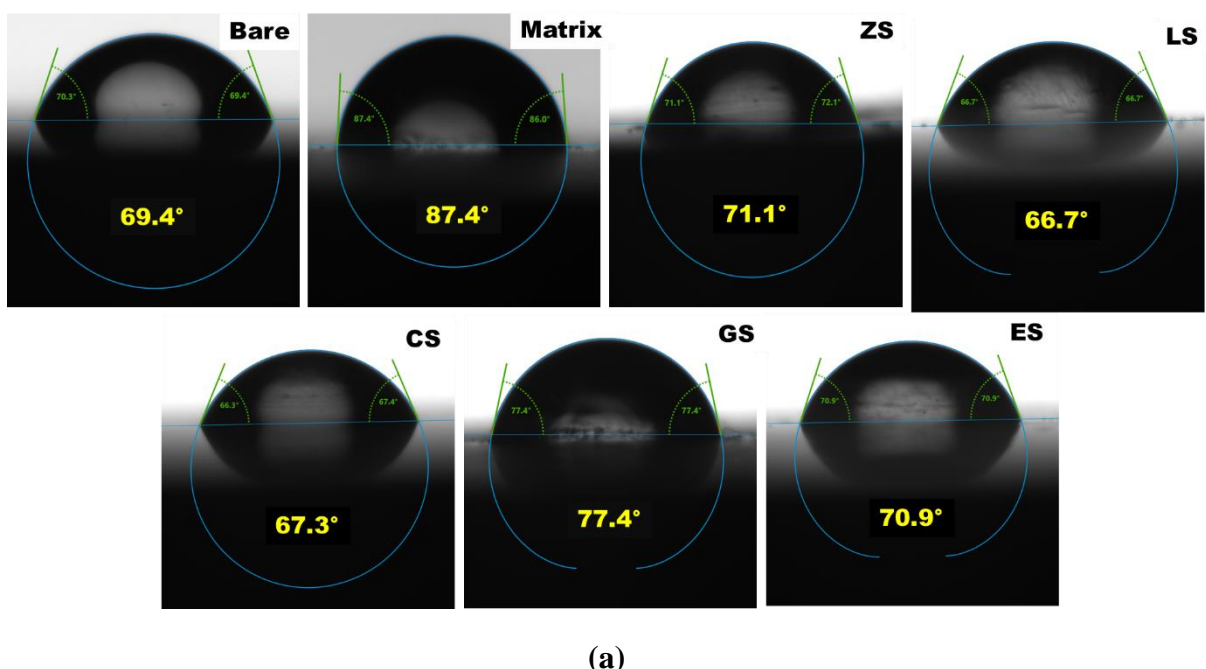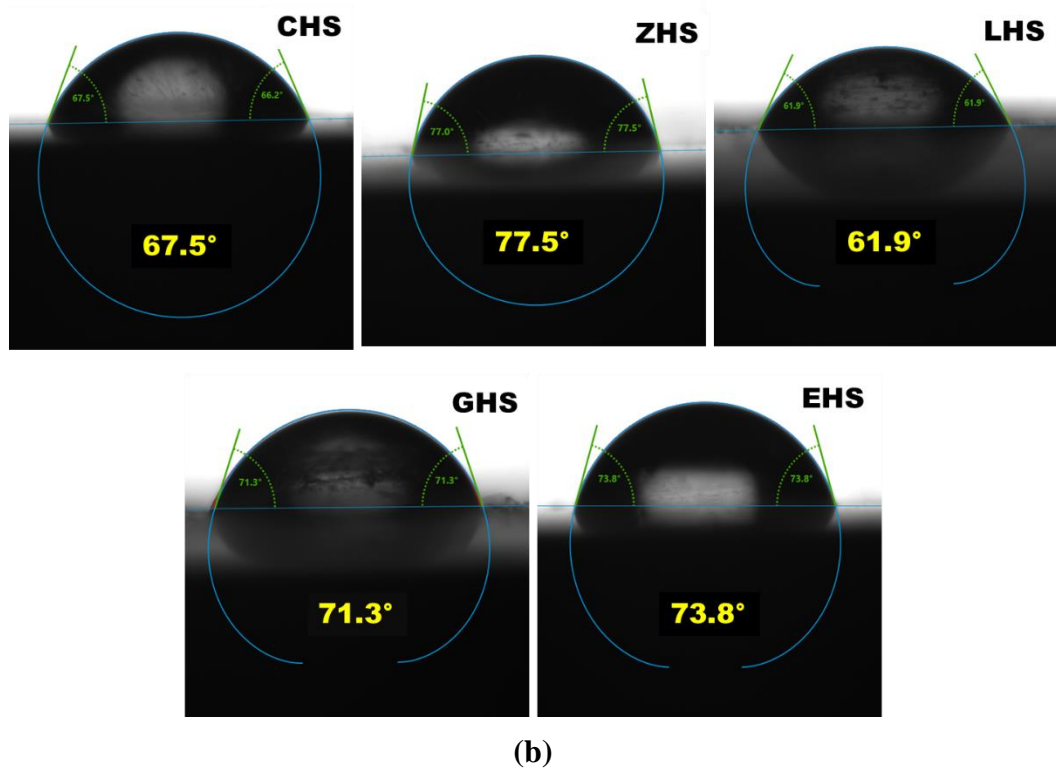
Fig. 6.10. Water drop images (a) for bare and coatings based on direct addition of corrosion inhibitors, and (b) coatings based on corrosion inhibitor encapsulated into halloysite nanotubes

6.2.3.3 Electrochemical impedance spectroscopy (EIS) and potentiodynamic polarization studies (PPS):

Figure 6.11 shows the electrochemical equivalent circuits used for fitting the impedance data. The impedance data of CS coated MS substrates were fitted using three-time constants as shown in Fig. 6.11 (c). Fig. 6.11 (a) shows the electrical circuit used for bare MS, and (b) corresponds to other coatings. R_s is for solution resistance, R_{coat} is the coating resistance, R_{ct} is charge transfer resistance, R_{diff} is the diffusion resistance, C_{coat} is coating capacitance, C_{dl} is capacitance due to electrical double layer and C_{diff} is capacitance due to diffusion.
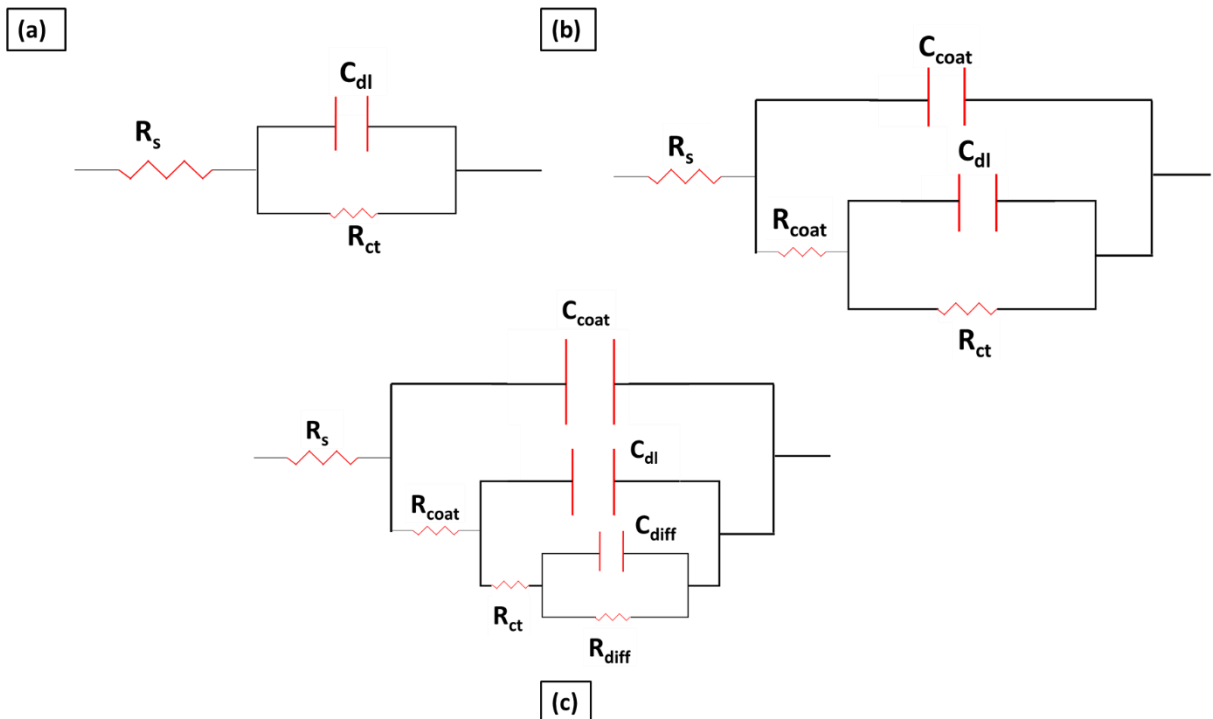
Fig. 6.11. Equivalent circuits for (a) bare MS, (b) all coatings except cerium matrix-coatings and (c) Cerium-matrix coating

(a) Effect of the direct addition of rare-earth corrosion inhibitors into the matrix sol:

Nyquist plots obtained for bare and different Z/RE-coated MS substrates after exposure to 3.5 wt% sodium chloride solution for 1 h are shown in Fig. 6.12. From the figure, it is evident that the impedance for ZS-coated substrate was very high followed by CS-coated substrate. The other RE-coated MS substrates have performed nearly the same; no major difference was observed in the corrosion resistance values.
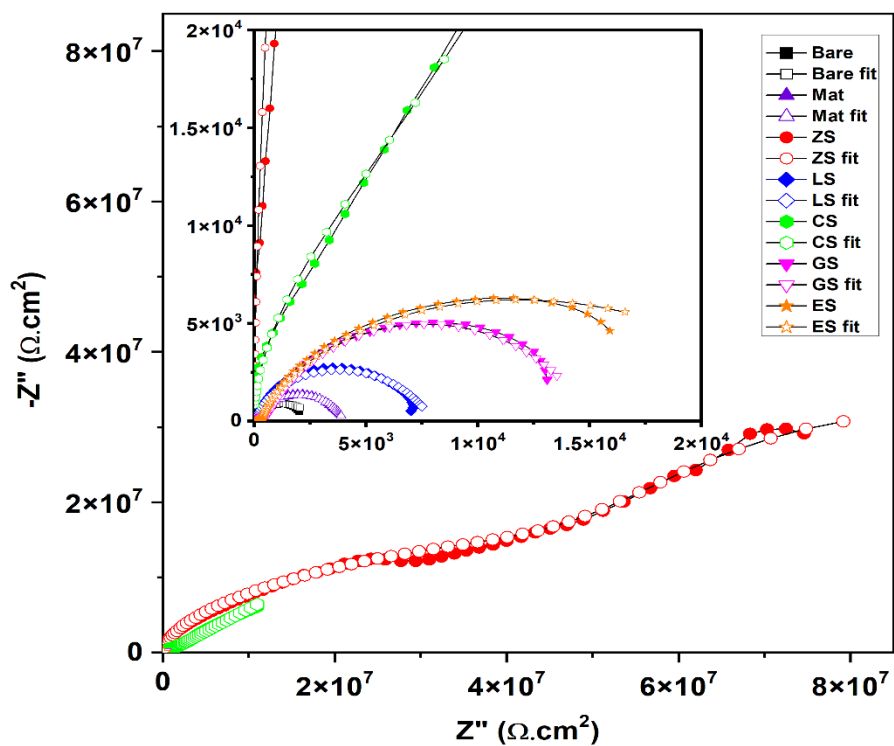
Fig. 6.12. Nyquist plots for bare and RE-coated MS substrates after immersion in 3.5 wt% sodium chloride solution for 1 h

The fitting parameters for bare and RE-coated substrates are shown in Table 6.2. The charge transfer resistance value for ZS coatings was the highest i.e., 4.88×10^7 $\Omega.cm^2$ when compared to other coatings, suggesting that this coating possesses maximum barrier properties.

Table 6.2 Fit parameters obtained for electrochemical impedance data after 1 h immersion of bare and coated MS in 3.5 wt% sodium chloride solution

Sample ID	R_{coat} ($\Omega.cm^2$)	R_{ct} ($\Omega.cm^2$)	R_{diff} ($\Omega.cm^2$)	C_{coat} (F/cm^2)	C_{dl} (F/cm^2)	C_{diff} (F/cm^2)	CHI^2
Bare	-	2558	-	-	4.28×10^{-4}	-	5.36×10^{-3}
Matrix	158.1	3813	-	1.59×10^{-5}	5.61×10^{-5}	-	3.57×10^{-3}
ZS	2557	4.88×10^7	-	4.13×10^{-10}	2.05×10^{-8}	-	3.28×10^{-3}
CS	2.215×10^4	6.10×10^5	6.46×10^8	2.26×10^{-10}	9.00×10^{-10}	0.001296	4.05×10^{-3}
ES	425.5	2.63×10^4	-	92.35×10^{-6}	4.71×10^{-5}	-	4.01×10^{-3}
GS	785.2	1.42×10^4	-	4.59×10^{-6}	7.25×10^{-5}	-	6.88×10^{-3}
LS	124.7	7865	-	4.11×10^{-6}	2.76×10^{-5}	-	9.89×10^{-3}

Tafel plots for bare and Z/RE-coated substrates after immersion in 3.5 wt% sodium chloride solution are shown in Fig. 6.13. The polarization fit parameters are consolidated in Table 6.3. The corrosion potential values have shifted to more positive potentials for all coatings when compared to bare and matrix coated MS. Hence, all the coatings firmly exhibit the self-healing action as and when the corrosion process initiates. The current density value was the least for ZS coatings followed by CS, which is the same trend as obtained in the EIS measurements.
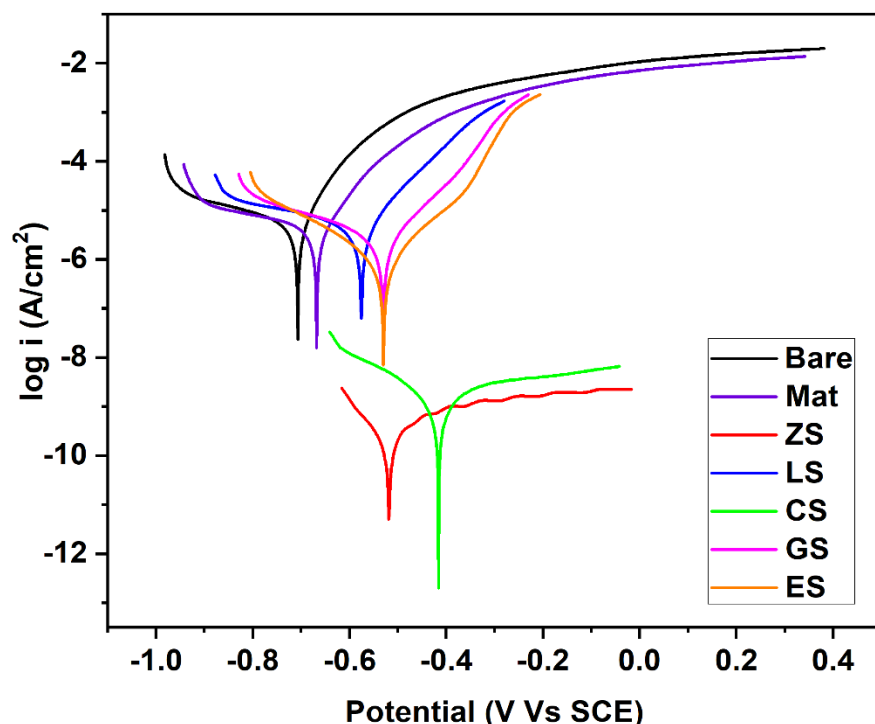
Fig. 6.13. Tafel plots for bare and RE-coated MS substrates after immersion in 3.5 wt% sodium chloride solution for 1 h

Table 6.3 Tafel fit parameters obtained for potentiodynamic polarization data after 1 h immersion of bare and coated MS in 3.5 wt% sodium chloride solution

Sample ID	E_{corr} (V Vs SCE)	I_{corr} (A/cm^2)	R_p ($\Omega.cm^2$)
Bare	-0.707	5.54×10^{-6}	4566
Matrix	-0.668	5.37×10^{-6}	6098
ZS	-0.519	0.00017×10^{-6}	93281608
LS	-0.576	4.57×10^{-6}	7244
CS	-0.416	0.0018×10^{-6}	26659758
GS	-0.530	2.51×10^{-6}	12044
ES	-0.547	1.58×10^{-6}	19220

The main reason for the increased coating performance of ZS is due to the presence of epoxide group in GPTMS, which is the primary constituent material in the matrix sol and has high activity in presence of zirconium. The zirconium helps polymerise the epoxide ring into polyethylene oxide, which in turn forms a long polymer chain, hence providing an excellent barrier and self-healing properties, as shown in equation 2 [9].
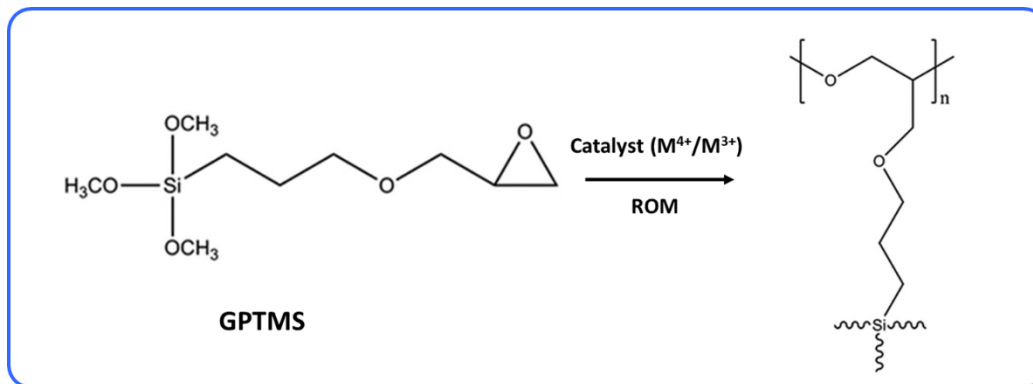
Equation 2: Epoxide ring opening of GPTMS to form long polymer chain

The CS-coated substrates have shown an increase in charge-transfer resistance and a decrease in current density, because of the formation of a thick layer of cerium hydroxide and cerium oxide on the MS substrate. This thick layer contributes to the increased barrier properties, which in turn passivates the MS surface and inhibits the entry of chloride ions into the coating [10]. This is the reason why the EIS data for CS-coated substrates was fitted using three-time constants. LS, GS and ES substrates have shown an increase in corrosion resistance based on their oxide formation. The stability of oxide formation of RE_2O_3 increases on moving left to right in the periodic table due to lanthanide contraction and decrease in ionic size, and therefore, the order of charge transfer resistance follows ES > GS > LS [11].

(b) Effect of encapsulation of inorganic corrosion inhibitors into HNT followed by dispersion into the matrix sol:

To observe the effect of encapsulation of corrosion inhibitors into nanocontainers, all the corrosion inhibitors used in our study were encapsulated into HNTs. Encapsulated HNT-derived sol-coated MS substrates were then exposed to 3.5 wt% sodium chloride solution for 1 h. Nyquist plots obtained are shown in Fig. 6.14, and the impedance data fit parameters are tabulated in Table 6.4. It is clear from the Nyquist plots that the ZHS coating has shown an increase in impedance values, suggesting improved coating performance against corrosion. The other REH-coated substrates have shown lower impedance values when compared to ZHS samples. EIS fit parameters also show that the charge transfer resistance of the ZHS coating was the highest against all REH-coated MS substrates.
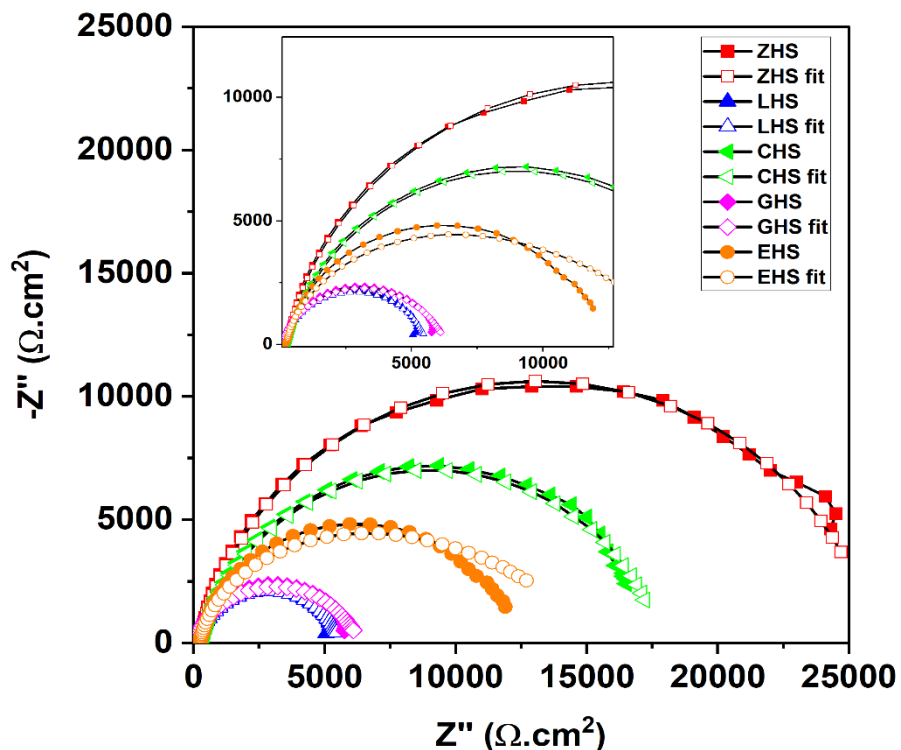
Fig. 6.14. Nyquist plots for different inhibitor-loaded halloysite nanotube sol coated MS substrates after immersion in 3.5 wt% sodium chloride solution for 1 h

Table 6.4. Fit parameters obtained for electrochemical impedance data after 1 h immersion of bare and coated MS in 3.5 wt% sodium chloride solution

Sample ID	R_{coat} ($\Omega.cm^2$)	R_{ct} ($\Omega.cm^2$)	C_{coat} (F/cm^2)	C_{dl} (F/cm^2)	CHI^2
ZHS	166.4	2.58×10^4	5.84×10^{-9}	7.53×10^{-5}	2.55×10^{-3}
CHS	306.7	1.75×10^4	1.79×10^{-8}	6.56×10^{-5}	0.66×10^{-3}
EHS	274.8	1.64×10^4	5.89×10^{-8}	6.21×10^{-5}	1.34×10^{-3}
GHS	77.61	6247	2.95×10^{-6}	6.61×10^{-5}	6.05×10^{-3}
LHS	39.23	5506	1.27×10^{-6}	1.21×10^{-4}	7.37×10^{-3}

To complement the electrochemical data, polarization studies were carried out. Figure 6.15 shows the Tafel plots for the coatings mentioned above, where the current density values for all the coatings are of the same order, i.e., 10^{-6} A/cm². The only difference was in the magnitude of the current density for all the coatings. Corrosion potential (E_{corr}) of the ZHS-coated MS substrate was the most positive among all the electrodes, confirming the high stability of the ZHS substrate against corrosion. The polarization fit data is consolidated in Table 6.5. The current density value for the ZHS-coated sample was the least, revealing that the coating is intact and thereby restricting the entry of electrolyte species. The order of decreasing corrosion protection is as follows: ZHS > CHS > EHS > GHS > LHS.
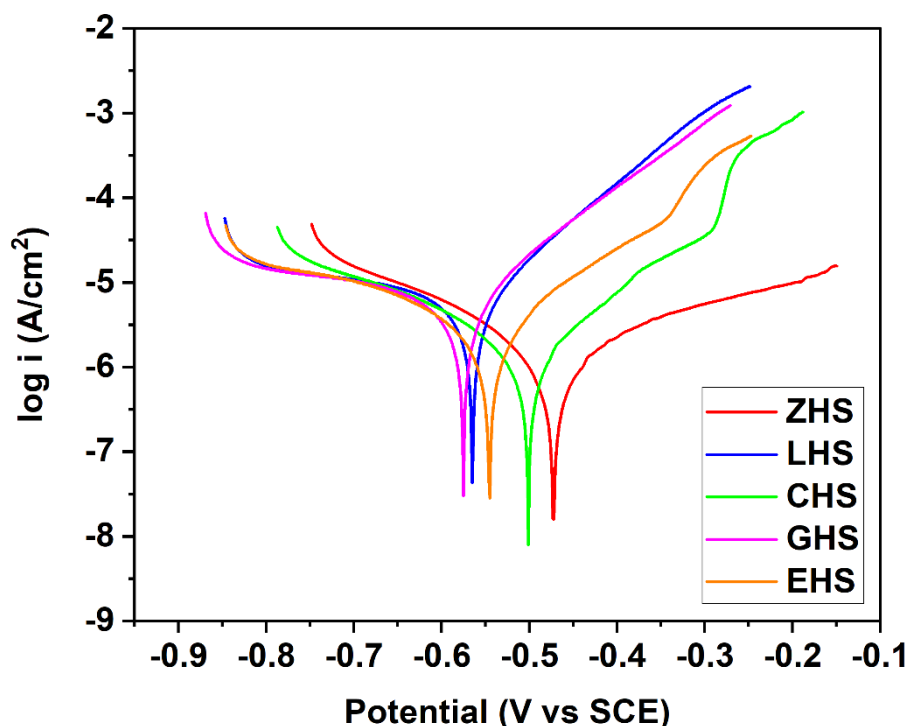

Fig. 6.15. Tafel plots for different corrosion inhibitor-loaded halloysite nanotube sol coated MS substrates after immersion in 3.5 wt% sodium chloride solution for 1 h

Table 6.5. Tafel fit parameters obtained for potentiodynamic polarization data after 1 h immersion of bare and coated MS in 3.5 wt% sodium chloride solution

Sample ID	E_{corr} (V Vs SCE)	I_{corr} (A/cm^2)	R_p ($\Omega.cm^2$)
ZHS	-0.472	1.25×10^{-6}	30240
CHS	-0.501	1.53×10^{-6}	20582
EHS	-0.545	2.65×10^{-6}	13159
GHS	-0.575	6.33×10^{-6}	6048
LHS	-0.565	6.83×10^{-6}	5495

(c) Effect of encapsulation of inorganic corrosion inhibitors into polyelectrolyte layers followed by dispersion into the matrix sol:

Compared to Gd^{3+} and Er^{3+}, Zr^{4+} and Ce^{3+} as corrosion inhibitors have provided better corrosion protection efficiency in electrochemical studies for direct addition as well as loading them into halloysite nanotubes. For La^{3+}, the salt spray test shows better inhibition when compared to Gd^{3+} and Er^{3+}, which will be discussed in a later section. Therefore, only Zr^{3+}, Ce^{3+} and La^{3+} were encapsulated into LbL nanocontainers-based on best performing corrosion inhibitors, and their anti-corrosion behaviour was examined. Nyquist plots for different LbL NCs based coatings are shown in Fig. 6.16. From the graph, it is clear that the impedance for Zr-LbL coating was highest with the increase in diameter of the capacitive loop. The impedance fit parameters are shown in Table 6.6. The corrosion resistance value for Zr-based LbL coating was highest followed by bare LbL. Ce based coatings possess nearly the same coating effect as that of bare matrix coated MS. Among all the coatings, La-LbL has shown the least corrosion resistance value.
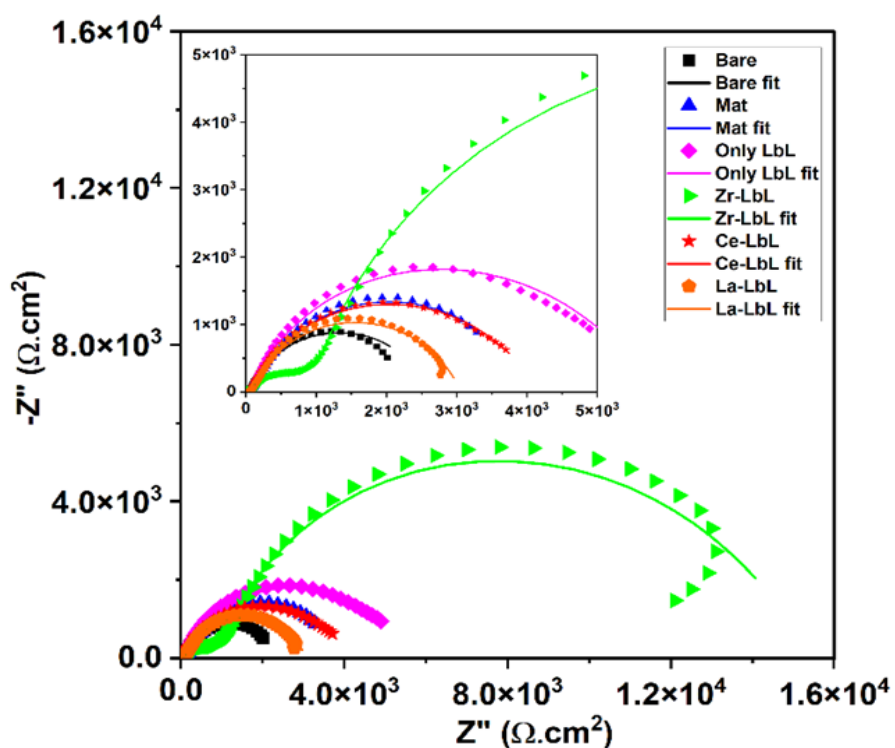
Fig. 6.16. Nyquist plots for bare MS substrate and substrates coated with different sols based on corrosion inhibitors encapsulated into layer-by-layer nanocontainers

Table 6.6. EIS fit data for bare and MS substrate and substrates coated with sols in which corrosion inhibitors are encapsulated into LbL NCs, after 1 h exposure to 3.5 wt% NaCl solution

Sample ID	R_{coat} ($\Omega.cm^2$)	R_{ct} ($\Omega.cm^2$)	C_{coat} (F/cm^2)	C_{dl} (F/cm^2)	CHI^2
Bare	-	2558	-	4.28×10^{-4}	5.36×10^{-3}
Matrix	158.1	3813	1.59×10^{-5}	5.61×10^{-5}	3.57×10^{-3}
Only-LbL	72.59	5888	1.27×10^{-5}	2.18×10^{-4}	4.71×10^{-3}
Zr-LbL	1258	1.42×10^4	1.91×10^{-6}	5.78×10^{-5}	1.22×10^{-3}
Ce-LbL	47.21	4090	7.45×10^{-6}	1.17×10^{-4}	5.34×10^{-3}
La-LbL	109.1	2900	1.67×10^{-5}	7.03×10^{-5}	5.84×10^{-3}

Figure 6.17 shows the Tafel plots for different LbL based coatings. As observed from Table 6.7 that the corrosion current for Zr-LbL was least among all the coatings. Ce and La-LbL coatings have shown nearly same corrosion current but have performed better when compared to bare and matrix coated mild steel substrates.
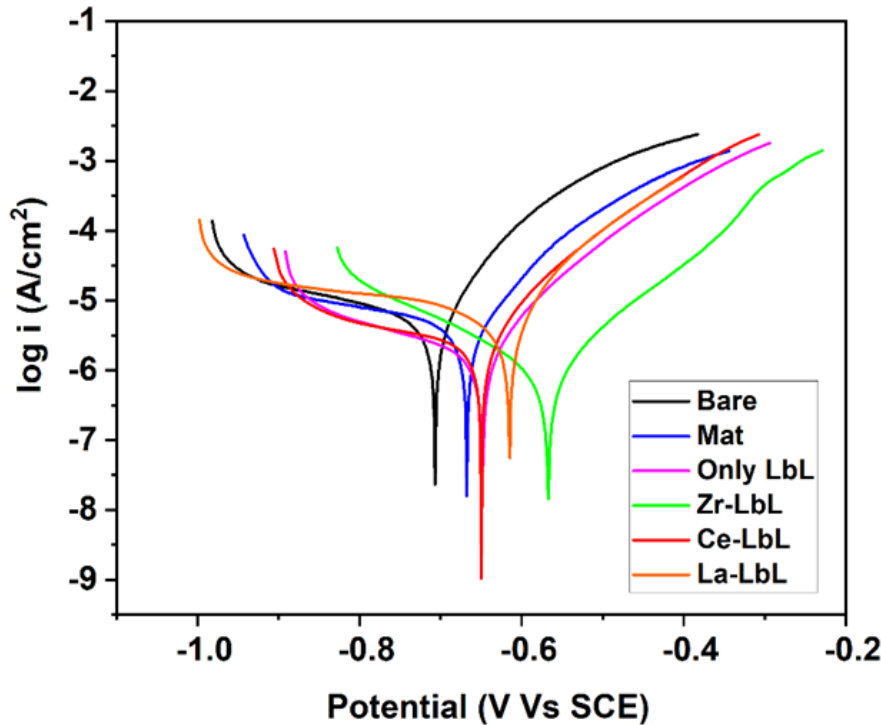
Fig. 6.17. Tafel plots for bare MS substrate and substrates coated with sols in which corrosion inhibitors are encapsulated into LbL NCs.

Table 6.7. Electrochemical polarization data for bare and substrates coated with sols in which corrosion inhibitors are encapsulated into layer-by-layer nanocontainers.

Sample ID	E_{corr} (V Vs SCE)	I_{corr} ($\mu A/cm^2$)	R_p ($\Omega.cm^2$)
Bare	-0.707	5.54×10^{-6}	4566
Matrix	-0.668	5.37×10^{-6}	6098
Only-LbL	-0.649	2.18×10^{-6}	13019
Zr-LbL	-0.567	1.07×10^{-6}	27043
Ce-LbL	-0.650	3.20×10^{-6}	9400
La-LbL	-0.615	3.65×10^{-6}	5346

(d) Comparison of direct addition of corrosion inhibitors and encapsulation of corrosion inhibitors into nanocontainers

The HNTs are composed of aluminosilicate layers, where the external surface is of negative charge from a Si-O-Si network and the inner surface is positively charged having Al-OH groups [12]. The inner arrangement of Al-OH groups is like an erected triangle where the top head comprises Al^{3+} ions protruding away from the tube's inner lining, and OH- ions are the two ends of the triangle attached to the surface of the inner tube, making the lumen positively charged from inside, as shown in Fig. 6.18 (a) [8].
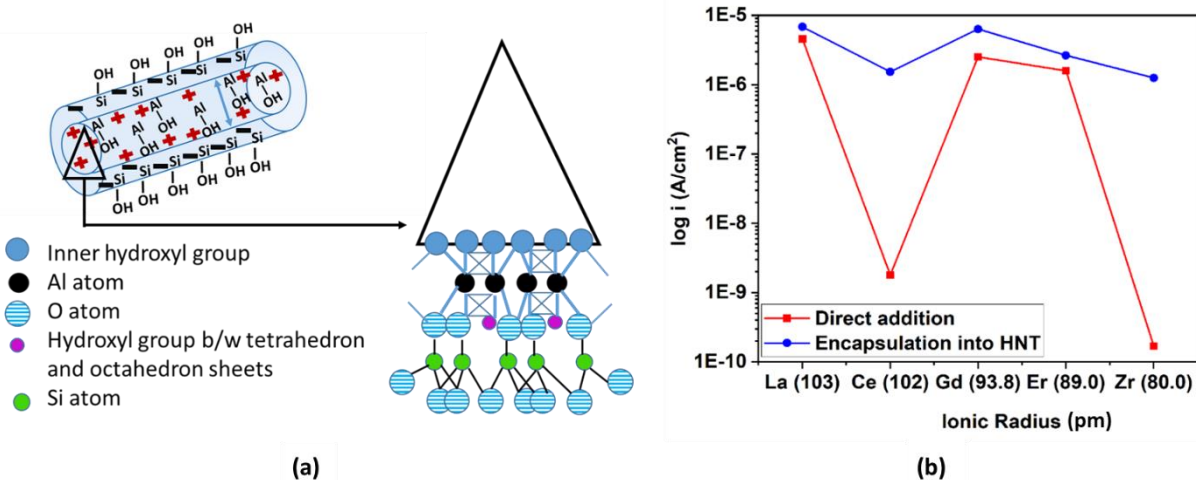
Fig. 6.18 (a) Schematic representation of the structure of halloysite nanotube (HNT), and (b) current density plot w.r.t ionic radius for direct addition and corrosion inhibitor loaded HNT sol-coated MS substrates after immersion in 3.5 wt% sodium chloride solution for 1 h

The inorganic/rare earth elements being cationic and hydrophilic makes it difficult to form a chemical bond with the Al^{3+} ions and thus may not completely load in the empty and positively charged lumen of HNT. Thus, loading efficiency may be less when compared to other organic molecules. On the other hand, the adsorption of these inorganic or RE on the outer surface of HNT is more prominent due to the affinity towards the hydroxyl groups present on the outer surface. Therefore, during the corrosion process, these ions are released slowly, thereby showing lesser corrosion protection when compared to direct addition [13]. On direct addition, these inorganic or cationic corrosion inhibitors are in close vicinity and show an immediate reaction to any stimuli caused due to corrosion, thus ensuring quick healing action by forming a stable oxide film on the mild steel surface. The trend of corrosion protection for direct addition

and encapsulation is still the same. Corrosion protection decreases with a decrease in the ionic radius of the constituent ions i.e., $Zr^{4+} > Ce^{3+} > Er^{3+} > Gd^{3+} > La^{3+}$.

Similarly, loading or entrapping these corrosion inhibitors into LbL NCs reduces its active corrosion inhibition as the ions responsible for this are not free. With respect to direct addition, the inhibition action of corrosion inhibitor encapsulated into LbL NCs follows the similar trend but with decreased self-healing ability. Zr-LbL coating has shown an increase in charge transfer resistance and a decrease in corrosion current, which is due to the barrier effect caused by the increased thickness of the coating and active inhibition of Zr^{4+}. Ce-LbL and matrix coatings have performed relatively the same. La-LbL coatings do possess the capability of active inhibition when compared to bare mild steel substrate, which has shown the least charge transfer resistance and increased corrosion current. Hence, confirming that during the electrochemical process these ions do show their inhibition action with Zr^{4+} performing more efficiently. During salt spray test, these ions have different corrosion mechanisms, where the barrier effect is more pronounced, as discussed in subsequent section.

6.2.3.4 Micro Raman Spectroscopic Analysis

In order to evaluate the self-healing action, Micro-Raman spectroscopic studies for bare, zirconium and cerium-coated MS samples were carried out on scribed bare and coated MS substrates after exposure to 3.5 wt% sodium chloride solution for 1 h. The Micro-Raman spectra were obtained for the scribed region and are shown in Fig. 6.19. Table 6.8 shows the peak shifts corresponding to different compounds in bare and coated MS substrates. It should be noted that the peaks observed for bare MS substrates are quite distinct from the coated MS substrates. The Raman analysis also confirms the self-healing action of the corrosion inhibitors, as Zr^{4+} and Ce^{3+}/Ce^{4+} ions have been released in the scribed region and formed a passive film of stable oxides of Ce and Zr (CeO_2 and ZrO_2). Salt spray analysis in the next section will provide a clear picture of the surface morphology of the rust products and self-healing products formed on bare and coated substrates after salt spray exposure.
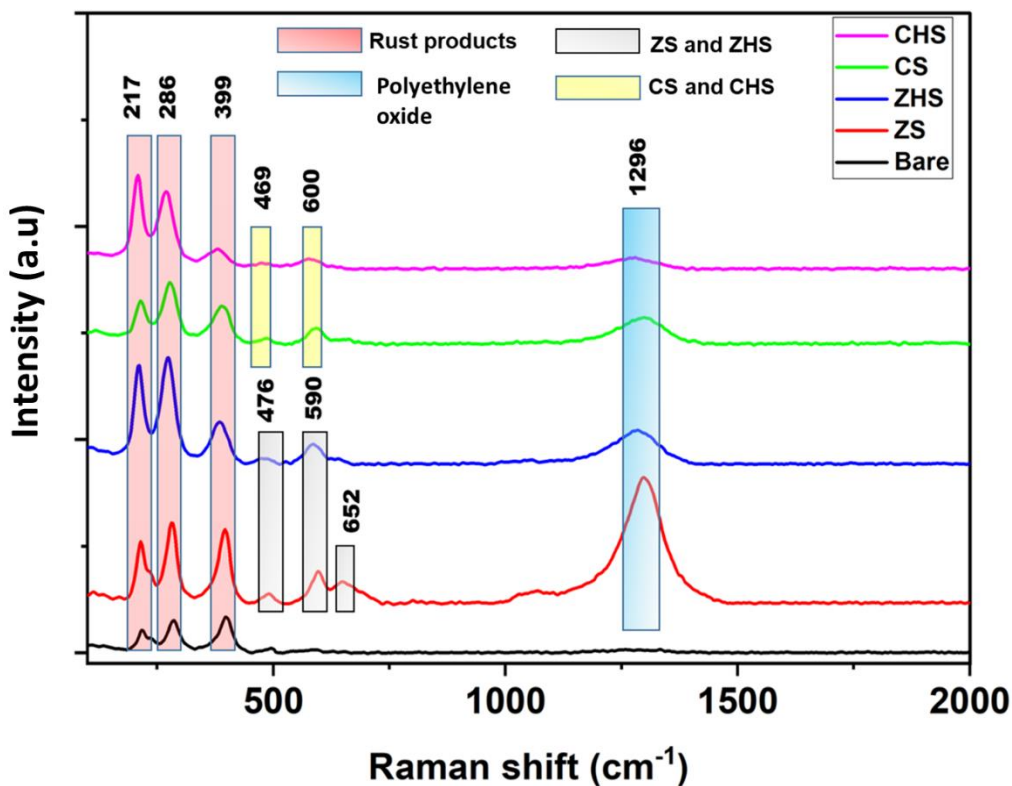
Fig. 6.19. Micro-Raman spectra for bare and coated substrates obtained after exposing the substrates in 3.5 wt% sodium chloride solution for 1 h

Table 6.8. Raman peak shift for scribed coated and bare MS substrates after exposure to 3.5 wt% sodium chloride solution for 1 h

Compound	Coating	Peak shift (cm^{-1})	Reference
Lepidocrocite (γ-FeOOH)	Bare and coated MS	217	[14,15]
Hematite (α-Fe_2O_3)	Bare and coated MS	286	[14,15]
Goethite (α-FeOOH)	Bare and coated MS	399	[14,15]
Polyethylene oxide	coated MS substrates	1296	[16]
Tetragonal ZrO_2	ZS and ZHS	652 and 590	[17,19]
Monoclinic ZrO_2	ZS	476	[18]
Fluorite structure of CeO_2	CS and CHS	469	[20,21]
Reduction of Ce^{4+} to Ce^{3+}	CS and CHS	600	[20,21]

6.2.3.5. Salt Spray Test

Bare and coated MS substrates were exposed to salt spray for 5 h as per ASTM B117 standard. The bare and coated substrates were cross-scribed and photographs were collected before and after exposure to the salt spray test (SST). FESEM/EDS analysis at 0 h (i.e. prior to SST) was employed to confirm the complete removal of coating by scribe process and that after 5 h SST to examine the self-healing action/rust product formation. Photographic and SEM images of MS coupons coated with (i) matrix sol alone, (ii) transition or rare-earth metal directly added matrix sols, (iii) transition or rare-earth metal encapsulated HNT added matrix sols, and (iv) transition or rare-earth metal encapsulated LbL added matrix sols were recorded before exposure to salt spray test and after 5 h exposure to salt spray test, and all they were shown in Figs. 6.20 to 6.24. Point 1 in all the SEM images corresponds to the scan area where EDS analysis was carried out. Table 6.9 shows the EDS analysis in the scribed area for bare/coated substrates before and after exposure to SST. Figure 6.20 shows the images of bare substrates at 0 and 5 h. The SEM image at 0 h confirms the complete removal of the coating. After 5 h of exposure, the visual image shows that the surface has been completely corroded with maximum rust products on the surface.
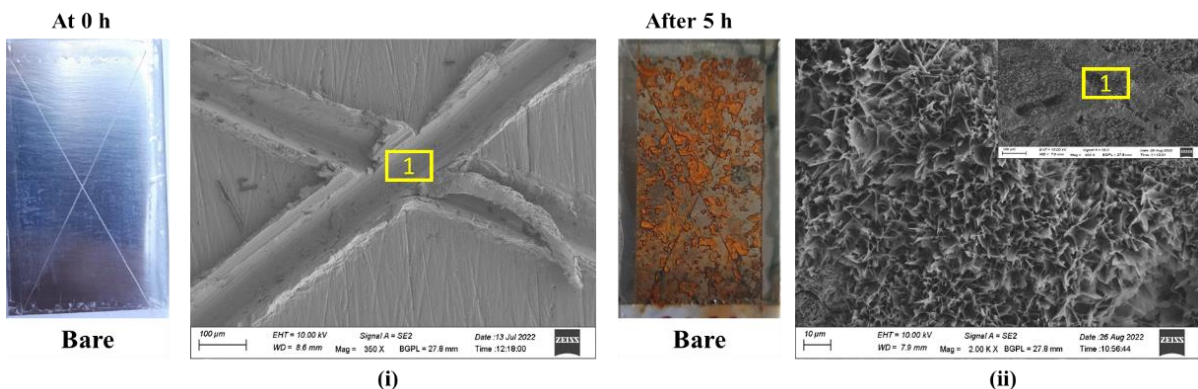
Fig. 6.20. Visual and FESEM image of bare substrate before and after exposure to salt spray

In Fig. 6.21, FESEM images of different rust products are observed on bare MS substrates. The FESEM data is in good agreement with the Micro-Raman spectroscopy data. In Fig. 6.21, images (a) and (b) correspond to needle-like sharp structures of Lepidocrocite. Figure (c) shows more of round cotton ball structures which resemble and represent Goethite, and Figure (d) and (e) have nearly the same morphological structures, which resemble rosette morphology of Akaganeite. Lepidocrocite, goethite and akaganeite are different crystalline structures of iron-oxyhydroxide (FeO(OH)). Lepidocrocite (γ-FeO(OH)) forms when iron-

containing substances rust in underwater conditions, and goethite is the main component of rust. Akaganéite (β-FeOOH, Cl) is a relatively rare iron oxyhydroxide that is found in chloride-rich environments such as marine environments. The observed different crystalline forms of rust are very much relevant to the experimental conditions of salt spray test, where the specimens were under high concentrations of chloride and underwater. High magnification FESEM images (Fig. 6.21) are in good agreement with the results of Micro-Raman spectroscopy analysis. These rust products are different stages of iron oxide which undergo phase transformation as the corrosion process initiates [22-25].
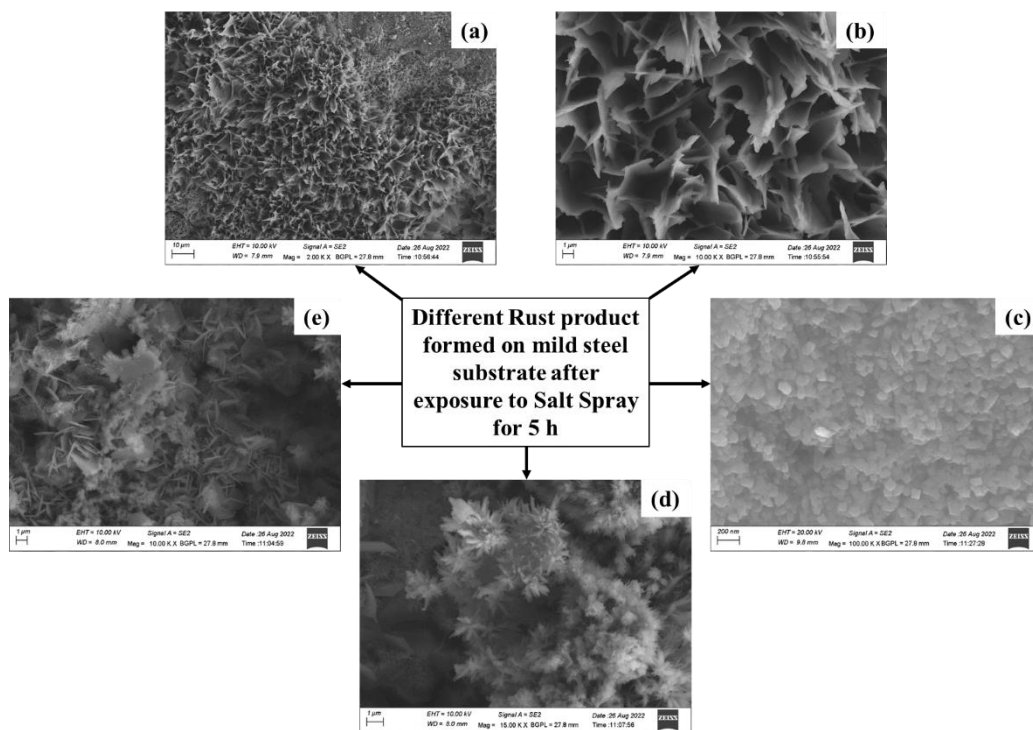
Fig. 6.21. Corrosion products formed on bare MS: (a) and (b) Lepidocrocite; (c) Goethite and (d and e) Akaganeite

Figure 6.22 (a) shows the image of matrix-coated MS substrates, where the surface after 5 h exposure looks similar to that of bare MS. The FESEM image at higher magnification shows the silica nanoparticles and Lepidocrocite structures in the scribed area (iii). For ZS, LS, CS, GS and ES coatings, as shown in Fig. 6.22 (b-f), image (i) presents the FESEM image at 0 h, and images (ii and iii) present FESEM images after 5 h. The corrosion products were prominent in the scribed area and on the surface adjacent to the scribed area, whereas with lesser rust products on all the other surface areas. Figure (ii) shows that the scribed area has been sealed by forming a thick layer. Figure (iii) shows the FESEM image of the scribed area

at a higher magnification, where cuboidal crystal or spherical structures correspond to oxides of corrosion inhibitor along with the rust product which may vary based on the coatings and extent of corrosion. The most prominent rust products observed on the surface belong to the Lepidocrocite, Goethite, and Akaganeite structure.

Figure. 6.23 shows photographic and FESEM images for MS substrates coated with transition or rare-earth metal encapsulated HNT added matrix sols. The SST confirmed that the self-healing action of direct addition of corrosion inhibitor is more when compared to the encapsulation of corrosion inhibitor into HNT. Visual and FESEM images for both the coating types clearly show that the rust product in the scribed area and on the surface of the coated samples are more on the halloysite-based coatings rather than the direct inhibitor-loaded coatings. The elemental analysis also supports this observation, as the rust product elements, i.e., Fe and O, have shown higher weight % in the scribed area for Halloysite-based coatings compared to direct addition as shown in Table 6.10. The trend for corrosion protection for direct addition is as follows: LS > GS > ES > CS > ZS > Matrix > Bare and for encapsulation into HNT is: LHS > GHS > EHS ≈ ZHS > CHS. The results of SST analysis were firmly supported by the results of electrochemical impedance and potentiodynamic polarization studies carried out after 1 h immersion in 3.5 wt% NaCl solution, which demonstrated superior corrosion resistance for MS substrates coated with transition or rare-earth metal added matrix sols without any encapsulation process.
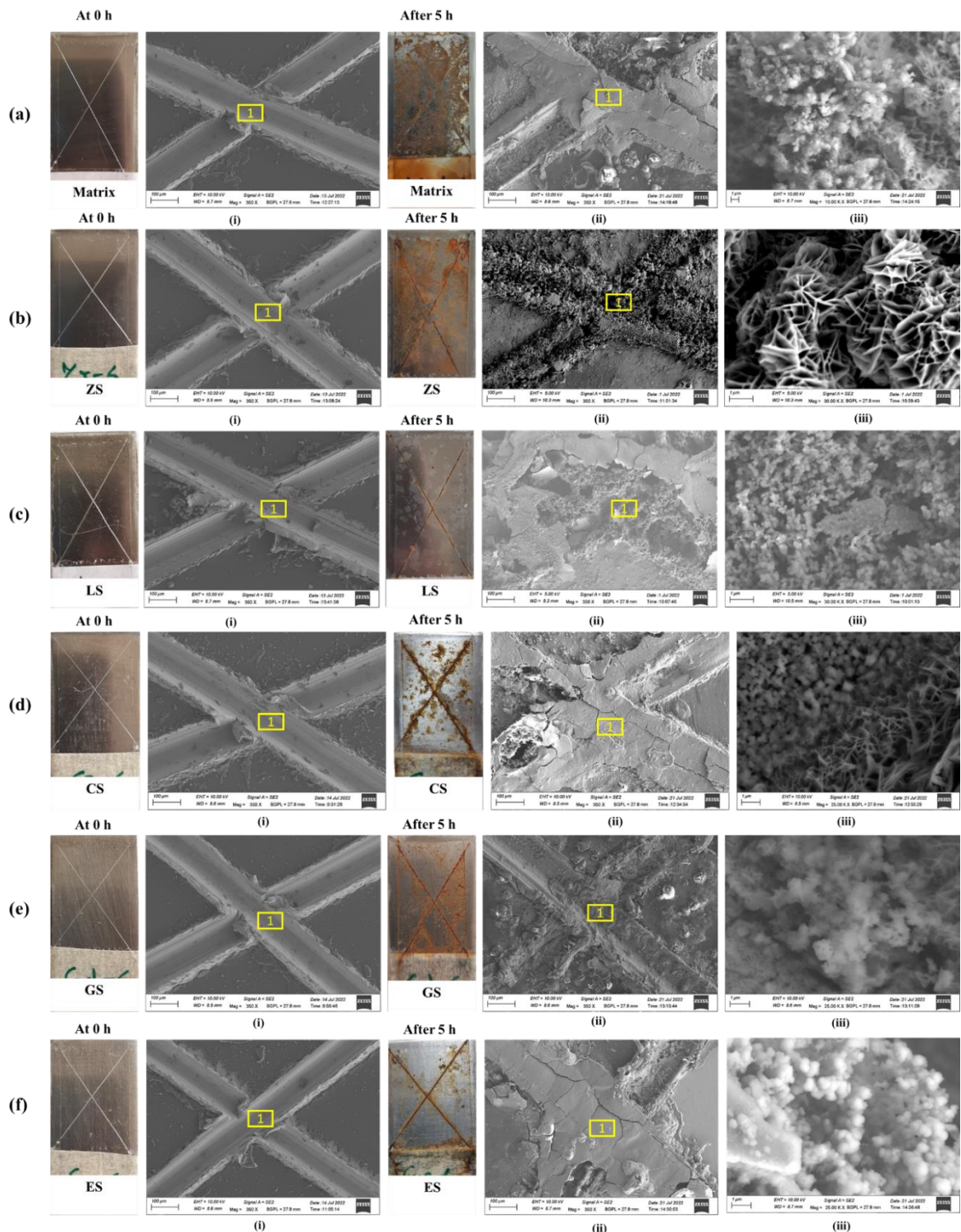
Fig. 6.22. Visual and FESEM images of (a) Matrix-coated, (b) ZS, (c) LS, (d) CS, (e) GS, and (f) ES-coated MS substrates before and after exposure to salt spray
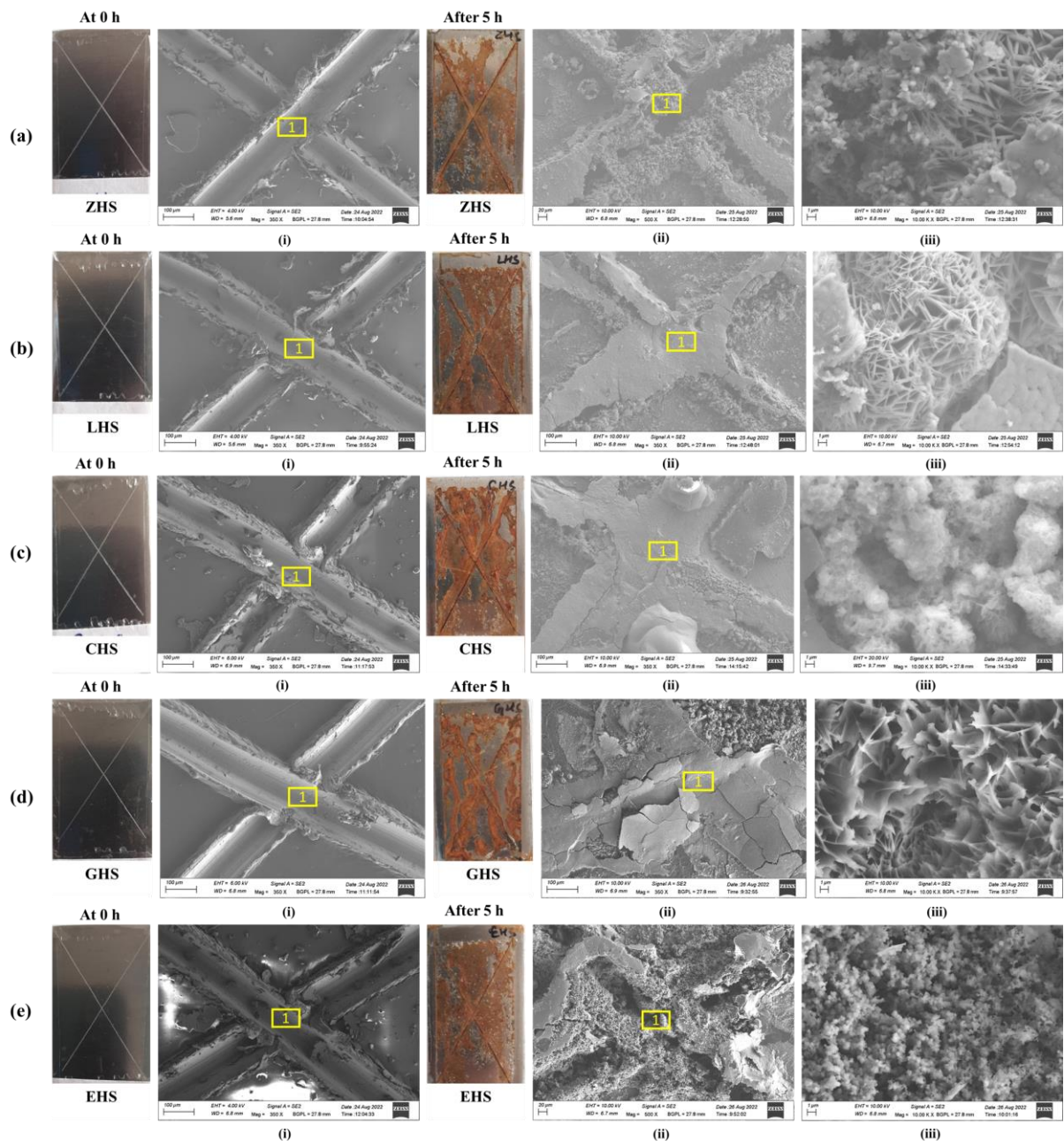
Fig. 6.23. Visual and FESEM images of (a) ZHS, (b) LHS, (c) CHS, (d) GHS, and (e) EHS-coated MS before and after exposure to salt spray

Table 6.9. EDS analysis for bare and coated MS substrates before and after exposure to SST

Sample Name	SST	C	O	Si	Fe	Corrosion Inhibitor
Bare	Before	2.88	1.55	-	95.57	-
	After	-	25.92	-	74.08	-
Matrix	Before	2.51	2.63	0.27	94.59	-
	After	5.65	44.47	0.48	49.40	-
ZS	Before	1.86	2.18	0.30	95.66	-
	After	5.46	22.38	7.46	51.24	0.24
CS	Before	2.73	1.28	0.32	95.67	-
	After	4.02	33.64	1.37	60.02	0.95
LS	Before	1.47	1.24	0.19	97.10	-
	After	5.06	26.76	2.84	64.23	1.12
GS	Before	0.39	1.70	0.25	97.66	-
	After	3.64	22.12	20.18	71.24	2.93
ES	Before	1.55	1.71	0.23	96.51	-
	After	5.21	23.40	1.78	68.33	1.27

Table 6.10. EDS analysis for bare and coatings based on corrosion inhibitor encapsulated HNTs on MS substrates before and after exposure to SST

Sample Name	SST	C	O	Al	Si	Fe	Corrosion Inhibitor
CHS	Before	0.21	0.66	-	0.29	98.84	-
	After	1.21	21.65	0.09	0.97	75.53	0.55
ZHS	Before	0.19	0.03	-	0.03	99.75	-
	After	1.29	17.18	0.08	1.06	80.1	0.29
LHS	Before	0.17	1.06	-	0.44	98.33	-
	After	4.55	37.01	0.14	0.63	57.43	0.25
GHS	Before	1.56	0.93	-	0.16	97.34	-
	After	0.97	16.63	0.63	0.67	80.75	0.35
EHS	Before	0.85	0.44	-	0.28	98.42	-
	After	-	22.50	1.01	0.86	75.36	0.27

For coatings based on LbL NCs, after 5 h of exposure to salt spray, Zr-LbL has shown better barrier protection, and, as a result, least corrosion products were visible on the surface when compared to other coatings (Fig. 6.24). The trend of SST results is in alignment with viscosity data and thickness of the coatings. Zr-LbL being more viscous and having highest coating thickness provides enhanced barrier protection as well as corrosion inhibition. The SST confirmed that the self-healing action in substrates coated with the direct addition of corrosion inhibitor is more when compared to the substrates coated with corrosion inhibitor-encapsulated HNT based and LbL nanocontainer. Visual and FESEM images for both the coating types clearly show that the rust products present in the scribed area and on the surface of the coated

samples are more on the LbL-based coatings rather than the direct inhibitor-loaded coatings. Table 6.11 shows the elemental analysis of before and after exposure to salt spray test.
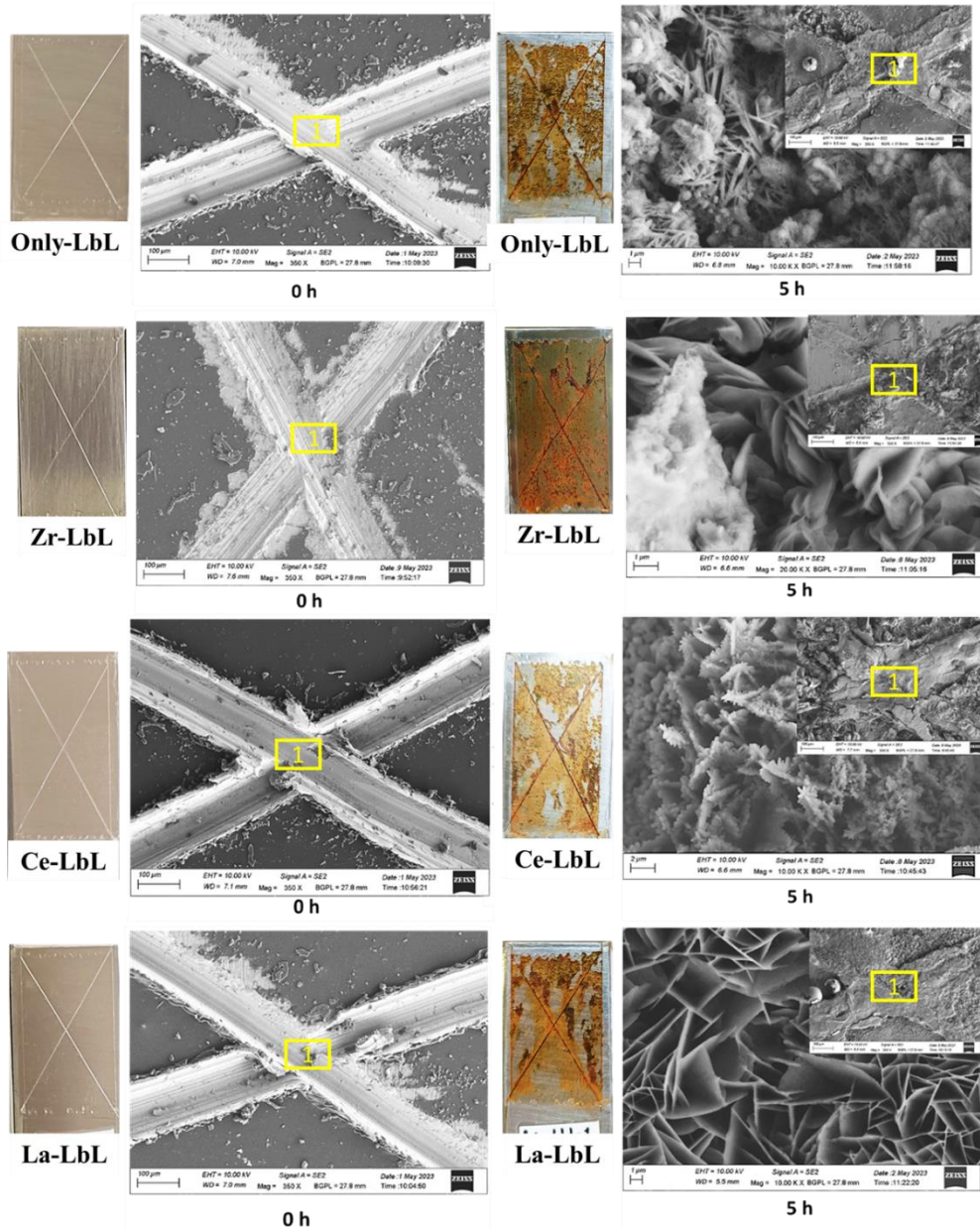
Fig. 6.24. Visual and FESEM images of (a) only-layer-by-layer nanocontainers (LbL), (b) Zr-LbL, (c) Ce-LbL, and (d) La-LbL before (0 h) and after exposure (5 h) to salt spray

Table 6.11. EDS analysis for bare and coatings based on corrosion inhibitor encapsulated into LbL nanocontainer on MS substrates before and after exposure to SST

Sample Name	SST	C	O	Si	Fe	Corrosion Inhibitor
Only LbL	Before	0.5	0.88	0.15	98.47	-
	After	5.6	36.19	0.93	57.28	-
Zr-LbL	Before	0.67	1.09	0.34	97.89	-
	After	17.93	34.17	0.73	46.86	0.31
La-LbL	Before	0.77	0.99	0.26	97.98	-
	After	8.37	34.41	0.56	55.99	0.66
Ce-LbL	Before	0.44	0.91	0.18	98.47	-
	After	10.22	32.62	4.32	52.64	0.20

6.3.2.6. Comparison of data from Electrochemical and Salt Spray tests:

From the electrochemical studies and salt spray test, it can be concluded that the direct addition of corrosion inhibitor into matrix sol coated MS substrates has provided better barrier as well as self-healing properties when compared to encapsulation of these corrosion inhibitors into HNTs or LbL nanocontainers. On close analysis, it can be observed that the trend of corrosion inhibition between the two techniques, i.e. the direct addition or the encapsulation, is somewhat different. Electrochemical studies confirm that the zirconium-based coatings gave better corrosion performance, whereas, in SST, lanthanum-based coatings have shown decreased corrosion rate. The data obtained in the electrochemical technique is basically about the interface chemistry between the coating and the substrate which provides quantitative test results. The charge transfer resistance values give insight into the coating performance and adherence to the metal substrate. The corrosion inhibitor is released only when there is a coating breakdown. Usually, during polarization studies, the coating breaks down on the application of external voltage, and then the inhibitor is released, which followed by the self-healing mechanism. SST describes the change on the surface of the substrate when exposed to an aggressive salt environment. During exposure in the SS chamber, the electrolyte (5 wt% NaCl solution) layer is continuously refreshed on the substrate, and the effect of the inhibitor may

differ at each time [26] [27]. In SST, the continuous fogging leads to the formation of rust product initially in the scribed area, followed by self-healing action of the corrosion inhibitor or vice-versa. As evident from SST FESEM images, it was observed that the rust product is beneath the thick self-healing layer in the cross-scribe.

During initial exposure, the rust product must have covered the exposed area, and the inhibitors from the near scribed area come slowly into the picture, initiating the passive film growth. Another reason to explain the effect of coated samples in SST is the Lepidocrocite structure formation. During corrosion process, γ-FeOOH (Lepidocrocite) is formed after the dissolution of Fe as Fe^{2+} ions, leading to the formation of amorphous FeOOH. The final product is Goethite, α-FeOOH; a solid-state transformation. The other rust products are formed in between these two significant phases.

$$Fe \xrightarrow{\text{dissolution}} Fe^{2+} \xrightarrow[\text{oxidation}]{\text{hydrolysis}} \gamma\text{-FeOOH} \xrightarrow[\text{precipitation}]{\text{dissolution}} FeO_x(OH)_{3-2x} \xrightarrow[\text{solid product}]{\text{transformation into}} \alpha\text{-FeOOH}$$

$$\text{(Lepidocrocite)} \qquad \text{(Amorphous ferric oxyhydroxide)} \qquad \text{(Goethite)}$$
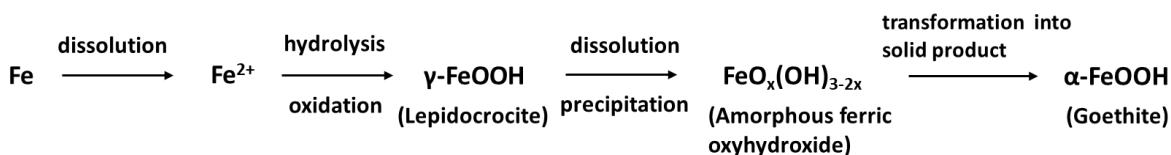
Therefore, in all the coated substrates after exposure to SST, the most significant rust product was γ-FeOOH, which reiterates that the corrosion process is still at its onset. The difference is just that the SST gives real-time test results, whereas electrochemical studies provide results based on the sensitivity of the interface during the corrosion process.

Since SST is an accelerated test, the corrosion is faster during the salt spray test than during the polarization and electrochemical impedance studies. As a result, we see iron oxidation products first, followed by self-healing products formed by corrosion inhibitor migration. Furthermore, the direct addition of a corrosion inhibitor is more effective since migration of corrosion inhibitor from the matrix is faster than from the narrow lumen of HNT. Moreover, as shown in Fig 6.18 (a), cationic corrosion inhibitors may not be effectively encapsulated into the positively charged lumen of HNT, which could be another reason for the lower corrosion resistance of coatings derived from corrosion inhibitors encapsulated into HNT Figure 6.25 shows the schematics of coated mild steel substrate when exposed to different corrosion methods.
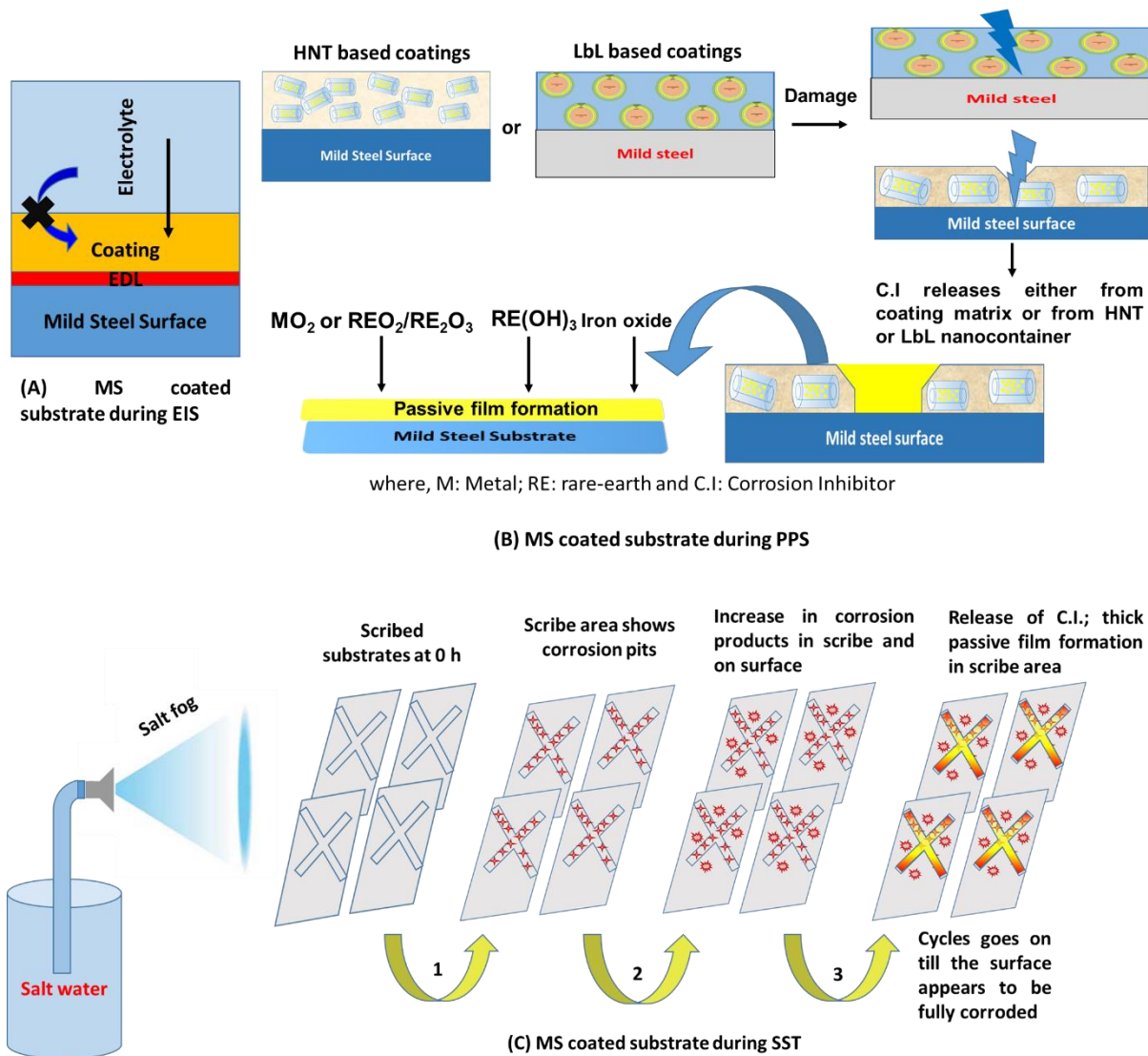
Fig. 6.25. Schematics of MS coated substrates during exposure to different corrosion techniques

6.3. Conclusions

- The present investigation confirmed that the silica sol consisting of inorganic corrosion inhibitors, i.e., transition metal and rare-earth elements, showed self-healing action on mild steel substrates.

- Electrochemical studies revealed that ZS coatings have shown better corrosion resistance than other RE based coatings, and the current density has decreased from 10^{-6} A/cm^2 measured for all other coatings to 10^{-10} A/cm^2 for ZS coatings.

191

- Coatings based on the encapsulation of corrosion inhibitor into HNT confirmed that the ZHS coating performed well in terms of corrosion resistance and self-healing action among all other REH-based coatings.

- As per electrochemical impedance studies, the charge transfer resistance of Zr-LbL was 1.42×10^4 $\Omega.cm^2$, which is much higher than the charge transfer resistances of Ce-LbL and La-LbL, 4090 $\Omega.cm^2$ and 2900 $\Omega.cm^2$, respectively. The encapsulation of Zr in LbL NC showed higher corrosion resistance and lower corrosion rate when compared to Ce in LbL NC and La in LbL NC coatings.

- Micro-Raman spectroscopic analysis for cerium and zirconium based coatings reveals that the inhibitor metal oxides are found in the scribed area, confirming the passive film formation leading to self-healing of the damaged region.

- Salt spray test revealed that the coatings based on direct addition of corrosion inhibitors into the sol exhibited higher corrosion resistance compared to encapsulation. The FESEM images confirmed that the corrosion is more pronounced on HNT and LbL-based coatings.

- All the investigations confirmed that the direct addition of inorganic corrosion inhibitors into the coating matrix exhibits higher corrosion protection when compared to encapsulation based coatings.

6.4. References:

[1] Yuan, P., Southon, P. D., Liu, Z., Green, M. E. R., Hook, J. M., Antill, S. J., Kepert, C. J., Functionalization of halloysite clay nanotubes by grafting with 3–aminoptopyltriethoxysilane, J. Phys. Chem. C. 112 (2008) 15742-15751.

[2] Gupta, S. K., Gupta, R., Vats, B. G., Gamare, J. S., Kadam, R. M., Inversion in usual excitation intensities from solid state phosphor and improved fluorescence of Eu^{3+} ion in type (IV) deep eutectic solvent, J. Lumin. 235 (2021) 118026.

[3] Rodic, P., Zanna, S., Milosev, I., Marcus, P., Degradation of sol-gel acrylic coatings based on si and zr investigated using electrochemical impedance, infrared and x-ray photoelectron spectroscopies, Front. Mater. 8 (2021) 756447.

[4] Joshi, A., Abdullayev, E., Vasiliev, A., Volkova, O., Lvov, Y., Interfacial modification of clay nanotubes for the sustained release of corrosion inhibitors, Langmuir. 29 (2013) 7439-7448.

[5] Kamburova, K., Boshkova, N., Boshkov, N., & Radeva, T., Design of polymeric core-shell nanocontainers impregnated with benzotriazole for active corrosion protection of galvanized steel, Colloids Surf. A: Physicochem. Eng. 499 (2016) 24–30.

[6] Gautam, A., Raju, K. R. C. S., Gobi, K. V., Subasri, R., Effect of transition metal and different rare-earth inhibitors-based sol–gel coatings on corrosion protection of mild steel, Met. Mater. Int. 29 (2023) 2909-2925.

[7] Oh, J., Orejon, D., Park, W., Cha, H., Sett, S., Yokoyama, Y., Thoreton, V., Takata, Y., Miljkovic, N., The apparent surface free energy of rare earth oxides is governed by hydrocarbon adsorption, iScience. 25 (2022) 103691.

[8] Lvov, Y., Wang, W., Zhang, L., Fakhrullin, R., Halloysite clay nanotubes for loading and sustained release of functional compounds, Adv. Mater. 28 (2016) 1227-1250.

[9] Milosev, I., Kapun, B., Rodic, P., Iskra, J., Hybrid sol-gel coating agents based on zirconium (IV) propoxide and epoxysilane, J. Sol-Gel Sci. Technol. 74 (2015) 447-459.

[10] Dastgheib, A., Attar, M., Zarebidaki, A., Evaluation of corrosion inhibition of mild steel in 3.5 wt% sodium chloride solution by cerium nitrate. Met. Mater. Int. 26 (2020) 1634-1642.

[11] Zhu, Y., Zhuang, J., Yu, Y., Zeng, X., Research on anti-corrosion property of rare earth inhibitor for X70 steel, J. Rare Earths. 31 (2013) 734-740.

[12] Abdullayev, E., Lvov, Y., Halloysite clay nanotubes as a ceramic skeleton for functional biopolymer composites with sustained drug release, J. Mater. Chem. B. 1 (2013) 2894.

[13] Massaro, M., Noto, R., Riela, S., Halloysite nanotubes: smart nanomaterials in catalysis, Catalysts. 12 (2022) 149.

[14] D. de la Fuente., Alcantara, J., Chico, B., Diaz, I., Jimenez, J. A., Morcillo, M., Characterization of rust surfaces formed on mild steel exposed to marine atmospheres using XRD and SEM/Micro-Raman techniques, Corros. Sci. 110 (2016) 253-264.

[15] Hostis, V. L., Amblard, E., Guillot, W., Paris, C., Bellot-Gurlet, L., Characterisation of the steel concrete interface submitted to chloride-induced-corrosion, Mater. Corros. 64 (2013) 185-194.

[16] Gnyba, M., Szczerska, M. J., Keranen, M., Suhonen, J., Sol-gel materials investigation by means of Raman spectroscopy, Proceedings, XVII IMEKO World Congress. (2003) 1-5.

[17] Manriquez, M. E., Michel, P., Bokhimi, X., Goerne, T. M. L., Quintana, P., Coronado, J. M., X-ray diffraction, Raman scattering study of nanostructured ZrO_2-TiO_2 oxides prepared by sol-gel, J. Nanosci. Nanotechnol. 8 (2008) 1-7.

[18] Ji, P., Wang, Z., Shang, X., Zhang, Yu., Liu, Y., Mao, Z., Shi, X., Direct observation of enhanced Raman scattering on nanosized ZrO_2 substrate: charge-transfer contribution, Front. Chem. 7 (2019) 245.

[19] Mashtaylar, D. V., Imshinetskiy, I.M., Nadaraia, K. V., Gnedenkov, A. S., Sinebryukhov, S. L., Ustinov, A. Y., Samokhin, A. V., Gnedenkov, S. V., Influence of ZrO_2/SiO_2 nanomaterial incorporation on the properties of PEO layers on Mg-Mn-Ce alloy, J. Magnes. Alloy. 10 (2022) 513-526.

[20] Aggoun, K., Chaal, L., Creus, J., Sabot, R.m Saidani, B., Jeannin, M., Marine Corrosion resistance of CeO_2/$Mg(OH)_2$ mixed coating on a low alloyed steel, Surf. Coat. Technol. 372 (2019) 410-421.

[21] Kainbayev, N., Sriubas, M., Virbukas, D., Rutkuniene, Z., Bockute, K., Bolegenova, S., Laukaitis, G., Raman study of nanocrystalline-doped ceria oxide thin films, Coatings. 10 (2020) 432.

[22] Fonna, S., Ibrahim, I. B. M., Gunawarman, Huzni, S., Ikhsan, M., Thalib. S., Investigation of corrosion products formed on the surface of carbon steel exposed in Banda Aceh's atmosphere, Heliyon. 7 (2021) 06608.

[23] D. de la Fuente, Diaz, I., Simancas, J., Chico, B., Morcillo, M., Long-term atmospheric corrosion of mild steel, Corros. Sci. 53 (2011) 604-617.

[24] Alcantara, J., D. de la Fuente., Chico, B., Simancas, J., Diaz, I., Morcillo, M., Marine atmospheric corrosion of carbon steel: A review. Materials. 10 (2017) 406.

[25] Xiao K., Li Z., Song, J., Bai Z., Xue W., Wu J., Dong C., Effect of concentrations of Fe^{2+} and Fe^{3+} on the corrosion behaviour of carbon steel in Cl^- and SO_4^{2-} aqueous environments, Met. Mater. Int. 27 (2021) 2623-2633.

[26] Buchheit, R. G., Cunningham, M., Jensen, H., Kendig, M. W., Martinez, M. A., A correlation between salt spray and electrochemical impedance spectroscopy test results for conversion-coated Al alloys, NACE International. 1998

[27] Kefallinou, Z., Zhou, X., Curioni, M., Electrochemical testing practices of environmentally friendly aerospace coatings for corrosion performance assessment, Surf Interface Anal. 51 (2019) 1173-1183.

CHAPTER-7

Summary and Conclusions

CHAPTER 7

Summary and Conclusions

7.1. Summary

Chapter 1 - Introduction: The importance of timely protection of mild steel against corrosion using autonomous self-healing protective coatings has been discussed in detail with the review of various literature reports. Mild steel (MS) is regarded as one of the desirable materials for construction because of its excellent mechanical properties such as ductility, tensile strength, etc [1]. A detailed literature review was carried out on the use of different types of corrosion inhibitors, different nanocontainers loaded with corrosion inhibitors followed by addition into the coating matrix for corrosion protection of mild steel. Nanocontainers encapsulating the corrosion inhibitors show controlled release and avoids excess of leaching. Such nanocontainer-based coatings possess enhanced anti-corrosion properties for longer durations.

The novelty of this thesis work is to analyze the effect of benzotriazole (BTA) and other inorganic corrosion inhibitors such as rare-earths encapsulated into halloysite nanotube and layer-by-layer nanocontainers. So far, there are no reports, (i) on the use of these nanocontainers into the silica matrix for corrosion protection of mild steel and (ii) on the use of the wide range of rare earth as well as a comparison of their protection efficiency among themselves and with the transition metal-based corrosion inhibitor, Zr^{4+}. The coatings generated were analyzed systematically for their anti-corrosion performance with the help of electrochemical impedance spectroscopy (EIS) and potentiodynamic polarization studies (PPS), salt-spray test and scanning vibrating electrode technique (SVET).

Chapter 2 - This chapter details the experimental procedures with precise quantities and conditions for the preparation of various matrix sols, loading of corrosion inhibitors into nanocontainers, cleaning and coating of mild steel substrates, characterization of substrates and electrochemical investigations. A detailed experimental schematic is shown in Figure 7.1.

Corrosion Inhibitor: Benzotriazole(BTA), Zr^{4+}, Ce^{3+}, La^{3+}, Gd^{3+} and Er^{3+}
↓
Loading into LbL (Zr^{4+}, Ce^{3+}, La^{3+}) and HNT nanocontainer
↓
Dispersing into the sol-gel matrix
↓
Dip-coating on Mild Steel Substrates
↓
Curing at 130 °C for 1 h

Characterization of Nanocontainers
- FESEM-EDS, TEM
- XRD, BET, FTIR
- Zeta Potential Measurements

Coating Characterization
- Thickness Measurements
- Tape Adhesion Test
- Electrochemical Studies: Electrochemical Impedance spectroscopy (EIS) and Potentiodynamic Polarization studies (PPS)
- Salt spray test (SST)
- Self-repairing activity: Scanning Vibrating Electrode Technique (SVET), Micro-Raman Spectroscopic analysis

Fig. 7.1. Schematic representation of experimental procedure

Techniques such as field emission scanning electron microscopy/ energy dispersive spectroscopy (FESEM/EDS), transmission electron microscopy (TEM), X-ray diffraction (XRD), Brunauer-Emmett-Teller (BET), and Fourier transform infrared (FTIR) were used to confirm the loading of the corrosion inhibitors into the nanocontainers. Potentiodynamic polarization studies and electrochemical impedance spectroscopy were used to validate the coatings corrosion properties. The self-healing action of the coatings was confirmed by exposing the scribed samples in salt spray followed by elemental analysis, Micro-Raman analyses and scanning vibrating electrode technique (SVET).

Chapter 3 – In this chapter, benzotriazole (BTA) encapsulated nanocontainer-based self-healing coatings has been investigated for corrosion protection of mild steel. SEM images for as-received iron oxide particles showed that particles have spherical structure with average diameter of 30 nm. After deposition of polyelectrolyte layers and BTA layer, the average particle diameter increased up to 200 nm and showed the presence of Fe, O, C, Na, Cl and N (Fig. 7.2 a,b). SEM images for as-received HNTs shows transparent hollow lumen with presence of Al, Si and O. After loading the BTA, the hollow lumen appears to be denser and EDS analysis confirms the presence of Al, Si, O, C and N (Fig. 7.2 c,d). XRD analysis for as-received iron oxide particles shows maximum intensity peak at 2θ value of $35°$ (Fig. 7.2e), indicating that the crystal structure of α-Fe_2O_3 was tetragonal (International Centre for Diffraction Data, ICDD File no. 04-014-7214). Zeta potential values after depositing each layer was in the range of $\pm$ 15 to $\pm$ 30 mV, thereby confirming that the particles are highly stable without the formation of any agglomerates. Electrophoretic mobility values as shown in Fig.

7.2f, confirmed the surface charge of each layer was in accordance with the charge of each layer and are in agreement with those reported in literature [2].
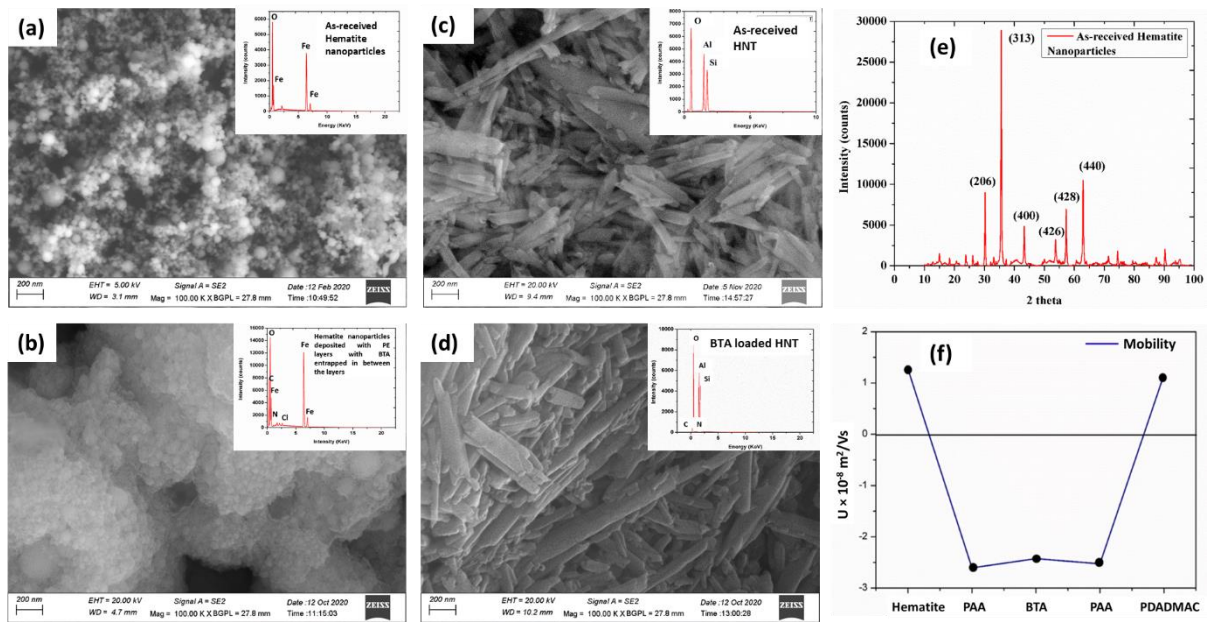

Fig. 7.2. SEM images of (a) as-received iron oxide nanoparticles, (b) polyelectrolyte layers and benzotriazole (BTA) layer deposited on iron-oxide nanoparticles, (c) as-received halloysite nanotubes (HNT), (d) BTA encapsulated into HNT, (e) XRD pattern for as-received iron-oxide nanoparticles, and (f) plot for electrophoretic mobility of layer-by-layer nanocontainer

Electrochemical studies confirmed that the loading of BTA into the nanocontainers provided better corrosion resistance and barrier properties when compared to direct addition into the sol-gel matrix. EIS data reveals that the BHS coatings possess higher impedance values. The corrosion current density for BTA encapsulated into HNT was very low in the order 10^{-10} A/cm^2, when compared to other coatings which shows higher current density in the order 10^{-6} A/cm^2. This indicates that the controlled release of BTA from HNT provided better self-healing properties and good corrosion resistance when compared to uncoated and other coated substrates.

Salt spray test confirmed that BTA loaded nanocontainer based coatings possess good corrosion inhibition, indicating that sustained release of BTA imparts self-healing action of the scribed area (Fig. 7.3). The BLLS coating showed enhanced corrosion protection even after 10 h exposure to salt spray, because of the swelling of the polyelectrolyte layers due to adsorption

of electrolyte solution imparting protection for longer durations when compared to other coatings. In addition, BTA acts as a next step protection by self-healing the surface defects [3].
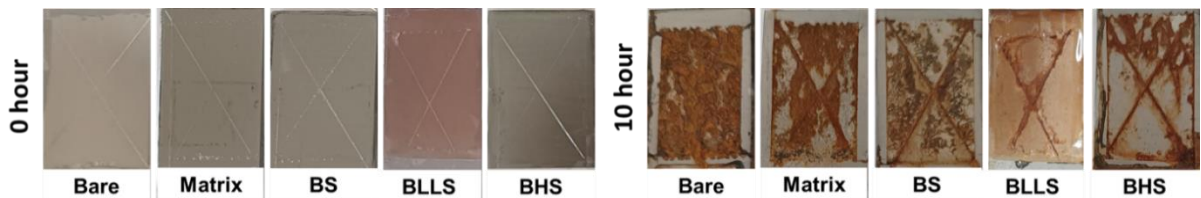

Fig. 7.3. Images of coated and bare mild steel substrates before and after salt spray exposure

Chapter 4 – In this chapter, capped BTA-encapsulated halloysite nanoclay-based self-healing silica coatings was investigated for corrosion protection of mild steel. To confirm the loading of BTA and capping of halloysite nanotubes, techniques such as TEM, BET, XRD and FTIR were employed. TEM analysis confirmed that the tube has empty lumen with internal diameter of 15 to 20 nm and length of the tube was 0.5 to 1.0 μm. After BTA loading, the inner lumen appeared dense, whereas after capping, the halloysite surface showed the presence of nanocapsules at the ends and on the surface.

For capped BTA loaded HNTs, maximum corrosion protection efficiency was found for 5 wt% loading into the sol-gel matrix. It should be noted that in the case of uncapped HNT, the optimum loading was only 2 wt%, whereas, in the case of capped HNT, the optimum loading was found to be 5 wt%. This difference in the optimum loadings could be due to an enhanced compatibility of the capping agent, UFNCs, with the silica gel coating matrix, which helps to disperse more amount of capped HNT into the coating matrix.

To confirm the corrosion protection efficiency of the 5 wt% capped inhibitor loaded HNT coating, the electrochemical studies were performed for maximum of 10 h duration. It was observed from Nyquist plots that the impedance values increased with an increase in exposure time. The loaded nanotubes and nanocapsules used for capping acted as a nanofiller to conceal the voids of the coating and make it more intact, thus showing advanced barrier action. Potentiodynamic polarization studies are also well in agreement with EIS studies. The decrease in corrosion current density confirmed the release of the corrosion inhibitor and thus imparting self-healing property to the coating.

SVET analysis was carried out for bare and only BTA loaded HNT based coating. The samples were exposed to 3.5 wt% NaCl solution (*in-situ*) and current density maps were obtained for different time durations. It was evident that with increase in time duration the anodic current on and near the scribe area for bare mild steel increases, red colour peaks become dominant and it decreases for BTA loaded HNT coating, confirming the self-healing action of the inhibitor by forming a passive film as shown in Fig. 7.4.
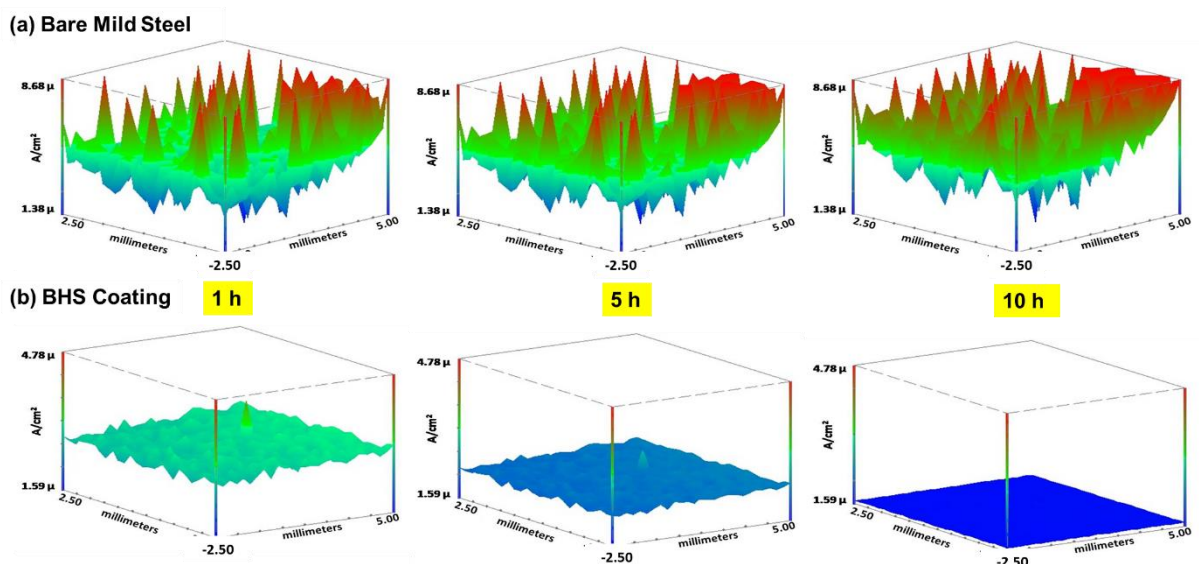

Fig. 7.4. Current density maps for bare and 2 wt% BTA-encapsulated HNT matrix sol coated (BHS) mild steel substrates after immersing in 3.5 wt% NaCl solution at different time intervals

Chapter 5 – The effect of pH on the controlled release of BTA from HNTs for corrosion protection of mild steel was investigated in this chapter. The amount of BTA released at three different pHs (pH = 3, 7 and 10) was monitored via UV-Vis spectroscopy. The highest amount of total BTA released at the end of 10 h was taken as 100% of the amount released, since the total amount of BTA released attained a saturation level at the end of 10 h of release. In the initial 30 min of time, there was a sharp increase in the release of BTA at all the pH values. At pH 3, 7 and 10, the extent of BTA released in the medium was 48%, 30% and 20%, respectively. After 1 h, the BTA release at pH 3 was maximum, whereas, for pH 7 and 10, the percentage of BTA release was nearly same. At pH 3, there was a sharp increase in the release rate of BTA, indicating that it could provide better self-healing action and protect the mild steel substrate from corrosion at its onset. Though the release rate for pH 7 is steady, it can be concluded that the amount of BTA released has become constant with time. Therefore, the amount of BTA

released at pH 7 may not be sufficient for corrosion protection, whereas, an optimum BTA release was observed at pH 10. Hence, among all the pH, the release rate at pH 10 has shown sustained and prolonged release of benzotriazole and, therefore, shows the self-healing action for a longer time duration.

Salt immersion test analysis helped further in understanding the inhibition action of BTA at different pH levels. The bare and BHS coated mild steel substrates were immersed in 3.5 wt% NaCl solution at pH 3, 7 and 10 for different time durations. At different time intervals, the samples were withdrawn and examined under an optical microscope to carefully analyse the extent of corrosion. Optical images as shown in Fig. 7.5 confirmed that at all pH, the bare mild steel sample corroded extensively, whereas for BHS coated MS substrates, at pH 10 the surface near to the scribe area is not affected much as compared to the other two pH i.e., 3 and 7.
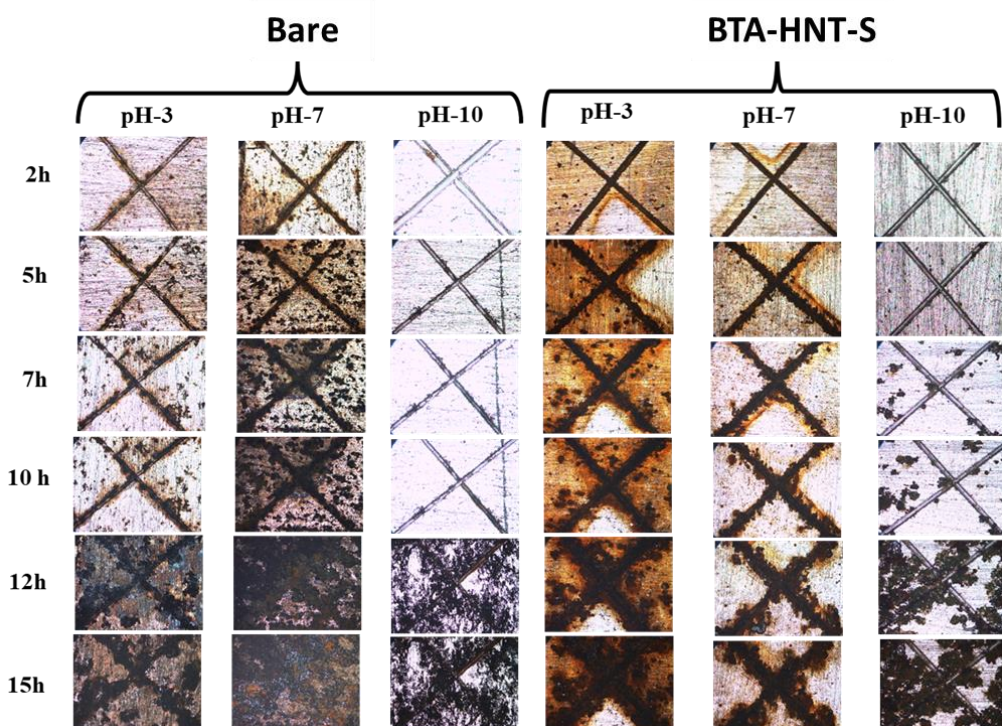
Fig. 7.5. Optical microscope images of bare and BTA-HNT sol coated mild steel substrates at different pH (3, 7, 10) at different intervals of time

From the literature, it is reported that the cracks and water absorption affect the coating resistance and capacitance, because chloride ion makes its way to enter inside the coating through water as it is soluble in water. Higher water absorption by the coatings causes chloride ions to penetrate and partially damage the coating [4]. Therefore, more amount of BTA is

released at pH 3 and 7 to repair the coating damage. With more release of BTA, the probability of freely available BTA after occupying the adsorbing site also increases. As a result, the coating takes in more water when the BTA concentration increases. This facilitates the entry of Cl^- ion into the coating, resulting in a poor anti-corrosion performance at pH 3 and 7. Therefore, the optimum condition for BTA to work efficiently is at pH 10, where the coating integrity, as well as the excessive leaching of BTA is controlled.

Chapter 6 – In this chapter, the effect of transition metal and different rare-earth inhibitors-based sol-gel coatings on corrosion protection of mild steel was studied. This chapter is divided into three parts: (i) direct addition of corrosion inhibitors into matrix sol, (ii) loading of corrosion inhibitors into halloysite nanotube, and (iii) loading selected corrosion inhibitors into layer-by-layer nanocontainers.

Different rare-earth metals such as La^{3+}, Ce^{3+}, Er^{3+} and Gd^{3+} and transition metal i.e., Zr^{4+} corrosion inhibitors were encapsulated into halloysite nanotube. Loading of the metals into HNTs was confirmed from FESEM/EDS, TEM, FTIR and XRD analyses. TEM images (Fig. 7.6) along with the elemental mapping for as-received HNTs and inhibitor loaded HNTs, confirmed the loading of corrosion inhibitor, Zr^{4+} into HNTs. SEM images confirmed that the morphology of the nanotubes was intact after loading the corrosion inhibitors.

XRD patterns for as-received HNT and different corrosion inhibitor loaded HNTs showed similar XRD patterns with no change in the interlayer spacing between silica and alumina layers of HNT. BET analysis also confirmed the loading of corrosion inhibitors into HNTs as the pore volume decreased for inhibitor-loaded HNTs when compared to as-received HNTs, **HNT-** 0.38 cc/g, **Zr-HNT-** 0.27 cc/g, **Ce-HNT-** 0.28 cc/g, and **Er-HNT-** 0.31 cc/g.

XRD pattern for in-house synthesized Fe_2O_3 nanoparticles showed that the particles have rhombohedral crystal structure (ICDD File no. 01-080-5409). Similar XRD patterns were observed for only layer-by-layer nanocontainer and corrosion inhibitor sandwiched in between the layers. SEM images of Fe_2O_3 nanoparticles showed that the particle's size is between 100 to 300 nm with a distorted rhombohedral-like structure. After deposition of polyelectrolyte layers and inhibitor layer, the particles appear to be more porous rather than crystalline. EDS analysis confirms the presence of added corrosion inhibitors i.e., Ce^{3+}, La^{3+} and Zr^{4+} was present in the Ce-LbL, La-LbL and Zr-LbL NCs, respectively. The zeta potential values of α-Fe_2O_3 nanoparticles at all layers were observed to be in the range of ±20 to ±40 mV,

demonstrating their extreme stability, devoid of any agglomeration. Electrophoretic mobility values confirmed the surface charge of each layer was in accordance with the charge of each deposited layer.
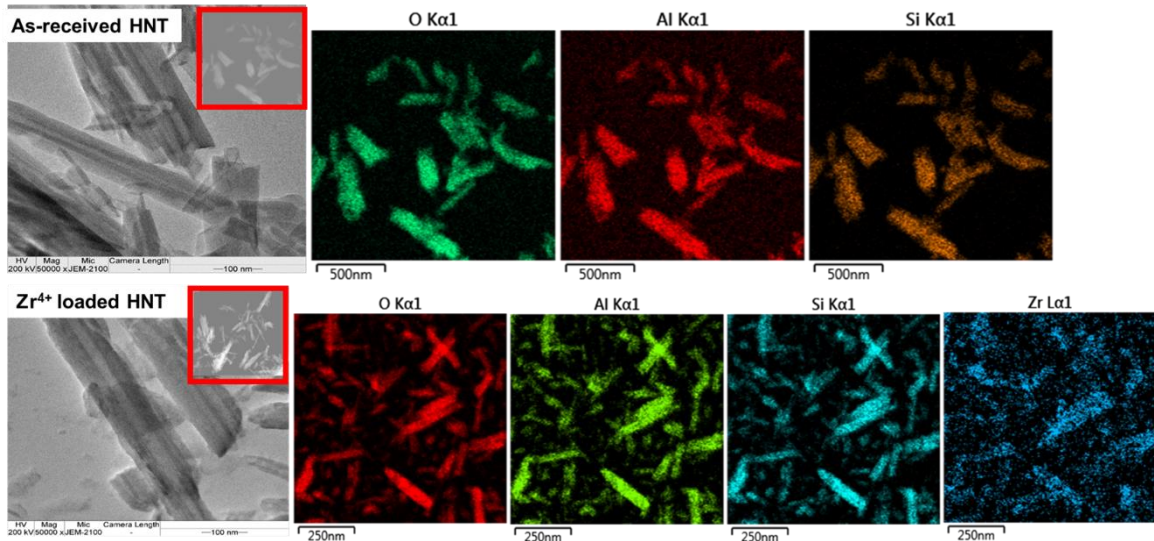

Fig. 7.6. TEM images along with EDS mapping for as-received halloysite nanotubes (HNT) and Zr^{4+} encapsulated into HNT

Zr^{4+}, La^{3+}, Ce^{3+}, Er^{3+} and Gd^{3+} corrosion inhibitors were directly added to matrix sol and coated on mild steel substrates. EIS and PPS (Fig. 7.7 a and b) confirmed that on Zr^{4+} based coatings have highest charge transfer resistance i.e., 4.88×10^7 $\Omega.cm^2$ and least corrosion current density i.e., 0.00017×10^{-6} A/cm^2 when compared to other coatings, suggesting that this coating possesses high barrier properties. The zirconium catalyses polymerisation of the epoxide ring of GPTMS into polyethylene oxide, which in turn forms a long polymer chain, hence providing excellent barrier and self-healing properties [5]. The order of corrosion resistance follows CS > ES > GS > LS.

Coatings based on corrosion inhibitor encapsulated into HNTs: From EIS and PPS data, it was confirmed that the ZHS based coating showed higher impedance and least corrosion current density when compared to other coatings as evident from Fig. 7.7 c and d. The inorganic/rare earth elements being cationic and hydrophilic makes it difficult to form a chemical bond with the Al^{3+} ions, due to which the inhibitors may not completely load in the empty and positively charged lumen of HNT. Thus, loading efficiency may be less when compared to other organic molecules. On the other hand, the adsorption of these inorganic or RE on the outer surface of HNT is more prominent due to the affinity towards the hydroxyl

group present on the outer surface. Therefore, during the corrosion process, these ions are released slowly, thereby showing lesser corrosion protection when compared to direct addition [6].

Similar effect was observed when selective corrosion inhibitors, i.e., Zr^{4+}, La^{3+} and Ce^{3+} were sandwiched in between the polyelectrolyte layers. Loading or entrapping these corrosion inhibitors into LbL NCs reduces its active corrosion inhibition as the ions responsible for this are not free. With respect to direct addition, the inhibition action of corrosion inhibitor encapsulated into LbL NCs follows the similar trend but with decreased self-healing ability. Figure 7.7 (e and f) shows impedance and polarization plots for different coatings. Zr-LbL coating have shown increase in charge transfer resistance and decrease in corrosion current which is due to the barrier effect caused by the increased thickness of the coating and active inhibition of the Zr^{4+}. Ce-LbL and matrix coatings have performed relatively same. La-LbL coatings do possess the capability of active inhibition when compared to bare mild steel substrates.
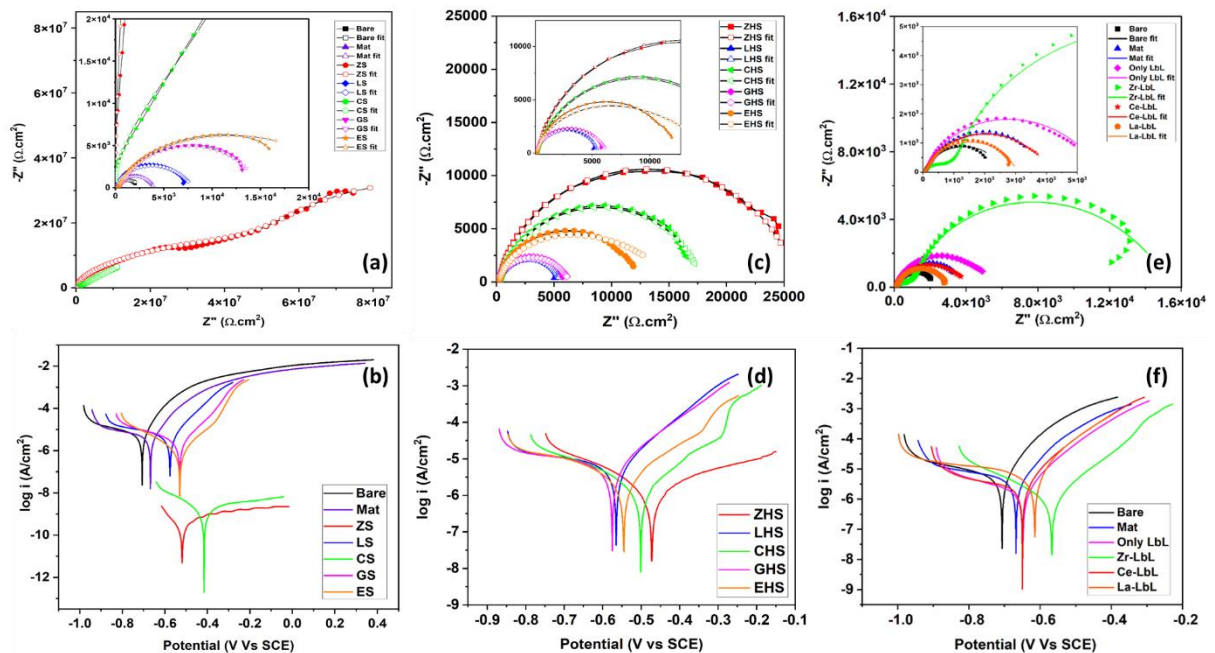

Fig. 7.7. (a & b) Nyquist and Tafel plots for coatings based on direct addition of inorganic corrosion inhibitor, (c & d) Nyquist and Tafel plots for coatings based on corrosion inhibitor encapsulated into halloysite nanotubes, and (e & f) Nyquist and Tafel plots for coatings based on corrosion inhibitor sandwiched in between the layer-by-layer nanocontainer

In order to evaluate the self-healing action, Micro-Raman spectroscopic studies for bare, zirconium and cerium-coated MS samples (ZS, ZHS, CS and CHS) were carried out on scribed bare and coated MS substrates, after exposure to 3.5 wt% sodium chloride solution for 1 hr. The Raman analysis (as depicted in Fig. 7.8) confirmed the self-healing action of the corrosion inhibitors, as Zr^{4+} and Ce^{3+}/Ce^{4+} ions have been released in the scribed region and form a passive film by forming stable oxides of CeO_2 and ZrO_2.
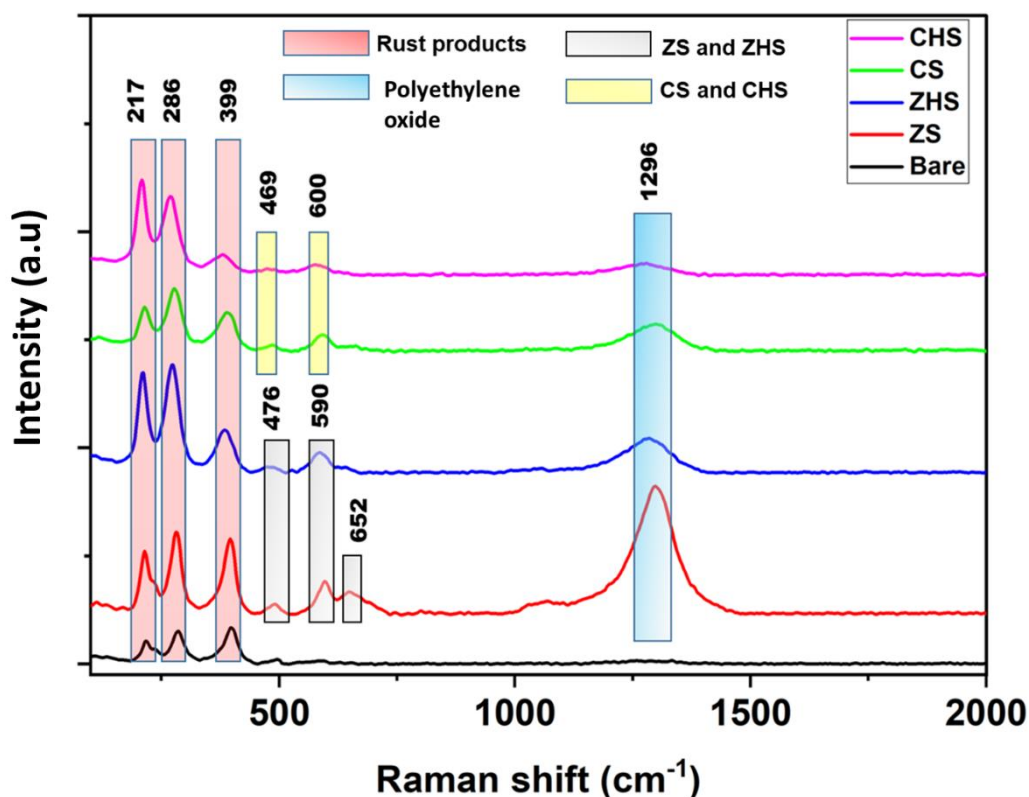
Fig. 7.8. Micro-Raman spectra for bare and coated substrates obtained after exposing the substrates in 3.5 wt% sodium chloride solution for 1 h

Salt spray test was carried out for direct addition, inhibitor loaded HNTs and inhibitor loaded LbL nanocontainer based coatings. It is clear from the images that direct addition of these corrosion inhibitors provided higher corrosion resistance when compared to encapsulation. The trend for corrosion protection for direct addition is as follows: LS > CS > ZS > Matrix > Bare and for encapsulation into HNT is: LHS > ZHS > CHS. The data obtained in the electrochemical technique is basically about the interface chemistry between the coating and the substrate which provides quantitative test results. During exposure in the SS chamber,

the electrolyte (5 wt% NaCl solution) layer is continuously refreshed on the substrate, and the effect of the inhibitor may differ at each time [7].

For coatings based on LbL NCs, Zr-LbL have shown better barrier protection as a result least corrosion products were visible on the surface when compared to Ce-LbL and La-LbL (Fig. 7.9). Zr-LbL being more viscous and having highest coating thickness provides enhanced barrier protection as well as corrosion inhibition.
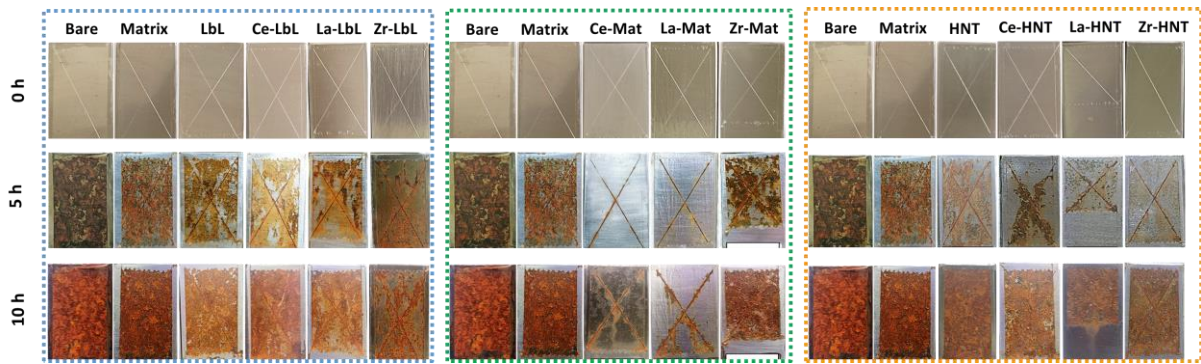

Fig. 7.9. Images of mild steel substrates coated with sols in which different corrosion inhibitors are directly added, corrosion inhibitors encpasulated into halloysite nanotubes and corrosion inhibitors sandwiched in between the layer-by-layer nanocontainers that are exposed to salt spray

7.2. Conclusions

Sol-gel matrix was found to be a promising coating material that provided good barrier protection to mild steel. This research work was more focused on the development of an eco-friendly coating for MS substrates as an alternative to carcinogenic chromate conversion coatings (CCC) or phosphate conversion coatings (PCC). The coating formulation is based on addition of self-healing additives, which impart autonomous-healing properties to the steel substrates, thereby increasing their durability. The halloysite nanotubes and layer-by-layer nanocontainers served as effective nanocontainers for loading different types of corrosion inhibitors. The smart coatings developed by using inhibitor loaded nanocontainers or direct addition of inorganic corrosion inhibitors provided prolonged corrosion protection by self-healing the damage.

For HNT-based coatings

The corrosion inhibitors BTA as an organic corrosion inhibitor, and other inorganic corrosion inhibitors (Zr^{4+}, La^{3+}, Ce^{3+}, Er^{3+} and Gd^{3+}) were successfully encapsulated into the halloysite nanotubes, which was confirmed by TEM, BET pore volume and XRD analyses. The developed self-healing coatings exhibited enhanced corrosion resistance and least corrosion rate when applied on mild steel. Capped BTA loaded HNT based coatings showed excellent corrosion protection when compared to uncapped BTA loaded HNTs. Release rate experiments also confirmed the controlled release of BTA from HNTs at different pH with maximum protection efficiency at pH 7. The coatings developed by directly adding inorganic corrosion inhibitors showed least corrosion rate and higher corrosion resistance compared to loading them into HNTs. The mechanism of self-healing by the formation of passive layer on the damage site of the coatings was confirmed by micro-Raman analysis and scanning vibrating electrode technique.

For LbL-based coatings

The developed coatings showed good corrosion resistance when organic or inorganic corrosion inhibitors were intercalated into LbL nanocontainers. Zr-LbL coatings showed better corrosion protection compared to BTA-LbL coatings. Direct addition of inorganic corrosion inhibitors (Zr^{4+}, La^{3+}, Ce^{3+}, Er^{3+} and Gd^{3+}) provided enhanced barrier and corrosion protection properties in comparison to BTA directly added to sol-gel matrix.

Comparison between the best of the coatings as discussed with phosphate and chromate conversion coatings is shown in Fig. 7.10. Figure 7.10 shows charge transfer resistance and corrosion current density plots. It is evident the charge transfer resistance was maximum for ZS based coatings i.e., 4.88×10^7 followed by CBHS (2.2×10^7), CCC (1.74×10^7), PCC (1.5×10^5), matrix and bare, confirming the excellent barrier effect provided by ZS and CBHS when compared to CCC and PCC, respectively. Similarly, corrosion current density decreases in the order: bare < matrix < PCC < CCC < CBHS < ZS. The prominent self-healing behaviour was observed for CBHS and ZS coatings, confirming that they are suitable replacements for CCC and PCCs.

The comparison of normalized charge transfer resistance with respect to the coating thickness is tabulated in Table 7.1. The relative charge transfer resistance value follows similar trend as mentioned above.
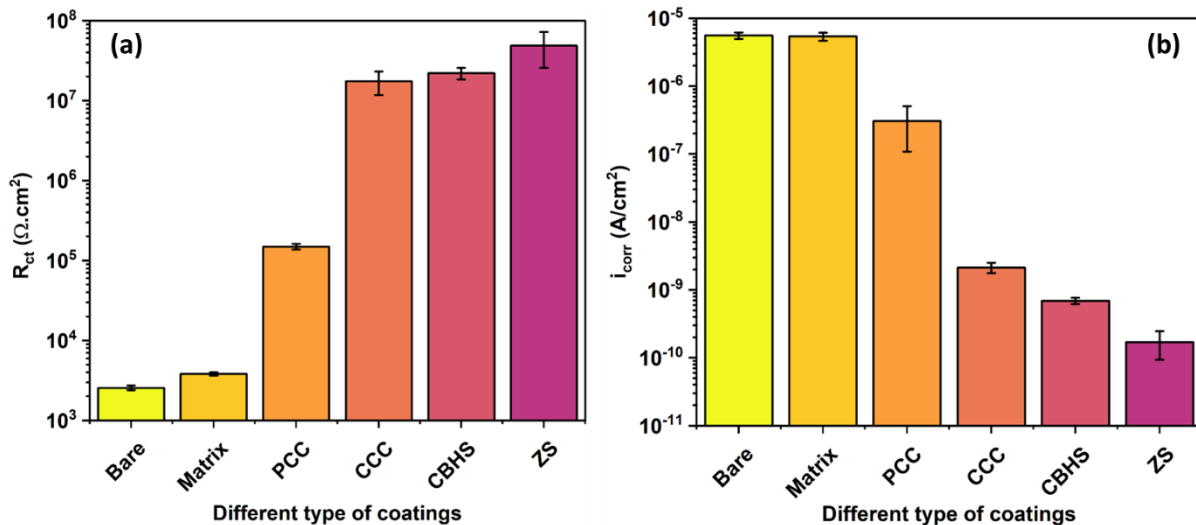
Fig. 7.10. Comparison of (a) charge transfer resistance and (b) corrosion current density for different type of coatings

Table 7.1. Comparison of normalized charge transfer resistance with respect to the coating thickness for best-performing coatings

Sample ID	Charge Transfer Resistance (R_{ct})	Coating Thickness (μm)	Normalized Charge Transfer Resistance (R_{ct})
ZS	4.88×10^7	8.0	6.1×10^6
CBHS	2.80×10^7	22.0	1.0×10^6
CCC	1.74×10^7	25.0	6.9×10^5
PCC	1.50×10^5	5.0	3.0×10^4
Matrix	3.80×10^3	3.3	1.1×10^3

WeatherOmeter test was carried out for best performing coatings to observe the ageing process in artificial weathering condition as per **ISO 11341**. From visual analysis as shown in Fig. 7.11 it was observed that the bare MS substrates have corroded aggressively with corrosion products covering the whole surface as exposure time increases. For matrix-coated MS, the corrosion product was seen only at the edges of the substrate along with some pit formation on the entire surface, suggesting that the corrosion is just initiated even after 100 h of exposure. For ZS coating, the corrosion products are more prominently observed near the edges with coating being intact even after 100 h of exposure. CBHS coating appear to be intact with no prominent corrosion either at the surface or at the edges. Therefore, the test analysis revealed

that the inhibitor-modified coated MS substrates exhibited enhanced performance, demonstrating superior active inhibition and excellent barrier properties, which consequently contributed to increased coating durability.
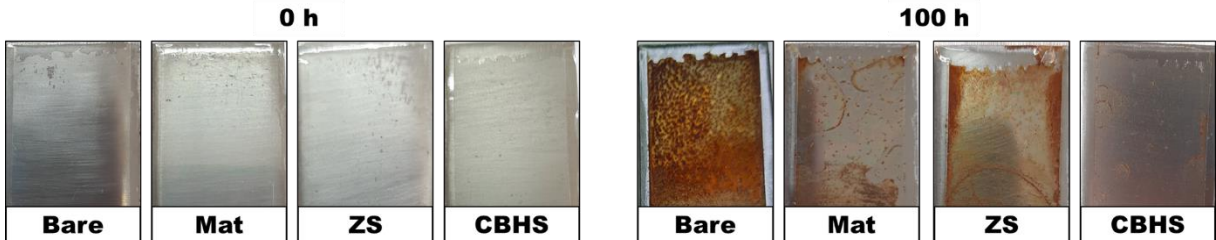
Fig. 7.11. Visual images of different coatings after exposing them to WeatherOmeter for 100 h

Scope for future work

• The developed eco-friendly self-repairing coatings can be used as a better replacement to carcinogenic chromate based coatings for corrosion protection of mild steel parts used in construction and oil-pipeline industries.

• As the synthesis and application strategy is simple and involves greener approach, it will allow for a reduction in huge economic losses and maintenance. The proposed research work can be scaled up and transferred into technology to industries looking for new and innovative corrosion protection methods.

7.3. References:

[1] Basik, M., Mobin, M., Chondroitin sulfate as potent green corrosion inhibitor for mild steel in 1 M HCl, J. Mol. Struct. 1214 (2020) 128231.

[2] Kamburova, K., Boshkova, N., Boshkov, N., Radeva, T., Design of polymeric core-shell nanocontainers impregnated with benzotriazole for active corrosion protection of galvanized steel, Colloids Surfaces A Physicochem. Eng. Asp. 499 (2016) 24–30.

[3] Ghazi, A., Ghasemi, E., Mahdavian, M., Ramezanzadeh, B., Rostami, M., The application of benzimidazole and zinc cations intercalated sodium montmorillonite as smart ion exchange inhibiting pigments in the epoxy ester coating, Corros. Sci. 94 (2015) 207–217.

[4] Sharifiyan, M. S., Sanaghi, A., Moradi, H., Chu, P. K., Effects of High Concentration of Benzotriazole on Corrosion Behavior of Nanostructured Titania-Alumina Composite Coating Deposited on Al 2024 By Sol-Gel Method, Surf. Coat. Technol. 321 (2017) 36-44.

[5] Milosev, I., Kapun, B., Rodic, P., Iskra, J., Hybrid sol-gel coating agents based on zirconium (IV) propoxide and epoxysilane, J. Sol-Gel Sci. Technol. 74 (2015) 447.

[6] Massaro, M., Noto, R., Riela, S., Halloysite Nanotubes: Smart Nanomaterials in Catalysis, Catalysts. 12 (2022) 149.

[7] Buchheit, R. G., Cunningham, M., Jensen, H., Kendig, M. W., Martinez, M. A., A Correlation Between Salt Spray and Electrochemical Impedance Spectroscopy Test Results for Conversion-Coated Aluminum Alloys, NACE International. (1998).

List of Publications

Publications in Peer-reviewed/Refereed International Journals

- Effect of Transition metal and Different Rare-Earth Inhibitors-based Sol-gel Coatings on Corrosion Protection of Mild Steel

  Aarti Gautam, K. R. C. Soma Raju, K. V. Gobi and R. Subasri

  Metals and Materials International 29 (2023) 2909-2925   **(I.F: 3.5)**

  https://doi.org/10.1007/s12540-023-01426-6

- Hybrid Silane Coatings based Benzotriazole loaded Aluminosilicate nanotubes for Corrosion Protection of Mild Steel

  Ramay Patra, **Aarti Gautam**, K. V. Gobi and R. Subasri

  Silicon 15 (2023) 6981-6996   **(I.F: 2.9)**

  https://doi.org/10.1007/s12633-023-02556-7

- Capped inhibitor-loaded halloysite nanoclay-based self-healing silica coatings for corrosion protection of mild steel

  Aarti Gautam, T. Siva, S. Sathiyanarayanan, K. V. Gobi and R. Subasri

  Ceramics International 48 (2022) 30151-30163   **(I.F. 5.5)**

  (https://doi.org/10.1016/j.ceramint.2022.06.288)

- **Nanocontainers for Self-Healing Coatings On Mild Steel**

  Aarti Gautam, K. V. Gobi, R. Subasri

  Journal of Innovative Materials in Extreme Conditions 2 (2021) 16-24

- Benzotriazole encapsulated nanocontainer-based self-healing coatings for corrosion protection of mild steel

  Aarti Gautam, K. R. C. Soma Raju, K.V. Gobi, R. Subasri

  "Recent Trends in Electrochemical Science and Technology", **Springer Proceedings in Materials, 15 (year) page-page** https://doi.org/10.1007/978-981-16-7554-6_1

Book chapters

- Book chapter entitled **"Bioinspired strategies for Corrosion Protection and Antifouling Coatings" authored by** K. R. C. Soma Raju, **Aarti Gautam**, Ramay Patra, K. Srinivasa

Rao, K. V. Gobi and R. Subasri submitted for publishing in **Scrivener Publishing (In-press) (2024)**

- Book chapter entitled "**Corrosion protection of metals/alloys through multifunctional sol-gel nanocomposite coatings**" authored by Swapnil H. Adsul, K. Pradeep Prem Kumar, S. Manasa, **Aarti Gautam**, K.V. Gobi, Shirish H Sonawane, R. Subasri has been published in e-book **"A Treatise in Corrosion Science, Engineering and Technology"** edited by U. Kamachi Mudali, Rani P. George, T. Subba Rao and S. Ningshen, Sep 2020. **(ISSN: 2509 6400).** https://doi.org/10.1007/978-981-16-9302-1_33

National and International Conferences/ Symposium/ Workshop Attended:

- Attended a two-day workshop on "Metallurgy for Non-Metallurgists: Industrial Practices (MNM-2023)" organized by Indian Institute of Metals, Hyderabad Chapter, at Hyderabad 6th – 7th November, 2023

- Presented a paper on "Anti-Corrosion Sol-gel Coating using Layer-by-Layer nanocontainer for Mild Steel Corrosion Protection" authored by **Aarti Gautam**, Ananya Behera, K. V. Gobi and R. Subasri during National Symposium on Electrochemical Science and Technology (NSEST)-2023 from 17th – 18th August, 2023, at ARCI-Hyderabad

- Presented a paper on "Slow and Sustained Release of Corrosion Inhibitors to Prolong the Corrosion Protection of Mild Steel" authored by **Aarti Gautam**, K. V. Gobi and R. Subasri during an International conference EUROCORR The Annual Congress of the European Federation of Corrosion, Belgium from 27th – 31st August, 2023

- Presented paper entitled "Self-healing Behavior of Smart Nanocontainer-based Sol-gel Coatings On Mild Steel" authored by **Aarti Gautam**, K. V. Gobi and R. Subasri during STREE 2020 National Conference & Expo from 24th- 26th November 2022, at Jawaharlal Nehru University, New Delhi

- Presented paper entitled "Comparison of Corrosion Protection of Organic and Inorganic Corrosion Inhibitors loaded Sol-gel Coatings on Mild Steel*"* authored by **Aarti Gautam**, K. V. Gobi and R. Subasri during International Conference on Corrosion and Coatings held from 07-08 December 2022, at CSIR-National Metallurgical Laboratory, Jamshedpur, India

- Presented a poster entitled "Smart Nanocontainer-based Environment Friendly Protective Coatings on Mild Steel" authored by **Aarti Gautam**, K. V. Gobi and R. Subasri during Bengaluru India Nano 2022 (BIN 2022) from 7th – 8th March 2022 (Online)

- Presented a paper entitled "Inhibitor Loaded Smart Nanocontainers as Self-Repairing Agents for Corrosion Protection Coatings On Mild Steel" on the occasion of National Science Day organized by ARCI on 28th February 2022

- Presented paper entitled "Investigations On Use of Inhibitor Loaded Halloysite Nanotubes and Polyelectrolyte Multi-layered Layer-by-layer as Self-Healing Materials for Corrosion Protection Coatings On Mild Steel" authored by **Aarti Gautam**, K. V. Gobi and R. Subasri during CORCON 2021 International Conference & Expo on Corrosion from 18th – 20th November 2021 at Mumbai (Online)

- Attended virtual workshop on "Metallurgy for Non-Metallurgist (MFNM-2021)" organized by "Indian Institute of Metals Baroda Chapter & Federation of Indian Chambers of Commerce & Industry (FICCI)" on March 20, 2021

- Attended virtual workshop on "Material Characterization" organized by "ARCI Hyderabad" on November 27, 2020

- Attended virtual workshop on "Surface engineering and Modification for Better Performance" organized by "IISc Bengaluru" on September 19, 2020

- Presented a paper on "Benzotriazole Encapsulated Nanocontainer based Self-Healing Coatings for Corrosion Protection of Mild Steel" at the "National Symposium on Electrochemical Science and Technology (NSEST -2020)" organized by "Electrochemical Society of India" from 21st – 22nd January, 2020 (Online)

Awards:

- Received the **"Best Paper Award"** for presenting a paper on Anti-corrosion Sol-gel Coating using Layer-by-Layer nanocontainer for Mild Steel Corrosion Protection" during National Symposium on Electrochemical Science and Technology (NSEST)-2023 from 17th – 18th August 2023, at ARCI-Hyderabad

- Received the **"Best Paper Award"** for presenting a paper on "Comparison of Corrosion Protection of Organic and Inorganic Corrosion Inhibitors Loaded Sol-gel Coatings on Mild Steel" at International Conference on Corrosion and Coatings (i3C) organized by IIM,

Jamshedpur in association with Tata Steel, CSIR-NML & NIT, Jamshedpur from 7th – 8th December, 2022

- Received the **"First Prize in Oral Presentation"** for presenting a paper on "Self-healing Behavior of Smart Nanocontainers-based Sol-gel Coatings On Mild Steel" during STREE 2020 National Conference & Expo from 24th- 26th November 2022, at Jawaharlal Nehru University, New Delhi

- Received "**Third prize"** for presentation entitled "Inhibitor Loaded Smart Nanocontainers as Self-Repairing Agents for Corrosion Protection Coatings On Mild Steel" on the occasion of National Science Day organized by ARCI on 28th February 2022

- Received **"Best Paper Award"** for presenting a paper titled "Investigations On Use of Inhibitor Loaded Halloysite Nanotubes and Polyelectrolyte Multi-layered Layer-by-layer as Self-Healing Materials for Corrosion Protection Coatings On Mild Steel" during CORCON 2021 NACE International Conference & Expo on Corrosion from 18th – 20th November, 2021 at Mumbai (Online)

Additional Information:

- Member of Electrochemical Society of India (ECSI) with Membership No. LM 356

- Member of Association of Materials Protection and Performance (AMPP) with Membership No. 11476666

- Popular writing Shortlisted among 300 best stories for AWSAR Award 2022

- Top 5 best oral presenters for K. V. Rao Young Scientist Award 2023 in Chemistry category

Personal Information of the Author:
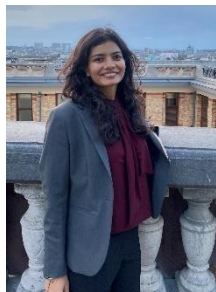
Aarti Gautam

Doctoral Researcher

📍 H.no. 8-93/1, Sai Nagar Colony, Road No.5, Balapur, Telangana

India, 500005

Email: aartigautam1993@gmail.com

Tel. (M): +91-8077013529

Passport No.: V3196439 (Valid up to 28/09/2031)

Gender: Female| **Date of Birth:** 13-10-1993| **Nationality:** Indian| **Languages known:** Hindi and English

❖ **CAREER OBJECTIVE:**

Motivated, adaptable and passionate Chemist with 4 years of research experience. I can contribute most of my learning and gain knowledge, experience and professional skills. I am determined to work in any challenging environment and willing to add value to organization's vision.

❖ **EDUCATION:**

❖ **Pursuing PhD (July 2019-Present):**

National Institute of Technology, Warangal, Telangana, 506004

Research Topic: *"Self-healing Corrosion Protection Coatings on Mild Steel"*

Course Work Completed: On the following subjects for one semester

1. Advanced Analytical Techniques

2. Advanced Electrochemical Methods

3. Modern Methods of Instrumental Analysis

4. Supramolecular Chemistry and Nanomaterials

5. English for Scientific Communication

❖ **Master of Science (M.Sc) in Polymer Science and Technology (2016-2018)**

Zakir Husain College of Engineering & Technology, Aligarh Muslim University, Aligarh 202002 INDIA.

Project Title- "Removal of crystal violet dye from aqueous solution PAni-Citrus sinesis composite as an efficient adsorbent"

Project Description-

- To adsorb toxic dye from water using low cost and natural adsorbent
- To examine various kinetic and adsorption isotherm models using UV-Visible Spectrophotometer.

Cumulative Grade Point Average (CGPA): 8.5 (First Division)

❖ **Bachelor of Science (B.Sc) in Chemistry (2013-2016):**

Women's College, Aligarh Muslim University, Aligarh 202002 INDIA.

Percentage: 69 (First Division)

❖ **Senior Secondary (2010-2011):**

CBSE

Percentage: 77 (First Division)

❖ **Higher Secondary (2008-2009):**

CBSE

Percentage: 73 (First Division)

❖ **WORK EXPERIENCE:**

❖ Expertise knowledge of synthesizing different type of sols using sol-gel technique

❖ Coating application by dip-coating and spray coating on metal surfaces such as mild steel

❖ Hands on experience in operating ***Electrochemical work station, Atomic Force Microscope, UV-Vis Spectrophotometer, Carbolite oven, Abrasive Cutting Machine, Precise Abrasive Cutter, Water Contact Angle, Dolly Testing for Scratch Test, Nabertherm Furnace, Zetasizer, Scanning Kelvin Probe, WeatherOmeter (ISO 11341) and Salt Spray Chamber (ASTM B117)***

❖ Expertise in data interpretation of various techniques such as FTIR, BET, XRD, SEM and TEM

❖ Expertise in using software's such as ZSimpwin, MENDLEY and Origin

❖ **OTHER SKILLS:**

❖ Guided many graduate and post-graduate students for their projects

❖ Good networking capabilities, communication and management skills

❖ Experience in writing technical papers, presentations and reports

❖ **REFERECES:**

1. Dr. R. Subasri

(Research Supervisor)

Head of Centre for Sol-gel Coatings

ARCI, Hyderabad-500005,

Telangana, India

Phone: +91-9849741875, 9014751191

E-mail: subasri@arci.res.in

2. Prof. K. V. Gobi

(Research Supervisor)

Professor,

Department of Chemistry,

National Institute of Technology

Warangal – 506004, Telangana, India.

Phone: +91-9701047107

E-Mail: kvgobichem@nitw.ac.in